Absolute Instability in Curved Liquid Jets

by

Rachan Bassi

A thesis submitted to
The University of Birmingham
for the degree of
DOCTOR OF PHILOSOPHY

School of Mathematics
The University of Birmingham
February 2011

Abstract

We present a study of absolute instability in liquid jets paying particular attention to curved jets formed in the industrial process of prilling. We illustrate the different types of break-up modes identified in experiments on curved jets and also explain the mathematical model used to describe them. Using this mathematical model, we study absolute instability in curved jets undergoing Mode 4 type break-up. The study is extended by including the effects of the density ratio of the liquid to the surrounding gas and gravity. We carry out an experimental study on curved liquid jets concentrating on the Mode 4 break-up regime. Our theoretical results are compared with experiments and very good agreement is found between the two. In addition, we examine absolute instability in thin ligaments that are formed as the jet approaches break-up. This study indicates that the jet undergoes a local absolute instability at pinch-off around its break-up point. A brief investigation of absolute instability in curved non-Newtonian jets is also carried out finding parameters corresponding to convective and absolute instabilities. We also look at jets on very small scales (having radius of the order of micrometers and nanometers) using the interface formation model. The results obtained by using the interface formation model are compared to the classical continuum model and molecular dynamics simulations.

Acknowledgements

Firstly, I would like to thank my supervisors, Professor Steve Decent and Dr. Mark Simmons. I am especially grateful to Professor Steve Decent and would like to express my sincere gratitude for his invaluable guidance and support throughout the writing of this thesis. I would also like to express my thanks to Chris Gurney for undertaking the tiresome task of proofreading my thesis and for all the useful discussions on jets. A special thanks goes out to Vicki Hawkins for sharing her experimental expertise and suggestions.

I would like to take this opportunity to acknowledge the tremendous love and support I received from my late aunt, Manjit Kaur, and would like to thank her for being more than just an aunt, for being my best friend and guide. I dedicate this thesis to her memory. I would like to thank my parents; without their best wishes and prayers this work would have never been possible. I am indebted to my mother for demonstrating what perseverance and determination can accomplish and to my father for instilling in me the importance of hard work and diligence. To my brother, Gurdish, for providing all the free holidays, fun and distractions from my work and for guiding me through the thick and thin of student life. To my sister, Nirjit, for never failing to bring a smile to my face when things look grey. To Daman, for all those pearls of wisdom because she is the 'older and wiser one'. I would also like to thank the '315 crew' for sharing all the ridiculous sporcle quizzes and introducing me to my true love, Troy. I am also very thankful to Postgrad Mathletic for making me their official head cheerleader.

I also acknowledge the financial support from the School of Mathematics.

Contents

Chapter 1

Introduction and Literature Review

In fluid mechanics, a jet can be described as a cylindrical column of fluid with disturbances travelling along its surface which consequently lead to its disintegration into droplets. Liquid jets form a subset of free-surface flows and span a broad range of applications in engineering, agriculture, inkjet printing, fuel injection and various other scientific fields. As the disturbances on the surface of the jet grow and rupture is approached, the radius of the jet becomes infinitesimally small. This topological transition causes the velocity to diverge and tend to infinity leading to a singularity in the equations of motion. These technical aspects of jet break-up along with their vast applications have motivated researchers over the years to attain a better understanding of jet dynamics.

1.1 Literature Review

The earliest scientific literature on liquid jets appears in a book by Mariotte [43] who considered the flow of water emerging from the bottom of a container which eventually disintegrates to form droplets and asserted that gravity is responsible for jet break-up. Savart [56] was the first to experimentally observe liquid jets. He illustrated that jet break-up depends on an intrinsic property of fluid motion. Figure 1.1, taken from Savart's original paper, shows a jet breaking up into droplets of different sizes. He observed the

Figure 1.1: A figure taken from Savart [56] showing the formation of primary and satellite droplets as the jet breaks down.

formation of small satellite drops between the main primary drops. But it was Plateau [50] who described the real source of jet break-up. He observed that long wavelength disturbances make the jet unstable by reducing the surface area and therefore discovering the vital role played by surface energy (or surface tension) in jet break-up.

Rayleigh [54] described a linear stability mechanism for an infinitely long cylindrical column of incompressible fluid by including surface tension. He considered travelling wave modes of the form $\exp(ikx + \alpha t + is\theta)$ where x is the distance down the jet, t is time, θ is the azimuthal coordinate, k is the real wavenumber, s is an integer, $Re(\alpha)$ is the growth rate and $Im(\alpha)$ is the frequency. For temporally growing disturbances, Rayleigh derived the following eigenvalue relation

$$\alpha^2 = \left(\frac{\sigma}{\rho a^3}\right)\left(\frac{I_s^{'}(ka)(1 - s^2 - k^2a^2)ka}{I_s(ka)}\right), \tag{1.1}$$

where ρ is the density of the liquid, σ is surface tension and I_s is the modified Bessel function of order s. The disturbances are axisymmetric for $s = 0$ and the jet is stable for $ka > 1$ and unstable for $0 < ka < 1$. The maximum growth rate was found by maximising $Re(\alpha)$ in (1.1) and corresponds to wavenumber $ka = 0.697$. The disturbances grow fastest at this wavenumber. For $s \neq 0$ the disturbances are non-axisymmetric and do not grow with time. Therefore, these disturbances are said to be stable. A good agreement was found between Rayleigh's theoretical results and Savart's experimental results.

One of the first to study the effect of viscosity on the stability of a liquid jet under the influence of surface tension was Weber [69]. He showed that for a given liquid and nozzle radius, the break-up length of the jet depends linearly on its velocity. He observed that the wavenumber of the most unstable mode increases with viscosity, consequently

producing larger droplets and smaller growth rates leading to an increased break-up time.

Tomotika [61] studied the linear stability of a long cylindrical viscous thread of fluid enclosed by an outer viscous fluid. He found that the maximum growth rate of the disturbance and the corresponding wavelength were dependent on the ratio of the viscosities and densities of the two fluids.

Keller, Rubinow & Tu [32] observed that in jet experiments, disturbances on the surface of the jet appeared to travel in space rather than with time. Before then, all research on the stability of liquid jets had concentrated on Rayleigh's temporal instability, where disturbances are taken to grow with time and remain uniform in space. Keller *et al.* [32] proposed a more physically relevant stability analysis which looks at spatially growing disturbances; disturbances are small at the orifice and grow as they propagate downstream. Therefore, in spatial stability analysis they assumed the wavenumber k to be complex and frequency α to be imaginary.

The linear stability theory accurately governs the initial stages of jet break-up but fails to predict the formation of satellite drops. It assumes that the size of the droplets is approximately equal to the wavelength of the disturbance. In their experimental studies on liquid jets, Chaudhary & Maxworthy ([8], [9]), Donnelly & Galberson [15] and Goedde & Yuen [25] observed the formation of satellite drops formed from the fine threads between successive primary drops.

Yuen [72] studied the instability of a liquid jet by considering the nonlinear effect of the disturbance. He found that the cut-off wavenumber and growth rate, which distinguish the unstable modes from the stable ones, predicted by the linear theory were different from those found by including nonlinear effects. Lee [35] performed linear and nonlinear analyses using a one-dimensional model. He found that the nonlinear set of equations result in satellite drop formation. Pimbley & Lee [49] investigated the behaviour of satellite drops experimentally and theoretically. They observed that the formation of satellite drops almost vanishes if the distance between primary drops is five to seven times the jet diameter.

A one-dimensional nonlinear model was developed by Schulkes [57] for long wavelength disturbances. He found his equations to be different from those presented by Lee [35]. Using his more accurate equations, he was able to correct the irregularities between other models and Lee's model. By solving the model numerically, he concluded that satellite drops are always formed during jet break-up. Papageorgiou [47] considered inviscid and viscous liquid jets by developing similarity solutions close to the break-up region and matching them to the full set of equations describing the jet. He provided an analytic explanation for the dynamics beyond the pinch-off point.

Hilbing & Heister [28] used a boundary element method to study the nonlinear nature of the instability. Their theory predicts the formation of primary and satellite droplets for disturbances with a fixed wavelength. They found that the size and formation of satellite drops depends on the wavelength and magnitude of the disturbance and the Weber number.

As the jet approaches pinch-off, the radius of the jet becomes very small and tends to zero, while the velocity at this point diverges to infinity, leading to a singularity. Eggers' [18] studied this singularity which appears at the tip of the jet by using Navier-Stokes equations to derive a one-dimensional model describing the pinch-off region.

Kowalewski [34] examined the separation of droplets from a liquid jet experimentally. As the jet approaches break-up, the formation of a very fine elongated neck is observed which connects the droplet to the jet. The features of this thread were investigated in terms of viscosity and jet radius. The radius of the thread just before break-up was found to be constant (of the order of micrometers) and independent of the effect of viscosity. On increasing the viscosity, the length of the thread was observed to increase. On comparison with Eggers' [18] results, Kowalewski's predictions show good agreement for the shape of the jet before it breaks up but Eggers' model fails to predict the correct retraction velocity and multiple jet break-ups.

The Weber number (defined as $We = \rho a U^2/\gamma$, where ρ is the density of the fluid, a is the radius of the orifice from which the jet emerges, U is the exit velocity of the

jet and γ is surface tension) is found to strongly affect the stability of a liquid jet. At $We = 1$ a singularity has been identified in several jet flow situations. Baird & Davidson [1] studied straight annular jets neglecting the effects of gravity. For $We > 1$, long thin jets are formed. However, at $We = 1$ they observed discontinuity in the jets. The large minisci of the jet at the base was believed to be the source of this singularity. Finnicum *et al.* [23] looked at the shape of a two-dimensional curtain falling under gravity. They found that the singularity at $We = 1$ can be eliminated if the curtain leaves the nozzle in a given direction. For $We < 1$, where the curtain is unstable to small disturbances, they found that the angle with which the curtain leaves the nozzle affects the stability of the jet. Ramos [53] examined inviscid incompressible axisymmetric annular liquid jets and derived a one-dimensional hydraulic model. For $We < 1$, he found that the jets form a circular arc and therefore the long wavelength approximation becomes invalid for $We < 1$.

The vast applications of non-Newtonian fluids have led various authors to extend research work on liquid jets to include non-Newtonian effects. This has mainly been done using the most common models applied to study non-Newtonian fluids: the Power-Law and Carreau rheologies. Doshi *et al.* [16] examined the effect of inertia as break-up is approached by carrying out an asymptotic study of the break-up dynamics of liquid bridges of non-Newtonian fluids. They found that the inertial forces become crucial as break-up is approached. Dravid *et al.* [17] developed a computational model which calculates the evolution of the non-Newtonian jet. Good agreement was found between their theoretical computations and experimental results. They also established that the non-Newtonian nature of the fluid enables control of the formation of satellite drops.

Li and Fontelos [38] and Clasen *et al.* [11] carried out a detailed study of the 'beads on a string' shape that the non-Newtonian jet takes as the surface tension driven non-linear disturbances grow on its surface. Li and Fontelos [38] found in their study that drop migration and oscillation are mainly caused by the elastic forces of the viscoelastic fluid. They also determined that these elastic forces not only impact drop migration and oscillation but also play a crucial role in the drop draining process, which involves the

liquid travelling from smaller drops into larger drops mainly due to the high capillary pressure in the smaller droplets.

Balmforth *et al.* [2] studied the flow of superposed fluid down an inclined plane by applying a lubrication approximation to the governing non-Newtonian equations using a Power-Law model. Hwang *et. al* [29] also looked at flow down an inclined plane using the Power-Law rheology and carried out a linear stability analysis. They concluded that when n (the power law exponent) is fixed, increasing the Reynolds number or decreasing the Weber number will destabilise the film flow. When only n is decreased, it results in a more unstable flow and a faster dimensional wave speed. Berezin *et al.* [3] included gravity into their study of a thin film flowing down an inclined plane, which can be modelled via the Power-Law model. They determined that when inertia is ignored, the flow is stable for small linear perturbations, while on the other hand, when inertia is included into the analysis its stability depends upon a critical Ostwald-de Waele number, O. Most studies in the past have mainly concentrated on straight non-Newtonian liquid jets. Uddin [65] studied the non-Newtonian effects on the centreline of a curved jet emerging from a rotating cylindrical container and carried out a linear stability analysis. This work is described in more detail in Chapter 8.

So far we have discussed what is termed as convective instability, where disturbances grow and propagate in a particular direction on the surface of the jet. Within convective instability there are two basic types: temporal and spatial instability. There is another type of instability, known as absolute instability which was first introduced in the context of plasma physics by Briggs [7]. Here the disturbance is observed to propagate not only in the downstream direction but also in the upstream direction. In convective instability, the disturbances propagate away from their point of origin, leaving the jet undisturbed as they travel away from it in the downstream direction; whereas in an absolutely unstable jet, the disturbance grows at its point of origin and causes instability as it travels away. A dripping jet is an example of absolute instability. Convective instability in liquid jets has been studied abundantly over the years. Some excellent reviews can be found in Yarin

[71], Chieger & Reitz [10], Eggers [19], Lin [39] and Eggers & Villermaux [22]. However, absolute instability in liquid jets is less studied.

Briggs [7] outlined a criterion for absolute instability by considering Fourier transforms of the dispersion relation of the system and solving it for the complex wavenumber and frequency. The Briggs criterion for absolute instability states that a disturbance of the form $e^{ikx+\omega t}$, where k and ω are complex, is absolutely unstable if it produces a solution to the dispersion relation which is a not only a saddle point but also a "pinch point" lying in the positive $Re(\omega)$ plane. A "pinch point" occurs as a result of an intersection between $k(\omega)$ curves in the complex ω-plane. This concept is explained in detail in Chapter 2.

The first to demonstrate the existence of absolute instability in liquid jets were Leib & Goldstein [37]. They showed that Rayleigh's capillary instability in a relatively slow moving inviscid incompressible jet eventually grows into absolute instability at small Weber numbers owing to surface tension. A critical Weber number which indicates a switch between convective and absolute instabilities was determined for an inviscid jet in the absence of gravity and ambient surrounding gas. The jet is absolutely unstable for $We < 3.15$ and convectively unstable for $We > 3.15$. Leib & Goldstein [36] included viscous effects into their previous analysis to determine the critical Weber number and compared it with the inviscid case. They found that the critical Weber number reduces with the inclusion of viscosity and is a function of the Reynolds number (defined as $Re = Ua/\nu$ where U is the exit velocity of the jet, a is the radius of the orifice and ν is kinematic viscosity). They obtained a critical curve in the Reynolds and Weber numbers plane separating the convective instability region from the absolute instability region. The jet is convectively unstable above this curve and absolutely unstable below it.

Lin & Lian [41] used the Briggs method to find the transition boundary between convective and absolute instabilities for an incompressible viscous liquid jet taking into account the density of the ambient surrounding gas. They found that by increasing the density ratio the absolute instability region is slightly enlarged, concluding that the critical Weber number is weakly dependent on the density ratio. Their method of finding

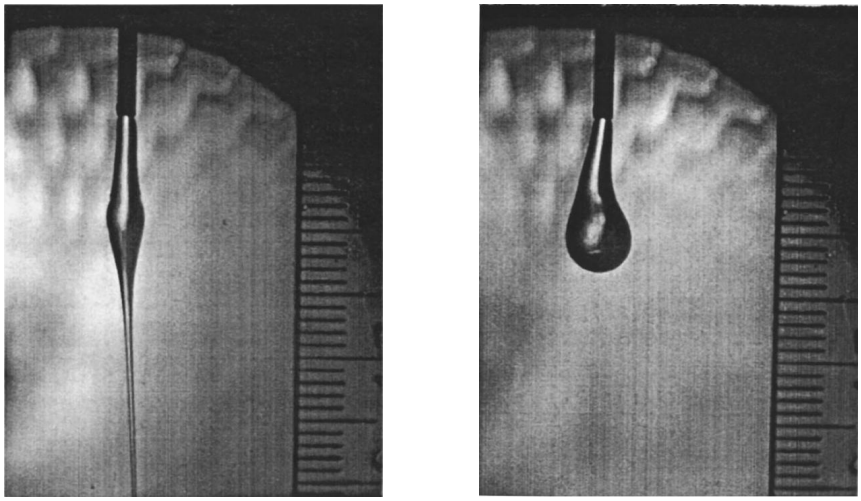

(a) 0.2 seconds after emerging from the nozzle.

(b) 0.4 seconds after emerging from the nozzle.

Figure 1.2: Photographs from [67] of a glycerin jet taken 0.2 and 0.4 seconds after emerging from the nozzle. In (a) the upstream propagating disturbance travels towards the nozzle forming a pendant drop while the disturbance propagating downstream grows along the fine thread before it detaches to form a drop. The photograph of the jet shown in (b) is taken after the droplet has detached from the jet.

the saddle point which marks the onset of absolute instability is described in more detail in Chapter 2. Lin & Lian [42] extended the parameter space by including the Froude number (incorporating gravity), viscosity, diameter and density ratios of the liquid and gas phases along with the Reynolds and Weber numbers. They found the critical curve to be only weakly dependent on the Froude number, viscosity and diameter ratios.

Zhou & Lin [73] studied absolute instability in an inviscid compressible jet. They found two kinds of absolute instabilities to exist, one caused by capillary pinching and the other by pressure fluctuations. They also found that compressibility of the surrounding fluid increases the domain of absolute instability.

Vihinen *et al.* [67] carried out experiments in order to study the physical appearance of a jet which undergoes a transition from convective to absolute instability neglecting the effects of gravity. They considered fluids having small Reynolds numbers in a microgravity environment using a NASA Lewis 2.2 sec Drop Tower. The disturbances were observed to travel in upstream and downstream directions as predicted by theory. Figure

1.2 taken from [67] shows a glycerin jet emerging from a nozzle. Figure 1.2(a) shows an absolutely unstable jet of glycerin 0.2 seconds after emerging from the nozzle. The disturbance travelling upstream towards the nozzle forms a pendant drop while the downstream propagating disturbance grows along the fine thread before it breaks up to from a droplet. Between 0.2 seconds and 0.4 seconds after emerging from the nozzle, the pendant drop detaches itself. Figure 1.2(b) shows the jet after 0.4 seconds.

O'Donnell *et al.* [46] experimentally determined the critical Weber number marking the onset of absolute instability by taking into account the effect of gas viscosity in a gravity free environment. Absolute instability in a viscous liquid jet surrounded by a viscous gas was found to exist even at large Reynolds numbers. However, they found no transition from dripping to jetting in their experiments.

1.2 Thesis Outline

This thesis concentrates on absolute instability of liquid jets. Liquid jets subject to convective instability have already been studied in much detail, with research still being carried out in this area. In the previous section we gave a brief literature review on the instability of liquid jets, describing work on both convective and absolute instabilities. Previous studies on absolute instability ([37], [41]) have looked only at straight jets. We extend the study of absolute instability to curved liquid jets.

In Chapter 2, we explain the work of Lin & Lian [41] in detail who determined a critical curve which marks the boundary between absolute and convective instability in the Reynolds and Weber numbers space. We reproduce the critical curve for large Reynolds numbers and also calculate the critical curve for smaller values of the Reynolds number than previous authors. The industrial process of prilling, used in the large scale manufacture of fertilisers and magnesium pellets, is introduced in Chapter 3. This chapter provides a brief overview of the theoretical and experimental work carried out on curved liquid jets at the University of Birmingham. The different regimes of break-up of curved liquid jets, identified in laboratory experiments by Wong *et al.* [70], are described. We

explain the mathematical model (discussed in [68]) used to describe curved liquid jets produced during the prilling process. Also, the linear stability analysis performed in [68] is presented and its results are discussed in this chapter.

Chapter 4 looks at absolute instability in curved liquid jets by using a multiple scales approach and introducing the concept of the local Reynolds and Weber numbers. Based on this concept, we determine a region in the Reynolds and Weber numbers plane (neglecting gravity), above the critical absolute instability curve in the convective instability region, where jets having Reynolds and Weber number values belonging to this region are initially convectively unstable but become absolutely unstable as they grow. These jets had been observed, but not fully understood, in [70]. This problem is extended in Chapter 5 by including the effects of gravity and density ratio of the liquid and the surrounding gas and examining their influence on absolute instability in curved liquid jets.

In Chapter 6, we carry out a comparison of our theoretical predications with experimental results of Wong *et al.* [70]. We also conduct original experiments concentrating on parameter regimes in which Wong *et al.* [70] found jets that were subject to absolute instability. In order to carry out a comparison with theory, we plot our experimental parameters in the Reynolds and Weber numbers space and examine their position with respect to the critical boundary determined theoretically in Chapter 2 and the regions which have Reynolds and Weber numbers corresponding to jets which start off as being convectively unstable but become absolutely unstable as they grow (found in Chapters 4 and 5).

Chapter 7 examines the effect of absolute instability on ligaments that are formed between the main primary drops as the jet approaches pinch-off. We use the nonlinear model derived in Parau *et al.* [51], presenting full jet equations in this chapter. These ligaments thin as the jet evolves in time and form a local absolute instability as pinch-off is approached causing the ligaments break-up and form satellite drops. In Chapter 8, we incorporate non-Newtonian effects into the curved jet model (as done in Uddin [65]) and study the impact of absolute instability on curved non-Newtonian jets. A primitive study

is carried out finding preliminary results for the three types of solutions.

Chapter 9 looks at jets on micron and nano scales. Here we use the interface formation model to study the instability of microjets and compare the results produced by the interface formation model to those produced by the classical continuum model and test their accuracy by comparing with molecular dynamics simulations.

Finally, in Chapter 10 we briefly discuss the main results obtained in this thesis and make suggestions for future work and further extensions of the research carried out in this thesis.

Chapter 2

Absolute Instability in Straight Liquid Jets

The onset of an instability in a liquid jet, which eventually leads to its break-up into droplets, is marked by the movement of wave packets along the length of the jet. If these disturbances cause the wave packets to travel in the downstream direction while leaving the flow behind them unaffected, the instability is said to be convective. On the other hand, the jet is said to be absolutely unstable if a disturbance on the surface of the jet, originating from a fixed point in space, causes wave packets to propagate in both upstream and downstream directions, disturbing flow along the length of the jet. Essentially, convective instabilities grow and propagate away from their point of origin, causing jet rupture elsewhere on the jet while leaving the jet at the point of origin of the instability unaffected; in comparison absolute instabilities propagate away from their point of origin, but destabilise the jet everywhere, including at their point of origin.

Rayleigh [54] introduced the classical linear stability analysis by considering temporally growing disturbances in infinitely long inviscid liquid jets. The temporal stability analysis involves travelling wave modes of the form $e^{ikx+\omega t}$ where k is the real wavenumber, ω is the complex frequency with $Re(\omega)$ denoting the temporal growth rate of the disturbance and $Im(\omega)$ the frequency, x is the distance along the jet and t is time. In this case, the disturbance grows exponentially with time along the length of the jet. The dispersion

relation $D(k,\omega)$ (1.1) is then solved for complex ω for a given real value of k. If $Re(\omega) > 0$ the flow is considered to be unstable. For $Re(\omega) = 0$ and $Re(\omega) < 0$, the flow is said to be neutrally stable and stable, respectively.

Keller, Rubinow & Tu [32] were the first to analyse the stability of liquid jets by taking into account spatially amplifying disturbances. When analysing spatial instability, the disturbance is considered to grow with distance. Therefore, the wavenumber k is assumed to be complex, so as to incorporate the spatial amplification rate, while ω is taken to be purely imaginary. The dispersion relation $D(k,\omega)$ is solved for k, for a given value of ω.

Spatial and temporal instabilities are both forms of convective instability. For a more general stability analysis, both k and ω are assumed to be complex. This allows a better investigation into the spatial and temporal nature of the instability leading to its classification into convective or absolute instability.

Briggs [7] and Bers [4] introduced the idea of absolute instability in the context of plasma physics. Briggs [7] presented a general criterion based on Fourier-Laplace integration of the Green's function of the system, i.e. the inverse of the dispersion relation, to distinguish between convective and absolute instability. According to the Briggs criterion for absolute instability of a wave mode of the form $e^{ikx+\omega t}$ with k and ω both complex, the solution of the dispersion relation $D(k,\omega)$ must have $Re(\omega) > 0$. This is a necessary but not a sufficient condition. For the flow to exhibit absolute instability, the solution of the dispersion relation must also be a saddle point formed by the coalescence of spatially amplifying curves in the complex k-plane originating from opposite sides of the real k axis, i.e. the saddle must get pinched between the loci of the solutions of the dispersion relation to suffice absolute instability. Therefore, the saddle point must also be, what is called a "pinch point". The group velocity, i.e. the velocity with which the wave packets propagate $\partial\omega/\partial k$, vanishes at the pinch point since it is a saddle point. In other words, absolute instability is an instability with zero group velocity. Since group velocity is the speed of propagation of energy, it explains why absolute instability corresponds to waves

which remain unstable at their point of origin.

In this chapter we look at absolute instability in straight liquid jets by studying the work of Leib & Goldstein [37] and Lin & Lian [41] in detail. They found a critical boundary in the Re-We space (where Re is the Reynolds number and We the Weber number) above which the flow is convectively unstable and absolutely unstable below it. We will explain how this critical boundary was obtained mathematically in the next section and develop an efficient method to determine this boundary in Section 2.2.

2.1 Lin's Method of Determining the Critical Weber Number

Leib & Goldstein [37] were the first to detect absolute instability in straight liquid jets in a vacuum. They determined a transition curve in the Re-We plane identifying the onset of absolute instability.

Following on from their work, Lin & Lian [41] studied absolute instability in a viscous liquid jet taking into account the density of the ambient surrounding gas in the absence of gravity. They considered a circular cylindrical jet of an incompressible viscous Newtonian fluid emanating from a nozzle into an inviscid gas. The usual equations of motion, i.e. the Navier-Stokes equations, conservation of mass equations and the free-surface boundary conditions, were applied to the liquid and gas phases. The undisturbed radius of the jet r_0 and U, the uniform undisturbed jet velocity, serve as the exact steady solution to these differential equations subject to the standard boundary conditions and correspond to a basic state which is physically unstable. Fourier analysis of this basic state with respect to the normal mode disturbance $C_0 e^{\omega\tau + iky}$ in a reference frame that has its origin at the centre of the nozzle, results in the following dispersion relation (Sterling & Sleicher [60]

Quantity	Symbol
Undisturbed radius of the jet	r_0
Uniform undisturbed jet velocity	U
Non-dimensional time	τ
Non-dimensional axial length	y
Complex frequency	ω
Complex wavenumber	k
Density of liquid	ρ_1
Density of gas	ρ_2
Surface tension	σ
Kinematic viscosity	ν

Table 2.1: Physical Quantities

and Lin & Kang [40])

$$(\omega - ik)^2 + \frac{2k^2}{Re}\left(\frac{I_1'(k)}{I_0(k)} - \frac{2k\lambda}{\lambda^2+k^2}\frac{I_1(k)I_1'(\lambda)}{I_0(k)I_1(\lambda)}\right) \times (\omega - ik) + \quad \omega^2 Q \frac{\lambda^2 - k^2}{\lambda^2 + k^2}\frac{K_0(k)I_1(k)}{K_1(k)I_0(k)} \tag{2.1}$$

$$-\frac{1}{We}k(1-k^2)\frac{\lambda^2-k^2}{\lambda^2+k^2}\frac{I_1(k)}{I_0(k)} = 0$$

where λ is described by the relation

$$\lambda^2 = k^2 + Re(\omega - ik). \tag{2.2}$$

Table 2.1 summarises all the quantities. Here C_0 is the wave amplitude, τ is non-dimensional time normalised with respect to r_0/U_0, $\omega = \omega_r + i\omega_i$ is the complex frequency such that ω_r gives the temporal growth rate of the disturbances and ω_i gives the frequency of the disturbances, $k = k_r + ik_i$ is the complex wavenumber with k_r the wavenumber and k_i gives the spatial amplification rate of the disturbance, y gives the non-dimensional axial length of the jet measured in the opposite direction of the flow and non-dimensionalised with respect to r_0 and I and K are modified Bessel functions of the first and second kind, respectively, with subscripts denoting the order of the functions. Also, dashes denote differentiation. Here Re, We and Q denote the Reynolds number, Weber number and the

Parameter	Description
Reynolds number	$Re = Ur_0/\nu_1$
Weber number	$We = \rho_1 U^2 r_0/\sigma$
Density ratio	$Q = \rho_2/\rho_1$
Critical Weber number	We_c-Weber number value which marks the transition from convective to absolute instability

Table 2.2: Dimensionless parameters

density ratio, respectively, and are defined as

$$Re = \frac{Ur_0}{\nu_1}, \quad We = \frac{\rho_1 U^2 r_0}{\sigma}, \quad Q = \frac{\rho_2}{\rho_1}, \tag{2.3}$$

where ν is the kinematic viscosity, ρ the density and σ surface tension. Subscripts 1 and 2 correspond to liquid and gas phases, respectively. The group velocity of the disturbance, i.e. the velocity with which a wave packet travels, is given by $\partial\omega_i/\partial k_r$. The dimensional wavelength of the disturbances is therefore equal to $r_0/(2\pi k_r)$. Table 2.2 summarises all the dimensionless parameters used.

For a given set of parameters, the dispersion relation can be solved for two different results, (i) the loci of the two roots and (ii) the spatial amplification curves. These loci are a set of points in the complex k-plane found by solving the dispersion relation (2.1) for k by keeping ω_i constant and reducing ω_r from a constant positive value down to zero. The spatial amplification curves were found by solving the dispersion relation (2.1) for k by setting $\omega_r = 0$ and varying ω_i down to zero. For spatially growing disturbances, the loci curves move towards the spatial amplification curves as ω_r is reduced to zero.

The saddles are found by looking for solutions to (2.1) at which $\partial\omega/\partial k = 0$. At the saddle point, $\omega_r > 0$, which is a necessary but not a sufficient condition for absolute instability as found by Briggs [7]. Not every saddle point in the complex k-plane gives rise to absolute instability. According to the Briggs [7] criterion for absolute instability, the saddle point must also be a pinch point in the complex k-plane. The upper and

lower branches of the spatial amplification curves move closer to each other as the Weber number decreases. As the Weber number is reduced further, it reaches a critical value which marks the transition from convective to absolute instability. At the critical Weber number We_c, where pinching of the saddle occurs, the upper and lower branches of the spatial amplification curves intersect at the saddle. At this pinch point, the group velocity, $\partial\omega/\partial k = 0$. Reducing the Weber number below its critical value, reveals that the upper and lower branches of the spatial amplification curves split and form new branches. The upper half of the upper branch connects itself to the upper half of the lower branch and the lower half of the upper branch connects to the lower half of the lower branch.

This transition is shown in Figures 2.1, 2.2 and 2.3, where a Newton-Raphson algorithm is used to solve the dispersion relation numerically. These figures show the occurrence of a pinch point in the complex k-plane. The red and green curves (in Figures 2.1 and 2.2) on either side of the saddle point are the spatial amplification curves obtained by plotting the solution of the dispersion relation (2.1) for $Re(\omega) = 0$ and slowly increasing $Im(\omega)$ from 0 to 10. Each point on the curves represents a solution of the dispersion relation for $Re(\omega) = 0$ and fixed $Im(\omega)$. In Figure 2.1, the Weber number is above its critical value We_c and therefore lies in the convective instability region. The spatial amplification curves shown in Figure 2.2 are obtained by reducing the Weber number so it is just above We_c. As We approaches We_c, the spatial amplification curve moves closer to the saddle point, as shown in Figure 2.2. After intersecting at the pinch point, which appears at $We_c = 2.209$ for the set of parameters used in this case (the method for determining this critical value is described in the next section), the branches of the spatial amplification curves split up and form new branches by joining the upper and lower halves of the green and red curves from Figure 2.1. Figure 2.3 shows the new spatial amplification curves for $We < We_c$ in the absolute instability region. The existence of a pinch point in the complex k-plane confirms the transition from convective to absolute instability. Note that in Figures 2.1 and 2.2, $Re(\omega) < 0$ at the saddle. In Figure 2.3, $Re(\omega) > 0$ at the saddle point. Briggs [7] showed that $Re(\omega) = 0$ at the pinch point when $We = We_c$.

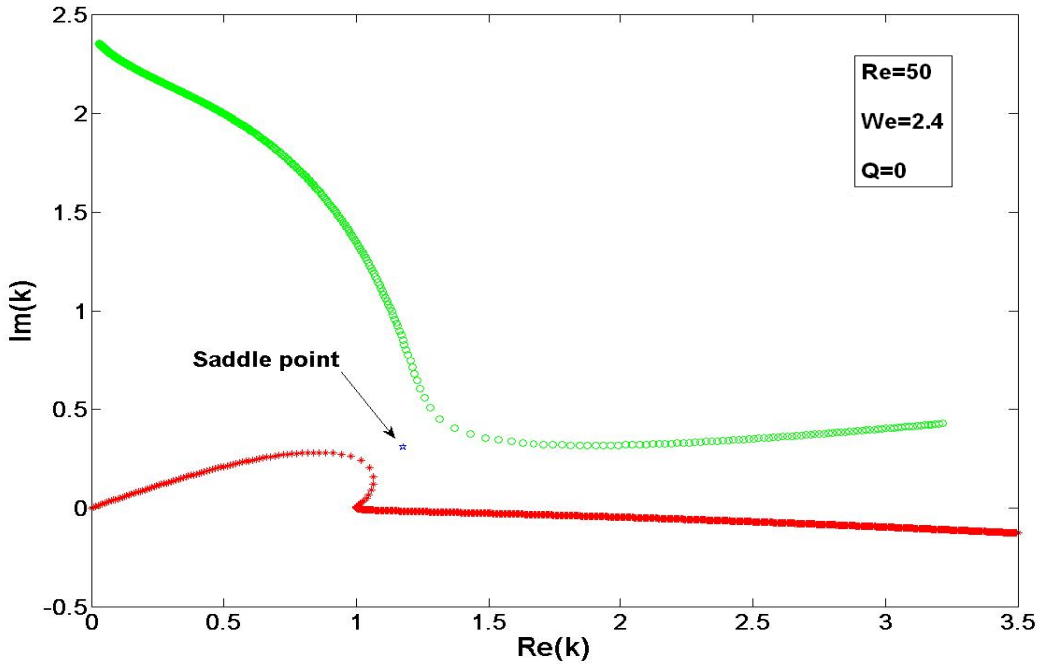

Figure 2.1: Graph showing the spatial amplification curves in the complex k-plane for $We = 2.4$ ($We > We_c$). Here $Re(\omega) < 0$ at the saddle point. $We_c = 2.209$ at $Re = 50$.

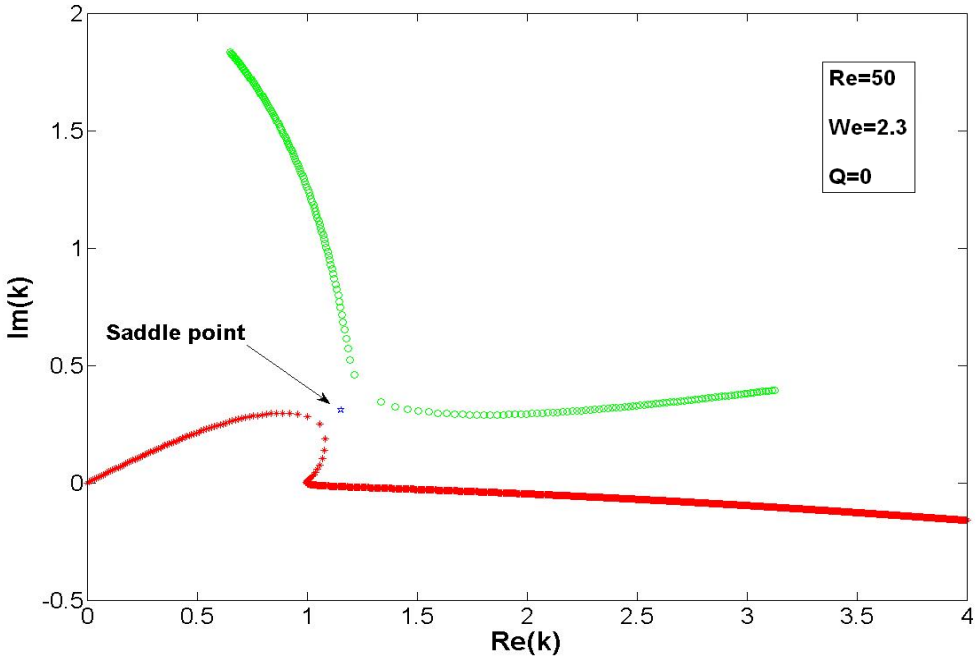

Figure 2.2: Graph showing the spatial amplification curves in the complex k-plane for $We = 2.3$ ($We > We_c$). As We is reduced, the branches move closer to the saddle point. Here $Re(\omega) < 0$ at the saddle point. $We_c = 2.209$ at $Re = 50$.

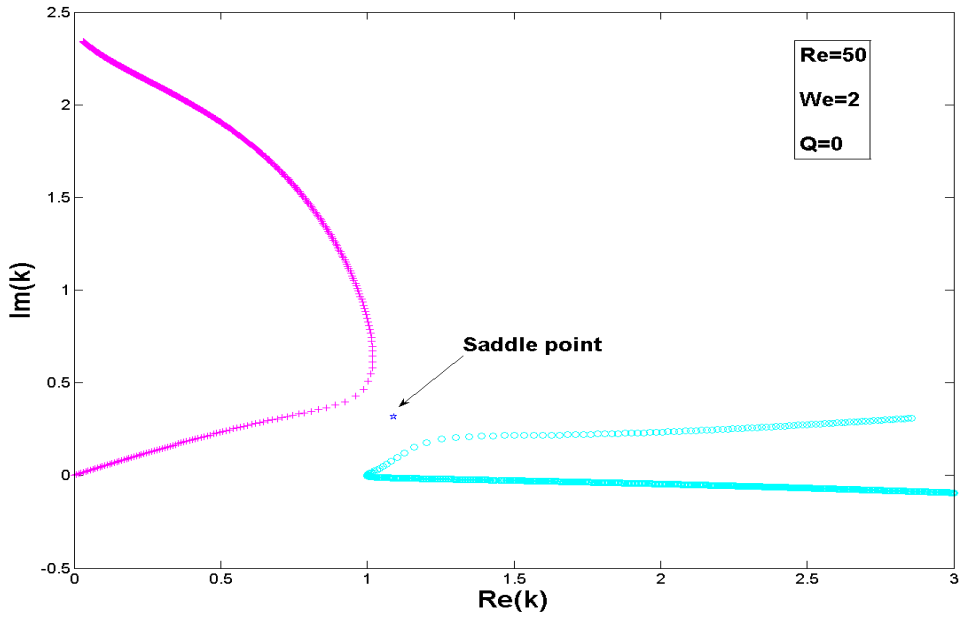

Figure 2.3: Graph showing the spatial amplification curves in the complex k-plane for $We < We_c$. At this stage, pinching has occurred and the upper and lower branches have disconnected and formed new branches. The upper half of the green branch in Figure 2.2 joins the upper half of the red branch and the lower half of the green branch joins the lower half of the red branch. Here $Re(\omega) > 0$ at the saddle point. $We_c = 2.209$ at $Re = 50$.

By repeating this process Lin & Lian [41] determined We_c for different values of the Reynolds number Re. The value of We_c at various Re is plotted in the Re-We plane making a 'critical curve' that marks the onset of absolute instability. The flow is absolutely unstable in the region under the critical curve and convectively unstable above it. They found the area under the critical curve to increase with density ratio Q. They also found that $Re(\omega)$ at the saddle point always changes sign on the critical curve. Leib and Goldstein [37] observed the same scenario but with zero density ratio, $Q = 0$. For the rest of this chapter we will consider $Q = 0$. We shall examine $Q > 0$ in Chapter 5.

2.2 Finding the Critical Weber Number

In this section, a more efficient method of finding the critical Weber number is obtained. Instead of carrying out a tedious search for the saddle pinch point in the complex k-plane, by solving the dispersion relation for various values of ω for a given set of parameters, a

different approach is applied in this section.

We solve the dispersion relation (2.1) for complex ω and k. Let (2.1) be denoted by

$$F(\omega(k), k) = 0. \tag{2.4}$$

Differentiating (2.4) once with respect to k, we obtain

$$G\left(\frac{\partial\omega}{\partial k}, \omega, k\right) = \frac{\partial}{\partial k}F(\omega(k), k). \tag{2.5}$$

At the onset of absolute instability the group velocity of the disturbance is zero, i.e. $\partial\omega/\partial k = 0$. Therefore, setting $\partial\omega/\partial k = 0$ in (2.5) gives

$$G\left(\frac{\partial\omega}{\partial k} = 0, \omega, k\right) = 0. \tag{2.6}$$

In other words, (2.6) is obtained by differentiating (2.1) with respect to k and then setting $\partial\omega/\partial k = 0$. Solving (2.4) and (2.6) simultaneously we obtain ω and k values which correspond to absolute instability at the saddle points. This was solved computationally using a two-dimensional Newton-Raphson method. Verification of the saddle point is done by checking $\partial F/\partial k_r = 0$ and $\partial F/\partial k_i = 0$ where $k = k_r + ik_i$.

To find We_c, the movement of the saddle point in the complex ω-plane is monitored as the Weber number is increased, keeping all other parameters constant. For a fixed Reynolds number, a We value below Lin's [41] critical curve is chosen. The Newton-Raphson algorithm starting with an initial guess for ω and k is used to find the ω and k values at the saddle point for that particular set of parameters. This process is repeated by gradually increasing We until it reaches a value at which ω_r changes sign from positive to negative (i.e. We value at which transition from absolute to convective instability takes place). This value of We marks the boundary of the critical curve between the absolute and convective instability regions and is the critical Weber number, We_c.

For various Reynolds numbers, a thorough search for We_c is carried out for several

initial values of ω and k. The signs of the initial values for ω_r, ω_i, k_r and k_i are changed in turn in the Newton-Raphson algorithm so that all possible combinations of these initial values originating from different quadrants of the complex ω and k planes are considered. (Since the equations are nonlinear the saddle points are unlikely to be unique.) This is done to ensure that $Re(\omega) > 0$ only in the absolute instability region and no solutions with $Re(\omega) > 0$ exist above the transition curve where the flow is considered to be convectively unstable. This rigorous search also confirms that the same We_c value is obtained irrespective of the signs or values of initial ω_r, ω_i, k_r and k_i put into the Newton-Raphson solver.

For a given Reynolds number, sixteen different initial conditions are used in the Newton-Raphson method each having a different combination of signs of ω_r, ω_i, k_r and k_i. This was carried out for $Re = 20$, $Re = 50$ and $Re = 100$. The initial value of the Weber number is chosen so that it is less than its critical value for that particular Reynolds number from [41] and therefore lies below the expected critical curve in the Re-We plane. The Weber number is then increased gradually with an increment of 0.05 at each step and the solution of the dispersion relation is determined using the solution calculated at the previous We value as the initial condition for the next step in the Newton-Raphson solver. We is increased until $Re(\omega)$ changes sign from positive to negative. The value of We at which $Re(\omega)$ changes sign gives We_c for that particular Reynolds number Re. Figure 2.4(a) shows the movement of the saddle point in the complex ω-plane for $Re = 20$. The initial condition $\omega = 0.15 + 0.747i$ is used in the Newton-Raphson method to find the solution of the dispersion relation at $We = 1$ and $Re = 20$. The Weber number is then increased by 0.05 and the solution of the dispersion relation is calculated at $We = 1.05$ by using the solution determined in the previous iteration (at $We = 1$) as the next initial condition for the Newton-Raphson solver. This process is then repeated up to $We = 2$ in steps of 0.05. Figure 2.4(b) shows the corresponding k values as We is increased. This procedure is followed for $Re = 20, Re = 50$ and $Re = 100$ to examine the movement of the saddle point using sixteen different initial conditions to solve the dispersion relation

for each Reynolds number, so that each saddle originates with initial conditions from a different quadrant. Initial conditions for each case are marked on the graphs. Figures 2.4-2.6 show the resulting graphs for each Reynolds number for some of the initial conditions used. The We_c corresponds to the We value at which $Re(\omega) = 0$. It can be seen from Figures 2.4-2.6 that a consistent result for We_c is obtained for each Reynolds number irrespective of the initial condition used in the Newton-Raphson solver.

Using this method to determine We_c for several values of Re, the critical curve in the Re-We plane is obtained. Figures 2.7 and 2.8 show the critical curves plotted for small and large Reynolds numbers, respectively. The jet is absolutely unstable below the curve and convectively unstable above it. At each value of Re, the above process is repeated to obtain We_c. At a few isolated values of Re, further calculations confirmed that this transition corresponded to a pinch point, using the approach described in Figures 2.1, 2.2 and 2.3. But this was not done for every value of Re because of the large computational time required. The curve shown in Figure 2.7 is for values of Re below that considered in [37] and [41] where the We_c curve was plotted only for large values of the Reynolds number.

2.3 Conclusion

In this chapter we have explained the approach used in [37] and [41] to determine the critical Weber number which marks the onset of absolute instability and have shown the existence of pinch points in the complex k-plane by applying a Newton-Raphson algorithm to solve the dispersion relation for $Re(\omega) = 0$ and constant $Im(\omega)$. We have also derived a more efficient technique for calculating the critical Weber number and have determined the critical boundary in the Re-We space indicating the transition between absolute and convective instability. The results confirm those of [37] and [41].

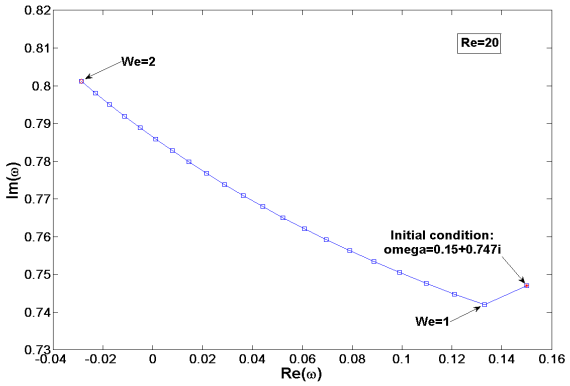

(a)

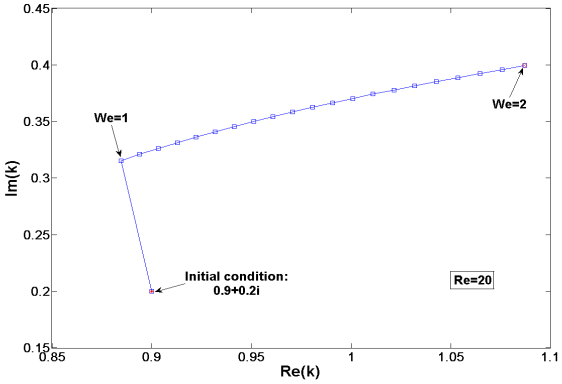

(b)

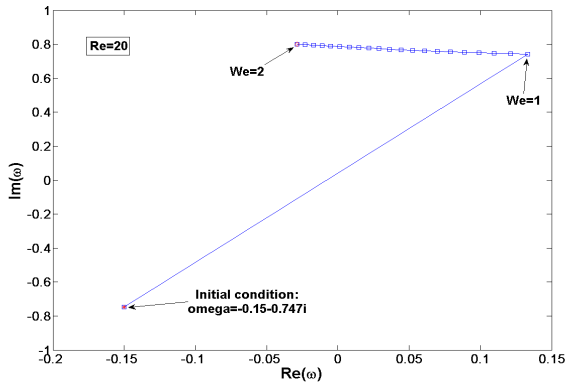

(c)

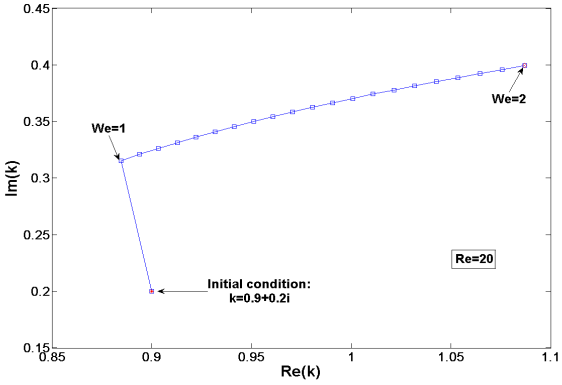

(d)

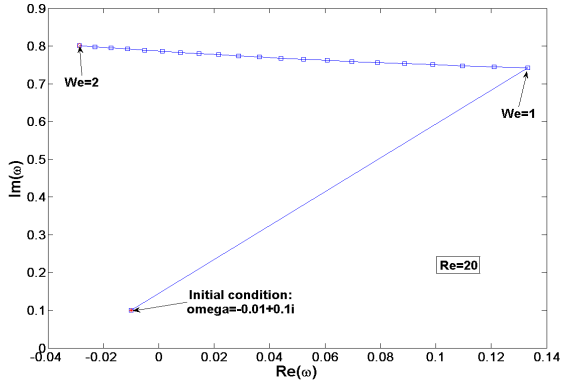

(e)

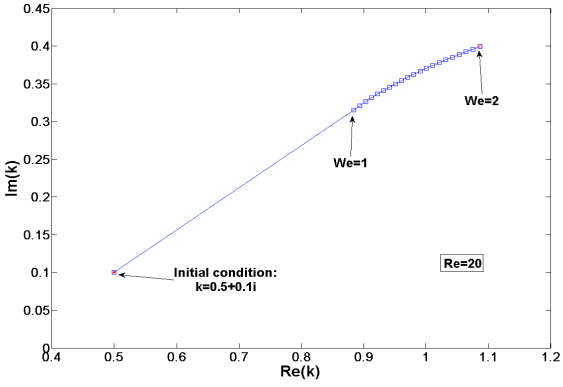

(f)

Figure 2.4: Graphs showing the movement of the saddle point in the complex ω and k planes with different initial conditions for $Re = 20$ as We is increased from 1 to 2 with an increment of 0.05 at each step. Initial conditions for ω and k used to solve the dispersion relation are given by: (a)-(b) $\omega = 0.15 + 0.747i, k = 0.9 + 0.2i$, (c)-(d) $\omega = -0.15 - 0.747i, k = 0.9 + 0.2i$ and (e)-(f) $\omega = -0.01 + 0.1i, k = 0.5 + 0.1i$. $We_c = 1.7599$ at $Re = 20$. This procedure was repeated by computing the saddle point for this particular Re using initial conditions for k and ω with combinations for the initial values of ω_r, ω_i, k_r and k_i originating from every quadrant.

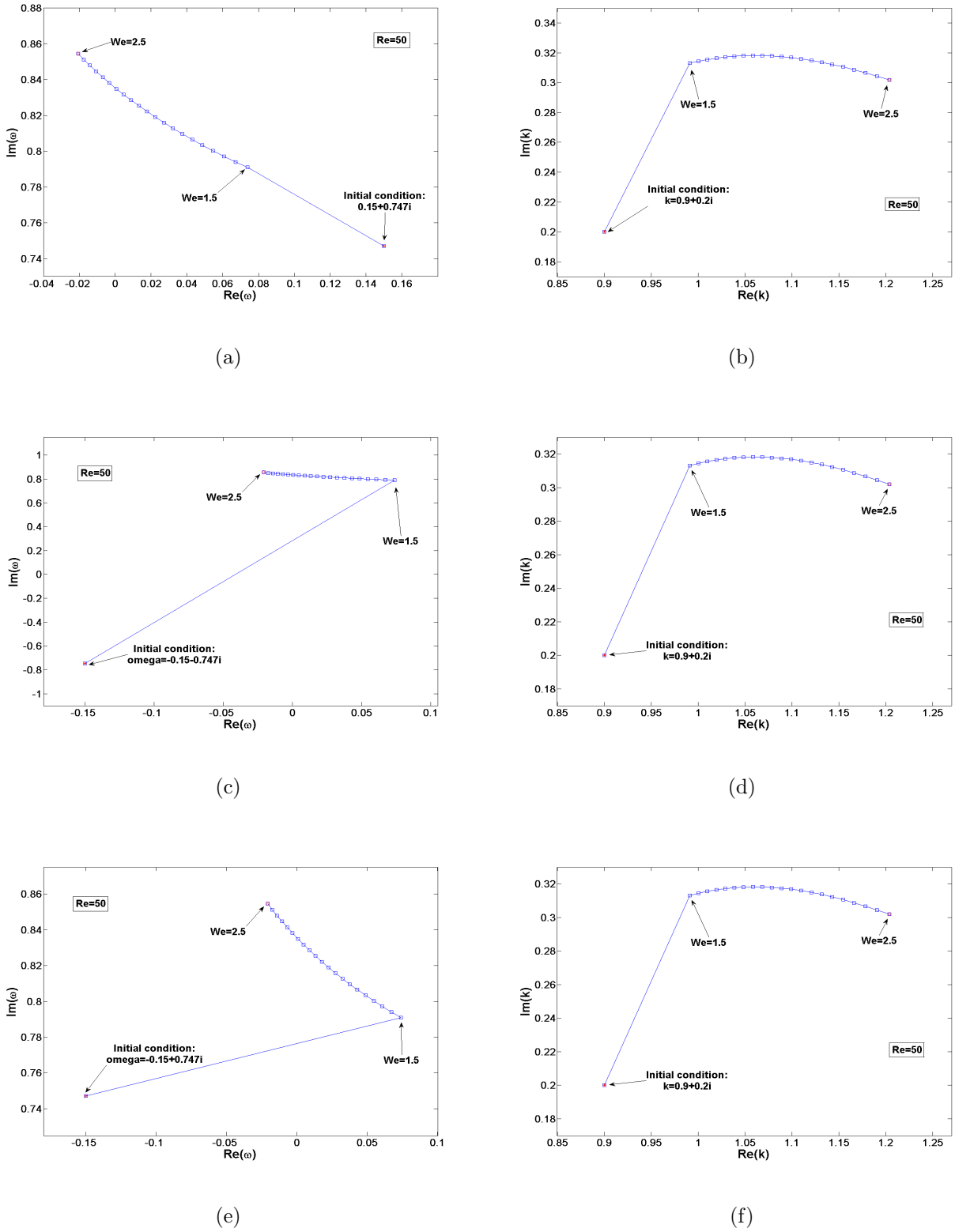

Figure 2.5: Graphs showing the movement of the saddle point in the complex ω and k planes with different initial conditions for $Re = 50$ as We is increased from 1.5 to 2.5 with an increment of 0.05 at each step. Initial conditions for ω and k used to solve the dispersion relation are given by: (a)-(b) $\omega = 0.15+0.747i, k = 0.9+0.2i$, (c)-(d) $\omega = -0.15-0.747i, k = 0.9+0.2i$ and (e)-(f) $\omega = -0.15 + 0.747i, k = 0.9 + 0.2i$. $We_c = 2.209$ at $Re = 50$. This procedure was repeated by computing the saddle point for this particular Re using initial conditions for k and ω with combinations for the initial values of ω_r, ω_i, k_r and k_i originating from every quadrant.

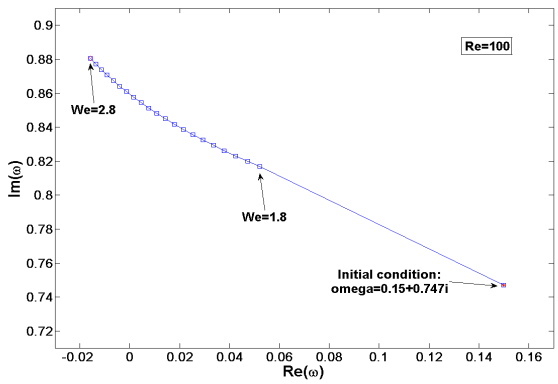

(a)

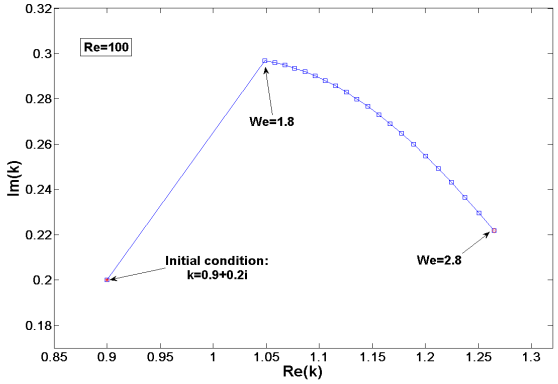

(b)

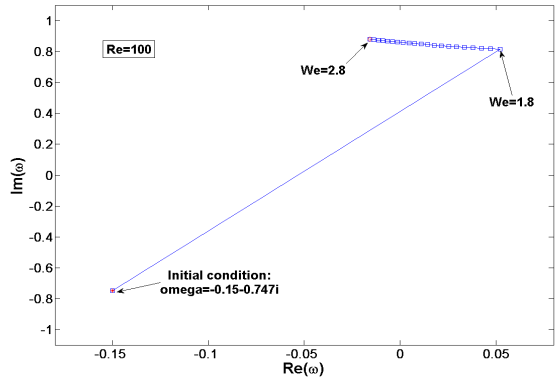

(c)

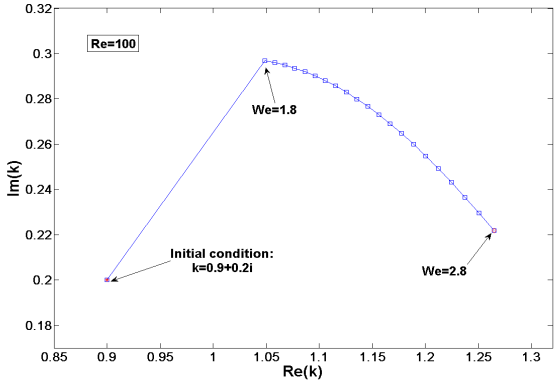

(d)

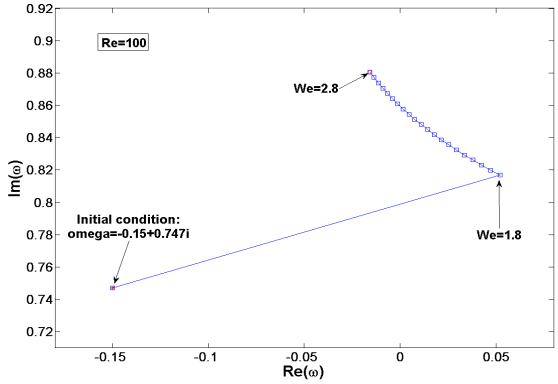

(e)

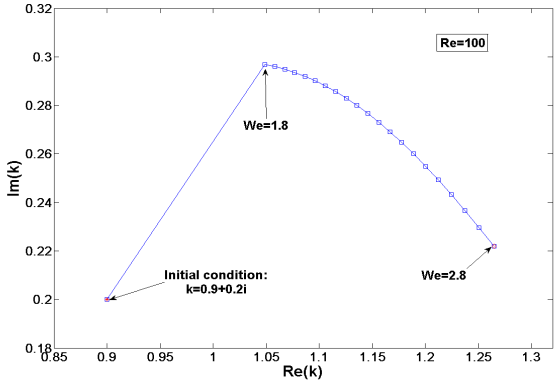

(f)

Figure 2.6: Graphs showing the movement of the saddle point in the complex ω and k planes with different initial conditions for $Re = 100$ as We is increased from 1.8 to 2.8 with an increment of 0.05 at each step. Initial conditions for ω and k used to solve the dispersion relation are given by: (a)-(b) $\omega = 0.15+0.747i, k = 0.9+0.2i$, (c)-(d) $\omega = -0.15-0.747i, k = 0.9+0.2i$ and (e)-(f) $\omega = -0.15 + 0.747i, k = 0.9 + 0.2i$. $We_c = 2.477$ at $Re = 100$. This procedure was repeated by computing the saddle point for this particular Re using initial conditions for k and ω with combinations for the initial values of ω_r, ω_i, k_r and k_i originating from every quadrant.

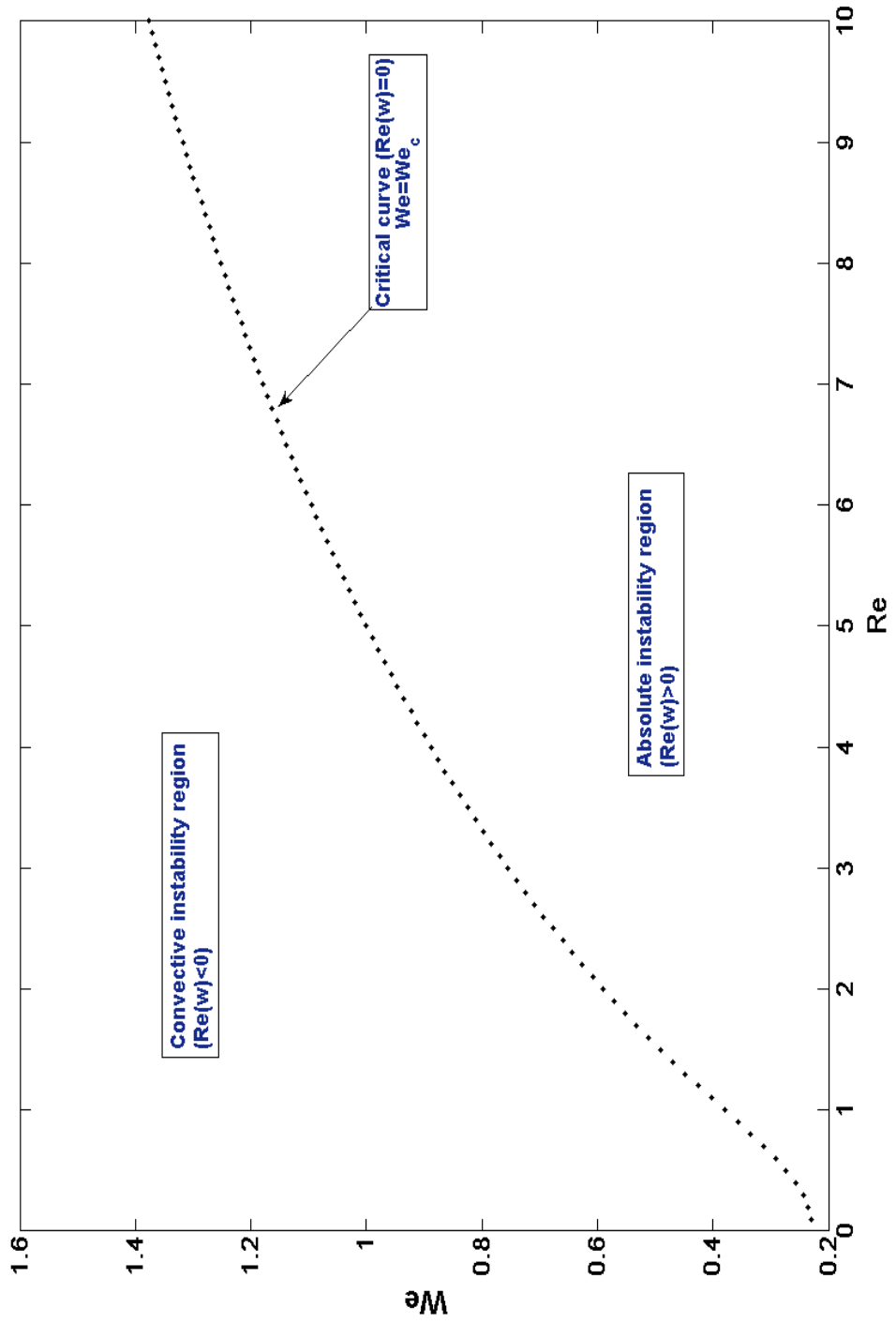

Figure 2.7: A plot of We against Re showing the critical Weber number values We_c for small ($0 < Re < 10$) Reynolds numbers. The jet is absolutely unstable in the region under the curve and convectively unstable above it.

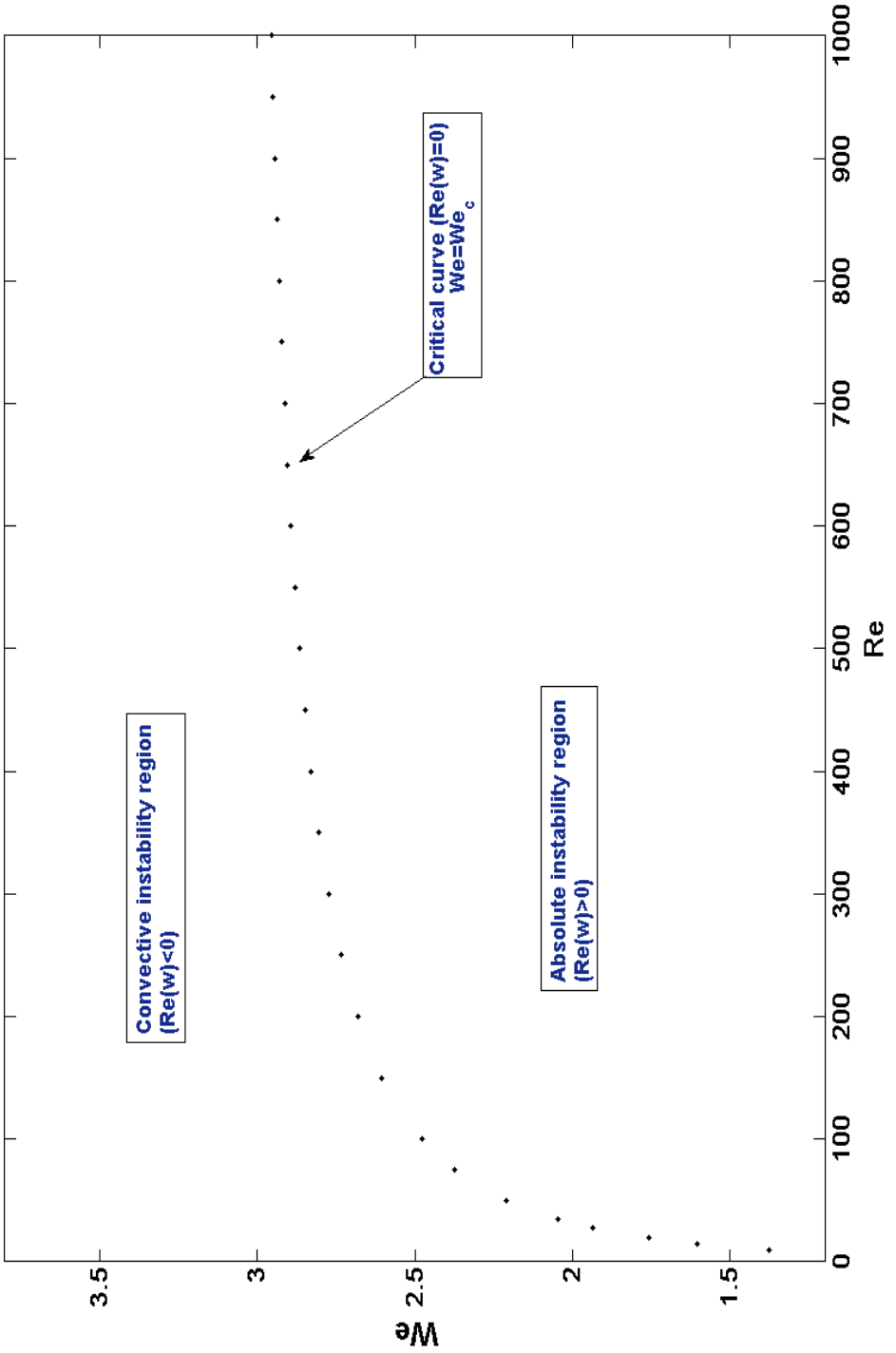

Figure 2.8: A plot of We_c against Re showing the critical Weber number values We_c for large ($0 < Re < 1000$) Reynolds numbers. The jet is absolutely unstable in the region under the curve and convectively unstable above it.

Chapter 3

A Brief Review of Curved Jets

So far we have reviewed absolute instability in straight jets and described the critical curve that marks the boundary between absolute and convective instability. Before moving on to examine the effect of absolute instability in curved liquid jets, we briefly review in this chapter the theoretical and experimental work carried out on curved jets at the University of Birmingham and introduce the model used to describe them. We start by introducing the industrial process of prilling which involves the large scale manufacture of fertilisers produced from the droplets formed through the break-up of curved liquid jets. Prilling is the primary motivation of the detailed and in-depth study of curved jets performed at the University of Birmingham.

3.1 Prilling

Prilling is a process used in industry for the large scale production of fertilisers and magnesium pellets. It involves the production of tiny droplets of molten fertiliser (or magnesium) which solidify to become fertiliser (or magnesium) pellets. A perforated cylindrical container filled with hot molten fertiliser (or magnesium) is placed at the top of a prilling tower where it is spun anti-clockwise about its axis. The centrifugal forces push the fluid out through the holes on the surface of the container leading to the formation of jets of molten liquid. These jets then break-up into droplets as a result of surface tension instabilities. The drops of liquid solidify as they fall freely after breaking

up and are collected at the bottom of the tower.

Norsk Hydro, a leading fertiliser company based in Norway, owns one of the largest prilling towers in the world, measuring about 30 m in height and 24 m in diameter. The cylindrical drum, suspended at the top of the prilling tower, into which the molten fertiliser is poured, is approximately 1 m high and 0.5 m wide and is drilled with approximately 2000 holes of diameter 4 mm around its cylindrical surface. Figure 3.1 shows the photograph of an industrial prilling can. Figure 3.2 shows jets emerging from the container and breaking up to form thousands of droplets which solidify to become fertiliser pellets. Formation of many unwanted satellite droplets between the main drops can also be observed. These satellite drops are formed due to the nonlinear nature of the instability on the surface of the jet. For economic reasons and to conserve energy and raw material, it is essential to maintain a uniformity in the size of these droplets.

3.2 Review of Experimental Work on Curved Jets

Experimental work in this area was carried out by Wong *et al.* [70] in the Department of Chemical Engineering at the University of Birmingham. They identified four different modes of break-up in curved liquid jets. Mode 4 is of particular interest to us due to its unique features (described in Section 3.2.1) which lead to the speculation of the existence of absolute instability in this break-up regime.

3.2.1 Break-Up Modes

Experiments performed in Wong *et al.* [70] adopt a similar experimental set-up to that used in prilling, but on a much smaller scale. The experimental methodology is presented in more detail in Chapter 6. The four break-up modes identified in [70] differ significantly in their break-up mechanisms and drop size distributions. We briefly describe the break-up modes in this section.

Mode 1: In this mode the waves on the surface of the jet are observed to travel downstream. As the surface tension driven instability grows, it causes the jet to break-up into droplets and leads to the rapid formation of primary drops. Very few or no satellite

Figure 3.1: A photograph of an industrial prilling container. Courtesy of GEA Niro A/S.

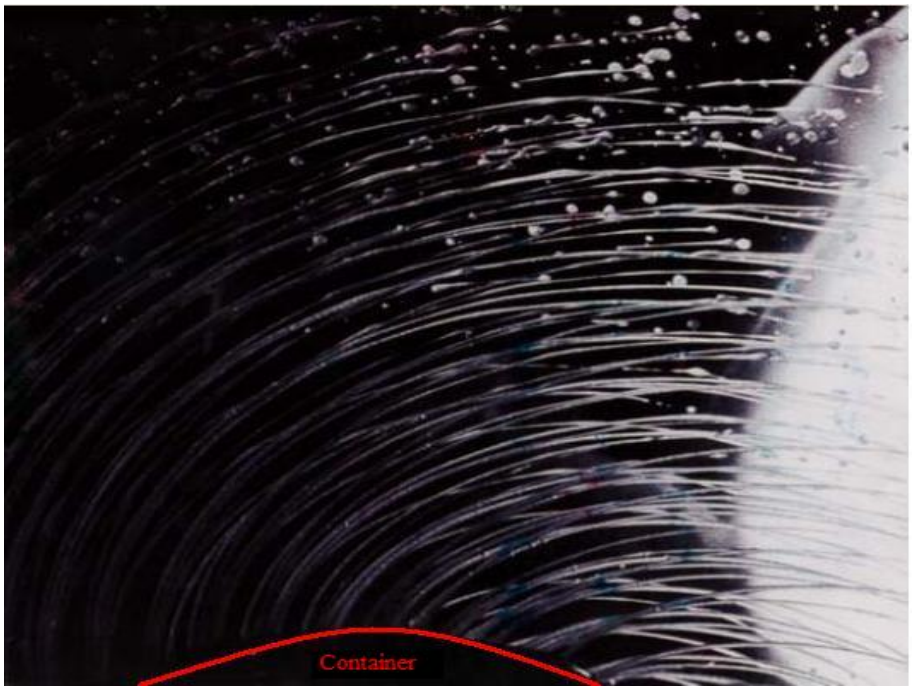

Figure 3.2: A photograph of jets emerging from a prilling can rotating anti-clockwise when viewed from above. The red curve marks the position of the can. Droplets formed as a result of jet break-up can also be seen. Photograph taken from [68].

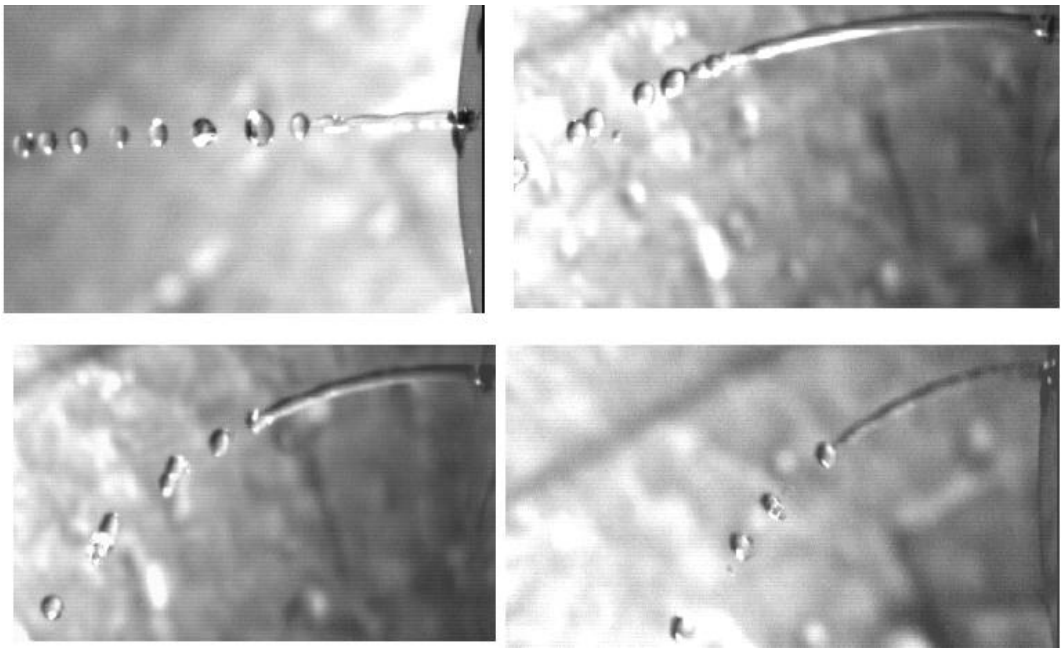

Figure 3.3: A sequence of photographs taken from [70] showing features of Mode 1 break-up. Very few satellite droplets can be seen in between primary droplets.

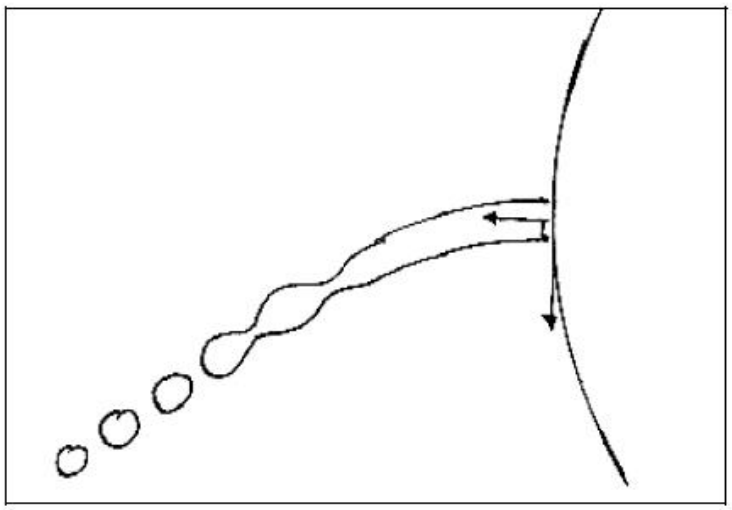

Figure 3.4: Sketch of Mode 1 break-up taken from [70].

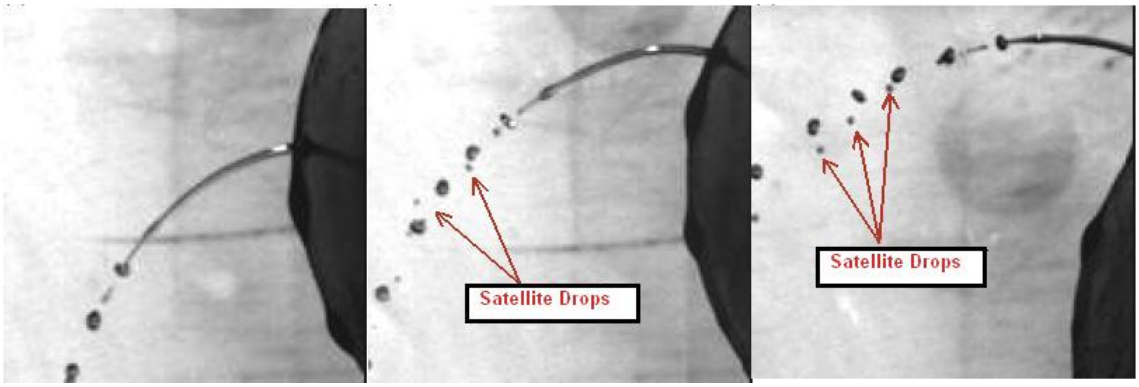

Figure 3.5: A sequence of photographs taken from [70] showing features of Mode 2 break-up. Satellite drops can be observed along with primary drops in this case.

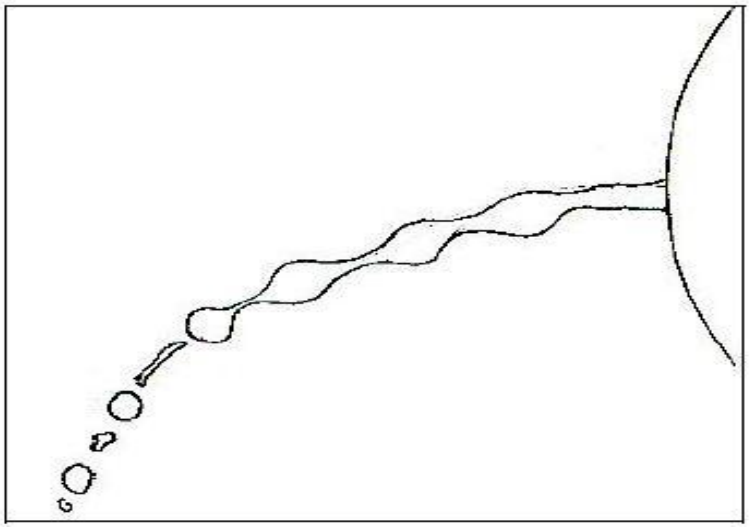

Figure 3.6: Sketch of Mode 2 break-up taken from taken from [70].

drops are formed in this case. For example, Mode 1 is observed in a water jet emerging from an orifice of diameter 0.001 m at a low rotation rate. Figure 3.3 shows a sequence of photographs displaying Mode 1 behaviour in this case and Figure 3.4 shows a sketch of Mode 1 break-up.

Mode 2: As the jet exit velocity is increased, transition from Mode 1 to Mode 2 occurs. Disturbances of short wavelength are seen growing rapidly on the surface of the jet. See Figures 3.5 and 3.6. Satellite drops are formed between primary drops from the fine ligaments of liquid that are created as the primary drops break off.

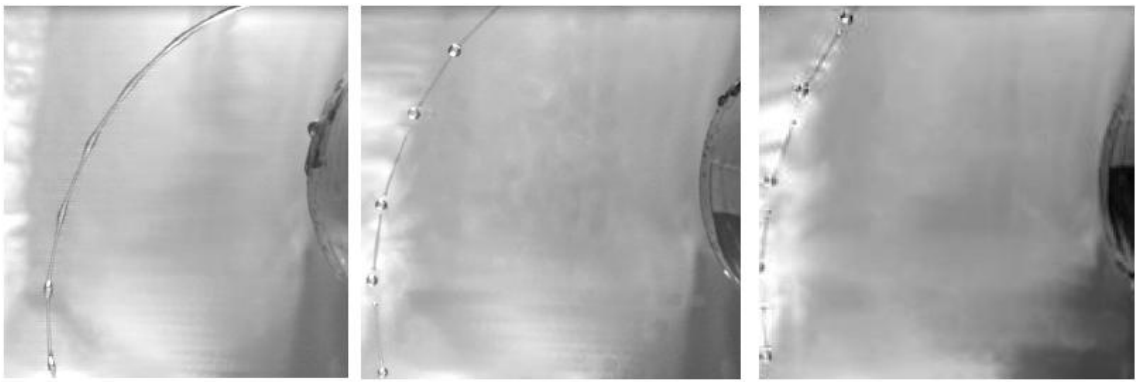

Figure 3.7: A sequence of photographs taken from [70] showing features of Mode 3 break-up. Long wavelength disturbances can be seen on the surface of the jet. Formation of satellite droplets is also observed.

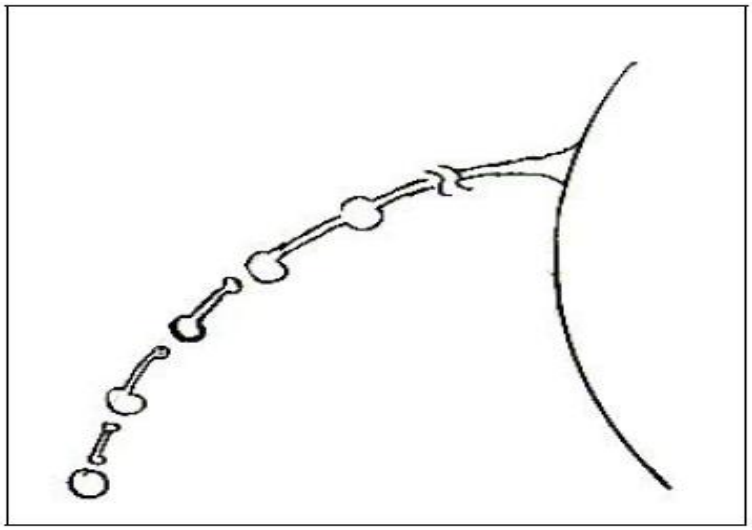

Figure 3.8: Sketch of Mode 3 break-up taken from [70].

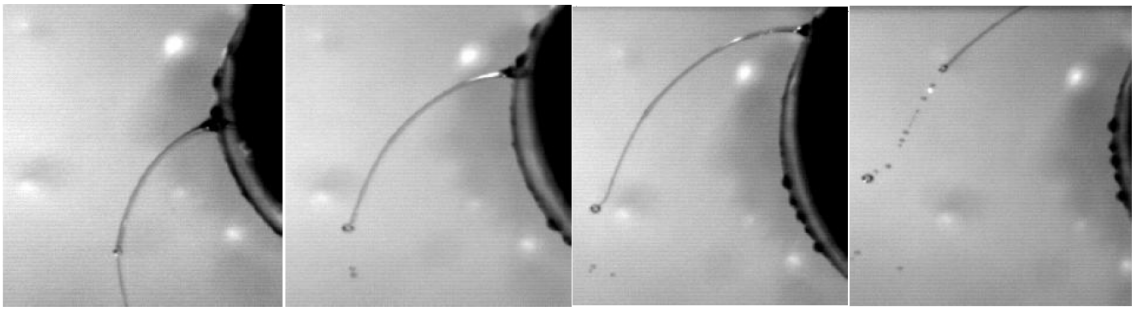

Figure 3.9: A sequence of photographs from [70] showing features of Mode 4 break-up. The photographs show the emergence of a bulge at the tip of the jet which causes the trajectory of the jet to alter.

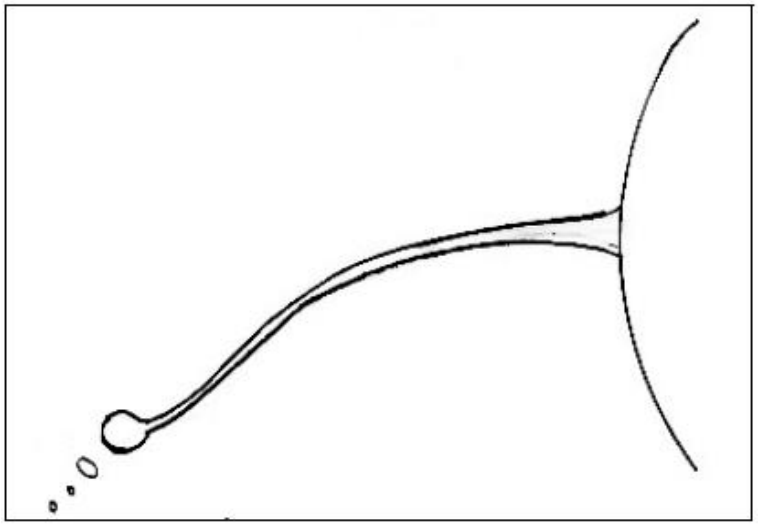

Figure 3.10: Sketch of Mode 4 break-up taken from [70].

Mode 3: This mode is observed in jets with a high exit velocity and high dynamic viscosity. See Figures 3.7 and 3.8. Disturbances with long wavelength are observed on the surface of the jet leading to its break-up at several points at the same time along the curved jet. Again satellite drops are formed from the liquid threads connecting the primary droplets.

Mode 4: This mode is observed in highly viscous liquids, with disturbances travelling upstream. The high viscosity suppresses the instability causing the jet to elongate. As the jet grows, it forms a bulge at its tip, the inertia of which alters the trajectory of the jet and disturbances are observed to travel towards the orifice. Finally, the jet becomes

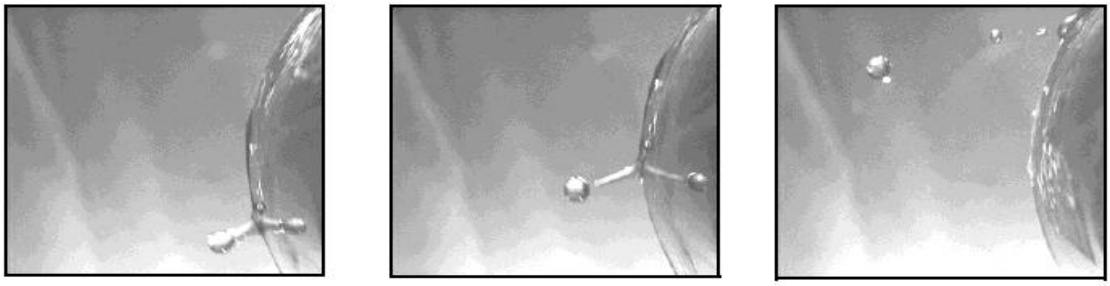

Figure 3.11: A sequence of photographs taken from [70] showing features of the No Jet situation.

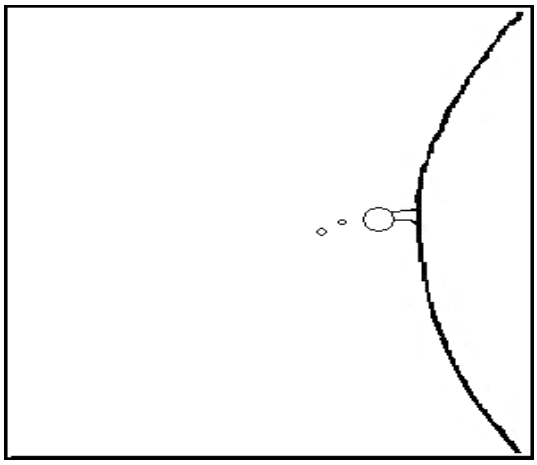

Figure 3.12: Sketch of the No Jet situation.

unstable and shatters to form satellite droplets. See Figures 3.9 and 3.10. A distinctive feature of this mode is the upstream propagation of disturbances that are observed on its surface at rupture. While the instabilities present in Modes 1-3 appear to be convective in nature, the upstream propagation of disturbances leads to the speculation of the existence of absolute instability in this jet. We believe that in Mode 4 the jet starts off as being convectively unstable near the orifice but eventually becomes absolutely unstable further down its length. Therefore, this mode is of particular interest in this thesis and will be studied in more detail mathematically.

In addition to the four modes identified above, another case was observed. At low rotation rates and low exit velocities the liquid starts dripping as soon as it leaves the orifice, even before a coherent jet is formed. This phenomenon is observed for $We < 1$. Figures 3.11 and 3.12 show the features of the No Jet situation. We believe that this flow is absolutely unstable at the orifice.

3.3 Review of Theoretical Work

In order to investigate the presence of absolute instability in Mode 4 and the No Jet situation in more detail, we use the mathematical model established in Wallwork [68]. This mathematical model is described in detail in the following section.

3.3.1 Mathematical Model for Curved Jets

To study the prilling problem mathematically, a theoretical model for curved jets was developed by Wallwork [68]. A liquid jet emanating from an orifice O of radius a located on the surface of a cylindrical container of radius s_0 rotating about its axis at a constant rate Ω is considered. A rotating reference frame (x, y, z) in which the position of the orifice is fixed is chosen to describe the problem. The position of the orifice is given by $(s_0, 0, 0)$ in the xyz coordinates with origin of the xyz coordinate system on the central axis of the container. The unit vectors in the Cartesian coordinate system are given by $\mathbf{i}, \mathbf{j}$ and $\mathbf{k}$ in the x, y and z directions, respectively. The unsteady centreline of the jet is described by $(X(s,t), Y(s,t), Z(s,t)$. Figure 3.13 shows the sketch of the cylindrical can

through which the jet emerges.

A separate curved cylindrical polar coordinate system (s, n, ϕ) is defined to describe the jet where s denotes the arc length along the centreline of the jet from the orifice, n denotes the radial coordinate and ϕ the azimuthal coordinate. A sketch of the curved jet is shown in Figure 3.14 along with the corresponding unit vectors $\mathbf{e}_s, \mathbf{e}_n$ and $\mathbf{e}_\phi$. The binormal and principal normal vectors to the centreline used in the calculation of the unit vectors in the (s, n, ϕ) coordinate system are denoted by $\mathbf{b}$ and $\mathbf{p}$, respectively (see Figure 3.14). In summation notation the relationship between the unit vectors of the two coordinate systems is given by

$$\mathbf{e_s} = X_{i,s}\mathbf{e_i}, \tag{3.1}$$

$$\mathbf{e_n} = \frac{1}{\sqrt{X_{L,ss}X_{L,ss}}}\left(\cos\phi X_{i,ss} + \sin\phi\ \epsilon_{ijk}X_{j,ss}X_{k,s}\right)\mathbf{e_i} \tag{3.2}$$

$$\text{and} \quad \mathbf{e}_\phi = \frac{1}{\sqrt{X_{L,ss}X_{L,ss}}}\left(-\sin\phi X_{i,ss} + \cos\phi\ \epsilon_{ijk}X_{j,ss}X_{k,s}\right)\mathbf{e_i}, \tag{3.3}$$

where $\mathbf{e_i}$ denotes the unit vectors in the xyz coordinate system; $\mathbf{e_1} = \mathbf{i}, \mathbf{e_2} = \mathbf{j}$ and $\mathbf{e_3} = \mathbf{k}$; X_i represents the position of the centreline with $X_1 = X, X_2 = Y$ and $X_3 = Z$; $\epsilon_{ijk} = 1$ when $ijk = 123, 231$ or 312, $\epsilon_{ijk} = -1$ when $ijk = 132, 321$ or 213 and $\epsilon_{ijk} = 0$ otherwise. Subscript s denotes differentiation with respect to s. The position vector of any point relative to the centre of the orifice is given by

$$\mathbf{r} = \int_0^s \mathbf{e}_s ds + n\mathbf{e}_n.$$

The structure functions defined as

$$h_i = \left|\frac{\partial \mathbf{r}}{\partial i}\right| \qquad \text{for} \quad i = s, n, \phi, \tag{3.4}$$

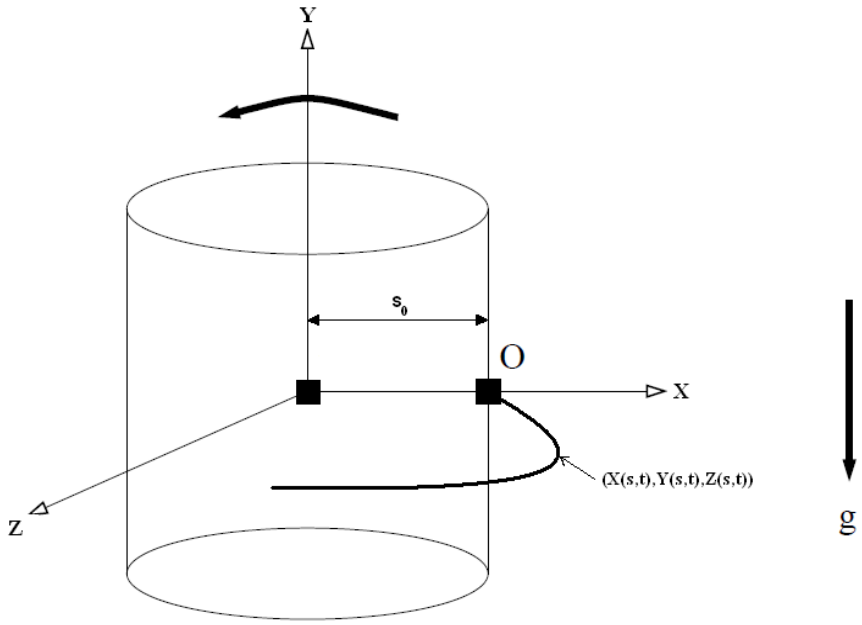

Figure 3.13: Sketch of the cylindrical container showing the X, Y and Z axes along with the orifice O through which the jet emerges. The unsteady centreline of the jet is given by $(X(s,t), Y(s,t), Z(s,t))$.

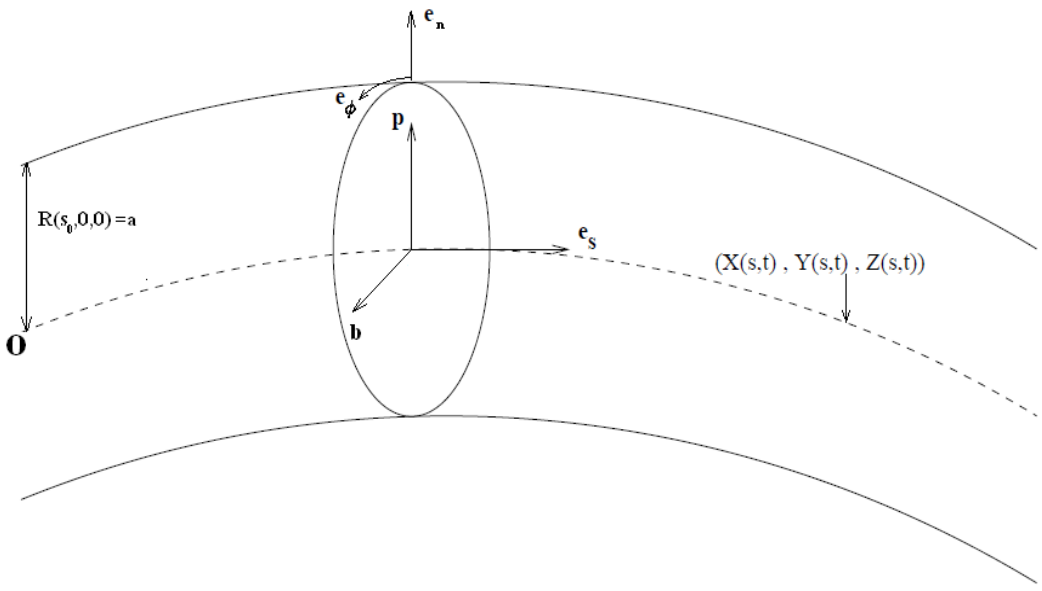

Figure 3.14: Sketch showing the centreline of a curved jet.

Quantity	Symbol	Dimensions
Radius of the orifice	a	L
Radius of the can	s_0	L
Rotation frequency	Ω	T^{-1}
Acceleration due to gravity	g	LT^{-2}
Exit velocity of the jet	U	LT^{-1}
Density of liquid	ρ	ML^{-3}
Surface tension	σ	MT^{-2}
Dynamic viscosity	μ	$ML^{-1}T^{-1}$
Kinematic viscosity	ν	L^2T^{-1}

Table 3.1: Physical Quantities

are calculated for this coordinate system and are found to be

$$h_n = 1, \tag{3.5}$$

$$h_\phi = n \tag{3.6}$$

$$\text{and} \quad h_s = \left| \left[X_{i,s} + n\frac{\partial}{\partial s}\left(\frac{1}{\sqrt{X_{L,ss}X_{L,ss}}} \left(\cos\phi X_{i,ss} + \sin\phi\, \epsilon_{ijk} X_{j,ss} X_{k,s}\right)\right)\right] \mathbf{e_i} \right|. \tag{3.7}$$

The continuity equation and Navier-Stoke's equations are used to describe the flow. The continuity equation can be written as

$$\nabla.\mathbf{u} = 0 \tag{3.8}$$

and Navier-Stoke's equations are given by

$$\frac{\partial \mathbf{u}}{\partial t} + (\mathbf{u}.\nabla)\mathbf{u} = -\frac{1}{\rho}\nabla p + \nu\nabla^2\mathbf{u} + \mathbf{g} - 2\boldsymbol{\omega} \times \mathbf{u} - \boldsymbol{\omega} \times (\boldsymbol{\omega} \times \mathbf{r}'), \tag{3.9}$$

where $\mathbf{u} = u\mathbf{e}_s + v\mathbf{e}_n + w\mathbf{e}_\phi$ is the velocity field, p the liquid pressure, $\mathbf{g} = -g\mathbf{j}$ is acceleration due to gravity, $\boldsymbol{\omega} = \Omega\mathbf{j}$ is the vector representing angular velocity of the cylindrical container, Ω is the rotation rate of the container, $\mathbf{r} = x\mathbf{i} + y\mathbf{j} + z\mathbf{k}$ and $\mathbf{r}' = s_0\mathbf{i} + \mathbf{r}$, with s_0 being the radius of the container.

The boundary conditions applied are the kinematic condition

$$\frac{\partial F}{\partial t} + \mathbf{u} \cdot \nabla F = 0, \tag{3.10}$$

where $F(\mathbf{r}, t) = R(s, \phi, t) - n$ gives the position of the free-surface and R the radius of the jet, the tangential stress condition

$$\mathbf{n} \cdot \mathbf{T} \cdot \mathbf{t}_i = 0, \tag{3.11}$$

where $\mathbf{t}_i$ are tangent vectors to the surface and $i = 1, 2$ and the normal stress condition

$$\mathbf{n} \cdot \mathbf{T} \cdot \mathbf{n} = \sigma\kappa, \tag{3.12}$$

where σ is the surface tension, $\mathbf{n}$ is a normal vector to the surface of the jet and the curvature of the free-surface is given by $\kappa = \nabla \cdot \mathbf{n}$. The stress tensor $\mathbf{T}$ is given by the expression $p\mathbf{I} + \mu[\nabla\mathbf{u} + (\nabla\mathbf{u})^T]$ where $\mathbf{I}$ is the second Identity Tensor and ^{T} denotes transpose. We also assume tangential flow down the centreline of the jet, or no flow through the centreline, i.e.

$$v = w = 0 \qquad \text{on } \ n = 0. \tag{3.13}$$

Finally, the arc length condition is given by

$$X_s^2 + Y_s^2 + Z_s^2 = 1. \tag{3.14}$$

In this chapter we have shown the governing equations and boundary conditions used to describe our curved jet model in vector form. We present the full equations in scalar form in more detail in Chapter 7.

For simplicity, the origin of the xyz system is translated to the centre of the orifice.

Parameter	Description
Weber number	$We = \frac{\rho U^2 a}{\sigma}$
Rossby number	$Rb = \frac{U}{s_0 \Omega}$
Ohnesorge number	$Oh = \frac{\mu}{\sqrt{\sigma a \rho}}$
Froude number	$F = \frac{U}{(s_0 g)^{1/2}}$
Reynolds number	$Re = \frac{\rho U a}{\mu}$
Aspect ratio	$\epsilon = \frac{a}{s_0}$

Table 3.2: Dimensionless parameters

The initial conditions at the orifice when $s = 0$ are given by

$$X = Y = Y_s = Z = Z_s = 0, X_s = 1, R = a \text{ and } u = U \tag{3.15}$$

where U is the exit speed of the jet in the rotating reference frame and a is the radius of the orifice.

The non-dimensional groups that enable us to analyse the dynamics of jet flow are

$$We = \frac{\rho U^2 a}{\sigma}, \ Rb = \frac{U}{s_0 \Omega}, \ Oh = \frac{\mu}{\sqrt{\sigma a \rho}}, \ F = \frac{U}{(s_0 g)^{1/2}}, \ Re = \frac{\rho U a}{\mu}, \ \epsilon = \frac{a}{s_0}$$

where We is the Weber number and gives the ratio of inertia to surface tension, Rb the Rossby number is the ratio between inertia and rotation, the Ohnesorge number Oh gives the ratio between surface tension and viscosity, F is the Froude number and gives the ratio between inertia and gravity and ϵ is the small aspect ratio. Here ρ is the liquid density, σ is surface tension, μ is dynamic viscosity and g is the acceleration due to gravity. Table 3.1 lists all the physical quantities and their dimensions and Table 3.2 lists all the dimensionless parameters used.

Non-dimensionalisation of the equations is carried out using the following scales

$$\begin{aligned} \tilde{u} = \frac{u}{U}, \tilde{v} = \frac{v}{U}, \tilde{w} = \frac{w}{U}, \tilde{p} = \frac{p}{\rho U^2}, \tilde{n} = \frac{n}{a}, \epsilon = \frac{a}{s_0}, \\ \tilde{R} = \frac{R}{a}, \tilde{s} = \frac{s}{s_0}, \tilde{t} = \frac{tU}{s_0}, \tilde{X} = \frac{X}{s_0}, \tilde{Y} = \frac{Y}{s_0}, \tilde{Z} = \frac{Z}{s_0}. \end{aligned} \tag{3.16}$$

Tildes represent the non-dimensionalised quantities. Substituting these scalings into equations (3.8)-(3.14) produces lengthy equations which are presented in Wallwork [68]. In the next section we show the three-dimensional steady state equations that were derived in [68].

3.3.2 Three-dimensional Steady State Problem

We will now consider the steady state problem and solve the above model for a steady inviscid fluid, for simplicity, by taking the $Re \to \infty$ limit. Decent *et al.* [14] showed that for linear analysis the effect of viscosity appears only at higher order and does not affect the trajectory of the jet or its steady state solution. Therefore, we will illustrate the analysis for an inviscid jet in this section (the analogous results for a the viscous case can be found in Wallwork [68] and Decent *et al.* [14]).

The non-dimensionalised equations (with tildes dropped for simplicity) are solved asymptotically to determine a steady state solution. On the assumption that the jet is slender (i.e. ϵ small), the following asymptotic expansions are introduced

$$
\begin{aligned}
u =& u_0(s) + \epsilon u_1(s,n,\phi) + ... \\
v =& \epsilon v_1(s,n,\phi) + \epsilon^2 v_2(s,n,\phi) + ... \\
p =& p_0(s,n,\phi) + \epsilon p_1(s,n,\phi) + ... \\
R =& R_0(s) + \epsilon R_1(s,\phi) + ... \\
X =& X_0(s) + \epsilon X_1(s) + ... \\
Y =& Y_0(s) + \epsilon Y_1(s) + ... \\
Z =& Z_0(s) + \epsilon Z_1(s) + ... \quad .
\end{aligned}
\tag{3.17}
$$

We take $w = 0$ so that there is no rotation in the azimuthal direction. These expansions are then substituted into the non-dimensional equations and are solved to give the following

equations

$$p_0 = \frac{1}{R_0 We}, \tag{3.18}$$

$$u_0 = \left(1 - \frac{2Y}{F^2} + \frac{1}{Rb^2}\left(X^2 + 2X + Z^2\right) + \frac{2}{We}\left(1 - \frac{1}{R_0}\right)\right)^{\frac{1}{2}}, \tag{3.19}$$

$$v_1 = -\frac{n}{2}\frac{du_0}{ds}, \tag{3.20}$$

$$p_1 = -\frac{n}{WeR_0}\cos\phi\left(X_{ss}^2 + Y_{ss}^2 + Z_{ss}^2\right)^{\frac{1}{2}} - h_1(s), \tag{3.21}$$

$$\begin{aligned} &\frac{Z_s X_{ss} - X_s Z_{ss}}{F^2} - \frac{2Y_{ss}u_0}{Rb} \\ &+\frac{(X+1)\left(Y_{ss}Z_s - Z_{ss}Y_s\right)}{Rb^2} + \frac{Z\left(Y_s X_{ss} - Y_{ss}X_s\right)}{Rb^2} = 0, \end{aligned} \tag{3.22}$$

$$\begin{aligned} &\left(u_0^2 - \frac{1}{WeR_0}\right)\left(X_{ss}^2 + Y_{ss}^2 + Z_{ss}^2\right) \\ &= -\frac{Y_{ss}}{F^2} + \frac{2u_0}{Rb}\left(X_s Z_{ss} - Z_s X_{ss}\right) + \frac{1}{Rb^2}\left((X+1)X_{ss} + ZZ_{ss}\right) \end{aligned} \tag{3.23}$$

$$\text{and} \quad \frac{dR_0}{ds} = \frac{R_0\left(Y_s/F^2 - \left((X+1)X_s + ZZ_s\right)/Rb^2\right)}{2\left(u_0^2 + 1/(2WeR_0)\right)}, \tag{3.24}$$

where $h_1(s)$ could be found at next order. For simplicity we relabel X_0, Y_0, Z_0 as X, Y, Z, respectively. From the above equations we numerically solve the following set of equations

for X, Y, Z, u_0 and R_0 by using a Runge-Kutta method

$$\left.\begin{aligned} u_0 &= \left(1 - \frac{2Y}{F^2} + \frac{1}{Rb^2}\left(X^2 + 2X + Z^2\right) + \frac{2}{We}\left(1 - \frac{1}{R_0}\right)\right)^{\frac{1}{2}}, \\ &\frac{Z_s X_{ss} - X_s Z_{ss}}{F^2} - \frac{2Y_{ss}u_0}{Rb} \\ &+ \frac{(X+1)\left(Y_{ss}Z_s - Z_{ss}Y_s\right)}{Rb^2} + \frac{Z\left(Y_s X_{ss} - Y_{ss}X_s\right)}{Rb^2} = 0, \\ &\left(u_0^2 - \frac{1}{WeR_0}\right)\left(X_{ss}^2 + Y_{ss}^2 + Z_{ss}^2\right) \\ &= -\frac{Y_{ss}}{F^2} + \frac{2u_0}{Rb}\left(X_s Z_{ss} - Z_s X_{ss}\right) + \frac{1}{Rb^2}\left((X+1)X_{ss} + ZZ_{ss}\right), \\ &\frac{dR_0}{ds} = \frac{R_0\left(Y_s/F^2 - \left((X+1)X_s + ZZ_s\right)/Rb^2\right)}{2\left(u_0^2 + 1/(2WeR_0)\right)}, \\ &\text{and} \quad X_s^2 + Y_s^2 + Z_s^2 = 1 \\ &\text{subject to the initial conditions} \\ &X = Y = Y_s = Z = Z_s = 0, X_s = 1, R_0 = 1 \ \text{ and } \ u_0 = 1. \end{aligned}\right\} \tag{3.25}$$

Figure 3.15 shows the trajectory of the centreline of the jet in three dimensions (as obtained in [68]) for different Weber numbers, computed by solving (3.25) numerically for X, Y and Z.

We now carry out small s asymptotics of the above equations which depict the singularity that appears in the model at $We = 1$. We introduce the following expansions

$$\begin{aligned} X =& X_1 + sX_2 + s^2X_3 + s^3X_4 + \dots, \\ Y =& Y_1 + sY_2 + s^2Y_3 + s^3Y_4 + \dots, \\ Z =& Z_1 + sZ_2 + s^2Z_3 + s^3Z_4 + \dots, \\ R_0 =& R_1 + sR_2 + s^2R_3 + s^3R_4 + \dots, \\ \text{and} \quad u_0 =& u_1 + su_2 + s^2u_3 + s^3u_4 + \dots. \end{aligned} \tag{3.26}$$

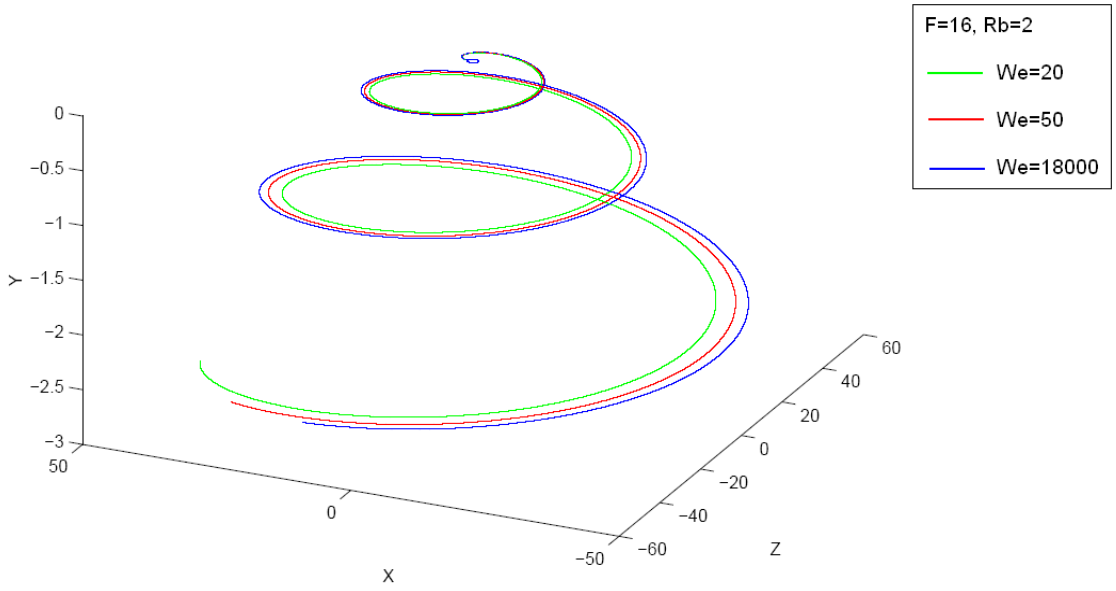

Figure 3.15: Graph (taken from [68]) showing the centreline of a jet in three dimensions for different Weber numbers (F=16, Rb=2). The green line is $We = 20$, the red line is $We = 50$ and the blue line is $We = 18000$. The small circle from which the jet originates represents the container.

Substituting these expansions into equations (3.25) and solving them produces

$$X = s - \frac{We^2\,(Rb^2 + 4F^4)}{6F^4 Rb^2 (1 - We)^2} s^3 + O(s^4)\,, \tag{3.27}$$

$$Y = \frac{We}{2F^2(1 - We)} s^2 + O(s^3)\,, \tag{3.28}$$

$$Z = \frac{We}{Rb(We - 1)} s^2 + O(s^3)\,, \tag{3.29}$$

$$R_0 = 1 - \frac{We}{Rb^2(2We + 1)} s + O(s^2) \tag{3.30}$$

$$\text{and} \quad u_0 = 1 + \frac{2We}{Rb^2(2We + 1)} s + O(s^2)\,. \tag{3.31}$$

These equations show the singularity that appears in the model at $We = 1$. This singularity was also observed by Keller & Geer [31], Baird & Davidson [1], Finnicum *et al.* [23] and Ramos [53].

3.3.3 Linear Stability Analysis

In this section we describe the linear stability analysis performed in [68] for an inviscid jet. The effect of viscosity on the trajectory and linear stability of the curved jet were studied in Decent *et al.* [14]. We start by applying a small perturbation about the steady state solutions using a small dimensionless parameter δ as shown below

$$\begin{aligned} \mathbf{u} &= \mathbf{u}(s,n,\phi) + \delta\tilde{\mathbf{u}}(s,\bar{s},n,\phi,t,\bar{t}), \\ R &= R(s,\phi) + \delta\tilde{R}(s,\bar{s},\phi,t,\bar{t}), \\ p &= p(s,n,\phi) + \delta\tilde{p}(s,\bar{s},n,\phi,t,\bar{t}) \\ \text{and} \quad \mathbf{X} &= \mathbf{X}(s) + \delta\epsilon\tilde{\mathbf{X}}(s,\bar{s},t,\bar{t}), \end{aligned} \tag{3.32}$$

where $\tilde{\mathbf{u}} = \tilde{u}\mathbf{e_s} + \tilde{v}\mathbf{e_n} + \tilde{w}\mathbf{e}_\phi$, $\mathbf{X} = X\mathbf{i} + Y\mathbf{j} + Z\mathbf{k}$, $\tilde{\mathbf{X}} = \tilde{X}\mathbf{i} + \tilde{Y}\mathbf{j} + \tilde{Z}\mathbf{k}$ and δ is a small dimensionless number representing the amplitude of the disturbance. We introduce a short length scale $\bar{s} = s/\epsilon$ and a short time scale $\bar{t} = t/\epsilon$ in order to introduce a wavelength of $O(\epsilon)$ and consider travelling wave modes of the form $\exp(ik\bar{s}+\lambda\bar{t}+im\phi)$, where $\bar{s} = s/\epsilon$ is a short length scale, $\bar{t} = t/\epsilon$ is a short time scale, k is the wave number with $k = k(s) = O(1)$, λ is the wave frequency or temporal growth rate with $\lambda = \lambda(s) = O(1)$ and m is an integer associated with the azimuthal motion. The wavelength of the perturbation is of $O(\epsilon)$. The wave number $k(s)$ and frequency $\lambda(s)$ are both made functions of s and thus vary down the jet.

In (3.32), $\mathbf{u}, R, p$ and $\mathbf{X}$ are the steady state solutions and $\tilde{\mathbf{u}}, \tilde{R}, \tilde{p}$ and $\tilde{\mathbf{X}}$ are time dependent. These are substituted into the jet equations presented in Wallwork [68] retaining only linear terms in δ. Examining normal modes, gives rise to the following eigenvalue relation

$$(\lambda_m + iku_0)^2 = \frac{1}{We}\left(\frac{1}{R_0^2}\left(1-m^2\right) - k^2\right) k\frac{I_m'(kR_0)}{I_m(kR_0)}, \tag{3.33}$$

where I_m is the mth order modified Bessel function.

3.3.3.1 Temporal Instability

To study temporal instability, a wave mode of the form $\exp(ik\bar{s} + \lambda\bar{t} + im\phi)$ is considered where k is real and λ is complex. For the wave mode to be unstable we must have $Re(\lambda) > 0$. An infinite number of neutrally stable eigenvalues (for which $Re(\lambda_m) = 0$) and one unstable eigenvalue is obtained from the eigenvalue relation (3.33). The neutrally stable modes are given by

$$\lambda_m = -iku_0 \pm \sqrt{\frac{1}{We}\left(\frac{1}{R_0^2}(1-m^2) - k^2\right)k\frac{I'_m(kR_0)}{I_m(kR_0)}}, \tag{3.34}$$

for $m \neq 0$. The unstable mode occurs when $m = 0$ and is given by

$$\lambda_0 = -iku_0 \pm \sqrt{\frac{1}{We}\left(\frac{1}{R_0^2} - k^2\right)k\frac{I_1(kR_0)}{I_0(kR_0)}}. \tag{3.35}$$

This eigenvalue is unstable when $0 < k < 1/R_0$, since $Re(\lambda_0) > 0$ in this range. The most unstable wavenumber is then found to be $k = k^* = 0.697/R_0$ and the corresponding value of $Re(\lambda_0)$ gives the maximum growth rate value. Therefore, the wavenumber of the most unstable mode depends on arclength s since $R_0(s)$. Figures 3.16, 3.18 and 3.20 show the growth rate of the most unstable mode plotted against arc length s and Figures 3.17, 3.19 and 3.21 show the corresponding wavenumbers plotted against arc length s of the jet for different values of Weber, Rossby and Froude numbers, respectively. From Figure 3.16, it can be seen that for smaller Weber numbers the disturbance is more unstable. Figure 3.17 shows that larger Weber numbers correspond to large k^*. Figure 3.18 shows that smaller Rossby numbers (i.e. lower rotation rates) have larger growth rates, while Figure 3.19 shows that smaller Rossby numbers have larger wavenumbers. Figure 3.20 shows that smaller the Froude number greater the growth rate and Figure 3.21 shows that smaller Froude numbers correspond to larger values of the most unstable wavenumbers of the disturbance.

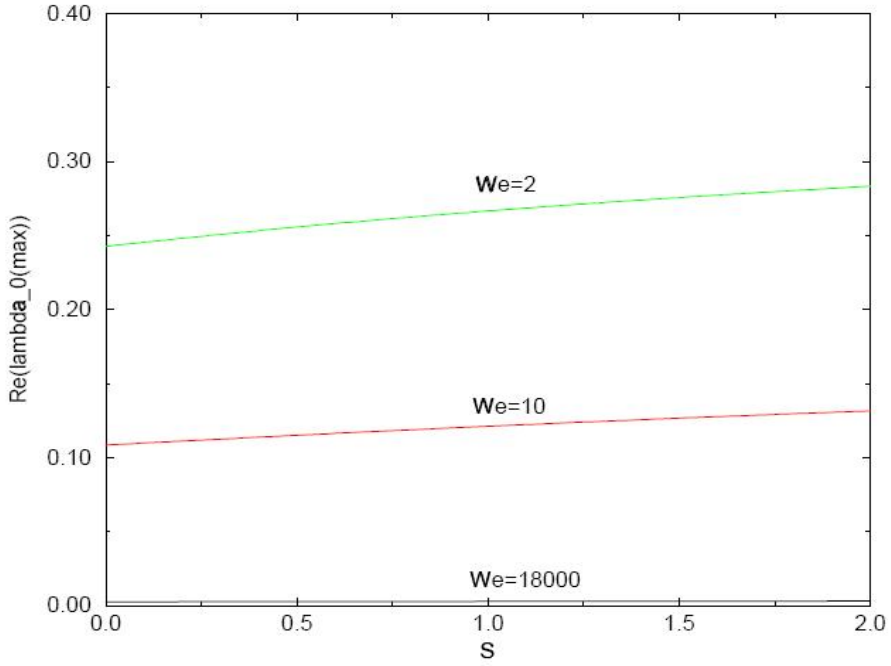

Figure 3.16: Graph (taken from [68]) showing growth rate $Re(\lambda_0)$ plotted against s for different values of We ($Rb = 2, F = 16$).

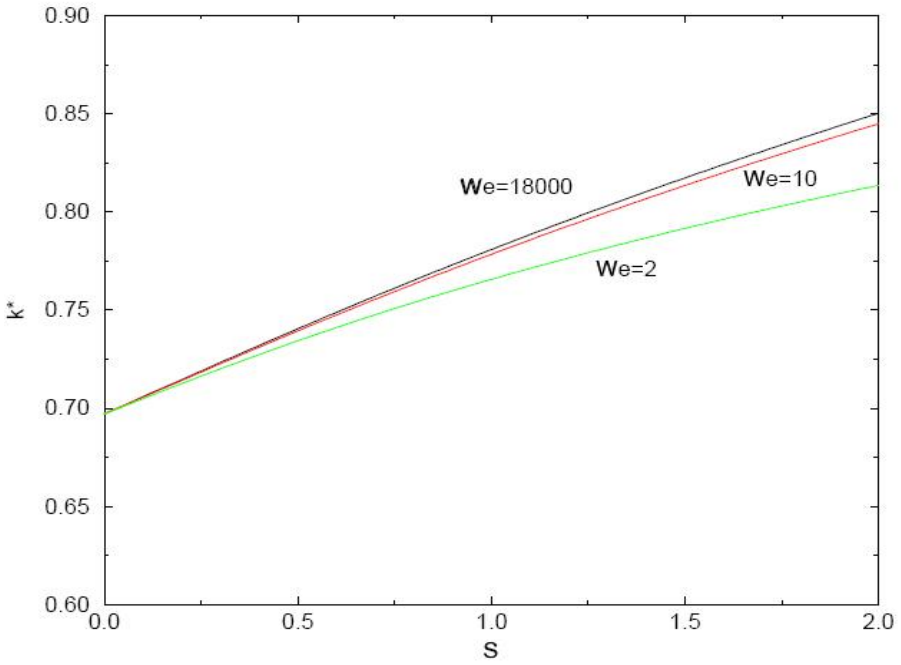

Figure 3.17: Graph (taken from [68]) showing the most unstable wavenumber k^* plotted against s for different values of We ($Rb = 2, F = 16$).

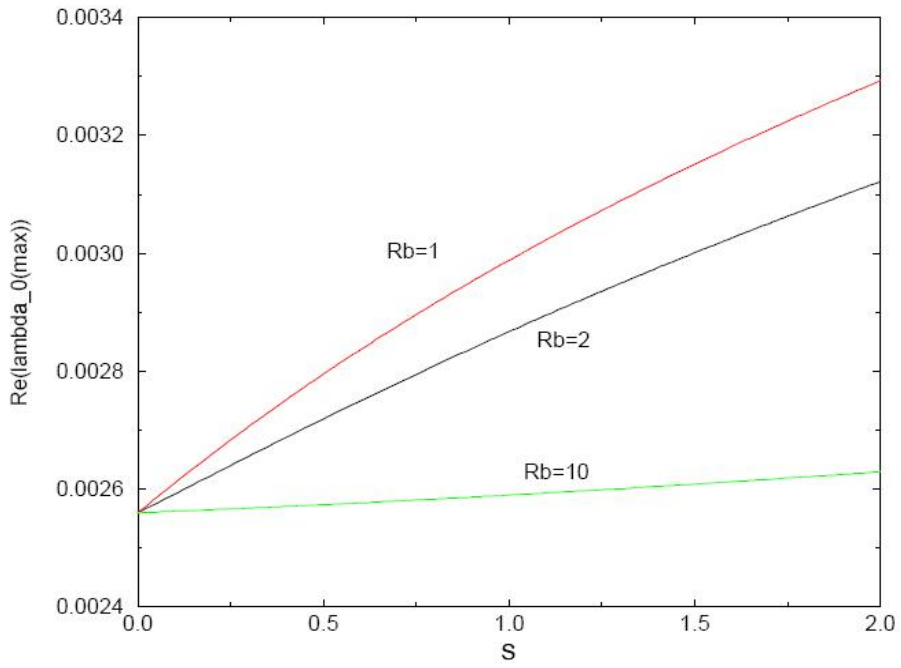

Figure 3.18: Graph (taken from [68]) showing growth rate $Re(\lambda_0)$ plotted against s for different values of Rb ($We = 18000, F = 16$).

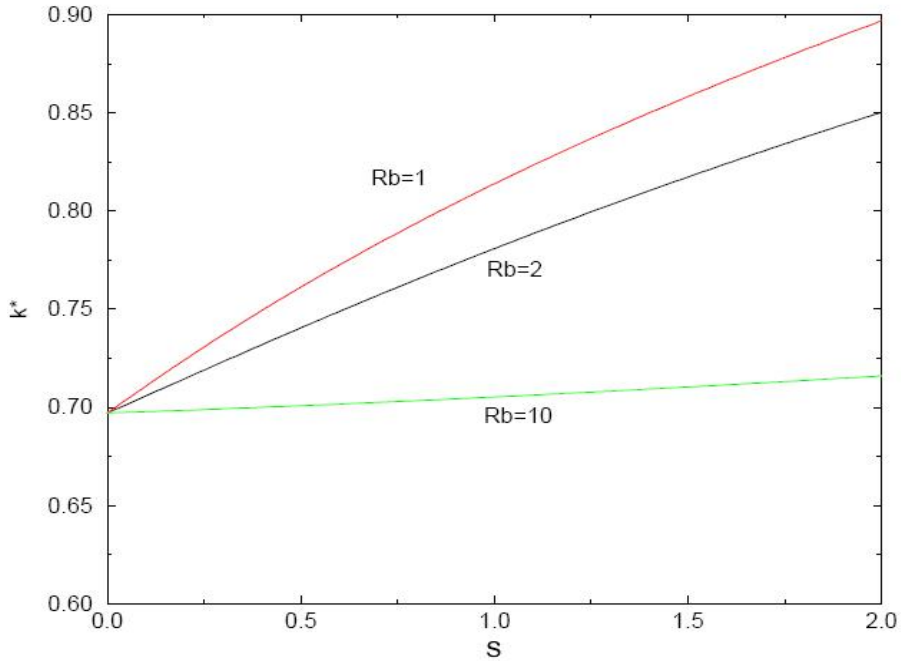

Figure 3.19: Graph (taken from [68]) showing the most unstable wavenumber k^* plotted against s for different values of Rb ($We = 18000, F = 16$).

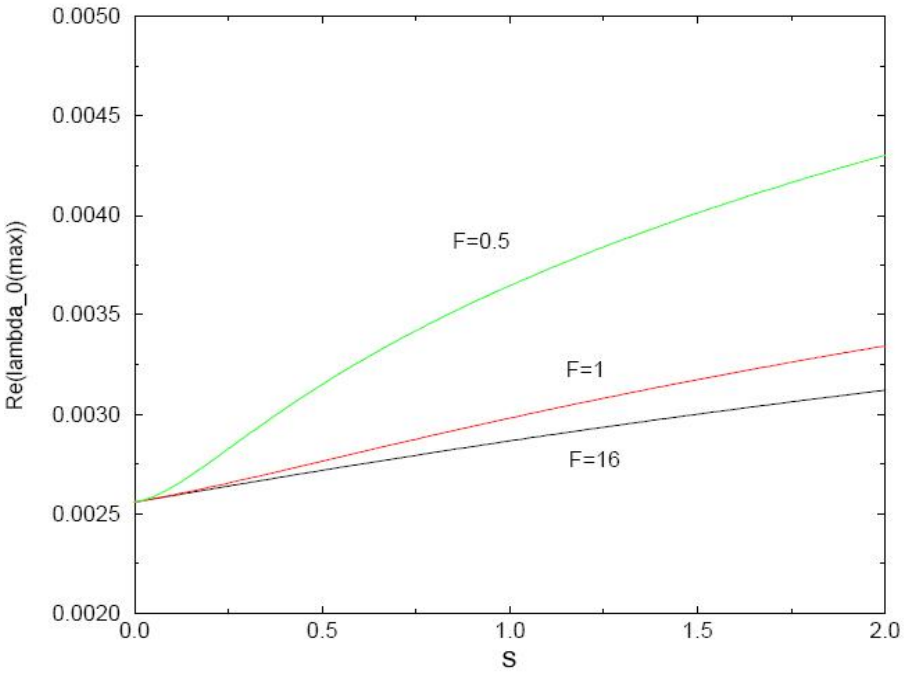

Figure 3.20: Graph (taken from [68]) showing growth rate $Re(\lambda_0)$ plotted against s for different values of F ($We = 18000, Rb = 2$).

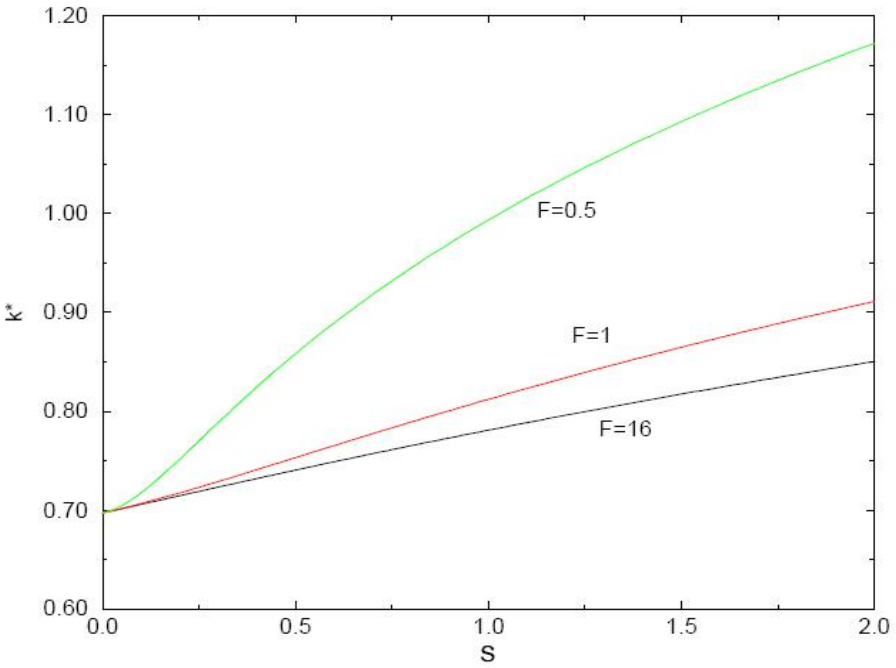

Figure 3.21: Graph (taken from [68]) showing the most unstable wavenumber k^* plotted against s for different values of F ($We = 18000, Rb = 2$).

3.3.3.2 Spatial Instability

Next we look at spatial instability of a jet by considering a wave mode of the form $\exp(ik\bar{s} + \lambda\bar{t})$ with $m = 0$ but in this case k is assumed to be complex and $\lambda(= -i\omega)$ is purely imaginary where ω denotes the real frequency of the mode. For the disturbance to be unstable, we must have $Im(k) < 0$ where the largest growth rate corresponds to the most negative value of $Im(k)$ since $\bar{s} > 0$. The eigenvalue relation in this case is given by (3.35) and solved using Newton-Raphson.

Figure 3.22 shows the frequency of the most unstable mode ω_{max} plotted against s for different values of Froude and Rossby numbers. It can be seen that the frequency of the disturbances is greater for smaller values of Rossby and Froude numbers. Figure 3.23 shows the modulus of the growth rate (scaled with We) plotted against the arc length s for different values of Froude and Rossby numbers. Figures 3.24 and 3.25 show the solution of the eigenvalue relation (3.35) found by using a Newton-Raphson method for different values of s for varying values of ω. The most unstable mode occurs at the minimum value of $Im(k)$ on each curve and can be seen to vary with s. From Figures 3.24 and 3.25 we observe that for larger values of s we obtain smaller values of $|Im(k)|$.

3.3.4 Two-dimensional Steady State Problem

In the prilling process, the container rotates fast enough for the jet to break-up before it can significantly fall under gravity ($s_0^2\Omega >> g$). Therefore, to simplify the analysis, Wallwork [68] neglected the effect of gravity and examined the jet in the xz-plane, performing the same analysis in Section 3.3.2, but with $Y = 0$.

After non-dimensionalisation of the equations, the asymptotic expansions for u, v, p, R, X and Z are substituted into the non-dimensionalised equations to find the steady state equations. The resulting equations are simplified further to give the following set of leading

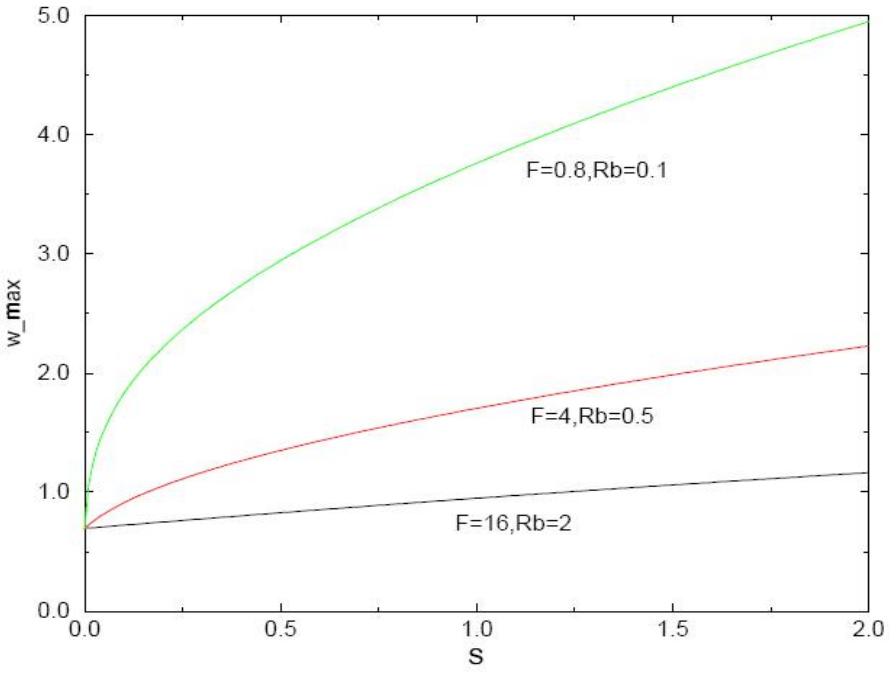

Figure 3.22: Graph (taken from [68]) showing frequency against s corresponding to the most unstable mode for different values of Froude and Rossby numbers ($We = 18000$).

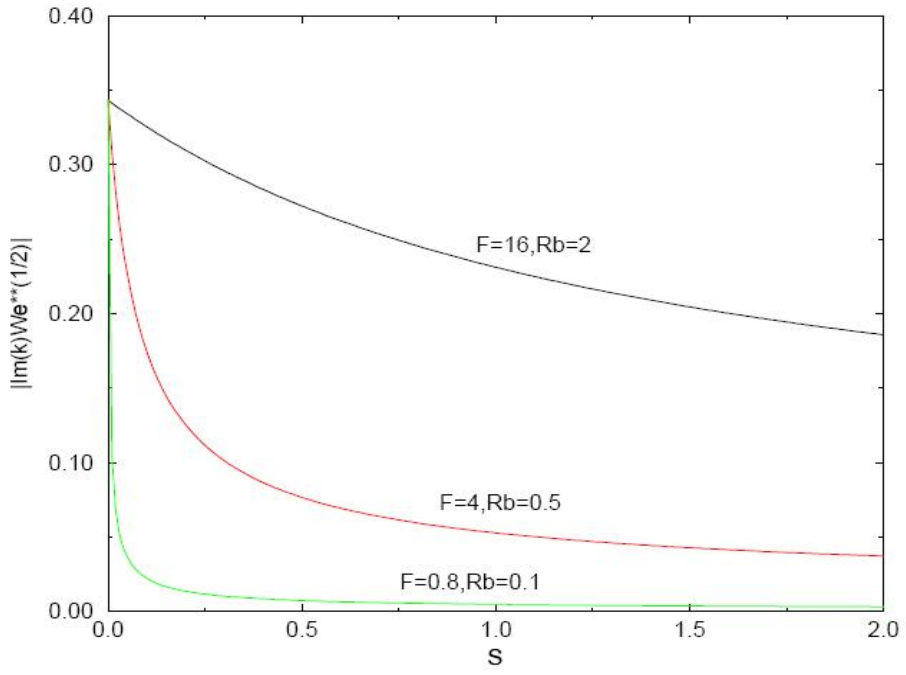

Figure 3.23: Graph (taken from [68]) showing a scaled modulus of the growth rate $|Im(k)We^{1/2}|$ of the most unstable mode plotted against s for different values of Froude and Rossby numbers ($We = 18000$).

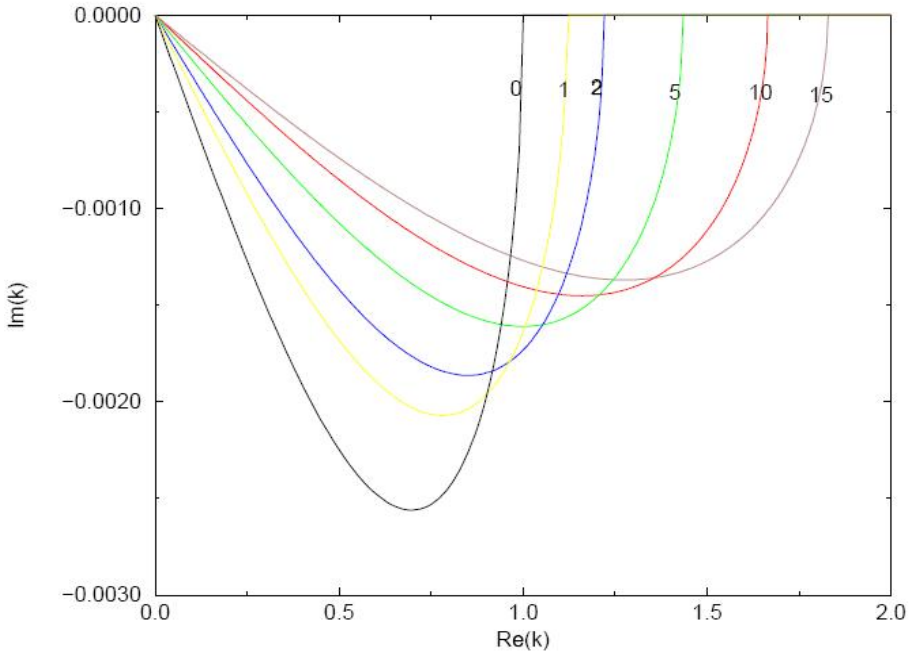

Figure 3.24: Graph (taken from [68]) showing the numerical solution of the eigenvalue relation in the k-plane for different values of s ($We = 18000, F = 16, Rb = 2$). The real frequency ω is varied from 0 to ∞ along each line from left to right. The value of s is shown by the figures at the top of the graph for each curve.

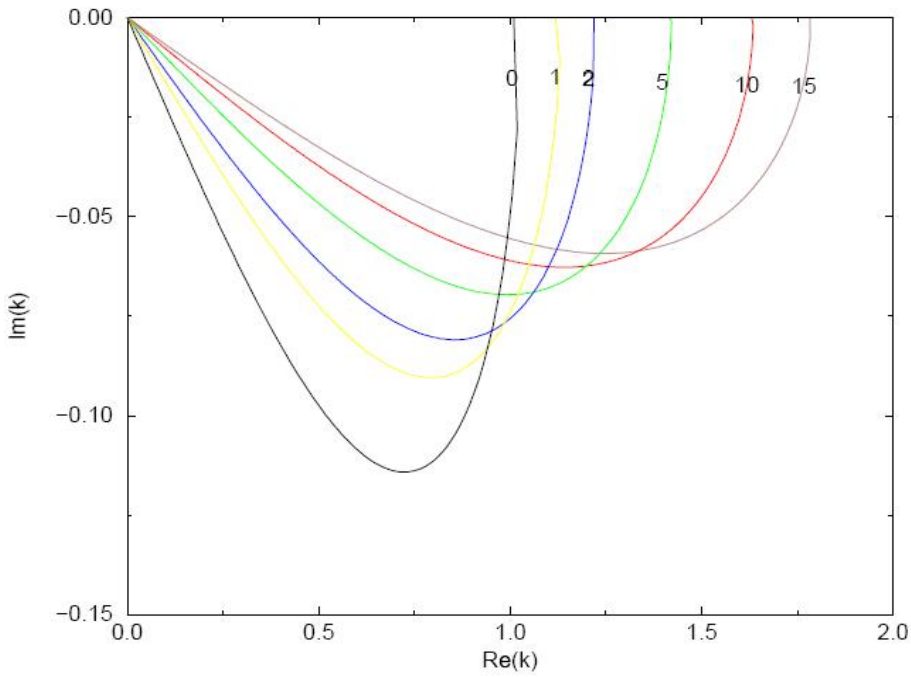

Figure 3.25: Graph (taken from [68]) showing the numerical solution of the eigenvalue relation in the k-plane for different values of s ($We = 10, F = 16, Rb = 2$). The real frequency ω is varied from 0 to ∞ along each line from left to right. The value of s is shown by the figures at the top of the graph for each curve.

order equations

$$p_0 = \frac{1}{R_0 We}, \tag{3.36}$$

$$u_0 = \left(1 + \frac{1}{Rb^2}\left(X^2 + 2X + Z^2\right) + \frac{2}{We}\left(1 - \frac{1}{R_0}\right)\right)^{\frac{1}{2}}, \tag{3.37}$$

$$v_1 = -\frac{n}{2}\frac{du_0}{ds}, \tag{3.38}$$

$$p_1 = \frac{n}{WeR_0}\cos\phi\left(X_s Z_{ss} - X_{ss} Z_s\right) + h_1(s), \tag{3.39}$$

$$Z_{ss} = \frac{X_s}{u_0^2 - \frac{1}{WeR_0}}\left(\frac{2u_0}{Rb} + \frac{ZX_s - (X+1)Z_s}{Rb^2}\right), \tag{3.40}$$

$$\text{and} \quad \frac{dR_0}{ds} = -\frac{R_0\left((X+1)X_s + ZZ_s\right)}{2Rb^2\left(u_0^2 + \frac{1}{2WeR_0}\right)}, \tag{3.41}$$

with $w = 0$ so there is no rotation in the azimuthal direction in the steady state. To obtain X, Z, u_0 and R_0 numerically, we solve the following set of equations using a Runge-Kutta method

$$\left.\begin{aligned} u_0 &= \left(1 + \frac{1}{Rb^2}\left(X^2 + 2X + Z^2\right) + \frac{2}{We}\left(1 - \frac{1}{R_0}\right)\right)^{\frac{1}{2}}, \\ Z_{ss} &= \frac{X_s}{u_0^2 - \frac{1}{WeR_0}}\left(\frac{2u_0}{Rb} + \frac{ZX_s - (X+1)Z_s}{Rb^2}\right), \\ \frac{dR_0}{ds} &= -\frac{R_0\left((X+1)X_s + ZZ_s\right)}{2Rb^2\left(u_0^2 + \frac{1}{2WeR_0}\right)}, \\ &\text{and} \quad X_s^2 + Z_s^2 = 1 \\ &\text{subject to the initial conditions} \\ X_s = 1, X = Z = Z_s = 0, R_0 = 1, u_0 = 1 \ &\text{ at } \ s = 0. \end{aligned}\right\} \tag{3.42}$$

Figure 3.26 shows the trajectory of the centreline of the jet in the xz-plane for different Weber numbers computed by solving (3.42) numerically for X and Z. The centreline with smaller Weber numbers is more tightly coiled than larger Weber numbers.

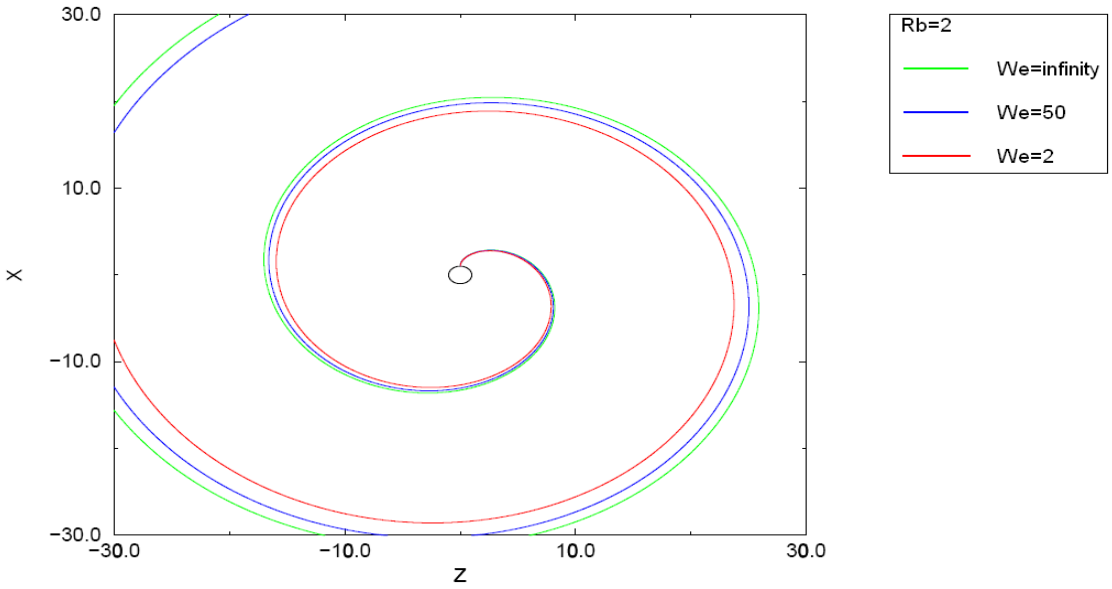

Figure 3.26: Graph (taken from [68]) showing the centreline of a jet in the xz-plane. The green line is $We = \infty$, the blue line is $We = 50$ and the red line is $We = 2$. Here $Rb = 2$. The small circle from which the jet originates represents the container.

Decent *et al.* [14] considered the corresponding viscous problem. The leading order steady state equations in the viscous case were found to be identical to those already described for the inviscid problem (3.42) and produce identical values for X, Z, u_0 and R_0 at leading order. The viscous terms appear only at higher-order in the steady expansion. Therefore, viscosity does not affect the leading order steady state equations. But, the linear dispersion relation is found to be different, equivalent to equation (2.1), studied in Chapter 2, but with multiple scales.

Părău *et al.* [51] extended the model for inviscid curved jets presented in [68] by including the nonlinear effects of the disturbance and developed one-dimensional equations using asymptotic methods, neglecting gravity. They solved the nonlinear model numerically to obtain nonlinear wave equations and found qualitative agreement with experiments. The nonlinear model is described in more detail in Chapter 7. Părău *et al.* [52] further extended their research by considering the corresponding viscous problem using the nonlinear model. Partridge *et al.* [48] carried out a pilot scale experimental study on the dynamics of break-up of curved jets and compared it to the theoretical results of the

nonlinear model of Părău *et al.* [51], finding good qualitative agreement between the two.

Uddin *et al.* [63] considered the linear instability of a non-Newtonian liquid jet by modifying Wallwork's [68] curved jet model to include non-Newtonian effects and compared the results to Newtonian results. Uddin *et al.* [62] examined the nonlinear evolution and studied the influence of rotation, surface tension and viscosity on a power law liquid jet. Uddin *et al.* [64] considered the effects of surfactants on the break-up dynamics of curved jets using the nonlinear model presented in Părău *et al.* [52]. We describe the non-Newtonian model in detail in Chapter 8.

The PhD thesis of Chris Gurney [26] carried out a detailed comparison of linear and nonlinear theories with experimental images and extended the work by adding an initial disturbance and performing a time dependent linear stability analysis. Victoria Hawkins, a current PhD student in the Chemical Engineering Department at the University of Birmingham, has been carrying out experiments on liquid jets using surfactants and non-Newtonian liquids. All these studies have emphasised the convective instability of Modes 1, 2 and 3 (see Figures 3.3, 3.5 and 3.7, respectively) and has been studied at length. In contrast, Mode 4 and the No Jet situation (see Figures 3.9 and 3.11, respectively) have not been looked at in detail previously and absolute instability in these situations needs to be studied and is thus the primary focus of this thesis.

3.4 Conclusion

In this chapter we have briefly described the experimental and theoretical work done on curved jets at the University of Birmingham. We have introduced the prilling problem, which has been the main motivation of all these studies and have described the experimental break-up modes that are observed in jets emerging from a rotating can.

Wallwork's [68] theoretical model and the steady state jet equations in both two and three dimensions are explained. The equations are solved computationally using a Runge-Kutta scheme to calculate the trajectory of the centreline of the jet along with its radius and velocity. A brief review of the linear stability analysis is also illustrated. The linear

dispersion relation derived in Wallwork [68] is presented and results for temporal and spatial instability are stated.

To date, all previous work done on curved jets has only looked at the convective nature of the disturbances that cause break-up. The unique and distinct features of break-up modes like Mode 4 and the No Jet case which hint the existence of absolute instability in their break-up dynamics, indicate the need for a study examining the effect of absolute instability in curved liquid jets.

Chapter 4

Absolute Instability in Curved Jets

In this chapter, we study the effect of absolute instability upon curved liquid jets, particularly in light of the industrial process of prilling and the Mode 4 break-up scenario described in the previous chapter. The unique features of this mode, including the upstream propagation of disturbances leading to the shattering of the jet, hint the existence of absolute instability and initiate an investigation into its effect on jets emerging from a rotating can. The instability described in the previous chapter (and studied in-depth by various authors) concentrates on the convective nature of disturbances on the surface of curved liquid jets, which has been extensively researched and has been the subject of many studies focussed on curved jets; this is not the case for absolute instability. The impact of absolute instability on curved liquid jets has not been analysed in the past.

To examine absolute instability in Mode 4, we use Wallwork's [68] mathematical model for finding the centreline of a curved jet as described in the previous chapter. Based on the results obtained from this model, we then define local Reynolds and Weber numbers and calculate the Re_{local}-We_{local} trajectory. The critical curve which marks the onset of absolute instability in the Re-We space (found in Chapter 2) is used to study absolute instability in Mode 4.

This chapter looks at the two-dimensional model in the xz-plane, neglecting gravity.

Quantity	Symbol
Radius of the orifice	a
Density of liquid	ρ
Exit speed of the jet	U
Leading order streamwise velocity component	u_0
Leading order position of free-surface	R_0
Kinematic viscosity	ν
Surface tension	σ

Table 4.1: Physical Quantities

We will consider the effect of gravity in the following chapter. We solve for $Q = 0$ (where Q is the density ratio; see equation (2.1)) and then extend to the $Q > 0$ situation in the next chapter.

4.1 Re_{local}-We_{local} Trajectory

In order to examine absolute instability using our curved jet model, we define a local Weber number We_{local} and a local Reynolds number Re_{local} adopting the multiple scales approach of Wallwork [68]. (Note that the Reynolds number in the previous chapter was written as R. We will denote the Reynolds number by Re in the remainder of this thesis.) These are defined as

$$We_{local}(s) = \frac{\rho U^2 a u_0^2(s) R_0(s)}{\sigma} = We u_0^2(s) R_0(s), \tag{4.1}$$

$$Re_{local}(s) = \frac{U a u_0(s) R_0(s)}{\nu} = Re u_0(s) R_0(s). \tag{4.2}$$

Table 4.1 lists all the physical quantities used. The expressions for the Reynolds and Weber numbers are equivalent to those used in Lin & Lian [41]; see (2.3). Comparing the Reynolds number here with that in Chapter 2, note that here the undisturbed jet radius $r_0 = a$. Re and We are the Reynolds and Weber numbers of the jet as a whole, while Re_{local} and We_{local} are the local Reynolds and Weber numbers at each point along the jet, which change as s increases. Then We_{local} and Re_{local} are functions of s.

The $We_{local}(s)$ and $Re_{local}(s)$ are calculated for every value of s in the Runge-Kutta

method which is used to solve the leading order two-dimensional steady state equations (3.42) numerically for X, Z, u_0 and R_0 subject to initial conditions when $s = 0$. Note that at $s = 0$, we have $u_0 = 1$ and $R_0 = 1$ and hence $We_{local}(0) = We$ and $Re_{local}(0) = Re$ at $s = 0$. The viscous linear dispersion relation is given by equation (2.1), but with We replaced by $We_{local}(s)$ and R replaced by $Re_{local}(s)$ and $Q = 0$ everywhere in (2.1). This then becomes identical to the linear viscous dispersion relation calculated by Wallwork in [68] for a curved viscous liquid jet. This makes use of the multiple scales formulation, with k, λ and ω in (2.1) and (2.2) becoming functions of s, so that $k = k(s)$, $\lambda = \lambda(s)$ and $\omega = \omega(s)$, with the modes used in the derivation of (2.1) being of the form $\exp(ik(s)\bar{s}+\omega(s)\bar{t})$, as discussed in Section 3.3.3.

Our methodology is then the same as for Wallwork [68]. We solve the two-dimensional steady state equations (3.42) numerically to obtain $u_0(s)$ and $R_0(s)$ which feed into the linear dispersion relation via multiple scales. But we do this for absolute instability unlike [68] where only convective instability was considered. The critical Re-We region for absolute instability remains as Figure 2.7, but now on a single jet, We and Re vary with s (since Re_{local} and We_{local} depend upon s), producing a path across Figure 2.7. This is illustrated in Figure 4.1; the $Re_{local}(s)$-$We_{local}(s)$ trajectory is calculated for every value of s used in the Runge-Kutta method which solves the two-dimensional steady state equations (3.42). The equations are solved for $Re = 7$, $We = 1.3$ and $Rb = 1.5$ with initial local values of $Re_{local}(0) = 7$ and $We_{local}(0) = 1.3$ (clearly we must have $Re_{local}(0) = Re$ and $We_{local}(0) = We$, by definition). The start point of the trajectory is marked by a red star. On closer inspection, we see that the trajectory oscillates in the Re-We plane. Figure 4.2 shows a zoomed in version of the $Re_{local}(s)$-$We_{local}(s)$ trajectory shown in Figure 4.1 which demonstrates its back and forth motion in the Re-We space. Figures 4.3 and 4.4 show the minimum and maximum points of the $Re_{local}(s)$-$We_{local}(s)$ trajectory, respectively. Figure 4.5 shows the graph of $Re_{local}(s)$ against s. As s is increased, $Re_{local}(s)$ increases initially, reaches a maximum, then decreases to a minimum value and continues to oscillate further. Figure 4.6 shows the graph of $We_{local}(s)$ against s. Similar behaviour

is observed for $We_{local}(s)$. Figures 4.7 and 4.8 show the graphs of u_0 and R_0 plotted against s for the same parameter values and provide u_0 and R_0 values which are used to compute Re_{local} and We_{local} for all s. Therefore, Figures 4.1, 4.2, 4.3, 4.4, 4.5 and 4.6 are consistent with Figures 4.7 and 4.8, i.e. the $Re_{local}(s)$-$We_{local}(s)$ trajectory in the Re-We plane moves upward first, reaches a maximum, drops down to a minimum and continues to oscillate in this way as s increases.

4.2 Absolute Instability in Mode 4

The Re_{local}-We_{local} trajectory is used to examine the onset of absolute instability. We obtain the critical curve in the Re-We plane as discussed in Chapter 2. We then pick a point in the convective instability region lying above the critical curve. Due to the oscillatory nature of the Re_{local}-We_{local} trajectory, for some values of Re and We, the trajectory crosses the critical curve. It is when this occurs that we assume the onset of absolute instability. This is illustrated in Figure 4.9 which shows the Re_{local}-We_{local} trajectory which crosses the critical curve for $Rb = 1.5$, $Re_{local}(0) = 7$ and $We_{local}(0) = 1.23$. The critical Weber number value corresponding to this $Re_{local}(0)$ is $We_c = 1.179$. The red star marks the starting point of the trajectory in the Re-We plane. Figure 4.9 shows that the initial point of the trajectory is above the critical curve. The trajectory first travels upwards on the graph, reaches a maximum, drops down to a minimum and in this case as it comes back down it crosses the critical curve after reaching its first maximum, implying a transition from convective to absolute instability at this point on the jet. The crossing of the $Re_{local} - We_{local}$ trajectory in theory corresponds to the unique experimental features of Mode 4, where the jet grows with convectively unstable disturbances travelling downstream on its surface initially, along with the observation of upstream propagation of disturbances towards the orifice which cause the jet to shatter, including at their point of origin.

As $We_{local}(0)$ is increased gradually keeping $Re_{local}(0)$ constant, it is found that $We_{local}(0)$ reaches a value above which the Re_{local}-We_{local} trajectory starting at this point

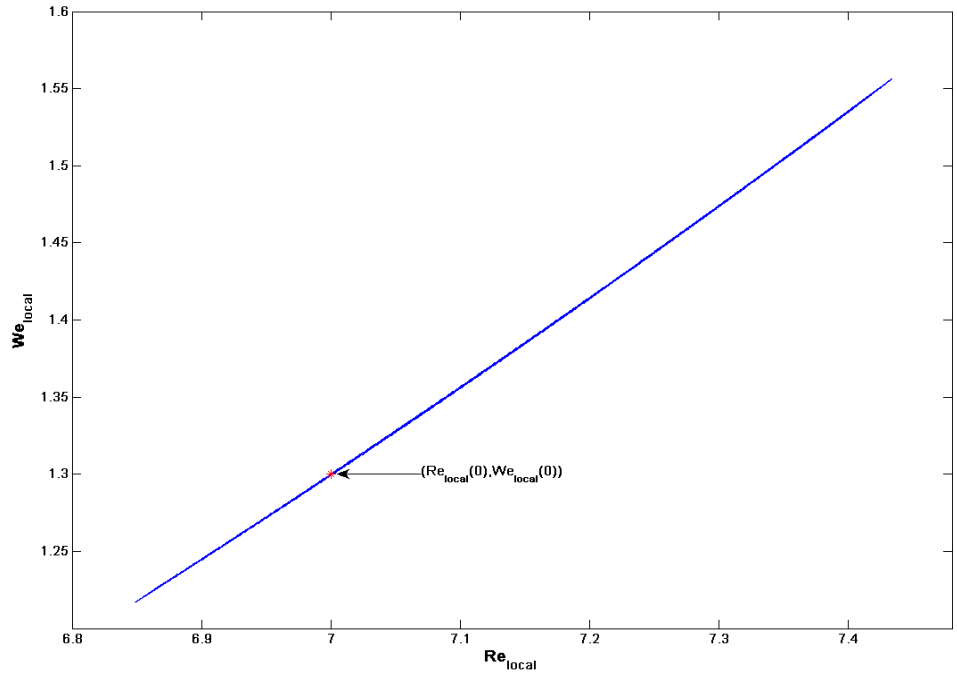

Figure 4.1: Graph showing the $Re_{local}(s)$-$We_{local}(s)$ trajectory. The red star marks the starting point of the trajectory. $Rb = 1.5, We = We_{local}(0) = 1.3, Re = Re_{local}(0) = 7$.

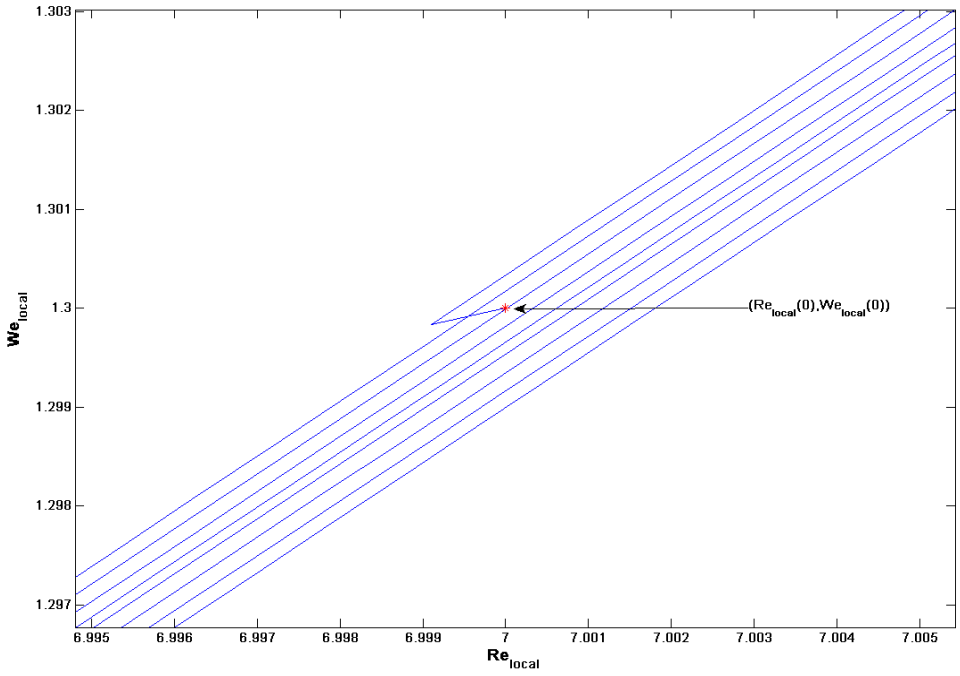

Figure 4.2: Graph showing the oscillatory nature of the $Re_{local}(s)$-$We_{local}(s)$ trajectory. The red star marks the starting point of the trajectory. $Rb = 1.5, We = We_{local}(0) = 1.3, Re = Re_{local}(0) = 7$.

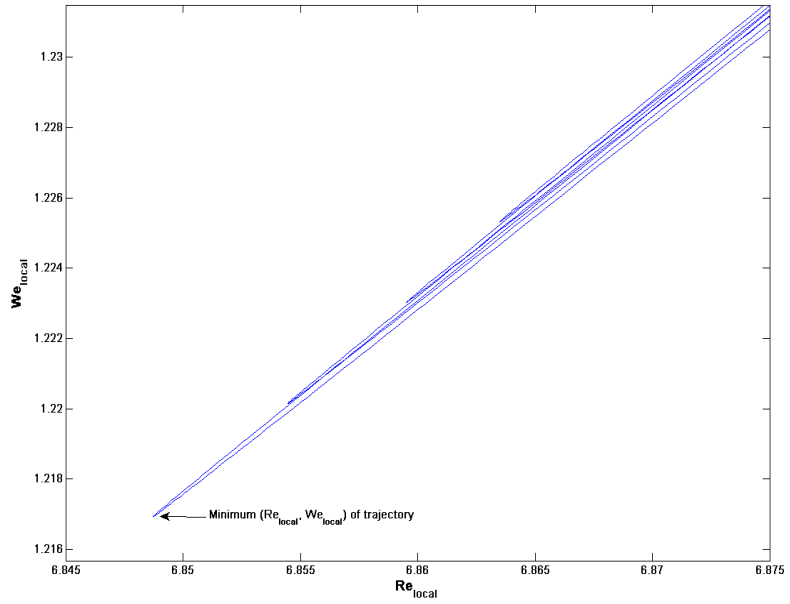

Figure 4.3: Graph showing the minimum point on the $Re_{local}(s)$-$We_{local}(s)$ trajectory. $Rb = 1.5, We = We_{local}(0) = 1.3, Re = Re_{local}(0) = 7$.

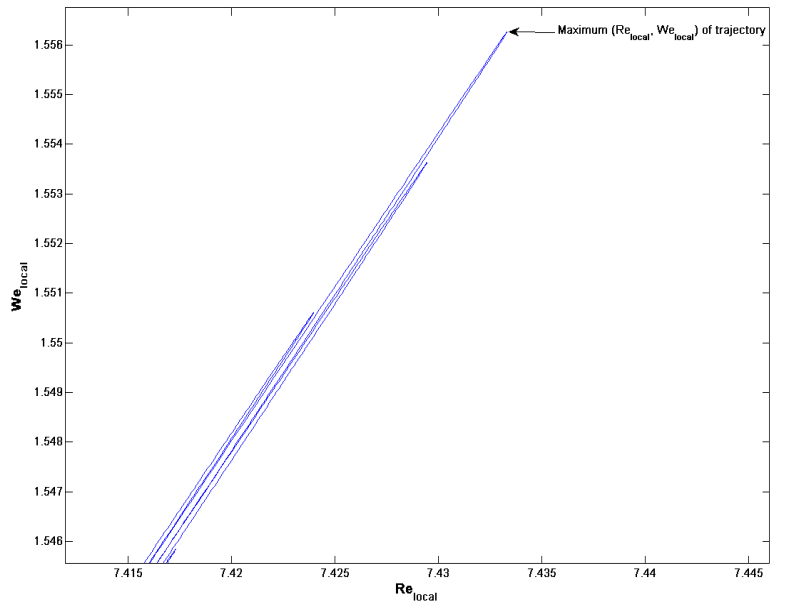

Figure 4.4: Graph showing the maximum point on the $Re_{local}(s)$-$We_{local}(s)$ trajectory. $Rb = 1.5, We_{local}(0) = 1.3, Re_{local}(0) = 7$.

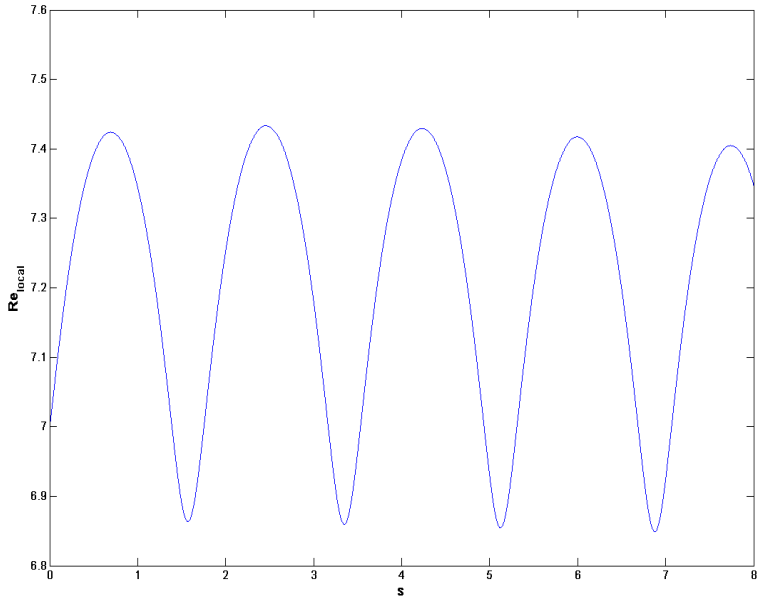

Figure 4.5: Graph showing $Re_{local}(s)$ plotted against s. $Rb = 1.5, We = We_{local}(0) = 1.3, Re = Re_{local}(0) = 7$.

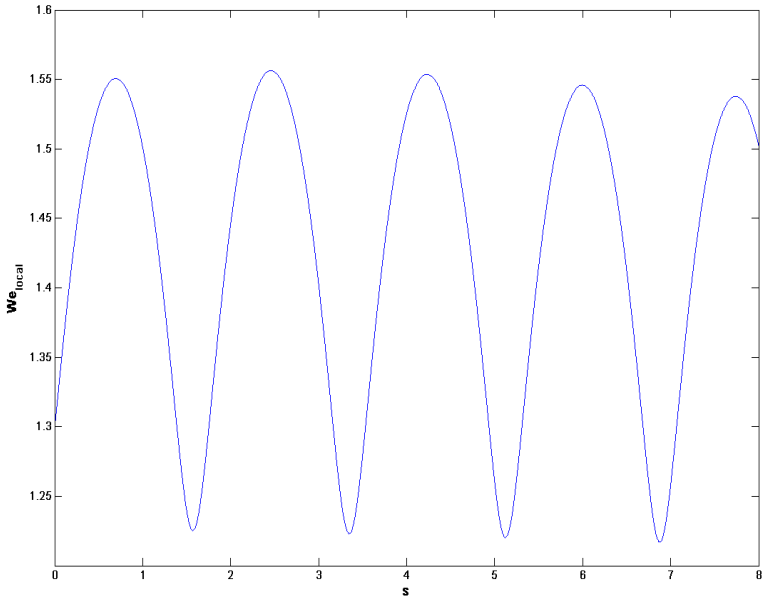

Figure 4.6: Graph showing $We_{local}(s)$ plotted against s. $Rb = 1.5, We = We_{local}(0) = 1.3, Re = Re_{local}(0) = 7$.

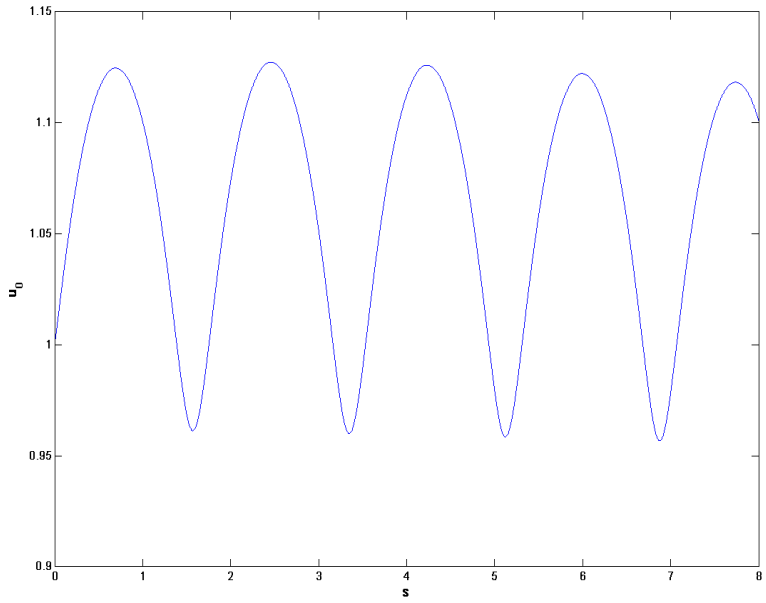

Figure 4.7: Graph showing u_0 plotted against s. $Rb = 1.5, We_{local}(0) = 1.3, Re = Re_{local}(0) = 7$.

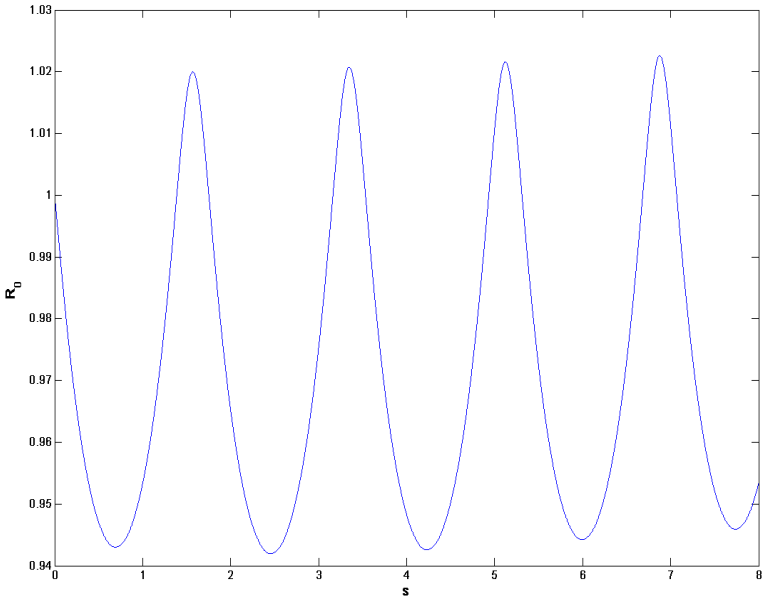

Figure 4.8: Graph showing R_0 plotted against s. $Rb = 1.5, We = We_{local}(0) = 1.3, Re = Re_{local}(0) = 7$.

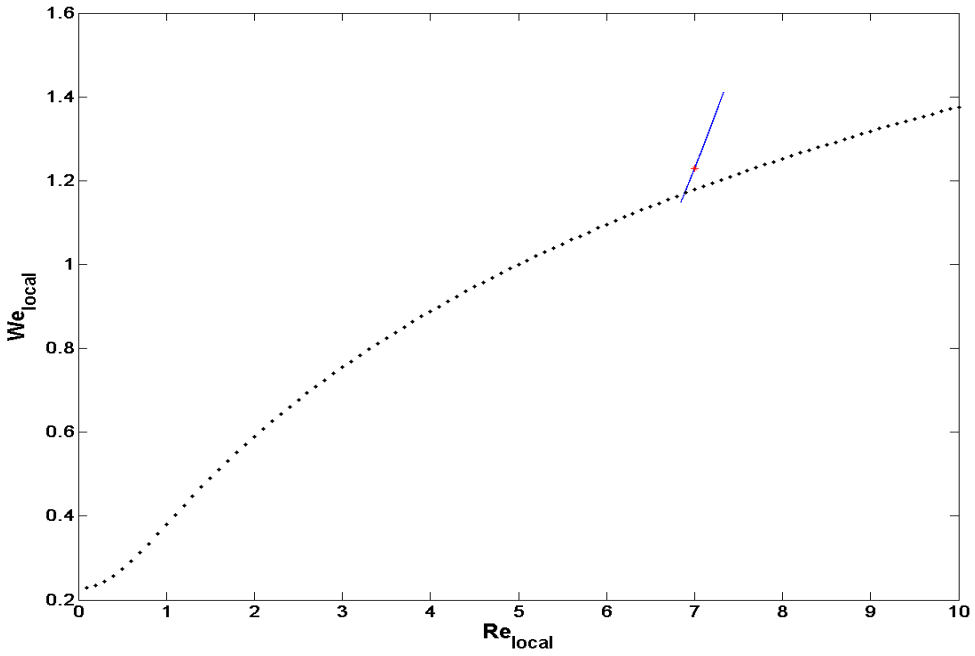

Figure 4.9: Graph showing the Re_{local}-We_{local} trajectory crossing the critical boundary between absolute and convective instability. The red star indicates the starting point of the trajectory. $Rb = 1.5$, $Re_{local}(0) = 7$, $We_{local}(0) = 1.23$ and $We_c = 1.179$.

on the graph never crosses the critical curve. Based on this idea, a region which exhibits Mode 4 behaviour is determined, i.e. a region where the jet is initially convectively unstable for small s and makes a transition to absolute instability for a certain value of s. This Mode 4 area which lies in the convective instability region, above the critical curve, is determined such that all Re_{local}-We_{local} trajectories starting at any point in this region always cross the critical curve for some positive values of s.

In order to find this region, a Re_{local}-We_{local} trajectory is found by fixing $Re_{local}(0)$ and choosing an initial $We_{local}(0)$ value lying slightly above We_c such that the trajectory crosses the critical curve if started at this point. $We_{local}(0)$ is then gradually increased until it reaches a value We^* at which the trajectory no longer intersects the critical curve for any s. This highest point (Re, We^*) in the Re-We plane marks the upper boundary of the Mode 4 region. Using this technique, We^* is determined for different values of Re. All Re_{local}-We_{local} trajectories starting in this Mode 4 region cross the critical curve at some s making a switch from convective to absolute instability.

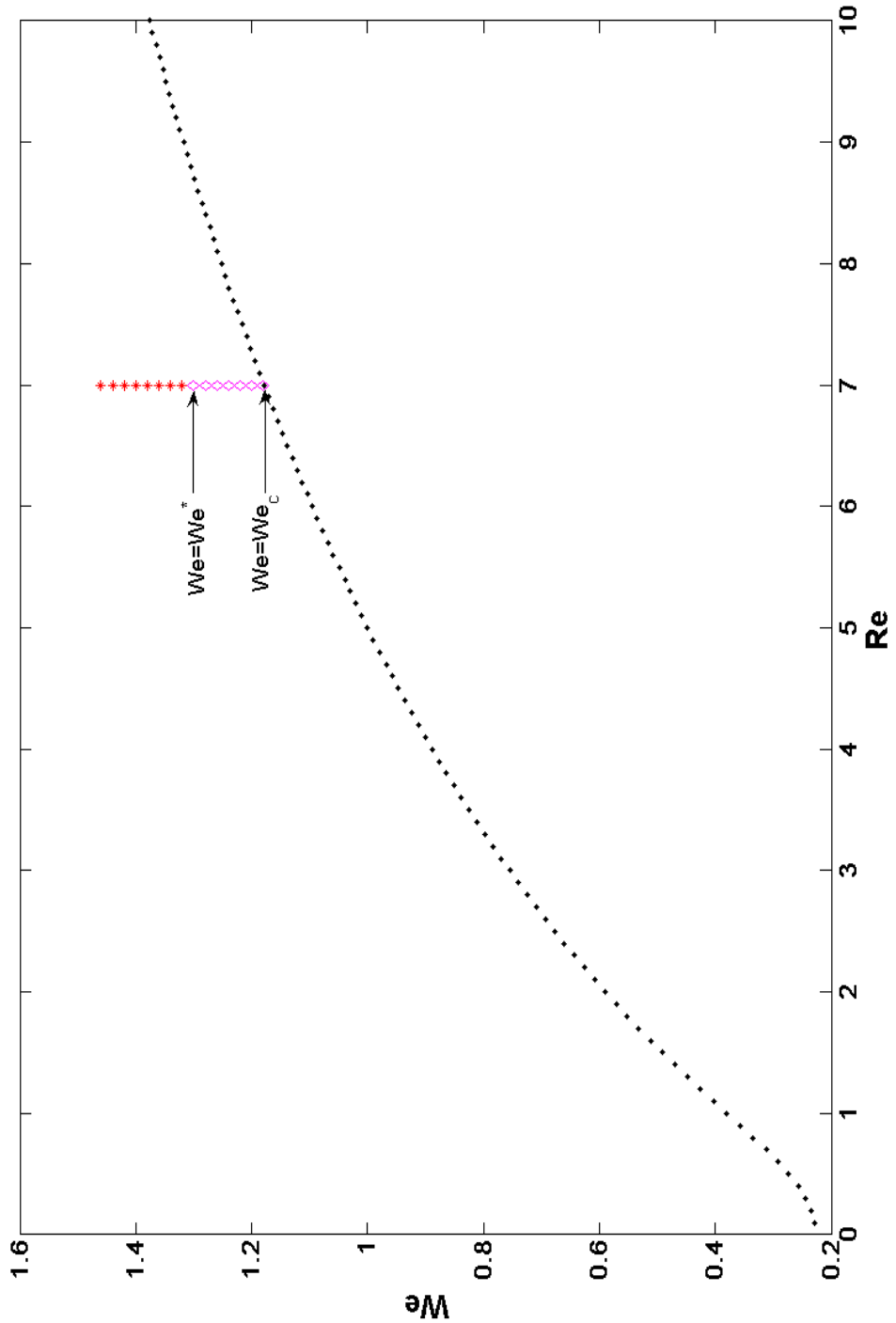

Figure 4.10: Graph showing the technique used to determine We^* - lowest We value for which the $Re_{local}(s)$-$We_{local}(s)$ trajectory starting at that point stops crossing the critical curve. The pink diamonds indicate initial values of the Re_{local}-We_{local} trajectories that cross the critical curve and the red stars indicate initial values of trajectories that do not cross the critical curve.

To automate the process of finding the smallest Weber number We^* closest to the critical curve for which the trajectory stops crossing the critical curve, a computer program using Matlab was written which evaluates the Re_{local}-We_{local} trajectory for a set of initial We_{local} values. For a fixed $Re_{local}(0)$, an initial $We_{local}(0)$ value is specified and the Re_{local}-We_{local} trajectory is calculated. If the trajectory starting at the specified value of $Re_{local}(0)$ and $We_{local}(0)$ crosses the critical curve, a pink diamond is plotted at this starting value. This process is repeated by increasing the $We_{local}(0)$ value. For trajectories that do not make the cross over, a red star is plotted. Figure 4.10 shows a plot of the points $(Re_{local}(0), We_{local}(0))$ for which the trajectory crosses the critical curve (marked by pink diamonds) and those for which it does not (marked by red stars). The Weber number value (We^*) closest to the critical curve for which the Re_{local}-We_{local} trajectory starting at that We value stops crossing the critical curve, marks the upper boundary of the Mode 4 curve. This process is repeated to find We^* for various Re.

Using this approach to find We^*, Mode 4 regions for different values of Rb were determined. Figures 4.11, 4.12 and 4.13 show the Mode 4 upper boundary curves for $Rb = 4, Rb = 2$ and $Rb = 0.8$, respectively. The black curve is the critical boundary which indicates the switch from convective to absolute instability with the jet being convectively unstable in the region above the critical curve and absolutely unstable below it. The region between the black critical curve and the red curve is the Mode 4 region. All Re_{local}-We_{local} trajectories starting in this region give rise to absolute instability further down the jet i.e. make a transition from convective to absolute instability by crossing over the critical boundary for a fixed value of s. As the Rossby number decreases, we find that the area of the Mode 4 region increases. From experiments carried out in Wong *et al.* [70], we know that Mode 4 occurs at higher rotation rates i.e. lower Rossby numbers; thus, this is in agreement with experimental observations. We compare experimental results to our theoretical results in Chapter 6.

Notice that there is a gap in the Mode 4 boundary curves as $We \to 1$. In this region, the Matlab program fails to converge well enough to give a sensible result. A

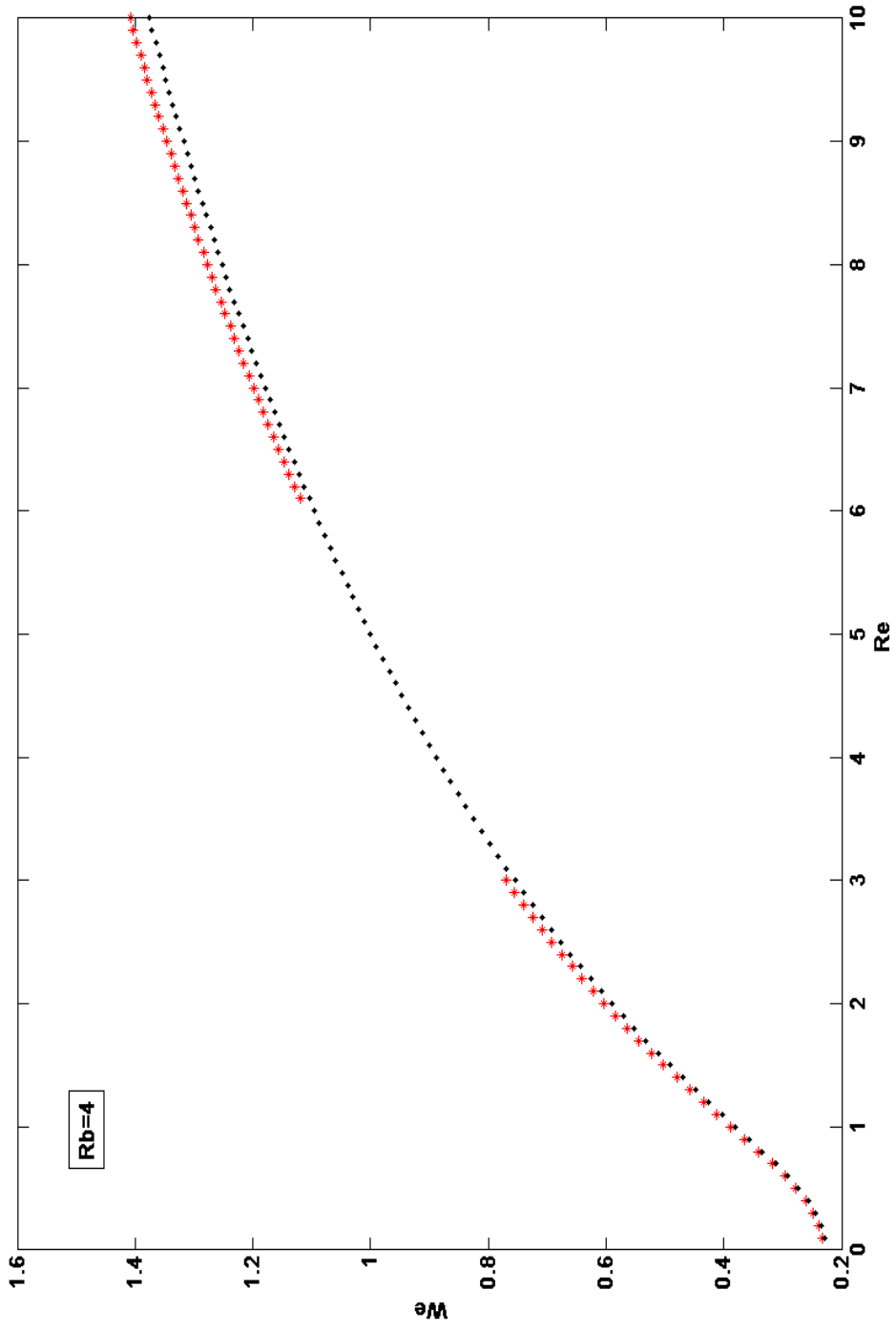

Figure 4.11: Graph showing the Mode 4 curve for $Rb = 4$. The red stars mark the upper boundary of the Mode 4 region. The gap in the Mode 4 curve as $We \to 1$ is due to the singularity in the jet equations at $We = 1$ where the Matlab program used to calculate the We^* values fails.

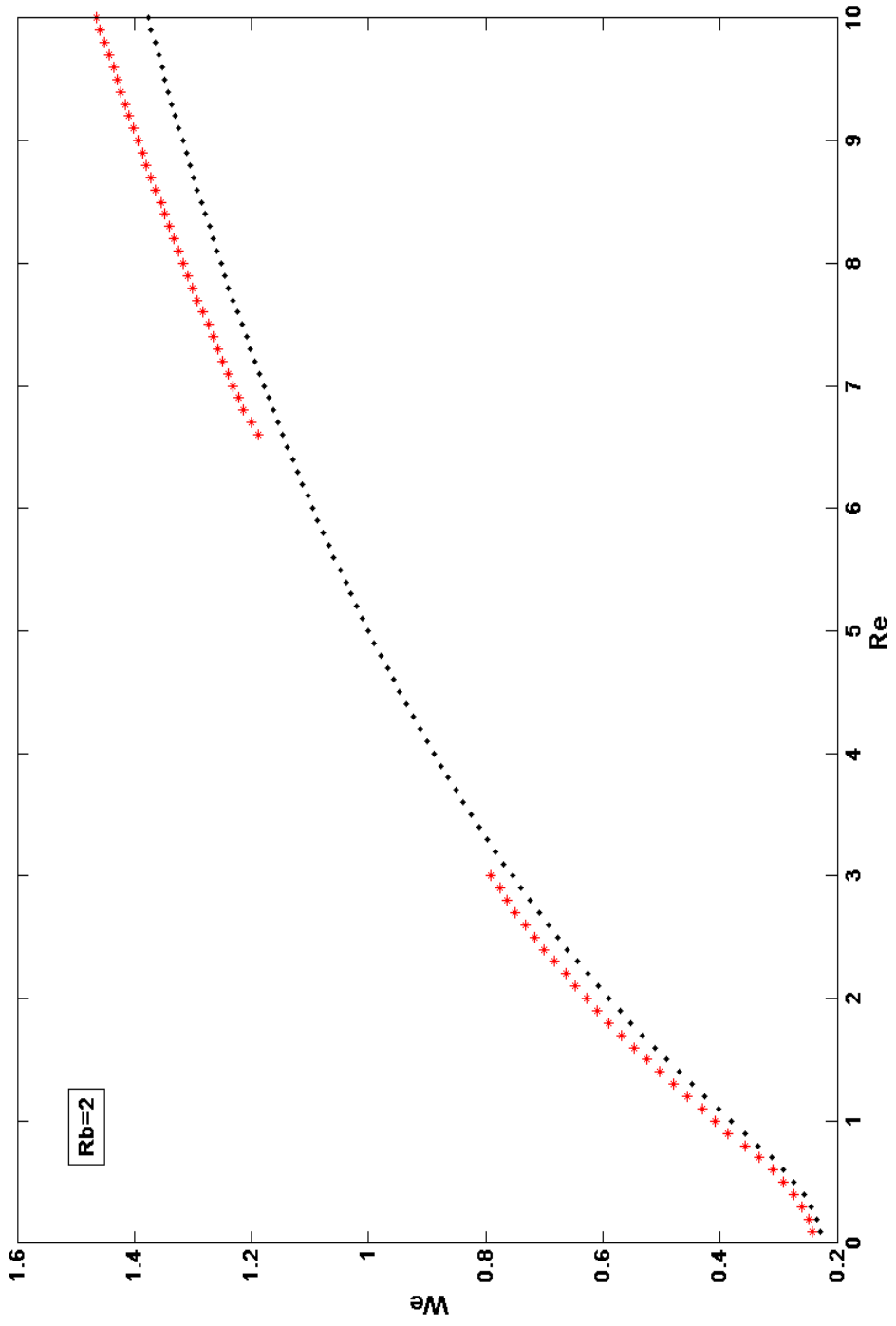

Figure 4.12: Graph showing the Mode 4 curve for $Rb = 2$. The red stars mark the upper boundary of the Mode 4 region. The gap in the Mode 4 curve as $We \to 1$ is due to the singularity in the jet equations at $We = 1$ where the Matlab program used to calculate the We^* values fails.

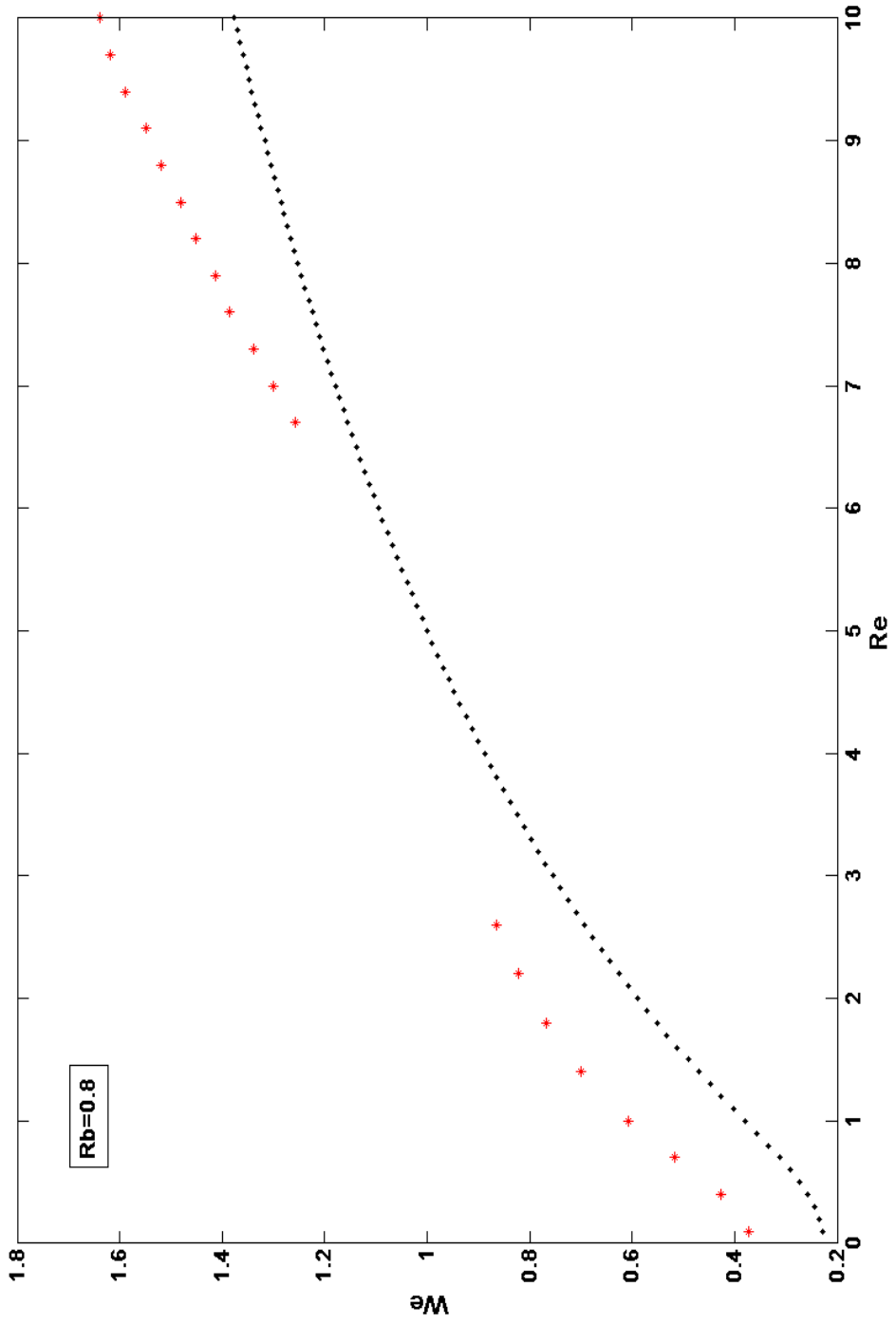

Figure 4.13: Graph showing the Mode 4 curve for $Rb = 0.8$. The red stars mark the upper boundary of the Mode 4 region. The gap in the Mode 4 curve as $We \to 1$ is due to the singularity in the jet equations at $We = 1$ where the Matlab program used to calculate the We^* values fails.

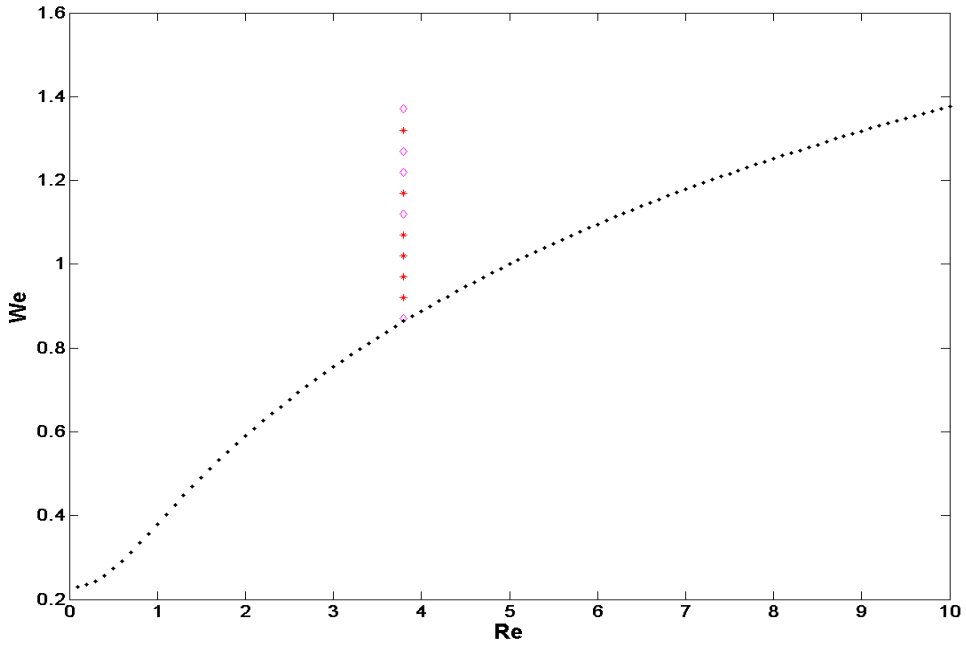

Figure 4.14: Graph showing a plot produced by the Matlab program in the region close to $We = 1$ where the program fails to produce a sensible result.

typical plot produced by the program in this region is shown in Figure 4.14 which shows initial values of Re_{local} and We_{local} for which the trajectory crosses the critical curve (pink diamonds) mixed with points for which it does not cross (red stars), demonstrating inconsistent behaviour. This is due to the singularity that arises in the curved jet equations at $We = 1$ (see equations (3.27)-(3.31).). Thus, in order to acquire a better understanding of this region we perform an asymptotic analysis on the two-dimensional steady state jet equations in the following section.

4.3 Asymptotic Analysis for $We \to 1$

We now scale into the singularity region, where we have difficulty in finding the Re_{local}-We_{local} trajectory correctly, by introducing the following asymptotic expansions

$$We = 1 + \alpha, \tag{4.3}$$

$$s = \alpha^n \hat{s}, \tag{4.4}$$

$$u_0 = 1 + \alpha^p u(\hat{s}), \tag{4.5}$$

$$R_0 = 1 + \alpha^q R(\hat{s}), \tag{4.6}$$

$$X = \alpha^n \hat{s} + \alpha^r x(\hat{s}), \tag{4.7}$$

$$Z = \alpha^t z(\hat{s}) \tag{4.8}$$

where $\alpha \to 0$. By substituting these expansions into the steady state equations (3.42), the distinguished limit $n = p = q = r = t = 1$ is obtained. These are substituted back into (3.42) to produce the following set of equations

$$R = -\frac{(\hat{s} + x)}{3Rb^2}, \tag{4.9}$$

$$u = \frac{2(\hat{s} + x)}{3Rb^2}, \tag{4.10}$$

$$x'' = \frac{-z' Rb^2}{Rb^2 + \hat{s} + x}\left(\frac{2}{Rb} - \frac{z'}{Rb^2}\right), \tag{4.11}$$

$$z'' = \frac{Rb^2(1 + x')}{Rb^2 + \hat{s} + x}\left(\frac{2}{Rb} - \frac{z'}{Rb^2}\right), \tag{4.12}$$

where $'$ represents differentiation with respect to $\hat{s}$. By solving these equations numerically subject to the initial conditions $x = z = x' = z' = u = R = 0$ at $\hat{s} = 0$ and using those results to find the Re_{local}-We_{local} trajectory in this new asymptotic region, we should be able to fill in the gap in the upper boundary of the Mode 4 curves.

However, the asymptotics reveal that at $We = 1$, we have $u_0 = R_0 = 1$ since $\alpha = 0$. As u_0 and R_0 become identically equal to one, Re_{local} and We_{local} become constants and therefore the trajectory remains fixed at its starting point $Re_{local}(0)$ and $We_{local}(0)$. This

implies that at $We = 1$ there is no Mode 4 at all. Moreover, as $We \to 1$, $We_{local}(s)$ and $Re_{local}(s)$ remain close to $We_{local}(0)$ and $Re_{local}(0)$ for all values of s. Therefore, the Mode 4 region must shrink as $We \to 1$. Also, the scaled s used in the aysmptotics suggests that the length scale of the oscillation in u_0 and R_0 also reduces to zero as $We \to 1$, implying that the step-size in the Runge-Kutta method used to solve the steady state equations must be reduced significantly, since We_{local} and Re_{local} start oscillating on a short length scale as $We \to 1$.

Incorporating the implications of our asymptotics and reducing the step-size in the Runge-Kutta method drastically in the Matlab program to determine We^*, we are able to fill the gap in the Mode 4 curve that arises as $We \to 1$. Figures 4.15, 4.16 and 4.17 show the complete Mode 4 regions for $Rb = 4$, $Rb = 2$ and $Rb = 0.8$ where the blue crosses are determined by significantly reducing the step-size in the Runge-Kutta method. The step-size is reduced to about 10^{-6} as $We \to 1$. As a result, the Matlab program becomes very slow, especially for smaller Rossby numbers and, thus, causing the program to take a lot longer to determine We^*. Figure 4.18 shows the Mode 4 region for $Rb = 0.4$. At this small Rossby number, it takes extremely long to determine the Mode 4 curve for $Re > 5$.

4.3.1 Numerical Solution

In order to validate the results obtained in the previous section, we now solve the asymptotic equations (4.9)-(4.12) numerically for x, z, u and R using a Runge-Kutta method. The resulting u and R values produced numerically are substituted into Re_{local} and We_{local} and consequently used to determine the Mode 4 curves. Taking into account the effects of the asymptotics, Re_{local} and We_{local} are redefined. Since $We = 1 + \alpha$ as $\alpha \to 0$ and $We \to 1$, we have $u_0 = 1 + (We - 1)u$ and $R_0 = 1 + (We - 1)R$. Substituting these

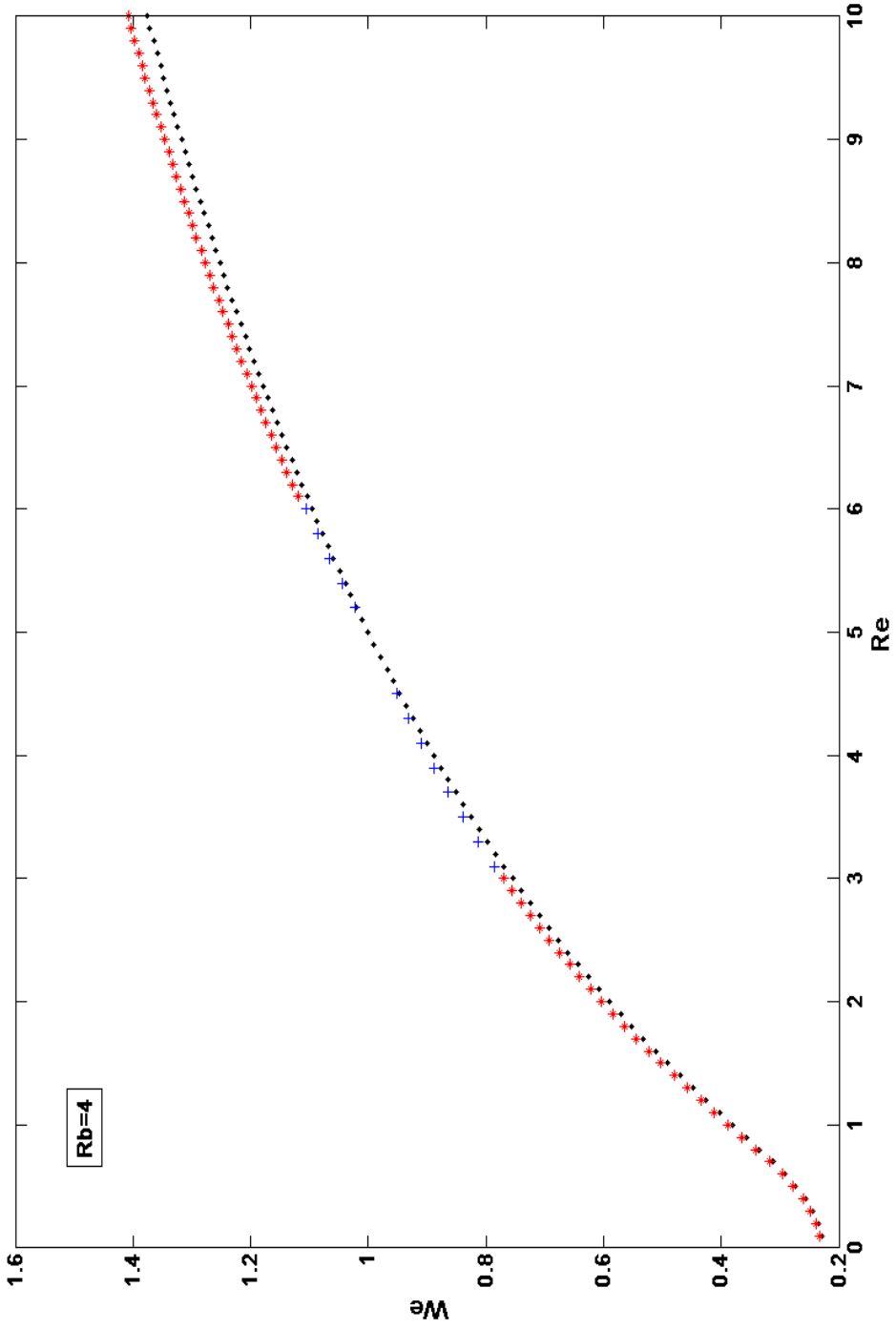

Figure 4.15: Graph showing the complete Mode 4 curve for $Rb = 4$. The red stars along with the blue crosses mark the upper boundary of the Mode 4 region. The blue crosses are the We^* values found by reducing the step-size in the Runge-Kutta method for solving the two-dimensional steady state equations.

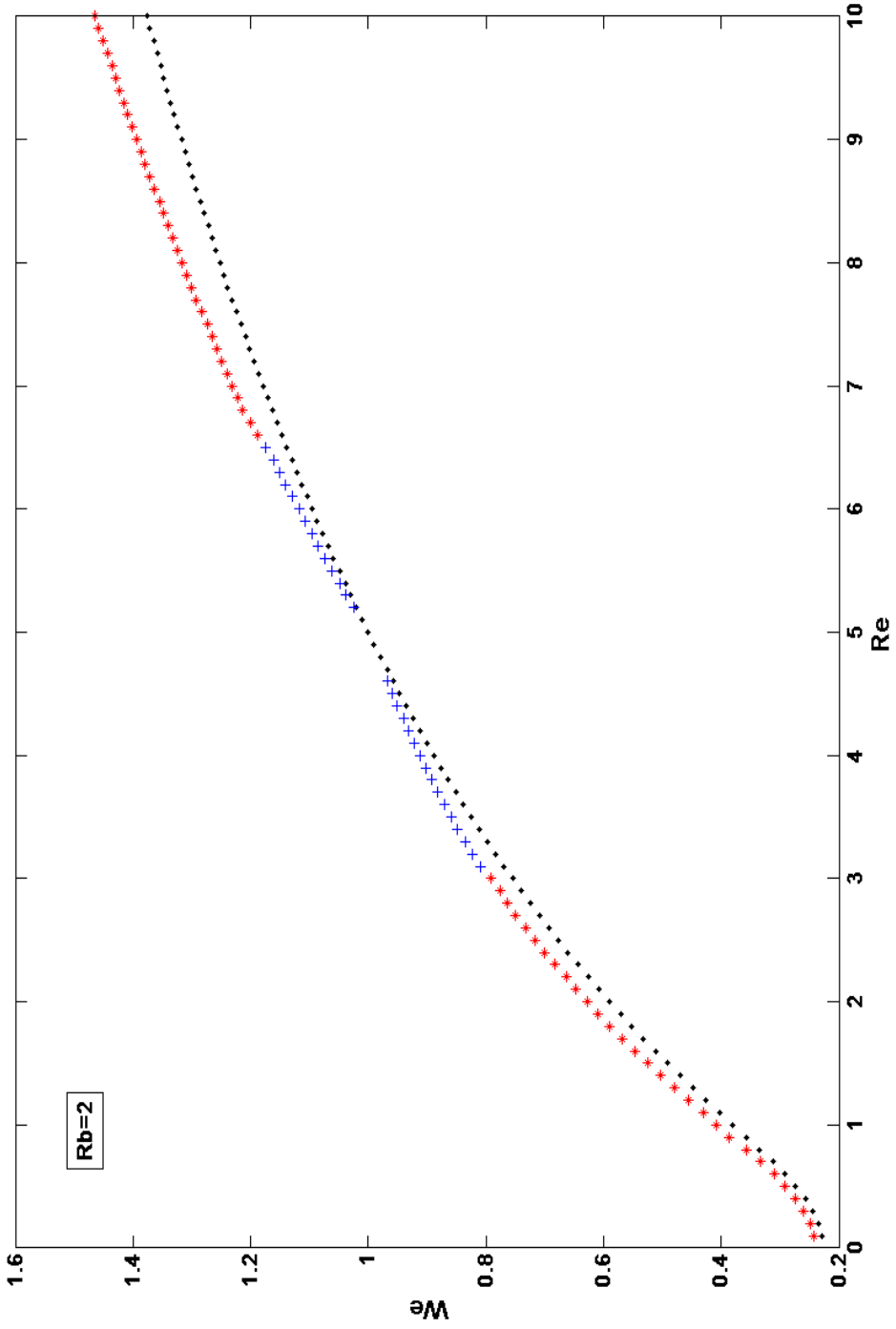

Figure 4.16: Graph showing the Mode 4 curve for $Rb = 2$. The red stars along with the blue crosses mark the upper boundary of the Mode 4 region. The blue crosses are the We^* values found by reducing the step-size in the Runge-Kutta method for solving the two-dimensional steady state equations.

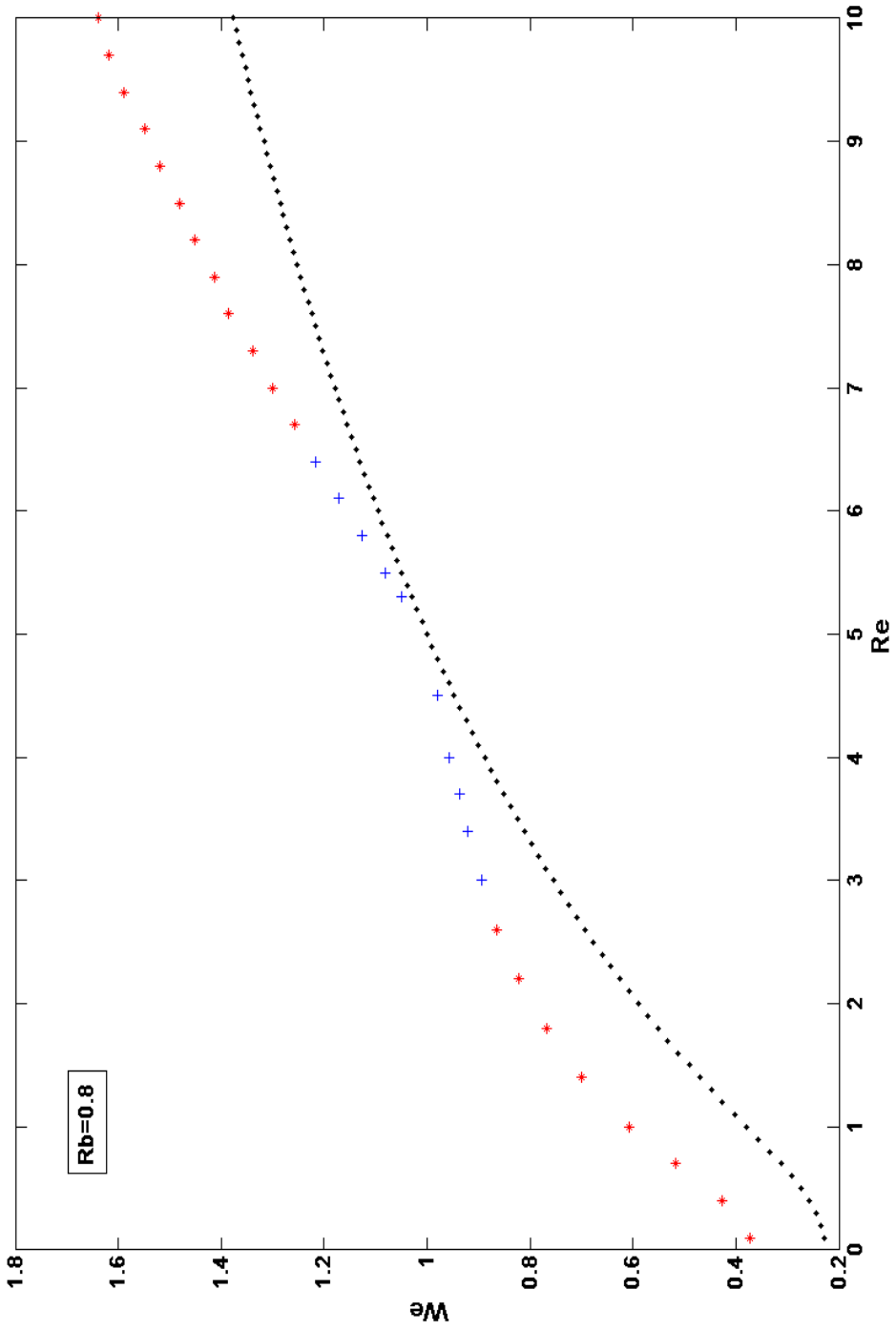

Figure 4.17: Graph showing the Mode 4 curve for $Rb = 0.8$. The red stars along with the blue crosses mark the upper boundary of the Mode 4 region. The blue crosses are the We^* values found by reducing the step-size in the Runge-Kutta method for solving the two-dimensional steady state equations.

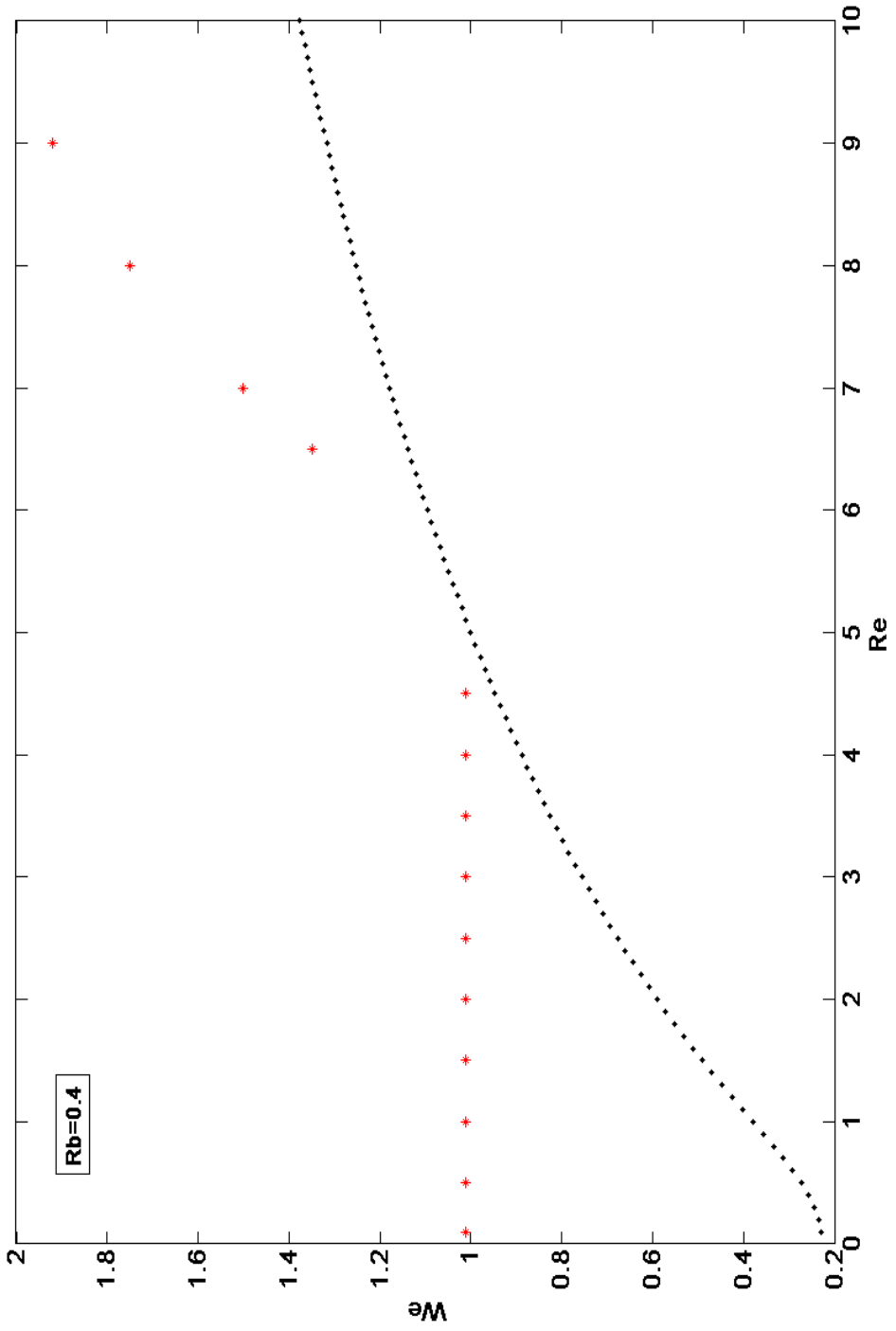

Figure 4.18: Graph showing the Mode 4 region for $Rb = 0.4$. The red stars mark the upper boundary of the Mode 4 region.

expressions for u_0 and R_0 into We_{local} and Re_{local} we have

$$\begin{aligned} We_{local}(\hat{s}) &= We\ {u_0}^2 R_0 \\ &= We(1+(We-1)u(\hat{s}))^2(1+(We-1)R(\hat{s})) \\ &= We(1+2u(\hat{s})(We-1))(1+(We-1)R(\hat{s}))+O((We-1)^2) \\ &= We(1+(We-1)(2u(\hat{s})+R(\hat{s})))+O((We-1)^2) \\ &= We+We(We-1)(2u(\hat{s})+R(\hat{s}))+O((We-1)^2). \end{aligned}$$

Hence for $We \to 1$, we have

$$We_{local}(\hat{s}) = We + We(We-1)(2u(\hat{s})+R(\hat{s})) \tag{4.13}$$

at leading order in $(We-1)$. To redefine Re_{local}, again we substitute for u_0 and R_0 to give

$$\begin{aligned} Re_{local}(\hat{s}) &= Re\ u_0 R_0 \\ &= Re(1+(We-1)u(\hat{s}))(1+(We-1)R(\hat{s})) \\ &= Re(1+(We-1)(u(\hat{s})+R(\hat{s}))+O((We-1)^2). \end{aligned}$$

So Re_{local} is now given by

$$Re_{local}(\hat{s}) = Re + Re(We-1)(u(\hat{s})+R(\hat{s})) \tag{4.14}$$

at leading order in $(We-1)$.

Using these new redefined expressions for Re_{local} and We_{local} we are able to work out the Re_{local}-We_{local} trajectory in the asymptotic region as $We \to 1$. The new Mode 4 curves in the singularity region close to $We = 1$ are calculated using the technique described earlier, i.e. by solving equations (4.9)-(4.12) subject to initial conditions $x =$

$z = x' = z' = u = R = 0$ and substituting the numerical results for u and R into the new redefined expressions for Re_{local} and We_{local} (4.13) and (4.14), respectively, to calculate the Re_{local}-We_{local} trajectory. Figures 4.19, 4.20 and 4.21 show the new Mode 4 curves found in the asymptotic region as $We \to 1$ for $Rb = 4, 2$ and 0.8, respectively. These new Mode 4 regions intersect the critical curve at $We = 1$ implying no Mode 4 at $We = 1$, agreeing with the results found earlier by reducing the step-size of the problem and thus are identical to Figures 4.15, 4.16 and 4.17.

4.4 Conclusion

By examining the Re_{local}-We_{local} trajectory we have shown that a jet in the Mode 4 parameter regime (small Weber, Reynolds and Rossby numbers) grows convectively initially, but eventually becomes subject to absolute instability as it evolves. For fixed Rossby numbers we have determined a Mode 4 region in the Re-We space lying in the convective instability region above the critical curve which marks the boundary between convective and absolute instabilities such that any Re_{local}-We_{local} trajectory starting in the Mode 4 region always crosses the critical curve at some s indicating the onset of absolute instability in a jet which was initially convectively unstable. The area of the Mode 4 region increases as $Rb \to 0$. This is in agreement with experiments where Mode 4 is found to increase for small Rossby numbers. More detailed comparison with experiments is carried out in Chapter 6.

Figures 4.15-4.18 all appear to show that the Mode 4 region shrinks to zero as $We \to 1$, as suggested by the asymptotics. Solving the asymptotic equations numerically, we found that Mode 4 regions calculated by using the numerical results from the asymptotic equations (Figures 4.19-4.21) agree exactly with Figures 4.15-4.18, which were found by solving equations (3.42) and reducing the step-size in the calculation close to $We \to 1$.

We finish this chapter with the following hypothesis. We claim that jets for which We and Re lie in the calculated Mode 4 region appear as in Figures 3.9 and 3.10. Jets for which We and Re are above this region, are convectively unstable (as Figures 3.3-3.8) and

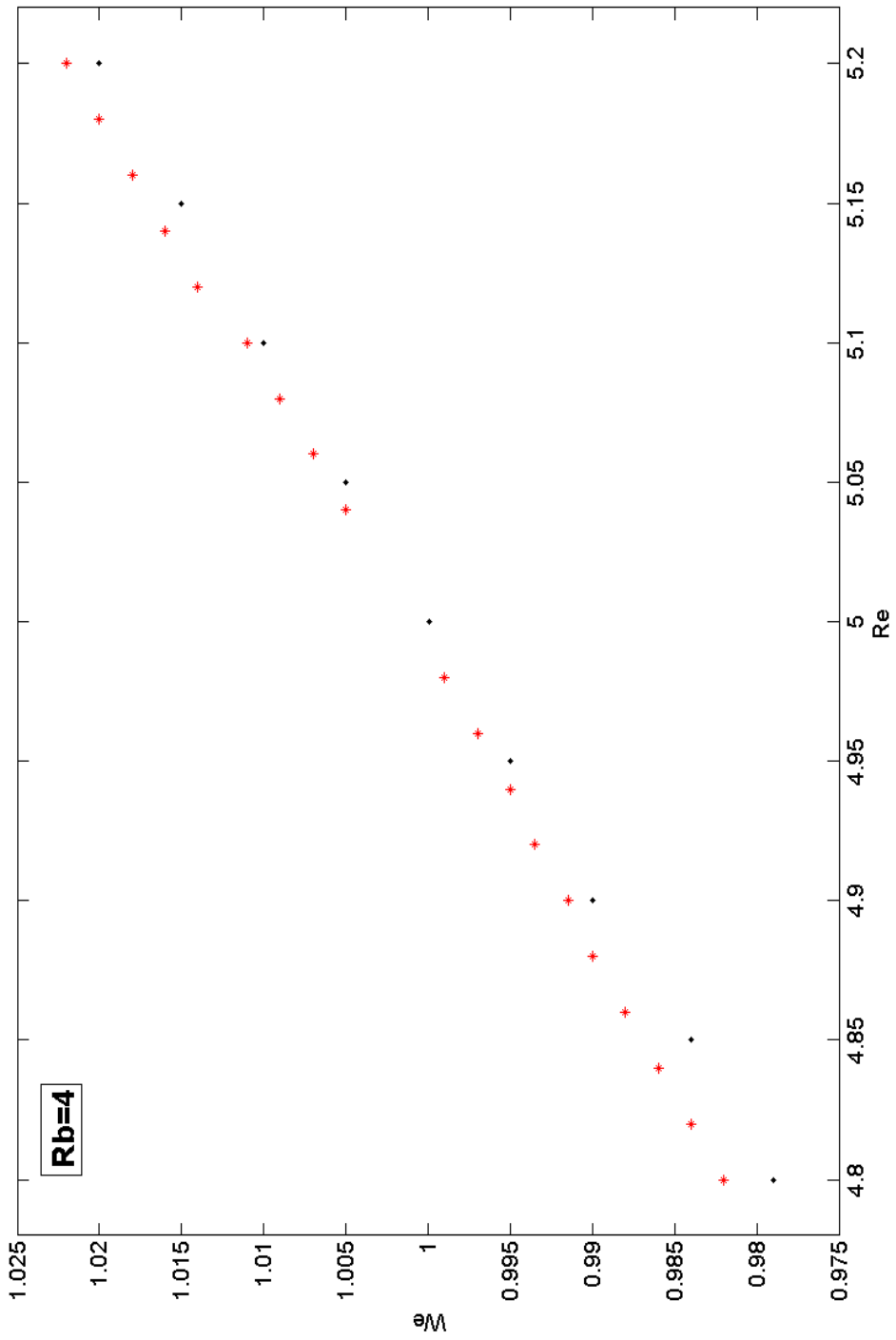

Figure 4.19: Graph showing the zoomed in Mode 4 curve for $Rb = 4$ in the region close to $We = 1$. The red stars mark the upper boundary of the Mode 4 curve, calculated by finding the Re_{local}-We_{local} trajectory by numerically solving the two-dimensional asymptotic equations for $We \to 1$ ((4.9)-(4.12)).

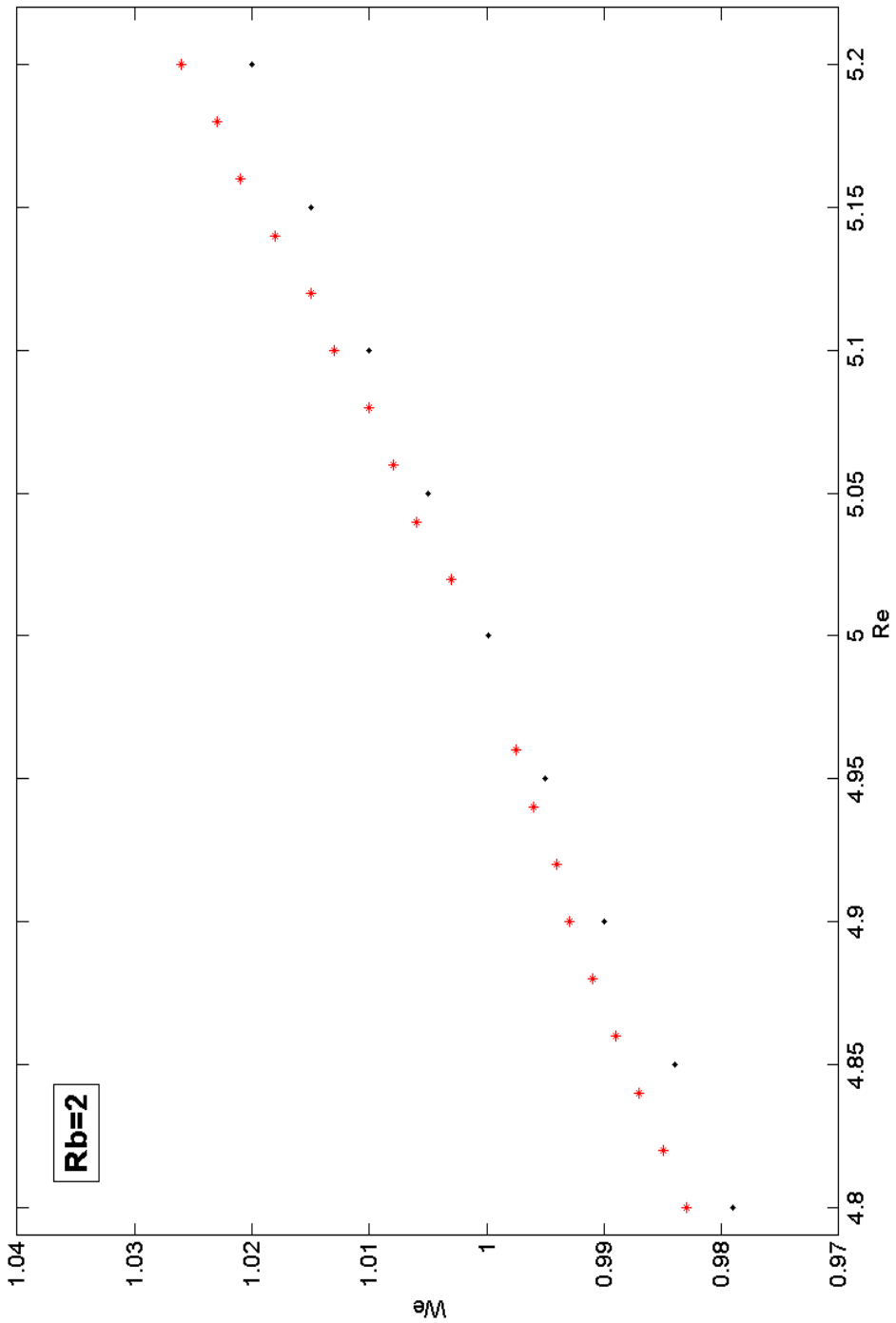

Figure 4.20: Graph showing the zoomed in Mode 4 curve for $Rb = 2$ in the region close to $We = 1$. The red stars mark the upper boundary of the Mode 4 curve, calculated by finding the Re_{local}-We_{local} trajectory by numerically solving the two-dimensional asymptotic equations for $We \to 1$ ((4.9)-(4.12)).

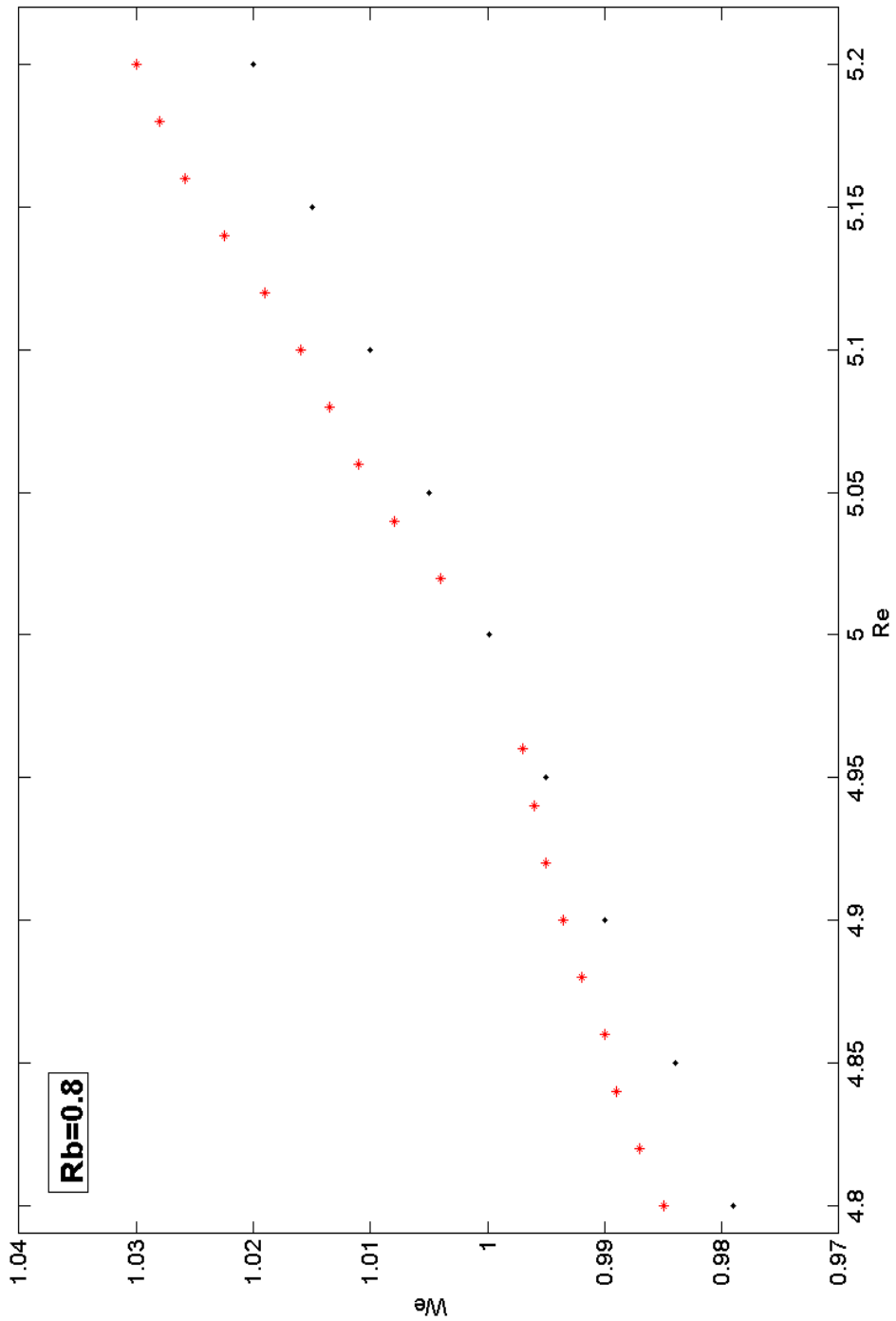

Figure 4.21: Graph showing the zoomed in Mode 4 curve for $Rb = 0.8$ in the region close to $We = 1$. The red stars mark the upper boundary of the Mode 4 curve, calculated by finding the Re_{local}-We_{local} trajectory by numerically solving the two-dimensional asymptotic equations for $We \to 1$ ((4.9)-(4.12)).

must be described using a convective instability methodology. Furthermore, jets for which We and Re are in the absolute instability region (i.e. below the black curve in Figures 4.15-4.18) are absolutely unstable to start with and hence must correspond to the No Jet photographs in Figure 3.11. We test out this hypothesis in Chapter 6 when we compare our analytical and numerical results with the experimental data. In the following chapter we extend this theory to include the effects of the density ratio of gas to liquid on the critical region in the Re-We space and the effect of gravity on the Mode 4 regions.

Chapter 5

Extending the Model

In this chapter we will extend our study of absolute instability by including the effects of gravity and density ratio. So far we have assumed in our theory that the outer gas does not oppose the jet or create resistance. However, it is important to study the effect of density of this outer gas surrounding the liquid. We consider the density ratio of the surrounding gas to that of the fluid and examine its impact on the critical curve marking the boundary between convective and absolute instability for $Q \neq 0$ (where Q is the density ratio of gas to liquid) at small and large Reynolds numbers using the approach described in Chapter 2.

We then proceed to include gravity in the curved jet model and consider the full three-dimensional jet equations described in Chapter 3 to find the Mode 4 regions for fixed Rossby and Froude numbers. The resulting Mode 4 curves incorporating the effects of gravity will then provide for a more realistic comparison with experiments.

5.1 Density Ratio

In this section we will examine the effect of the density ratio on the domain of absolute instability in the Re-We plane. We determine the critical curve, above which the jet is convectively unstable and absolutely unstable below it, by calculating the critical Weber number We_c using (2.1) for $Q \neq 0$. To determine We_c, we use the methodology described in Chapter 2. The dispersion relation (2.1) is solved using a Newton-Raphson method

assuming ω and k to be complex and the movement of the saddle point of the dispersion relation is examined in the complex ω-plane. At a fixed Reynolds number, the dispersion relation is solved for a Weber number chosen to lie below the expected critical curve and gradually increased until it reaches a solution at which $Re(\omega)$ changes sign from positive to negative. The critical curve is determined for $Q = 0.001$ (the approximate density ratio in experiments performed in Wong *et al.* [70], found by dividing the density of air by the average density of liquids used in [70]) and $Q = 0.03$ and compared to the critical curve for $Q = 0$ found in Chapter 2 (see Figures 2.7 and 2.8). The same values of Q were considered in Lin & Lian [41].

Figure 5.1 shows the critical curves calculated for $Q = 0$ (green points), $Q = 0.001$ (blue stars) and $Q = 0.03$ (red squares) at small Reynolds numbers. The jet is absolutely unstable in the region under the critical curve for a particular Q and convectively unstable above it. It can be seen from Figure 5.1 that at small Reynolds numbers, air density has almost no effect on absolute instability. The critical curves for all three values of Q nearly coincide with each other in this case. Figure 5.2 shows the critical curves calculated at large Reynolds numbers for $Q = 0$ (green points), $Q = 0.001$ (blue stars) and $Q = 0.03$ (red squares). The domain of absolute instability is found to increase for $Q \neq 0$ at higher Reynolds numbers as shown in Figure 5.2, but not very significantly.

In order to find the Mode 4 regions for different values of Q, we would have to incorporate density ratio into Wallwork's [68] model for curved jets. However, since Q does not seem to have a significant effect on the domain of absolute instability, its influence on the Mode 4 curves is not considered in this thesis.

5.2 Gravity

We now study how gravity affects absolute instability in curved liquid jets. We will obtain the Mode 4 regions for fixed Rossby and Froude numbers using the three-dimensional steady state model which includes gravity (described in Chapter 3).

The three-dimensional equations (3.25) are solved numerically using a Runge-Kutta

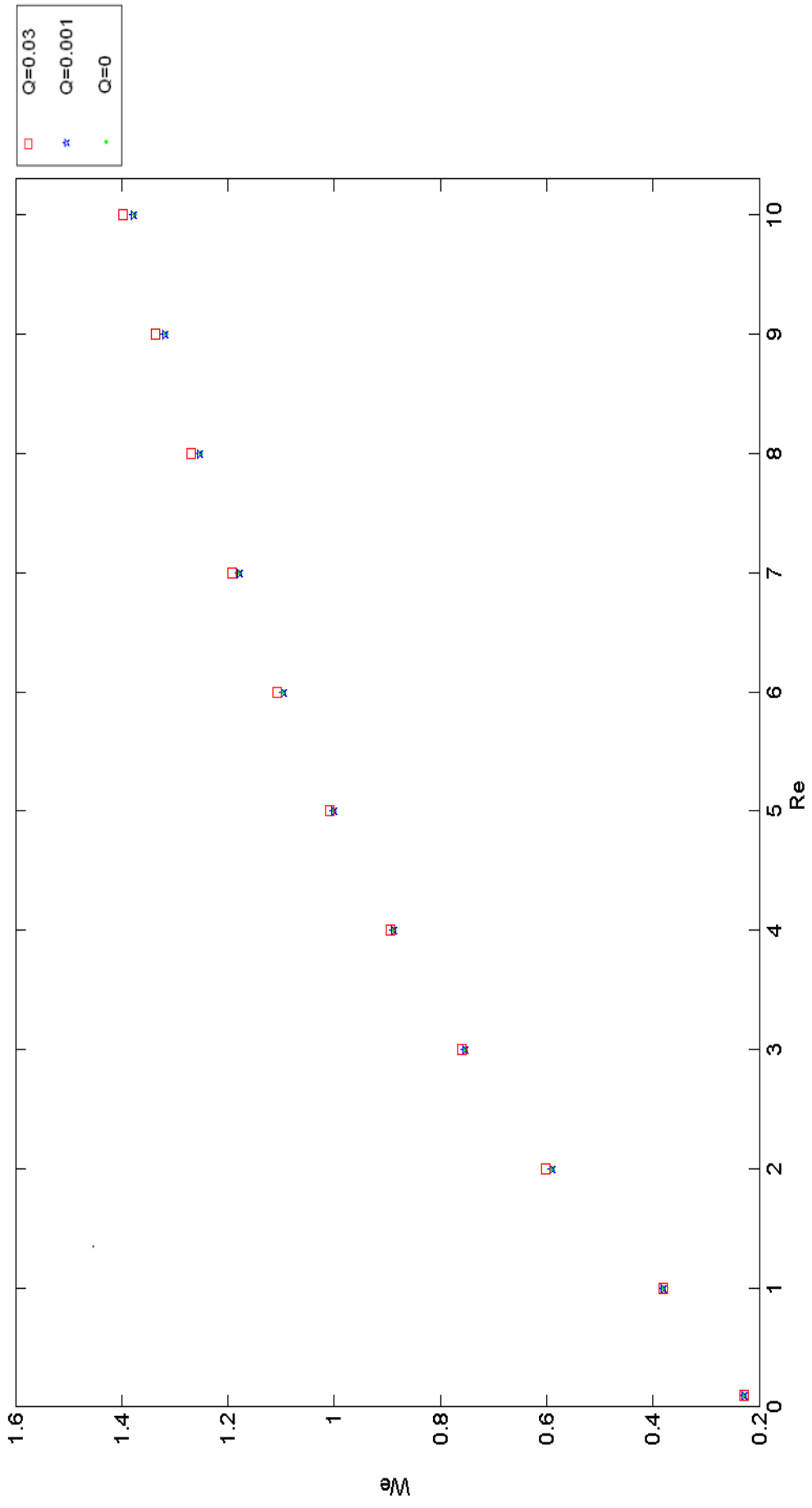

Figure 5.1: Graph showing the critical curves for $Q = 0$ (green dots), $Q = 0.001$ (blue stars) and $Q = 0.03$ (red squares) marking the transition between convective and absolute instability at small Reynolds numbers ($0 < Re < 10$). The jet is absolutely unstable in the region under the critical curve for a particular Q value and convectively unstable above it.

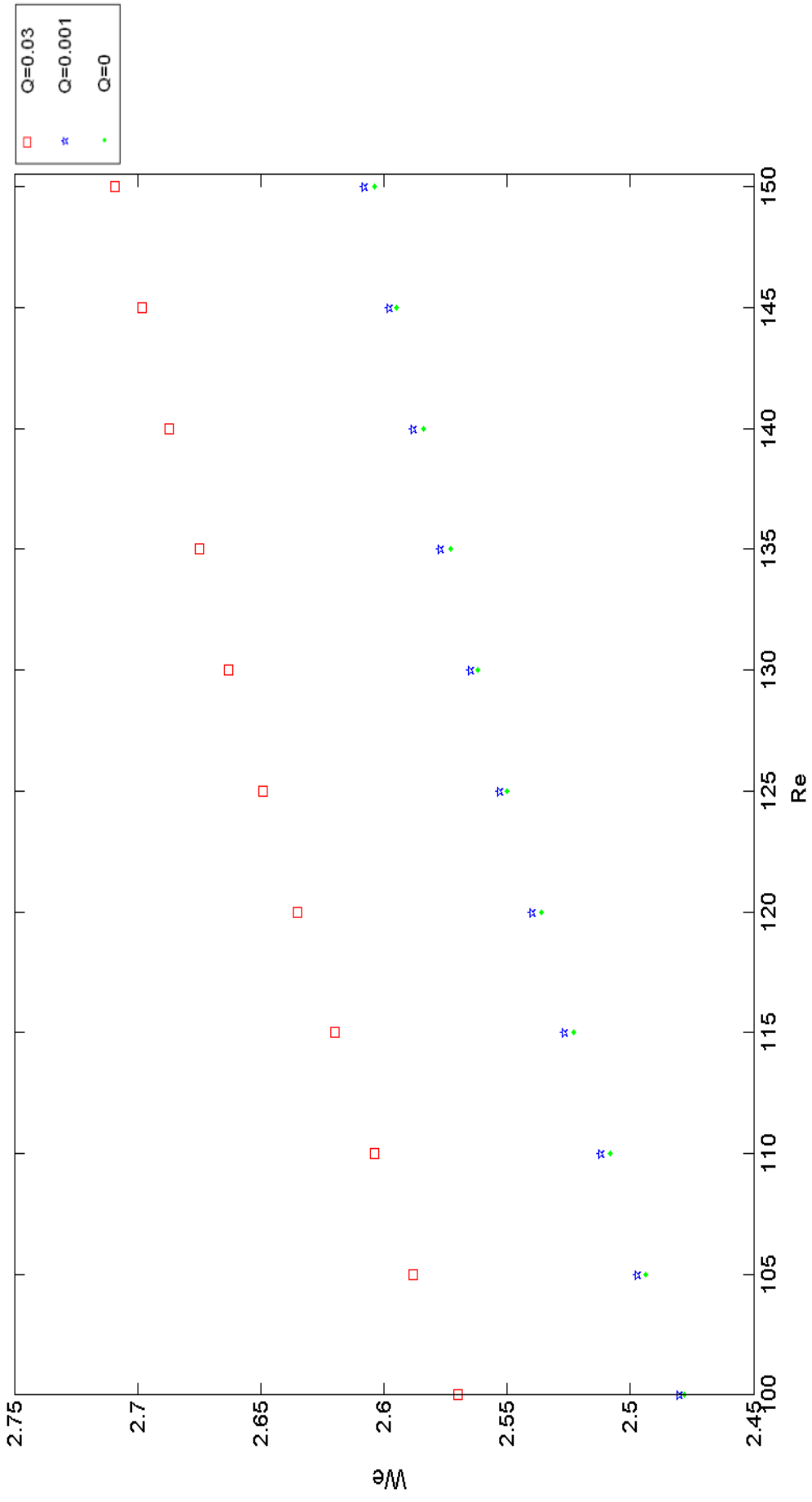

Figure 5.2: Graph showing the critical curves for $Q = 0$ (green dots), $Q = 0.001$ (blue stars) and $Q = 0.03$ (red squares) marking the transition between convective and absolute instability at large Reynolds numbers ($100 < Re < 150$). The jet is absolutely unstable in the region under the critical curve for a particular Q value and convectively unstable above it.

method. We then determine the $Re_{local}(s)$-$We_{local}(s)$ trajectory by calculating $Re_{local}(s)$ and $We_{local}(s)$ for every s produced by the Runge-Kutta method. (Note that the dispersion relation (2.1) is independent of F, but (3.18)-(3.24) do depend upon F.) Using the method described in Section 4.2, we determine the Mode 4 regions in the Re-We plane for fixed Rossby and Froude numbers. Any Re_{local}-We_{local} trajectory starting in this Mode 4 area (which lies in the convective instability region above the critical curve) always crosses the critical boundary making a transition from convective to absolute instability at some s.

When $F = \infty$ and $Y = 0$, gravity is switched off in the three-dimensional steady state equations (3.18)-(3.24) and we find that they become equivalent to the two-dimensional steady state equations (3.36)-(3.41). Solving equations (3.25) numerically for $F = \infty$ and using them to obtain Re_{local}-We_{local} trajectory via the technique explained in Section 4.2 gives Figures 5.3 and 5.4 which show the Mode 4 regions for $Rb = 4$ and $Rb = 0.8$ at $F = \infty$, respectively. These Mode 4 regions correspond to Figures 4.15 and 4.17, which are obtained by solving the two-dimensional model where gravity is neglected.

Figures 5.5 and 5.6 (obtained in the same way as Figures 5.3 and 5.4, i.e. by solving equations (3.25) to find the Re_{local}-We_{local} trajectory) show the Mode 4 regions for $F = 4, 0.8$, respectively, at $Rb = 4$. These figures show that the upper boundary of the Mode 4 region for $Re < 5$ occurs at a constant Weber number with $We^* = 1.01$ (where (Re, We^*) is the lowest point above the critical curve such that Re_{local}-We_{local} trajectories starting at this point or above it, do not cross the critical curve). For $Re > 5$ we find that the Mode 4 curve overlaps with the critical curve implying that there is no Mode 4 for $Re > 5$. Figure 5.7 shows the Re_{local}-We_{local} trajectory calculated for $Re_{local}(0) = 7$, $We_{local}(0) = 1.19$, $Rb = 4$ and $F = 4$. The critical Weber number value corresponding to $Re = 7$ is $We_c = 1.179$. We find that this trajectory never crosses the critical curve. Figures 5.8 and 5.9 show the graphs of Re_{local} and We_{local} plotted against s, respectively, for the trajectory shown in Figure 5.7. Figures 5.10 and 5.11 show the corresponding graphs of u_0 and R_0 plotted against s, respectively. Also, at small Froude numbers, we find that for

$We < 1$ the Matlab program which uses a fixed step-size Runge-Kutta method to solve the three-dimensional jet equations returns complex values for X, Y and Z, implying the break down of the slender jet theory as $R_0 \to \infty$ and $u_0 \to 0$. However, the slender jet assumption breaks down only after the Re_{local}-We_{local} trajectory has crossed the critical curve. Thus, the model only becomes invalid after the transition from convective to absolute instability has occurred (this is explained in Section 5.2.3).

Figures 5.12 and 5.13 show the Mode 4 regions for $F = 0.8, 0.16$, respectively, at $Rb = 0.8$. Again, we observe the same trend. The upper boundary of the Mode 4 region for $Re > 5$ coincides with the critical curve and for $Re < 5$ we find that this boundary is parallel to the x-axis with $We^* = 1.01$. Looking at Figures 5.5, 5.6, 5.12 and 5.13, it appears that Mode 4 is a high viscosity phenomenon as the amount of Mode 4 reduces drastically for higher Reynolds numbers. Therefore, more elaborative experiments using viscous liquids are conducted to gain a better understanding of this special case. The results of these experiments are shown in Chapter 6 where we make an in-depth comparison with our theoretical results.

5.2.1 Asymptotic Analysis for $We \to 1$

We carry out an asymptotic analysis for $We \to 1$ on the three-dimensional steady state equations (3.18)-(3.24), using the same methodology as the two-dimensional case in Section 4.3. We scale into the singularity region by using the same asymptotic expansions

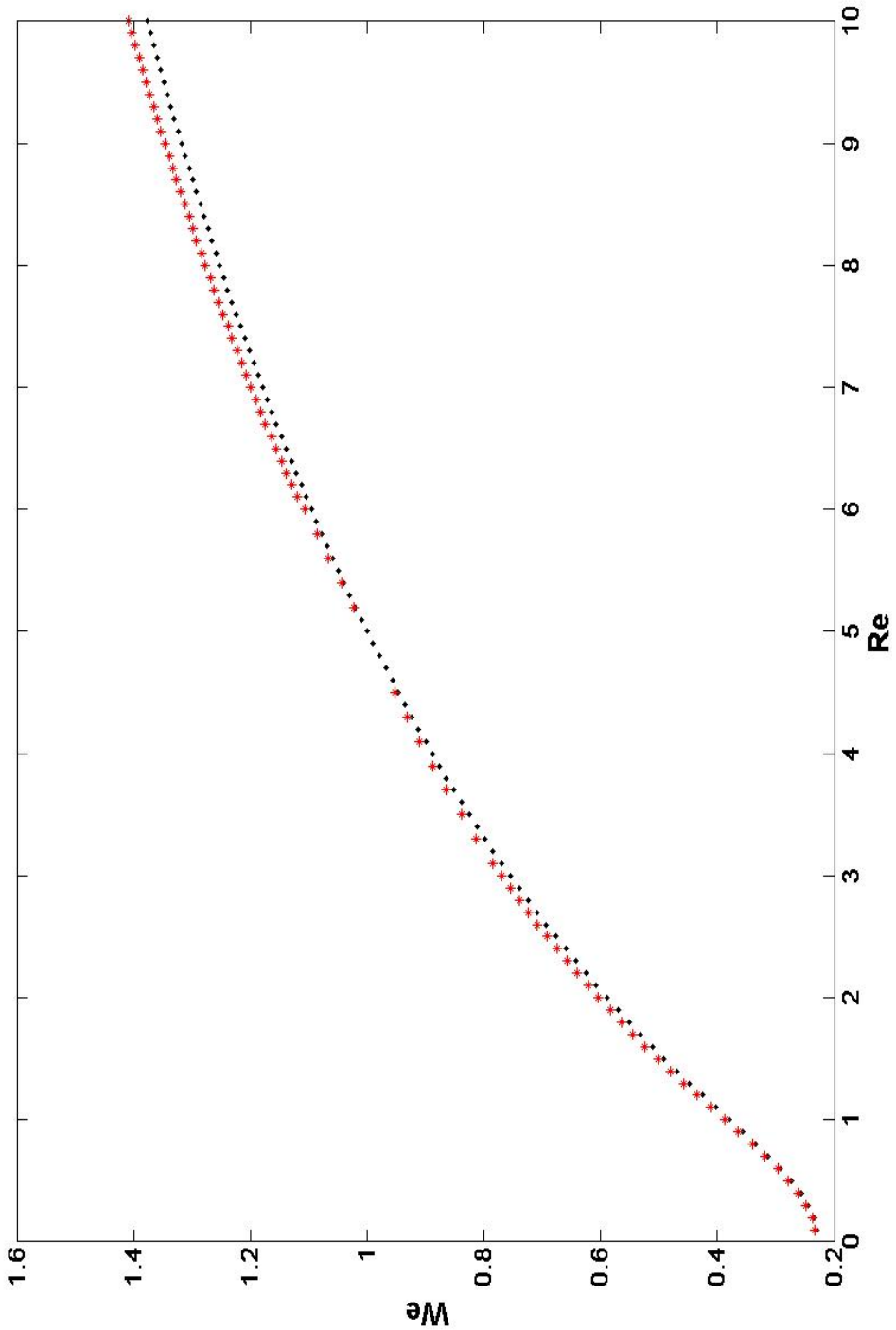

Figure 5.3: Graph showing the Mode 4 region for $Rb = 4$ and $F = \infty$. The red stars mark the upper boundary of the Mode 4 region.

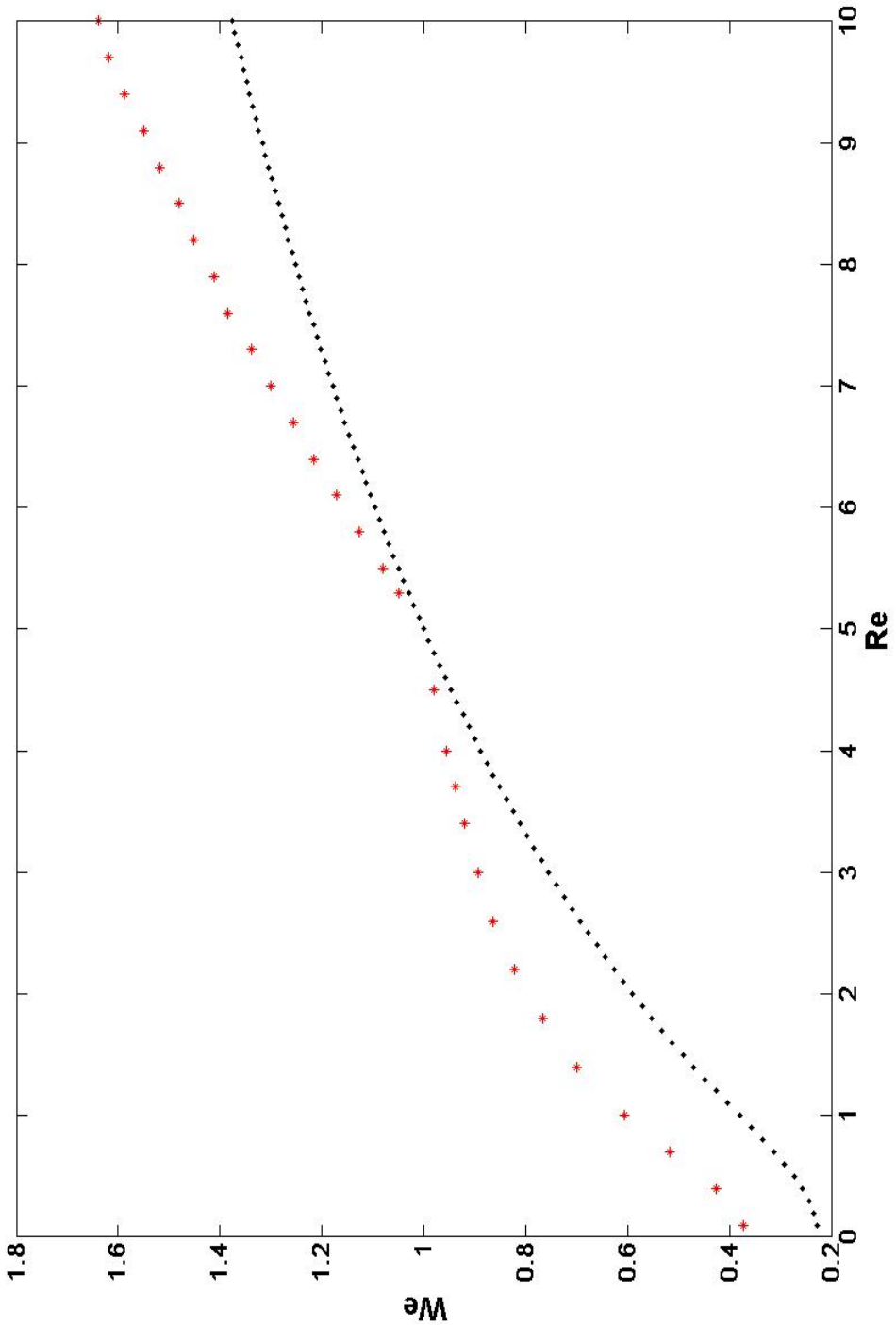

Figure 5.4: Graph showing the Mode 4 region for $Rb = 0.8$ and $F = \infty$. The red stars mark the upper boundary of the Mode 4 region.

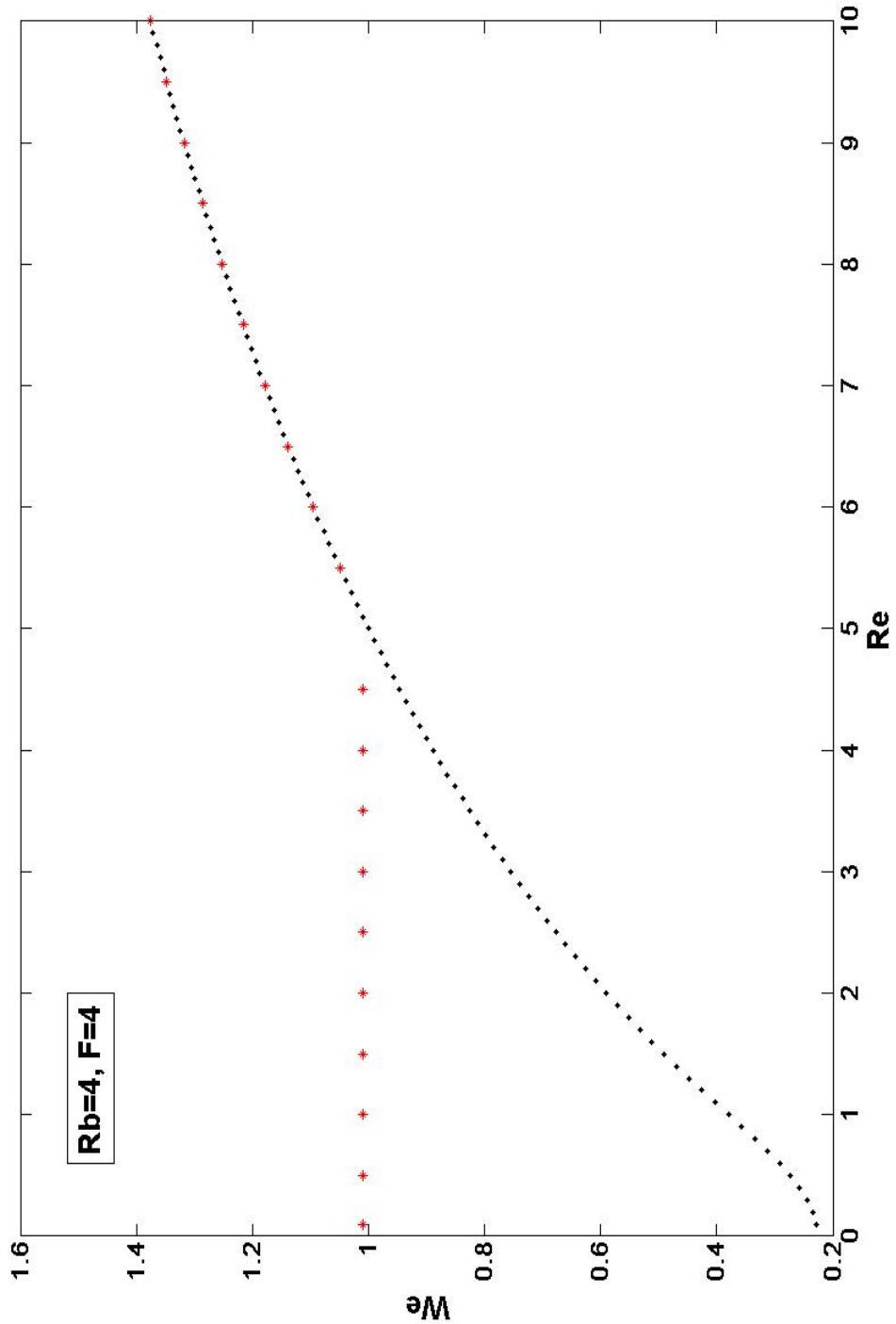

Figure 5.5: Graph showing the Mode 4 region for $Rb = 4$ and $F = 4$. The red stars mark the upper boundary of the Mode 4 region. For $Re > 5$ the upper boundary of the Mode 4 region overlaps with the critical curve.

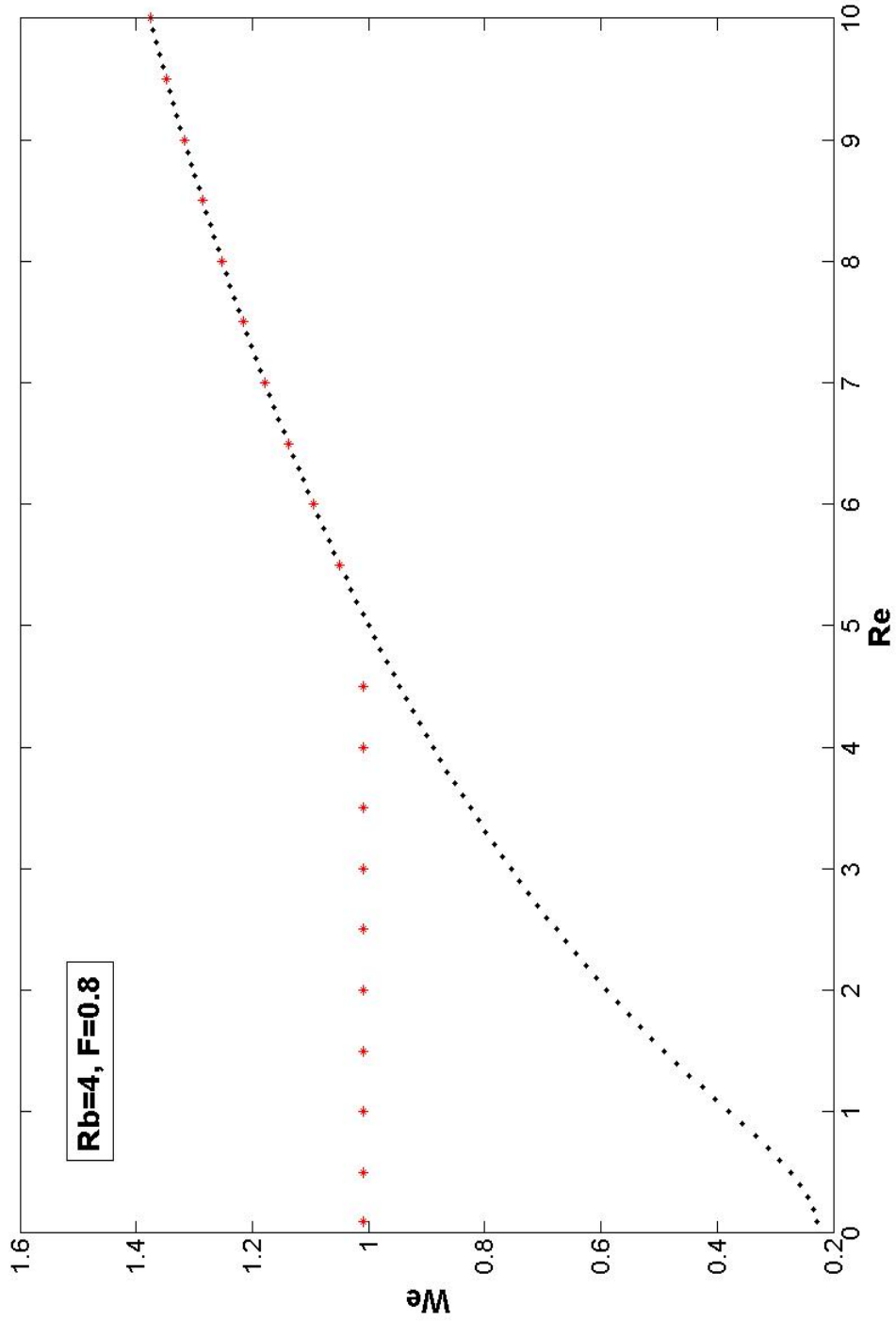

Figure 5.6: Graph showing the Mode 4 region for $Rb = 4$ and $F = 0.8$. The red stars mark the upper boundary of the Mode 4 region. For $Re > 5$ the upper boundary of the Mode 4 region overlaps with the critical curve.

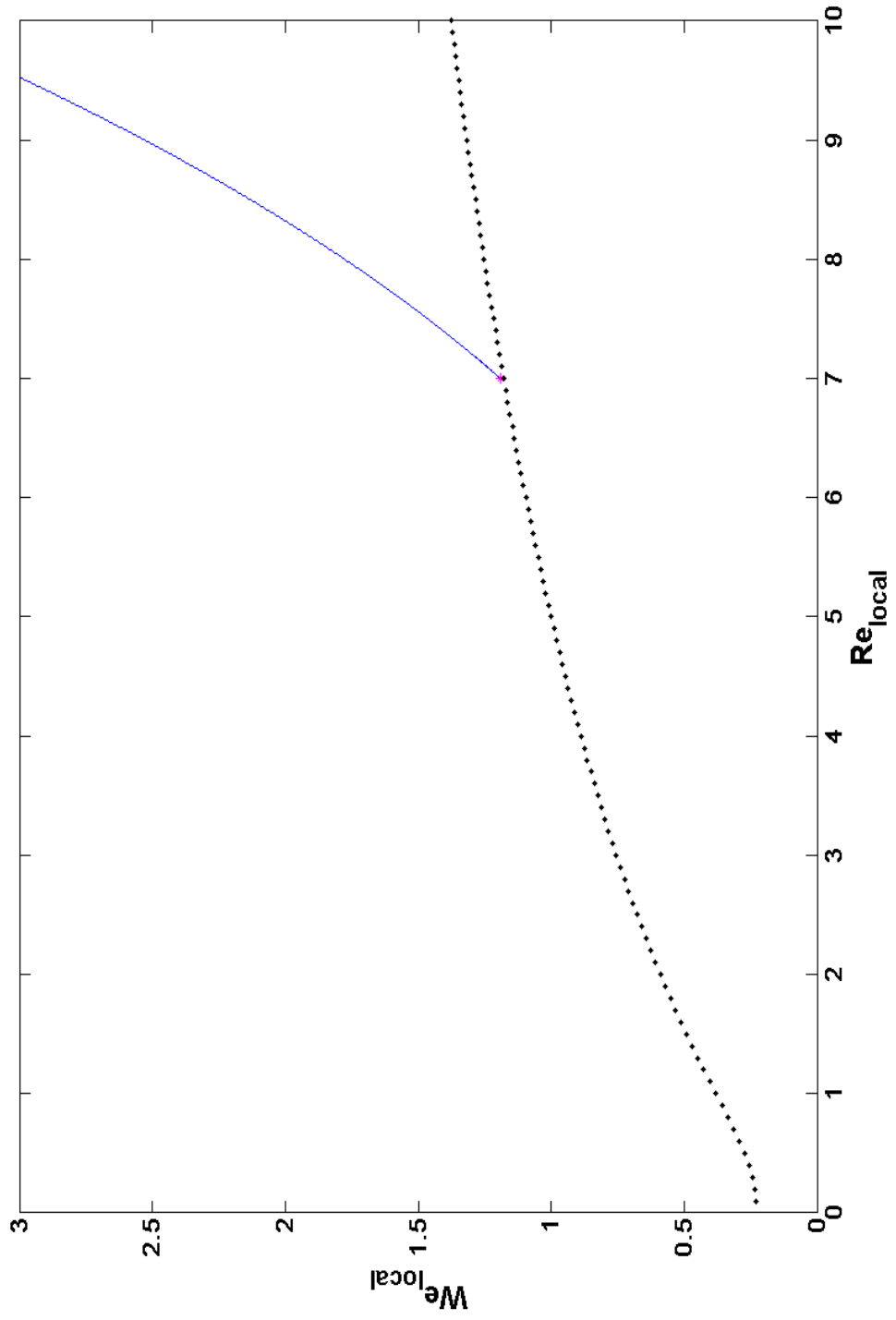

Figure 5.7: Graph showing the Re_{local}-We_{local} trajectory. The red point indicates the starting point of the trajectory. $Re_{local}(0) = 7$, $We_{local}(0) = 1.19$, $Rb = 4$, $F = 4$ and $We_c = 1.179$.

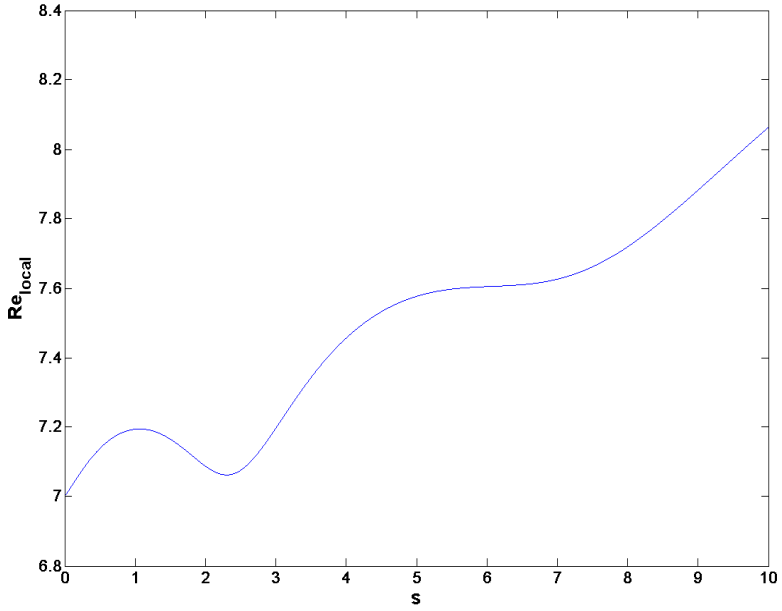

Figure 5.8: Graph showing $Re_{local}(s)$ plotted against s. $Re_{local}(0) = 7$, $We_{local}(0) = 1.19$, $Rb = 4$ and $F = 4$.

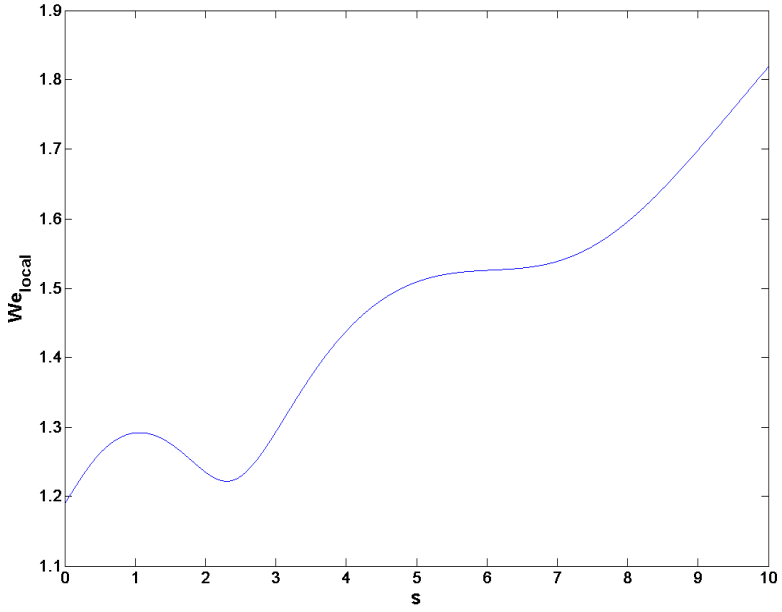

Figure 5.9: Graph showing $We_{local}(s)$ plotted against s. $Re_{local}(0) = 7$, $We_{local}(0) = 1.19$, $Rb = 4$ and $F = 4$.

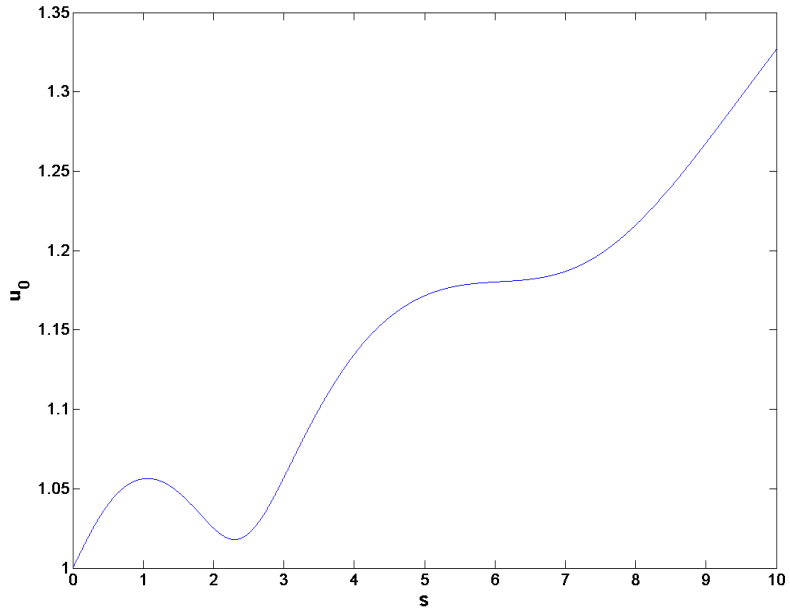

Figure 5.10: Graph showing u_0 plotted against s. $Re_{local}(0) = 7$, $We_{local}(0) = 1.19$, $Rb = 4$ and $F = 4$.

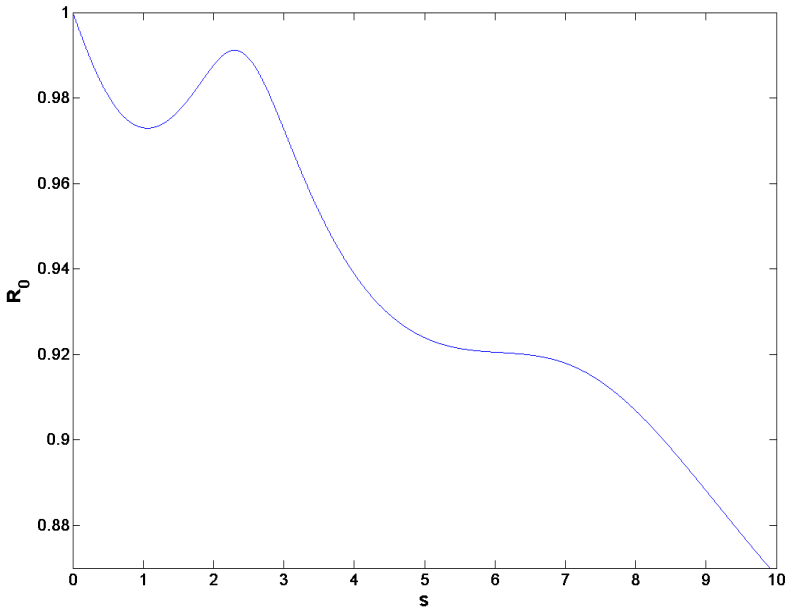

Figure 5.11: Graph showing R_0 plotted against s. $Re_{local}(0) = 7$, $We_{local}(0) = 1.19$, $Rb = 4$ and $F = 4$.

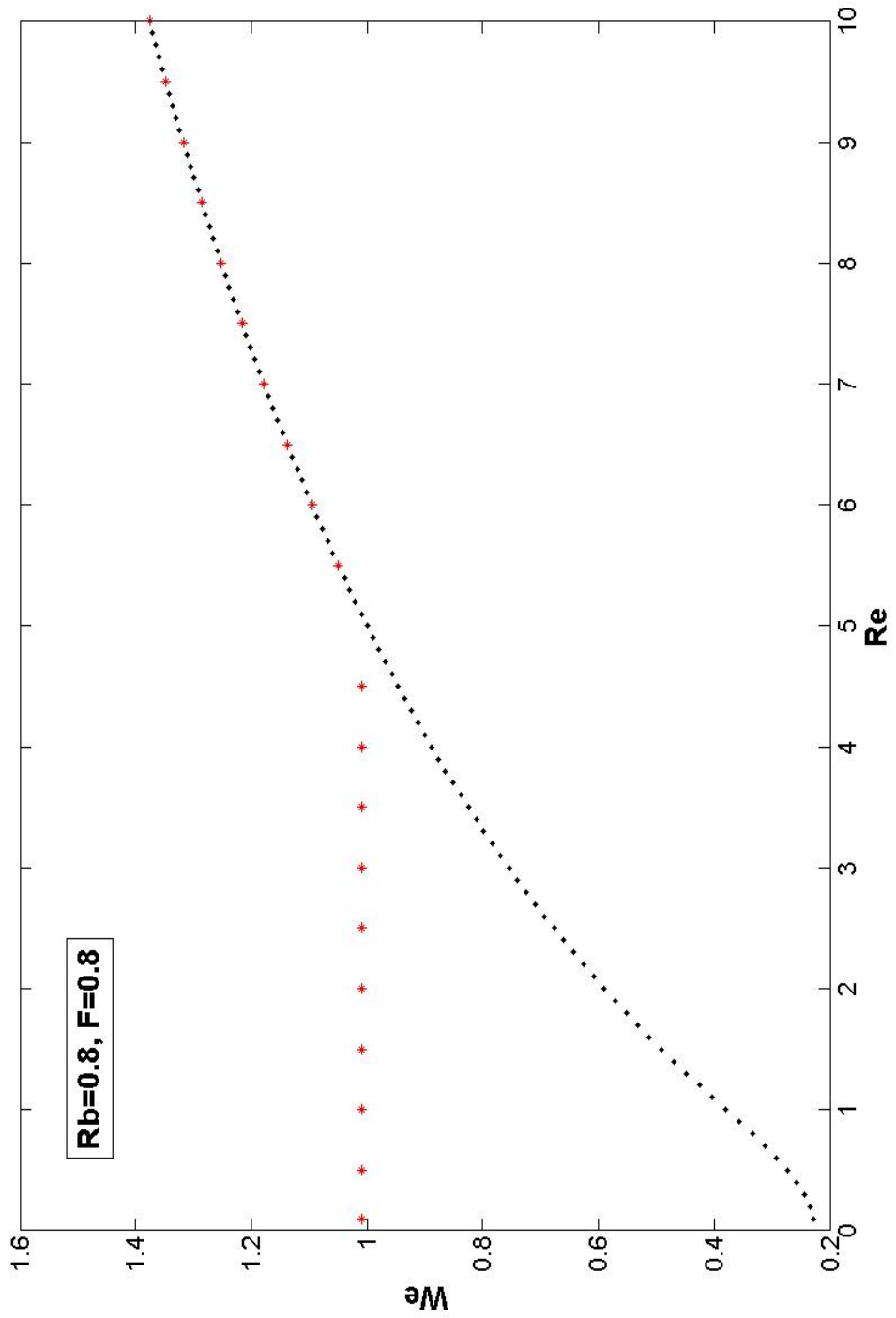

Figure 5.12: Graph showing the Mode 4 region for $Rb = 0.8$ and $F = 0.8$. The red stars mark the upper boundary of the Mode 4 region. For $Re > 5$ the upper boundary of the Mode 4 region overlaps with the critical curve.

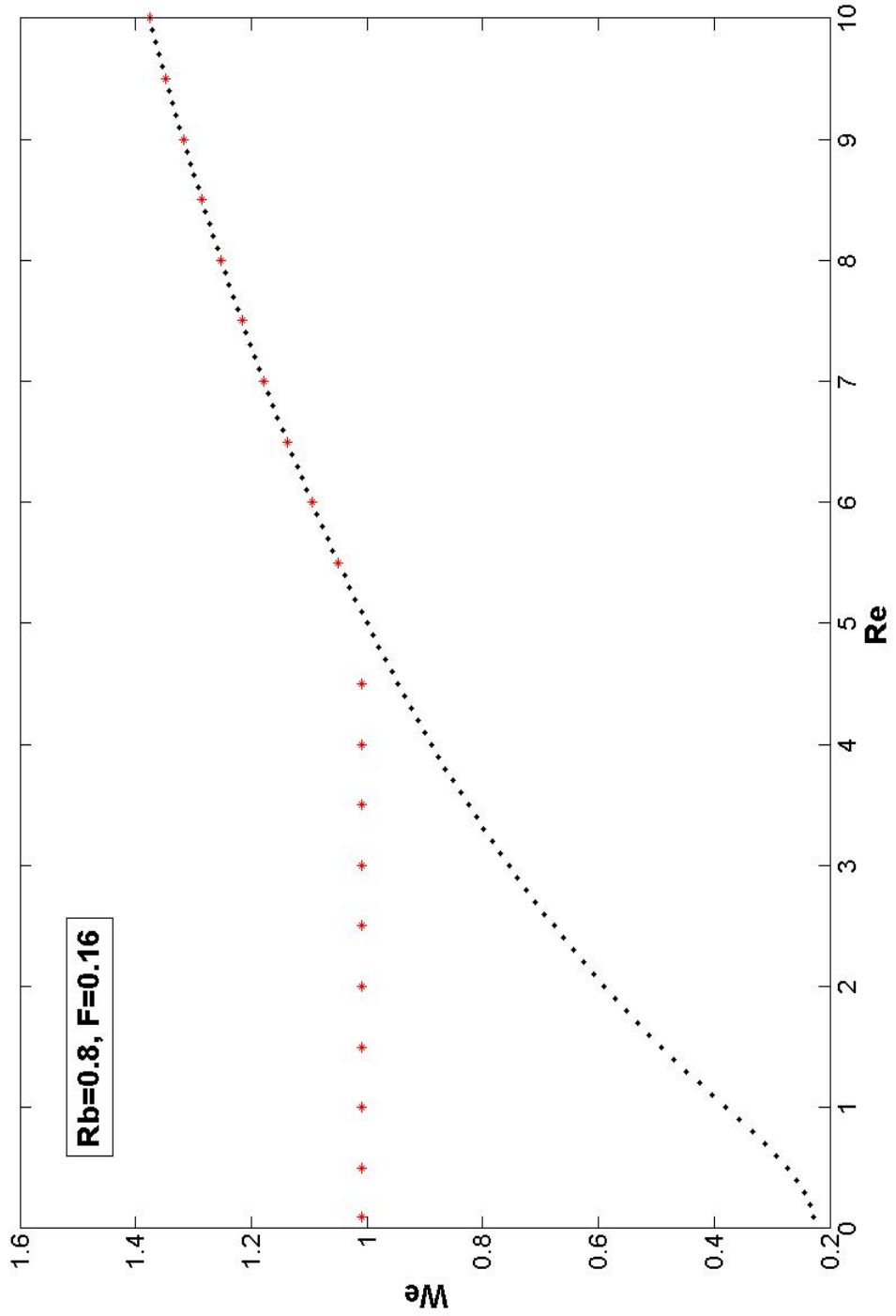

Figure 5.13: Graph showing the Mode 4 region for $Rb = 0.8$ and $F = 0.16$. The red stars mark the upper boundary of the Mode 4 region. For $Re > 5$ the upper boundary of the Mode 4 region overlaps with the critical curve.

introduced earlier in Section 4.3

$$We = 1 + \alpha, \tag{5.1}$$

$$s = \alpha^n \hat{s}, \tag{5.2}$$

$$u_0 = 1 + \alpha^p u(\hat{s}), \tag{5.3}$$

$$R_0 = 1 + \alpha^q R(\hat{s}), \tag{5.4}$$

$$X = \alpha^n \hat{s} + \alpha^r x(\hat{s}), \tag{5.5}$$

$$Y = \alpha^m y, \tag{5.6}$$

$$Z = \alpha^t z(\hat{s}) \tag{5.7}$$

where $\alpha \to 0$. By substituting these expansions into the three-dimensional steady state equations (3.25), we obtain the distinguished limit $n = m = p = q = r = t = 1$. Putting these limits into (5.2)-(5.7) and substituting the resulting expansions back into (3.25), we are left with the following set of leading order equations in α

$$u = \frac{2}{3}\left(\frac{-y}{F^2} + \frac{\hat{s}+x}{Rb^2}\right), \tag{5.8}$$

$$R = \frac{1}{3}\left(\frac{y}{F^2} - \frac{\hat{s}+x}{Rb^2}\right), \tag{5.9}$$

$$\left(\frac{-y}{F^2} + \frac{\hat{s}+x}{Rb^2} + 1\right)(x''^2 + y''^2 + z''^2) = \frac{-y}{F^2} + \frac{2}{Rb}((1+x')z'' - z'x'') + \frac{x''}{Rb^2}, \tag{5.10}$$

$$\frac{z'x'' - (1+x')z''}{F^2} - \frac{2y''}{Rb} + \frac{y''z' - z''y'}{Rb^2} = 0, \tag{5.11}$$

$$x'^2 + y'^2 + z'^2 + 2x' = 0 \tag{5.12}$$

where $'$ represents differentiation with respect to $\hat{s}$. We now solve these equations numerically subject to the initial conditions $x = y = z = x' = y' = z' = u = R = 0$ at $\hat{s} = 0$ and use the resulting u and R values to calculate We_{local} and Re_{local} given by (4.13) and (4.14), as defined previously for the two-dimensional case. The Re_{local}-We_{local} trajectories are computed and Mode 4 curves in the singularity region close to $We = 1$ are determined by applying the same technique used to determine Mode 4 curves previously.

Figures 5.14 and 5.15 show the Mode 4 curves for $Rb = 4$ and $F = 4, 0.8$, respectively, and Figures 5.16 and 5.17 show the Mode 4 curves for $Rb = 0.8$ and $F = 0.8, F = 0.16$, respectively. Figure 5.18 shows the Re_{local}-We_{local} trajectory plotted in the Re-We plane for $Rb = 4, F = 4, We = 0.998$ and $Re = 4.92$. The red star marks the starting point of the trajectory in the Re-We plane and we see that in this case ($We < 1$) the trajectory crosses the critical curve. Figures 5.19 and 5.20 show the corresponding plots of Re_{local} and We_{local} against s. Figure 5.21 shows the Re_{local}-We_{local} trajectory plotted in the Re-We plane for $Rb = 4, F = 4, We = 1.001$ and $Re = 4.92$. Again, the red star marks the starting point of the trajectory and in this case ($We > 1$), the trajectory travels away from the critical curve and grows in this direction without crossing the critical curve. Figures 5.22 and 5.23 show the corresponding plots of Re_{local} and We_{local} against s. We observe that the new Mode 4 curves in the asymptotic region for $We \to 1$ compare exactly to those found earlier (Figures 5.5, 5.6, 5.12 and 5.13).

5.2.2 Solving the Three-dimensional Steady State Equations Using a Variable Step-size Method

So far we have been using a fixed step-size Matlab program which uses a Runge-Kutta method to solve our two and three-dimensional steady state ODEs. We will now solve the three-dimensional steady state equations (3.25) for X, Y, Z, u_0 and R_0, using a Fortran 77 program calling a variable step-size NAG routine D02BBF, which employs a Runge-Kutta-Merson method. The variable step-size solver provides a more accurate program for solving the three-dimensional ODEs for small Froude and Rossby numbers by adjusting the step-size of the computation automatically at each step in order to meet the error tolerances specified, in contrast to the fixed step method used in the Matlab program, which works at a constant step-size for all simulations. Thus, the variable step-size method terminates when the slender jet theory becomes invalid and the model breaks down i.e. without producing complex results for X, Y, Z, u_0 and R_0 (as found in the calculations carried out using Matlab).

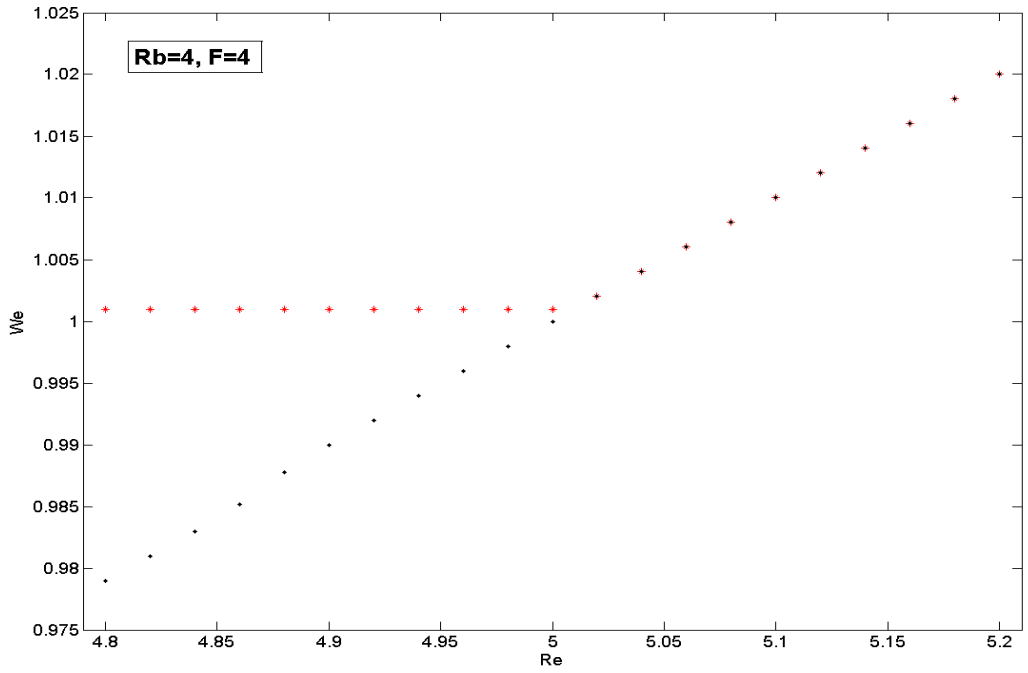

Figure 5.14: Graph showing the zoomed in Mode 4 curve for $Rb = 4$ and $F = 4$ in the region close to $We = 1$. The red stars mark the upper boundary of the Mode 4 curve, calculated by finding the Re_{local}-We_{local} trajectory by numerically solving the three-dimensional asymptotic equations for $We \to 1$ ((5.9)-(5.12)).

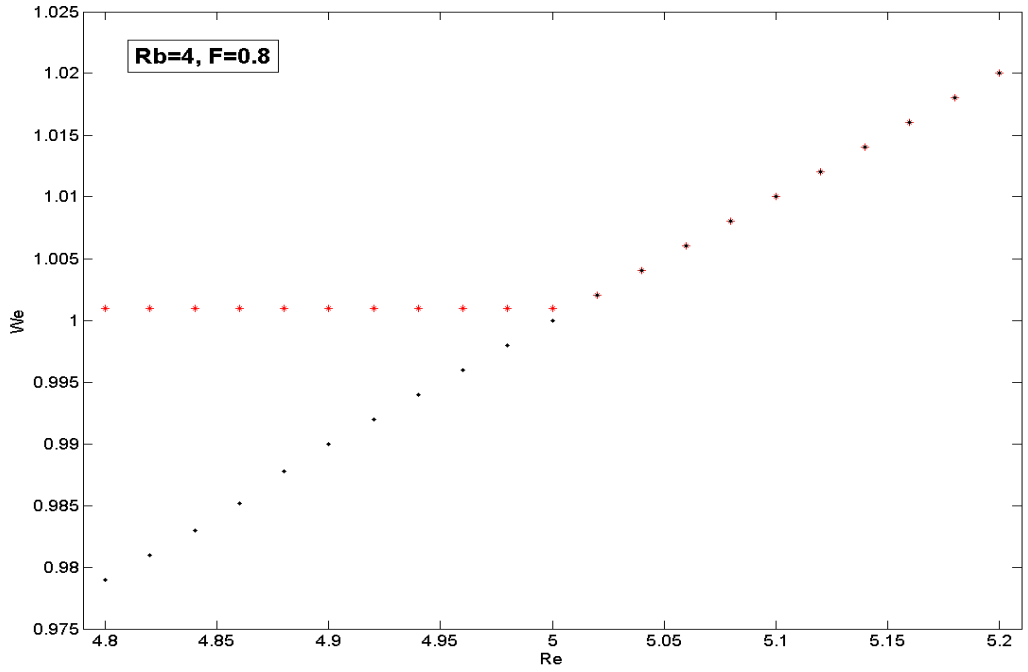

Figure 5.15: Graph showing the zoomed in Mode 4 curve for $Rb = 4$ and $F = 0.8$ in the region close to $We = 1$. The red stars mark the upper boundary of the Mode 4 curve, calculated by finding the Re_{local}-We_{local} trajectory by numerically solving the three-dimensional asymptotic equations for $We \to 1$ ((5.9)-(5.12)).

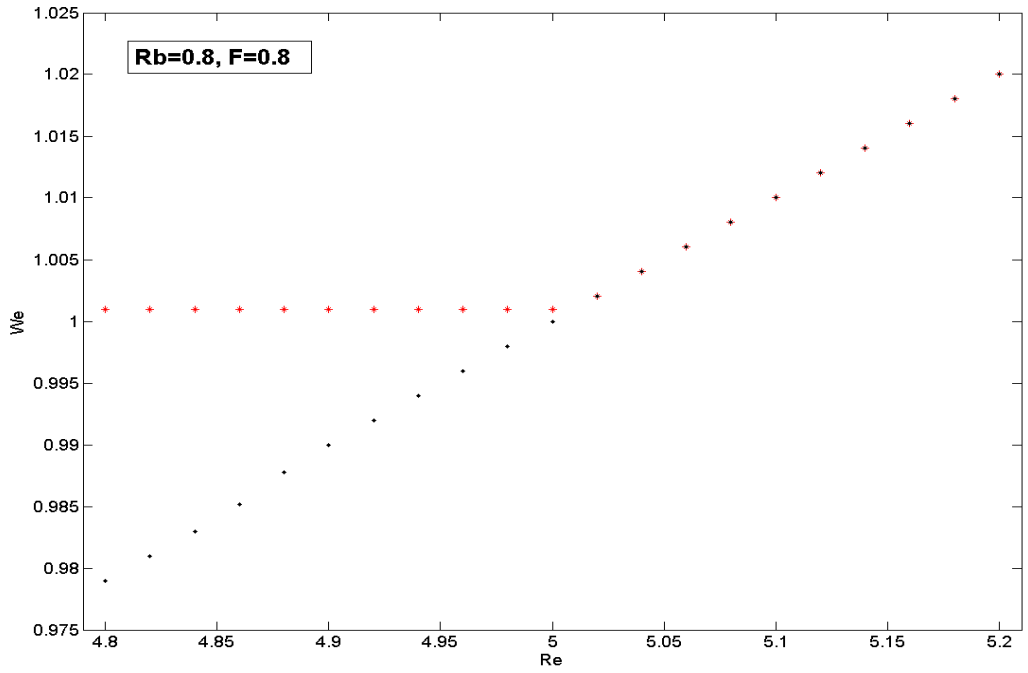

Figure 5.16: Graph showing the zoomed in Mode 4 curve for $Rb = 0.8$ and $F = 0.8$ in the region close to $We = 1$. The red stars mark the upper boundary of the Mode 4 curve, calculated by finding the Re_{local}-We_{local} trajectory by numerically solving the three-dimensional asymptotic equations for $We \to 1$ ((5.9)-(5.12)).

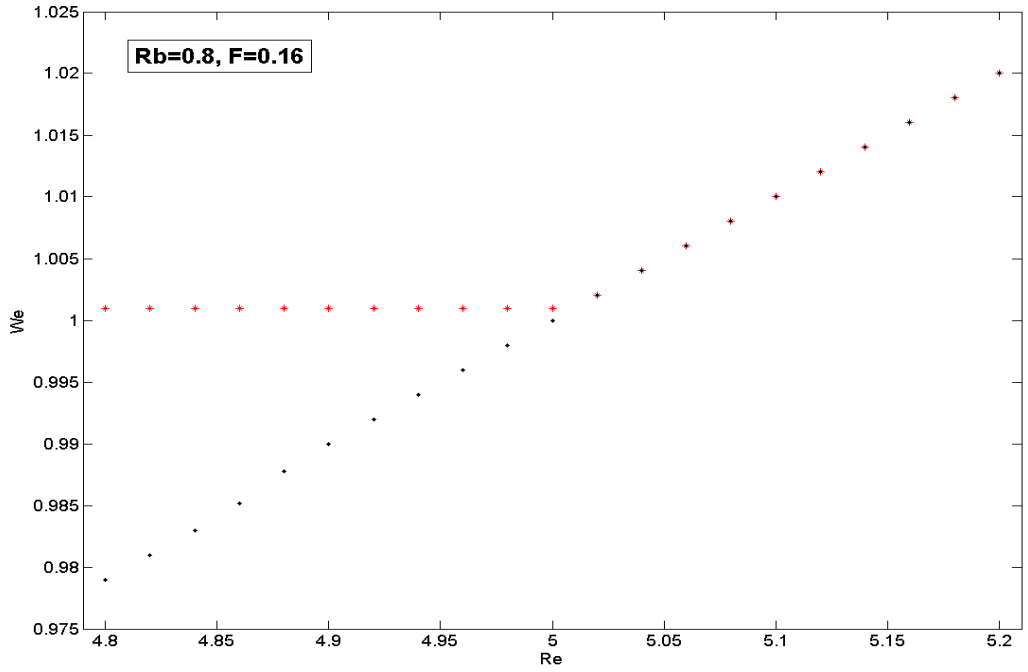

Figure 5.17: Graph showing the zoomed in Mode 4 curve for $Rb = 0.8$ and $F = 0.16$ in the region close to $We = 1$. The red stars mark the upper boundary of the Mode 4 curve, calculated by finding the Re_{local}-We_{local} trajectory by numerically solving the three-dimensional asymptotic equations for $We \to 1$ ((5.9)-(5.12)).

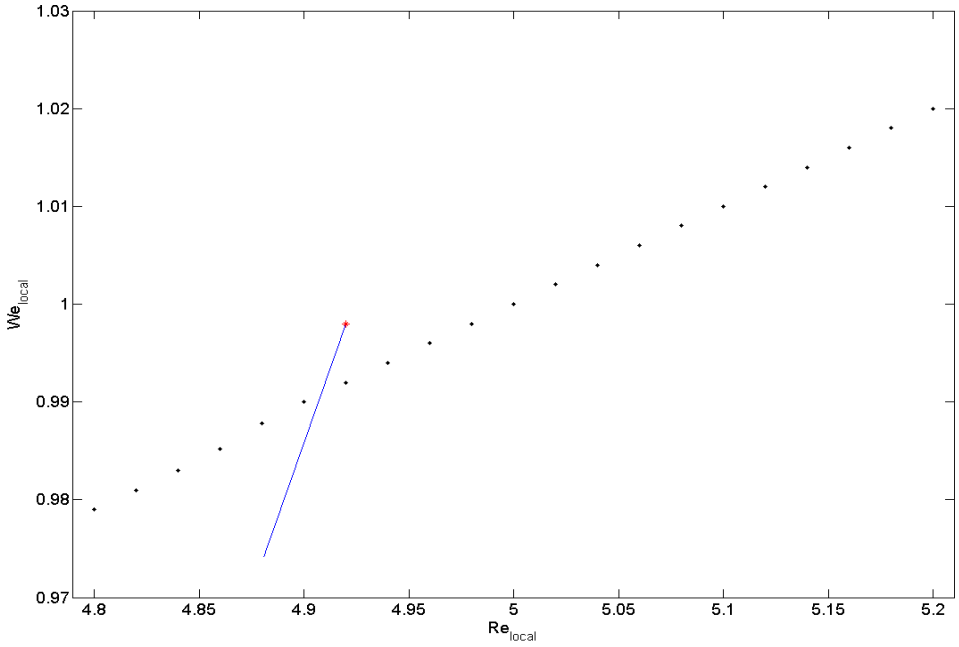

Figure 5.18: Graph showing the Re_{local}-We_{local} trajectory in the Re-We plane. The black dots mark the critical curve and the red star indicates the starting position of the trajectory. $Rb = 4, F = 4, We = 0.998$ and $Re = 4.92$.

The Re_{local}-We_{local} trajectory is computed using the resulting u_0 and R_0 values produced. Adopting the same technique as before, Mode 4 regions are determined from the new Re_{local}-We_{local} trajectories. These Mode 4 curves are found to overlap exactly with the ones found earlier. For large Froude numbers (gravity switched off), the Mode 4 regions coincide with those found previously by solving the two-dimensional jet equations (Figures 4.15, 4.16 and 4.17). For small Froude and Rossby numbers, we observe exactly the same sort of behaviour as before where the upper boundary of the Mode 4 region occurs at a constant Weber number at $We = 1.001$ and the Mode 4 curves look exactly like those in Figures 5.5, 5.6, 5.12 and 5.13.

Figure 5.24 shows the Re_{local}-We_{local} trajectories computed using both the variable step-size method in Fortran and the fixed step-size method in Matlab for $Re_{local}(0) = 0.5, We_{local}(0) = 0.99, Rb = 2$ and $F = 3$. The green line corresponds to the Re_{local}-We_{local} trajectory calculated using results from the Fortran program and the blue line represents the one calculated using the Matlab program. Both codes produce identical

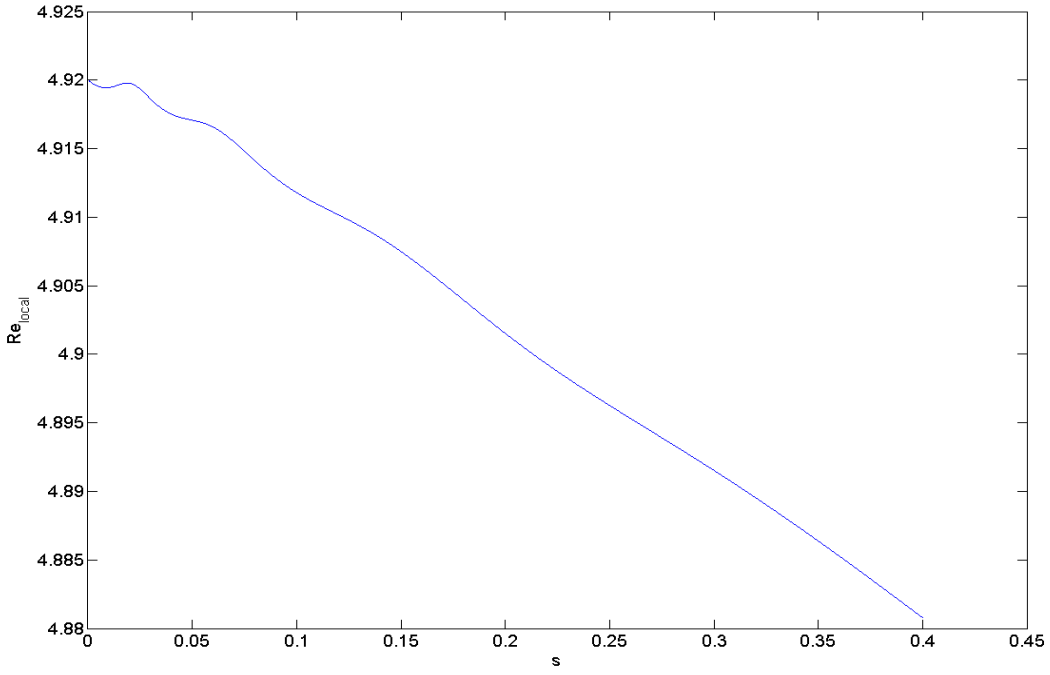

Figure 5.19: Graph of Re_{local} (found by solving three-dimensional asypmtotic equations (5.9)-(5.12)) plotted against s. $Rb = 4, F = 4, We = 0.998$ and $Re = 4.92$.

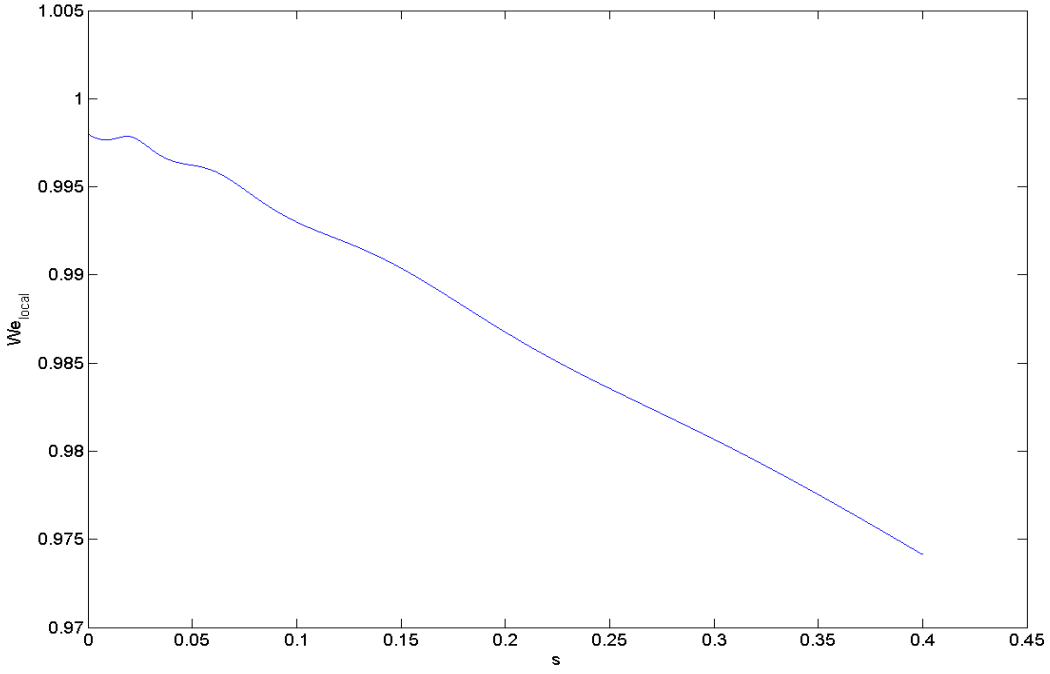

Figure 5.20: Graph of We_{local} (found by solving three-dimensional asypmtotic equations (5.9)-(5.12)) plotted against s. $Rb = 4, F = 4, We = 0.998$ and $Re = 4.92$.

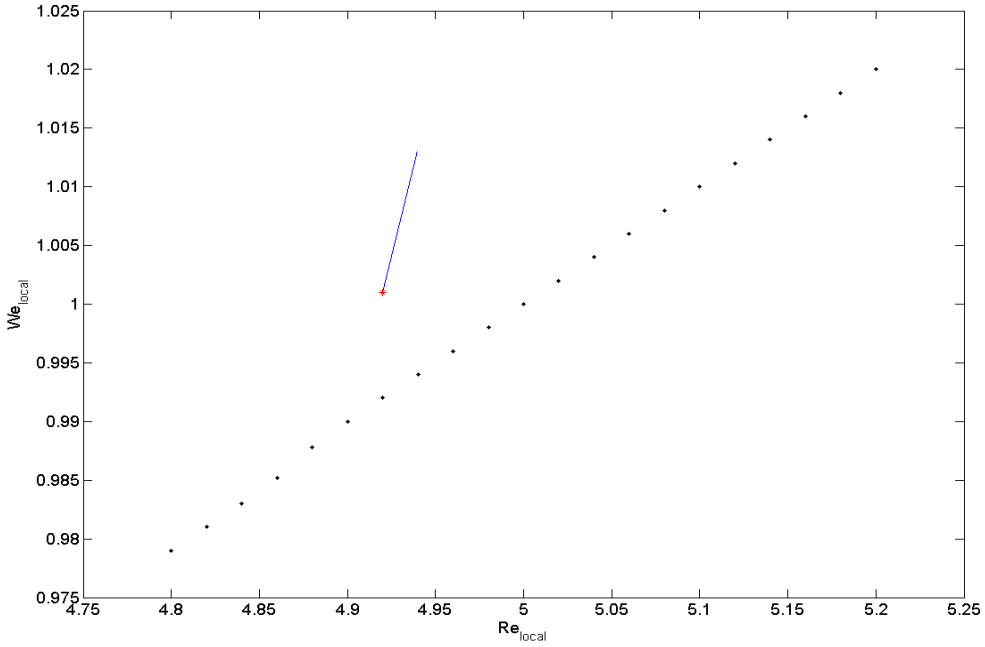

Figure 5.21: Graph showing the Re_{local}-We_{local} trajectory in the Re-We plane. The black dots mark the critical curve and the red star indicates the starting position of the trajectory. $Rb = 4, F = 4, We = 1.001$ and $Re = 4.92$.

trajectories which overlap as $Re_{local}, We_{local} \to 0$ up to the point where the slender jet assumption becomes invalid. The Fortran code terminates as Re_{local} and We_{local} become very small (as $u_0 \to 0$ and $R_0 \to \infty$) while the Matlab code continues to solve the ODEs producing incorrect results and finding complex values for X, Y and Z. At this point, $u_0 \to 0$ and $R_0 \to \infty$. Figures 5.25, 5.26, 5.27 and 5.28 show the graphs of u_0, R_0, Re_{local} and We_{local} (computed numerically in Fortran using a variable step-size method) plotted against s for the corresponding Re_{local}-We_{local} trajectory shown in Figure 5.24. These graphs show that for small Froude numbers $u_0, Re_{local}, We_{local} \to 0$ and $R_0 \to \infty$. Next, we examine the behaviour of the Re_{local}-We_{local} trajectory as $u_0 \to 0$ and $R_0 \to \infty$ when the slender jet assumption eventually becomes invalid.

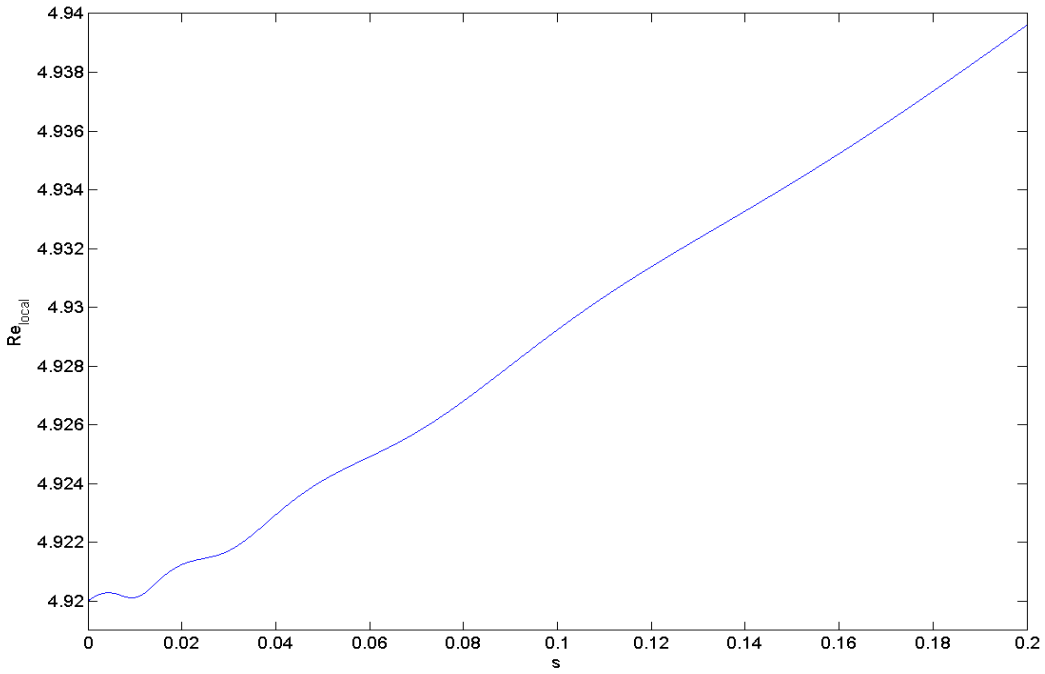

Figure 5.22: Graph of Re_{local} (found by solving three-dimensional asypmtotic equations (5.9)-(5.12)) plotted against s. $Rb = 4, F = 4, We = 1.001$ and $Re = 4.92$.

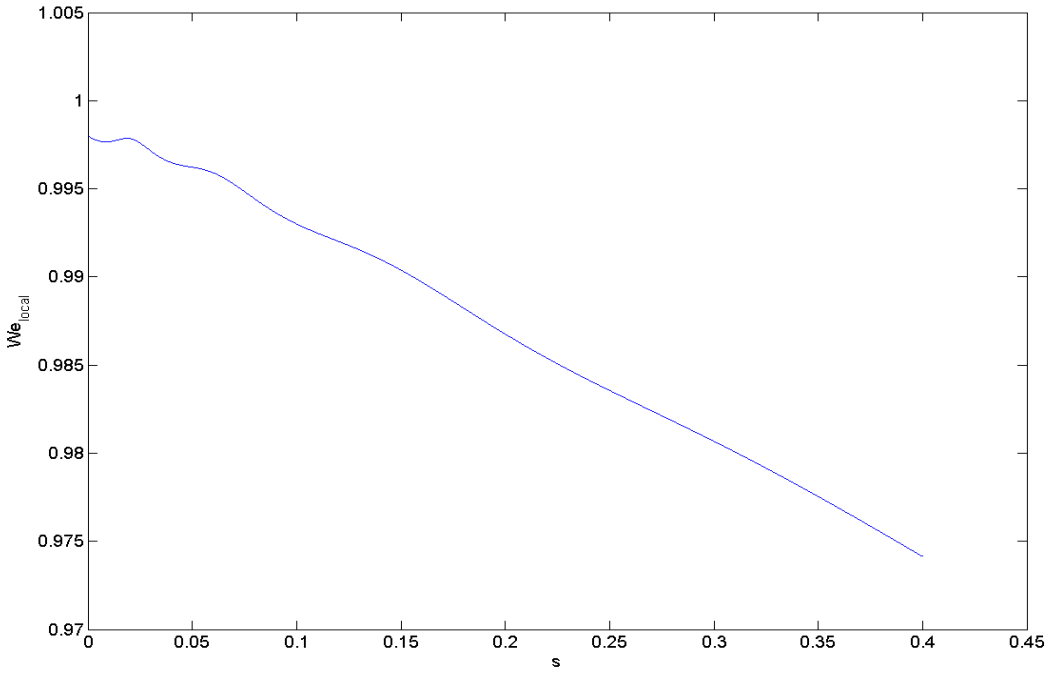

Figure 5.23: Graph of We_{local} (found by solving three-dimensional asypmtotic equations (5.9)-(5.12)) plotted against s. $Rb = 4, F = 4, We = 1.001$ and $Re = 4.92$.

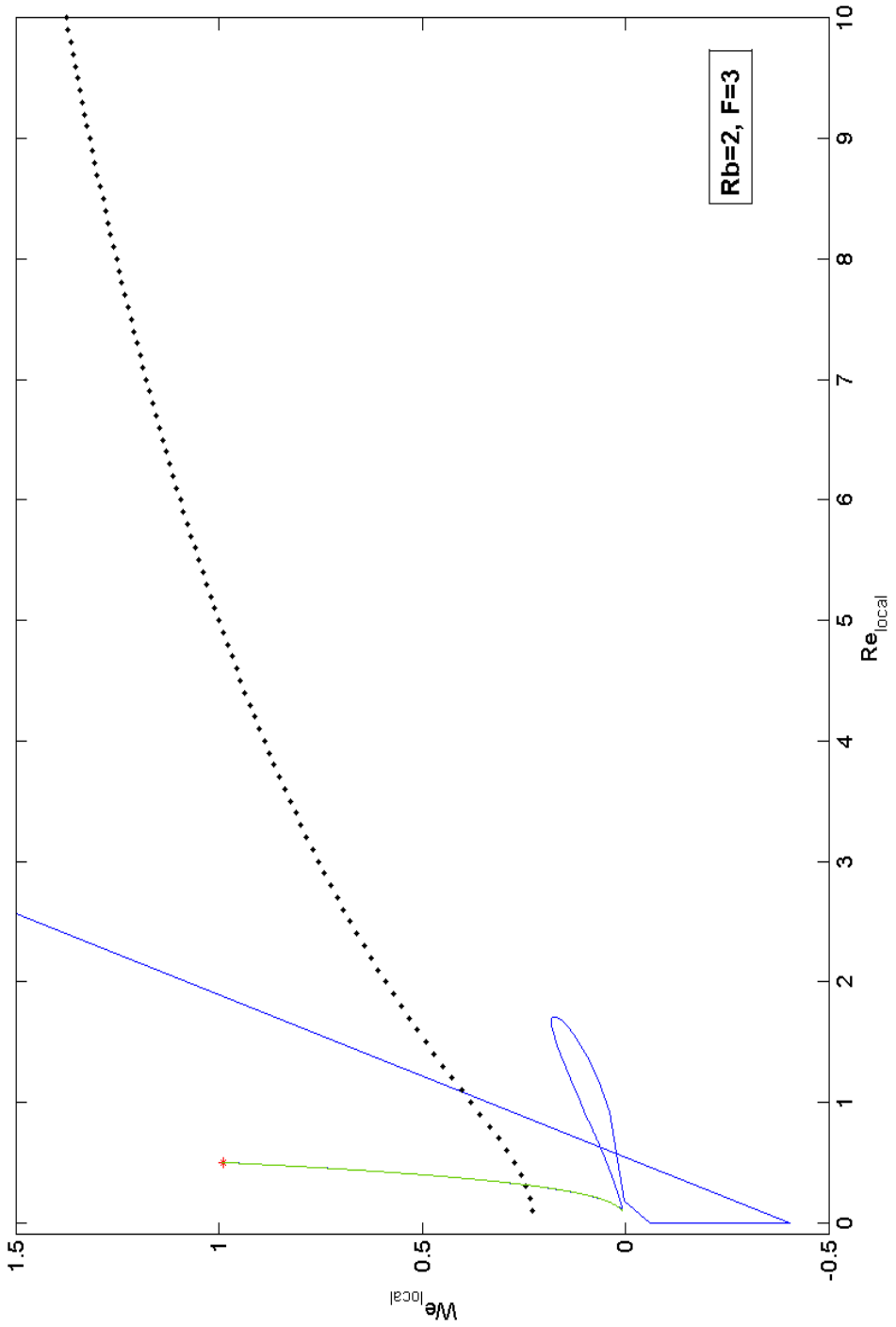

Figure 5.24: Graph showing the Re_{local}-We_{local} trajectories calculated using different codes. $Re_{local}(0) = 0.5, We_{local}(0) = 0.99, Rb = 2$ and $F = 3$. The green line shows the trajectory found by solving the ODEs using the Fortran program and the blue line represents the trajectory found by using the Matlab program. Both trajectories overlap as $Re_{local} \to 0$ and $We_{local} \to 0$, which is where the slender jet theory breaks up and the Fortran code stops while the Matlab code continues to solve the ODEs producing incorrect complex values for X, Y and Z.

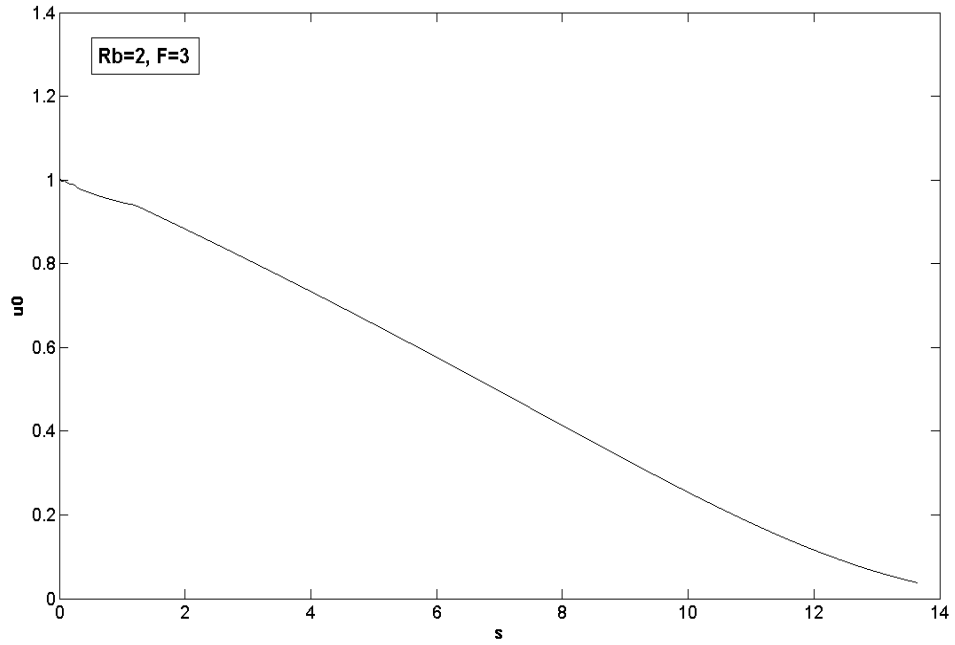

Figure 5.25: Graph showing the plot of u_0 against s for $Re_{local}(0) = 0.5, We_{local}(0) = 0.99, Rb = 2$ and $F = 3$.

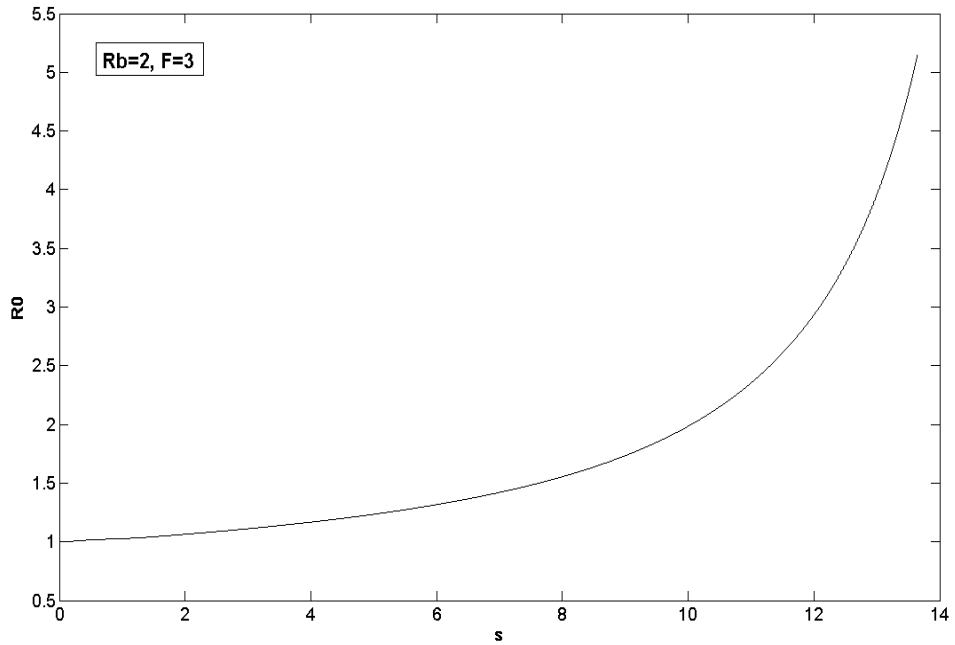

Figure 5.26: Graph showing the plot of R_0 against s for $Re_{local}(0) = 0.5, We_{local}(0) = 0.99, Rb = 2$ and $F = 3$.

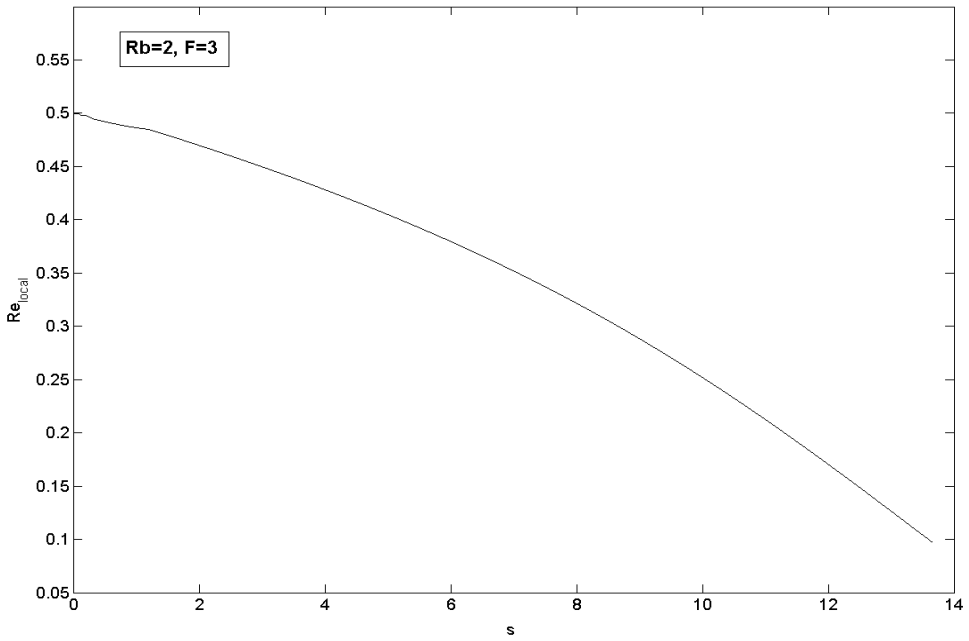

Figure 5.27: Graph showing the plot of u_0 against s for $Re_{local}(0) = 0.5, We_{local}(0) = 0.99, Rb = 2$ and $F = 3$.

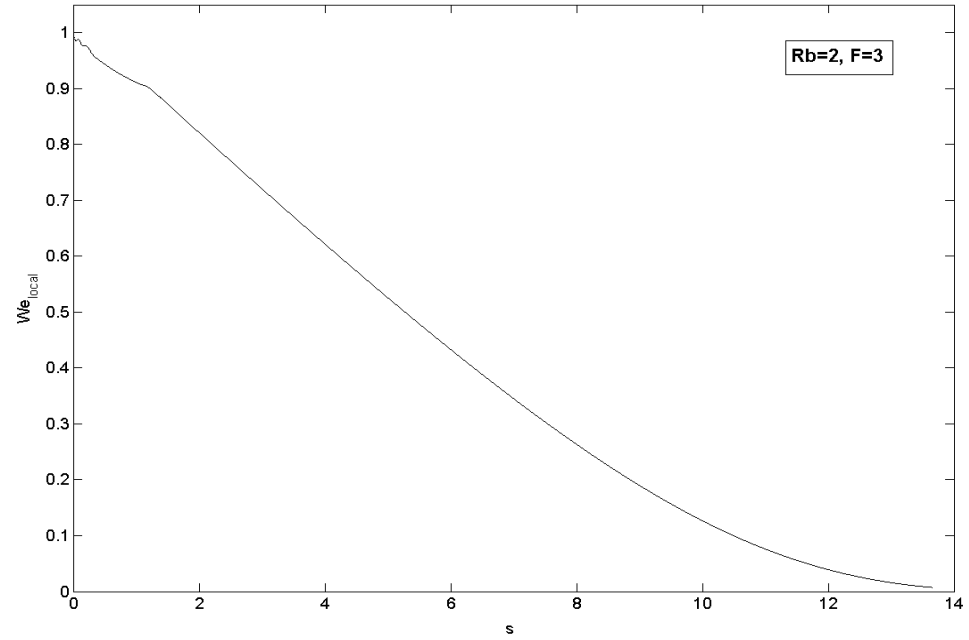

Figure 5.28: Graph showing the plot of R_0 against s for $Re_{local}(0) = 0.5, We_{local}(0) = 0.99, Rb = 2$ and $F = 3$.

5.2.3 Re_{local}-We_{local} Trajectory as $Re_{local}, We_{local} \to 0$

From the conservation of mass equation and the kinematic condition (detailed in Wallwork [68]) we have

$$v_1 = u_0 \frac{dR_0}{ds} \text{ and } v_1 = -\frac{1}{2} R_0 \frac{du_0}{ds}$$

on $n = R_0$. Thus, we have

$$\begin{aligned} u_0 \frac{dR_0}{ds} &= -\frac{1}{2} R_0 \frac{du_0}{ds} \\ \Rightarrow u_0 {R_0}^2 &= 1 \quad \forall s \text{ as } u_0 \to 0, R_0 \to \infty \end{aligned}$$

Substituting this into We_{local} and Re_{local} gives

$$\begin{aligned} We_{local}(s) = We u_0^2(s) R_0(s) \quad &\text{and} \quad Re_{local}(s) = Re u_0(s) R_0(s) \\ We_{local}(s) = \frac{We}{R_0^3(s)} \quad &\text{and} \quad Re_{local}(s) = \frac{Re}{R_0(s)} \\ \Rightarrow \quad We_{local}(s) &= \frac{We}{\left(\frac{Re}{Re_{local(s)}}\right)^3} \\ \therefore We_{local} &= M Re_{local}^3(s) \end{aligned} \tag{5.13}$$

where $M = \dfrac{We}{Re^3}$ is a constant. The expression (5.13) gives the Re_{local}-We_{local} trajectory in the region where the slender jet theory breaks down. Figure 5.29 shows these Re_{local}-We_{local} trajectories plotted in the Re-We plane along with the critical curve using the expression (5.13). The red star marks the starting point of the Re_{local}- We_{local} trajectory. These trajectories start in the convective instability region above the critical curve and make a transition from convective to absolute instability by crossing the critical boundary after which they head towards the origin where the singularity arises. The important thing to note here is that the jet has already undergone a transition from convective to absolute instability (which corresponds to the Re_{local}-We_{local} trajectory crossing the critical curve)

before the trajectory heads towards the origin and into the singularity region where model breaks down.

5.3 Conclusion

We have examined the effects of the density ratio of the surrounding gas to the liquid and gravity on absolute instability in curved jets. Critical curves for $Q = 0.001, 0.03$ are determined for small and large Reynolds numbers and compared to the critical curve for $Q = 0$ at these Reynolds numbers. We find that the critical boundary at small Reynolds numbers is not greatly affected by density ratio. Here the critical curves for different values of Q nearly overlap with each other. However, at higher values of Re, density ratio is found to have a slightly more significant affect on absolute instability.

To study the effect of gravity, we solve the three-dimensional model to determine the Re_{local}-We_{local} trajectory in the Re-We plane. Using this trajectory we compute the Mode 4 regions for different values of Rossby and Froude numbers. We find that the upper boundary of the Mode 4 region for $Re < 5$ occurs at a constant Weber number with $We^* = 1.01$ whereas for $Re > 5$ the Mode 4 boundary coincides with the critical curve, implying no Mode 4 type break-up for $Re > 5$. An asypmtotic analysis for $We \to 1$ is carried out and the Mode 4 curves are found using the new asymptotic equations, finding exact agreement with previous Mode 4 curves. Also, the Re_{local}-We_{local} trajectories are found in the region as $Re_{local}, We_{local} \to 0$ where the slender jet assumption breaks down and the model becomes invalid. These computations reveal that the Re_{local}-We_{local} trajectories always cross the critical curve (indicating a transition from convective to absolute instability) before they head into the singularity region. We also use a variable step-size method to solve our three-dimensional steady state jet equations. This method provides a more accurate solution as it terminates the computation as soon as the slender jet assumption becomes invalid (which always happens after the trajectory has crossed the critical curve).

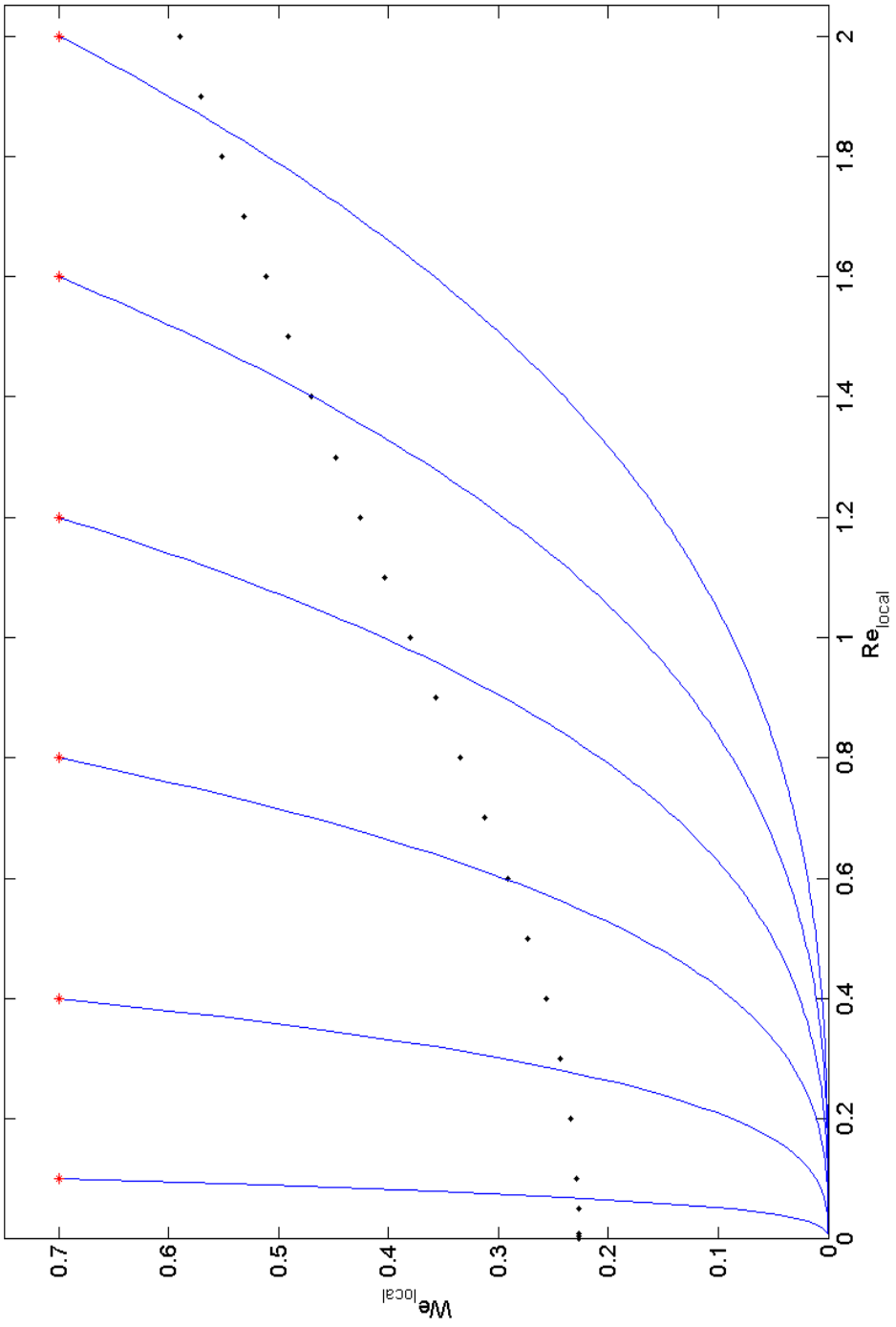

Figure 5.29: Graph showing the Re_{local}-We_{local} trajectories calculated using the expression 5.13 as $Re_{local}, We_{local} \to 0$. The red stars mark the starting point of these trajectories and the black dotted curve represents the critical boundary.

Chapter 6

Comparison with Experiments

So far, we have used the curved jet model described in Chapter 3 to study absolute instability in curved liquid jets by examining the trajectory of the local Reynolds and the local Weber numbers (Re_{local} and We_{local}, respectively) in the Re-We plane and found a Mode 4 region lying above the critical curve in the convective instability region. The Re_{local}-We_{local} trajectories starting at Re and We values belonging to this region, always cross the critical curve making a transition from convective to absolute instability. In this chapter we compare our theoretical results with experiments conducted by Wong *et al.* [70] and carry out more detailed experiments on the lab scale concentrating mainly on the Mode 4 and No Jet cases.

6.1 Review of Previous Experimental Work

Wong *et al.* [70] carried out a lab scale experimental study to examine the dynamics of the break-up of liquids jets emerging from a rotating orifice. A cylindrical container with radius $s_0 = 0.0425$m and height $H = 0.115$m was partially filled up with liquid so that the aspect ratio ($H/2s_0$) lies between $\frac{2}{3} - 1\frac{1}{4}$. A peristaltic pump (Waltson-Marlow 505s) was used to keep the level of the liquid in the container constant by continuously supplying fresh liquid into it. The container had two diametrically opposite orifices of diameters 0.001 and 0.003m from which the jets emerge. The trajectory of the jet was photographed using a high speed digital camera (Photron Fastcam Super 10k) which is able to record

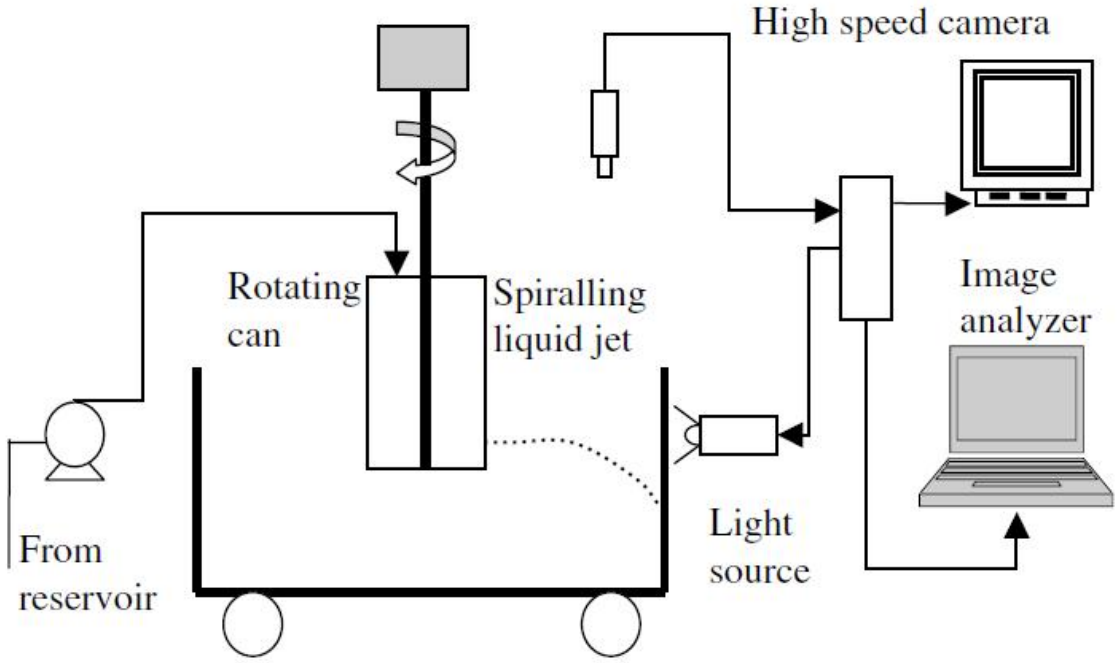

Figure 6.1: A schematic diagram of the apparatus used in the lab scale experiments carried out in [70].

at up to 10,000 frames per second. The images were analysed using Image-Pro Express software (Datacell Ltd., UK). The jet exit velocity was determined by dividing the total volume of liquid collected over a period of 1 minute by the cross-sectional area of the orifice. Solutions of water and glycerol (0-80% glycerol by volume) were used to give a range of viscosities lying between 0.001-0.09Pas. To lower the surface tension below that of water and to extend its range to $0.047 - 0.072 Nm^{-1}$, *n*-butanol was added to two solutions of water and an 80% by volume glycerol solution. The can was rotated with speeds varying from 50 to 300rpm. Figure 6.1 shows a diagram of the experimental set-up used.

They identified four different modes of break-up (see Section 3.1 for detailed explanation and photographs of these modes) and categorised the data into flow maps of the Ohnesorge number Oh against Weber number We, Rossby number Rb and $F/Rb = \Omega s_0/\sqrt{gH}$ (where F is Froude number), indicating the different modes of break-up over a range of operating parameters. Figure 6.2 shows a plot of Oh against We. Observe that Mode 4

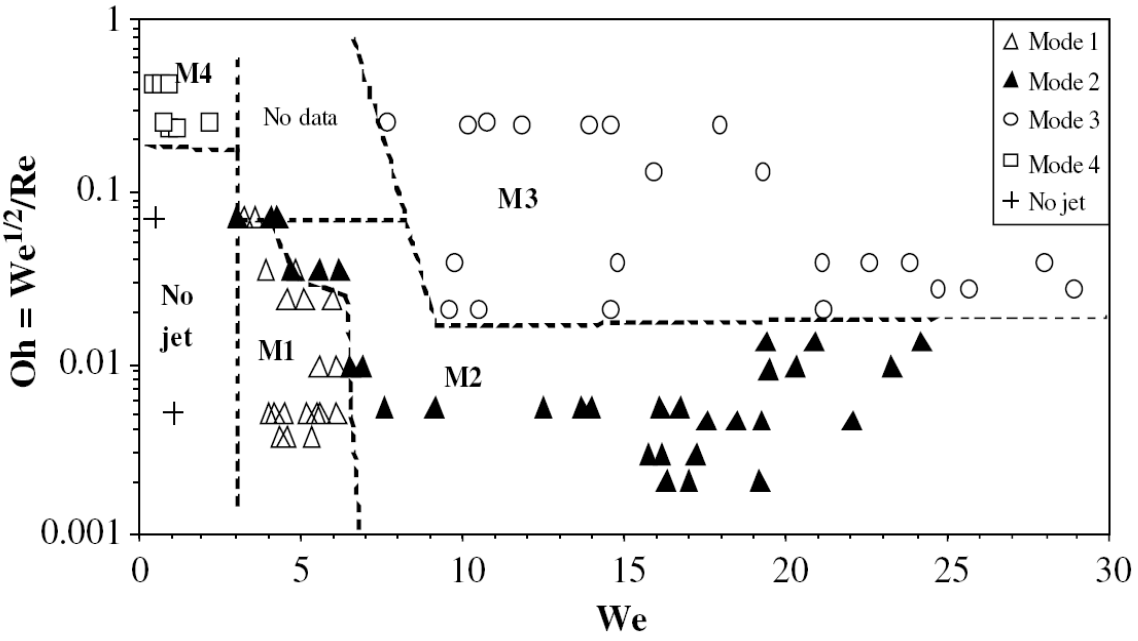

Figure 6.2: Flow map categorising data into different break-up modes plotted for Oh against We.

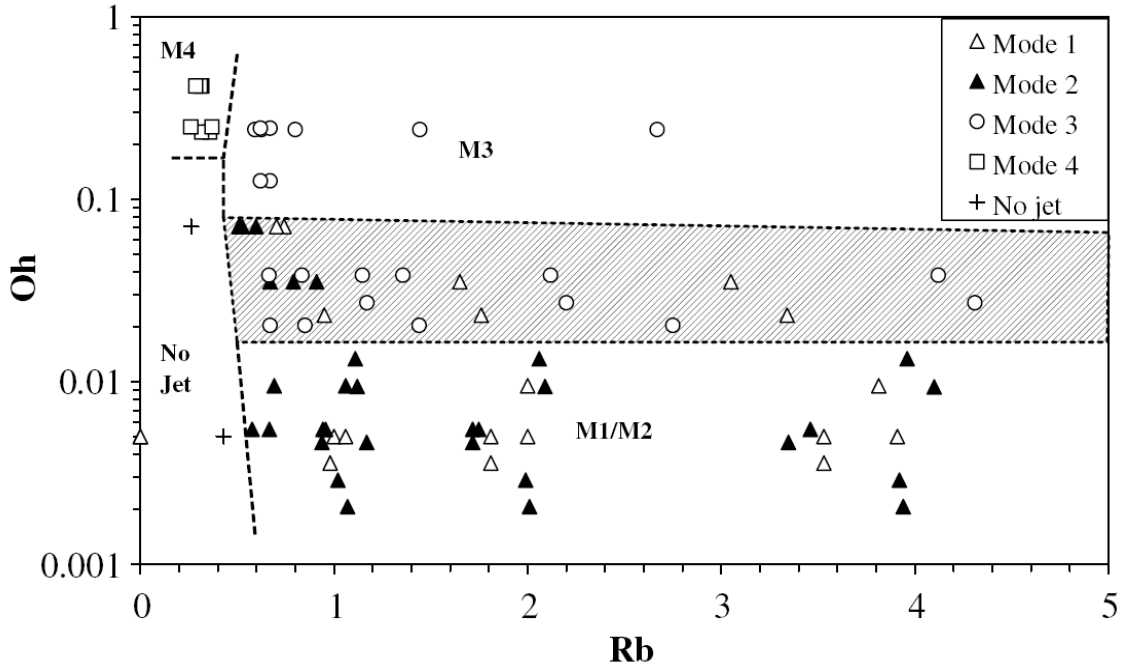

Figure 6.3: Flow map categorising data into different break-up modes plotted for Oh against Rb.

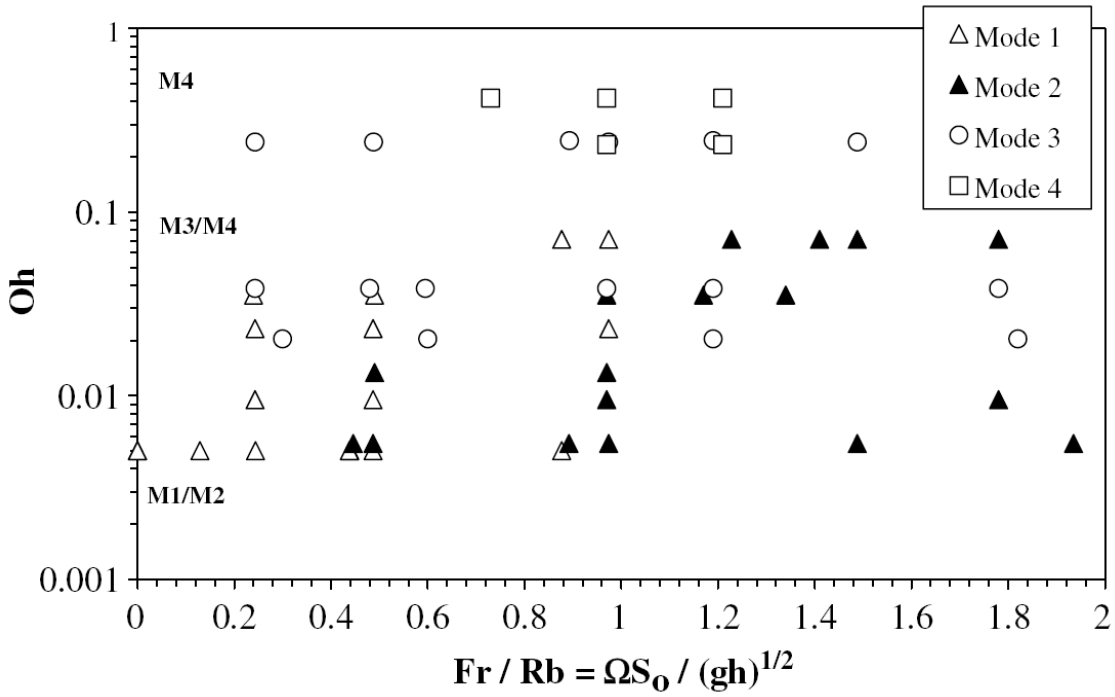

Figure 6.4: Flow map categorising data into different break-up modes plotted for Oh against F/Rb.

is predicted only at small values of We. Figures 6.3 and 6.4 show plots of Oh against Rb and F/Rb, respectively.

We are interested mainly in Mode 4 (where disturbances are observed to travel back upstream) and the No Jet situation (where a coherent jet fails to from as the liquid leaves the orifice) as we have hypothesised the existence of absolute instability in these two situations.

To compare the experimental and theoretical results, we solve the curved jet model for a given set of parameters, taken from the flow charts representing a particular mode of break-up. We calculate the Re_{local}-We_{local} trajectory with $We_{local}(0)$ and $Re_{local}(0)$ taken from the experimental data and examine the movement of the trajectory in the Re-We space (Re is calculated using the formula $Re = \sqrt{We}/Oh$). If the Re_{local}-We_{local} trajectory is determined using experimental parameters corresponding to Modes 1, 2 or 3, then the trajectory should start in the convective instability region and never make the crossover from convective to absolute instability (i.e. never cross the critical curve marking

the boundary between absolute and convective instability). Since the instability observed in these modes is convective, the Re_{local}-We_{local} trajectory must always remain above the critical curve in the convective instability region. However, if the Re_{local}-We_{local} trajectory is calculated with $Re_{local}(0)$ and $We_{local}(0)$ corresponding to experimental parameters for Mode 4 or the No Jet situation, then we expect the trajectory to start in the convective instability region and make a transition from convective to absolute instability (in the case of Mode 4) or to start in the region under the critical curve (i.e. in the absolute instability region) for the No Jet situation. This chapter investigates the extent to which our hypothesis is true.

We first compare theoretical results produced by using the two-dimensional curved jet equations to experiments in Section 6.1.1 and then in Section 6.1.2 we incorporate gravity into our theory by solving the three-dimensional equations to calculate the Re_{local}-We_{local} trajectory and compare our theoretical predications to experimental data from the flow maps.

6.1.1 Comparison with Experiments (neglecting gravity)

In this section we calculate the Re_{local}-We_{local} trajectory, with $Re_{local}(0)$ and $We_{local}(0)$ taken from the experimental data points from the flow maps, by solving the two-dimensional steady state equations (3.42) numerically using a Runge-Kutta method. We determine Re using the formula $Re = \sqrt{We}/Oh$.

Table 6.1 shows the experimental results and the theoretical predictions for the set of parameters listed in the table. If the Re_{local}-We_{local} trajectory starting in the convective instability region for a particular set of parameters, calculated by using the two-dimensional equations, crosses the critical curve then the theoretical result predicts a Mode 4 situation where the jet becomes absolutely unstable for some s. On the other hand, if the trajectory remains in the convective instability region and never crosses the critical curve, we then have a convectively unstable jet representing Modes 1, 2 or 3. However, if the Re_{local}-We_{local} trajectory starts in the absolute instability region below

Exp. No.	Oh	We	Re	Rb	Experimental result	Theoretical result
1.	0.07	3.6	27.11	0.73	Mode 1	Convective
2.	0.035	4	57.14	1.67	Mode 1	Convective
3.	0.005	6.1	494	1	Mode 1	Convective
4.	0.07	2.9	24.33	0.6	Mode 2	Convective
5.	0.035	4.8	62.6	0.68	Mode 2	Convective
6.	0.0055	7.6	501.2	0.59	Mode 2	Convective
7.	0.25	7.8	11.17	0.62	Mode 3	Convective
8.	0.037	9.8	84.61	0.68	Mode 3	Convective
9.	0.45	0.5	1.57	0.3	Mode 4	Mode 4
10.	0.45	0.7	1.86	0.36	Mode 4	Mode 4
11.	0.45	0.96	2.18	0.37	Mode 4	Mode 4
12.	0.26	0.7	3.22	0.26	Mode 4	Mode 4
13.	0.26	2.1	5.57	0.41	Mode 4	Convective
14.	0.24	1.01	4.19	0.36	Mode 4	Convective
15.	0.24	1.1	4.37	0.38	Mode 4	Convective
16.	0.07	0.5	10.1	0.28	No Jet	No Jet
17.	0.005	1.01	201	0.43	No Jet	No Jet

Table 6.1: Table showing the comparison between experimental and theoretical results found by neglecting gravitational effects. The theory predicts a convectively unstable jet if the Re_{local}-We_{local} trajectory starting in the convective instability region never crosses the critical curve. A jet corresponding to Mode 4 type break-up is predicted if the Re_{local}-We_{local} trajectory starting in the convective instability region crosses the critical curve at some s, while a jet representing the No Jet situation is predicted if the Re_{local}-We_{local} trajectory starts in the absolute instability region under the critical curve.

the critical curve, then the theory predicts a No Jet situation where the jet is absolutely unstable to start with. It can be seen that the theory and experiments agree in cases 1 to 12 and in cases 16 and 17, but disagree in cases 13, 14 and 15.

6.1.2 Comparison with Experiments (including gravity)

We will now incorporate gravity into our theoretical model and compare the results to the experimental results of Wong *et al.* [70]. To determine the Re_{local}-We_{local} trajectory, we solve the three-dimensional steady state equations (3.25) numerically using a Runge-Kutta method.

We use the same approach as that described in Section 6.1.1 to construct Table 6.2 which shows the comparison of the experimental and theoretical results. We use experimental data from flow maps in Figures 6.2, 6.3 and 6.4. The Froude number is calculated

Exp. No.	Oh	We	Re	Rb	F	Experimental result	Theoretical result
1.	0.07	3.6	27.11	0.73	0.6862	Mode 1	Convective
2.	0.035	4	57.14	1.67	0.7682	Mode 1	Convective
3.	0.005	6.1	494	1	0.24	Mode 1	Convective
4.	0.07	2.9	24.33	0.6	0.738	Mode 2	Convective
5.	0.035	4.8	62.6	0.68	0.6596	Mode 2	Convective
6.	0.0055	7.6	501.2	0.59	0.2596	Mode 2	Convective
7.	0.25	7.8	11.17	0.62	0.1488	Mode 3	Convective
8.	0.037	9.8	84.61	0.68	0.306	Mode 3	Convective
9.	0.45	0.5	1.57	0.3	0.216	Mode 4	Mode 4
10.	0.65	0.7	1.86	0.36	0.3384	Mode 4	Mode 4
11.	0.65	0.96	2.18	0.37	0.4514	Mode 4	Mode 4
12.	0.45	0.7	3.22	0.26	0.2444	Mode 4	Mode 4
13.	0.45	2.1	5.57	0.41	0.5002	Mode 4	Convective

Table 6.2: Table showing the comparison between experimental and theoretical results found by including the effects of gravity. The theory predicts a convectively unstable jet if the Re_{local}-We_{local} trajectory starting in the convective instability region never crosses the critical curve. A jet corresponding to Mode 4 type break-up is predicted if the Re_{local}-We_{local} trajectory starting in the convective instability region crosses the critical curve at some s, while a jet representing the No Jet situation is predicted if the Re_{local}-We_{local} trajectory starts in the absolute instability region under the critical curve.

using the data available from the flow map in Figure 6.4 for F/Rb at a given Rb value. It is not clear from the flow maps what the Froude number is for data points 14, 15, 16 and 17 in Table 6.1. Therefore, Table 6.2 has less data points than Table 6.1. The results agree in cases 1 to 12, but not in case 13.

Comparison between experiments and theory is not carried out for all data points representing Modes 1, 2 and 3 in the flow charts. We have considered experimental results with small Weber numbers, as absolute instability is observed at small values of We. Tables 6.1 and 6.2 show a good comparison between experiments and theory. Since the experimental study carried out in [70] concentrated mainly on convective instability of Modes 1, 2 and 3, there is not enough data available corresponding to Mode 4 and the No Jet situation to implement a full comparison between experiments and our theoretical Mode 4 and No Jet absolute instability results. Therefore, despite fairly good agreement being found with experiments, more detailed experiments were carried out for small Weber numbers concentrating mainly on viscous jets undergoing Mode 4 type break-up or

situations where a No Jet scenario is observed.

6.2 Lab-scale Experiments Concentrating on Mode 4 and No Jet

In this section we describe original experiments carried out on the lab-scale in the Chemical Engineering Department at the University of Birmingham. These experiments were mainly carried out to study the features and parameter regimes of liquid jets where absolute instability is dominant and plays a role in the dynamics of the jet, causing Mode 4 and No Jet type break-up and compare the experimental results to the Mode 4 curves determined in Chapters 4 and 5.

6.2.1 Methods and Materials

We use a similar experimental set-up as that of Wong *et al.* [70] where a cylindrical can of radius $s_0 = 0.0425$m and height $H = 0.115$m having two orifices of diameters $a = 0.001$m and $a = 0.003$m is used. Solutions of water and glycerol are used and different rheologies are obtained by varying the percentage of glycerol. The can is attached to a stirrer with a controlled rotation rate. Liquid is poured into the can up to a certain height and the desired rotation rate is set on the stirrer prior to running the experiment. The bung is then taken out of the nozzle, while simultaneously switching on the stirrer and stopwatch. A curved liquid jet emerges from the orifice. The can is allowed to rotate for a certain length of time t during which images of the curved jet emerging from the rotating can are captured after the jet has reached a steady state. We used a Photron Fastcam SA3 high speed digital camera which is able to record at up to 60,000 frames per second and has a 1024 x 1024 pixel resolution with shutter speeds varying between 16.7ms to 2μs, creating sharp images. After the experiment has run for a certain time t the stirrer is switched off, the bung is plugged back into the nozzle and the exact duration of the experiment is noted. Also, the drop in height of the liquid dH before and after the experiment is run, is recorded. The method of measuring the exit velocity is different from that used in

Wong *et al.* [70]. Rather than measuring the volume of liquid lost in a single run of the experiment, we measure the drop in height dH and use the following formula to compute the exit velocity U,

$$U = \frac{{s_0}^2 dH}{a^2 t}. \tag{6.1}$$

To run the next experiment we start off at the height where the previous one was stopped. The hydrostatic pressure exerted by the liquid is greater when the height of liquid in the can is high. Higher hydrostatic pressure leads to higher exit velocity at the orifice and since we know that Modes 1, 2 and 3 (i.e. the convective modes) occur at high exit velocities, we start our experiment at a high aspect ratio and gradually reduce it through a series of experimental runs, as we hope to see a transition from the convective modes to Mode 4 and then eventually to the No Jet situation which occurs at very low exit velocities. The entire series of experimental runs is then repeated all over again by filling the can up to the same height and performing the experiments for the same intervals of time as for the series of previous experimental runs. We assume that the exit velocity of the jet during an experiment remains constant since $dH \ll H$ and that the dynamics of the jet are not greatly affected by the flow within the can.

6.2.2 Break-up Regimes

The primary focus of these experiments was to examine the absolute instability region and expand upon the limited data provided by Wong *et al.* [70] in the Mode 4 parameter regime. We identified different types of break-up modes that exhibit Mode 4 like behaviour and classified each type of behaviour based on its distinct features. These variations of Mode 4 are described below.

Mode 4A (M4A) - This is the classic Mode 4 identified by Wong *et al.* [70] where a viscous jet grows as it emerges from the orifice and develops a bulge at its tip. The inertia of this bulge causes the tip to move away from the can, consequently altering the trajectory of the jet. As the tip bends away, disturbances are observed to travel upstream. The bulge then detaches itself from the jet, forming a droplet. Disturbances travelling

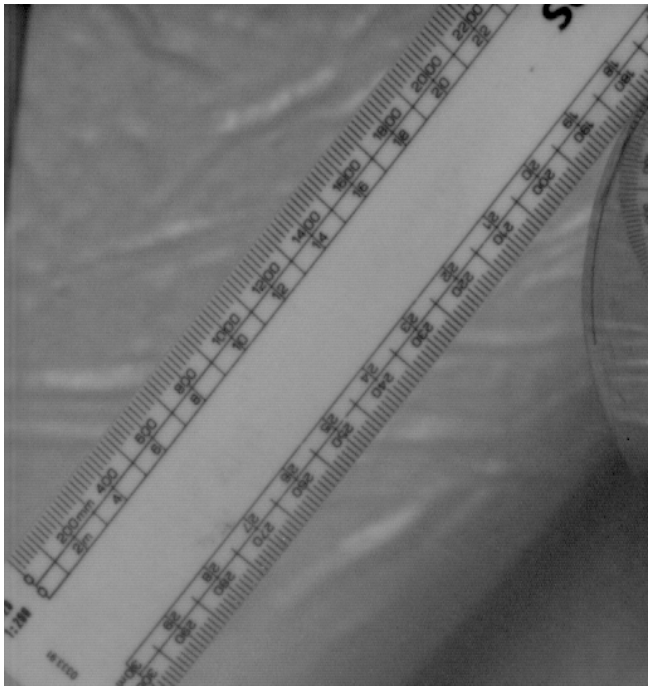

Figure 6.5: Calibration image giving reference length scales for Figures 6.6 and 6.7.

upstream destabilise the section of the jet from where they originate and grow, causing that section to shatter, leaving behind a shorter jet attached to the orifice which then grows back. Figures 6.6(a)-6.6(d) show a sequence of images of a jet undergoing M4A type break-up. Figure 6.5 provides a calibration image giving reference length scales for Figure 6.6 and 6.7.

Mode 4B (M4B) - The main characteristics here are very similar to M4A with the jet growing and developing a bulge at its tip which alters its trajectory and disturbances are observed to propagate upstream. As the jet grows further the bulge detaches from the tip of the jet and upstream disturbances cause a large section of the jet to break off from a point close to the orifice, leaving behind a very short jet attached to the can. The length of the jet left connected to the can distinguishes it from M4A. The disconnected jet then shatters to form satellite drops and the short jet left connected to the orifice then grows back again. Features of this break-up mode can be seen in Figures 6.7(a)-6.7(d).

Long Mode 4/No Jet - Observed in very viscous fluids at high rotation rates. In this case, high viscosity makes it difficult for the fluid to emanate from the orifice and

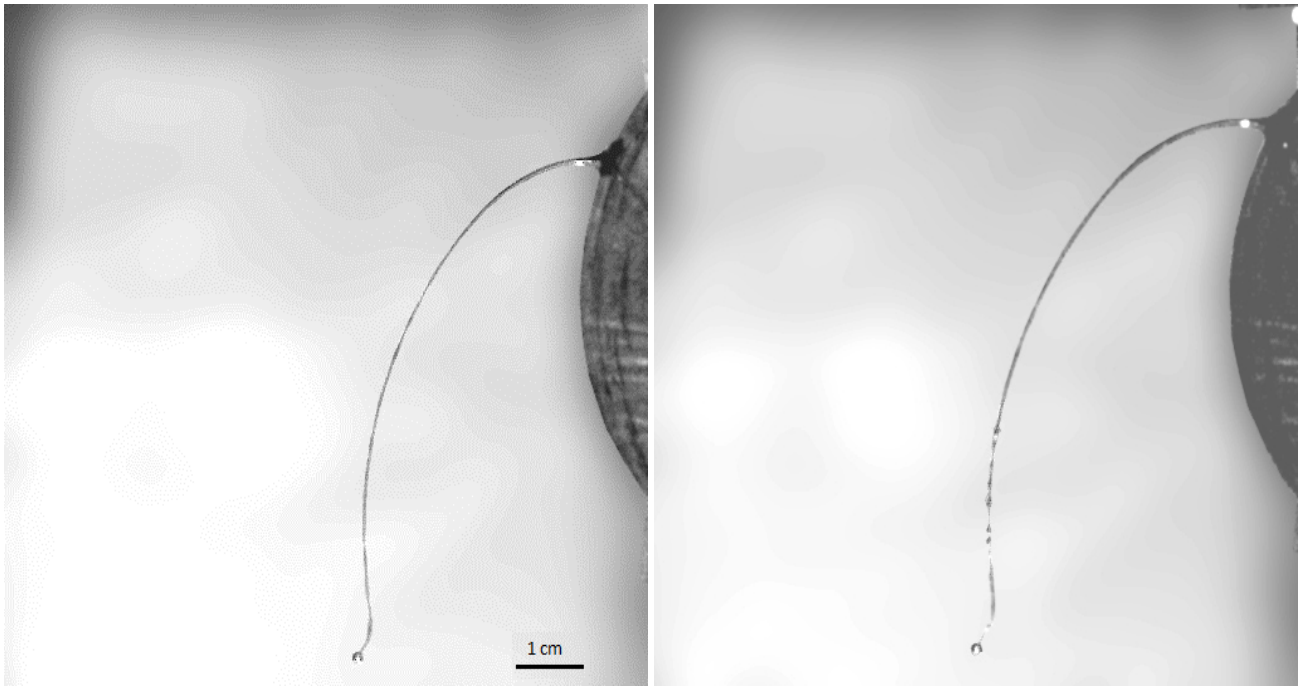

(a) (b)

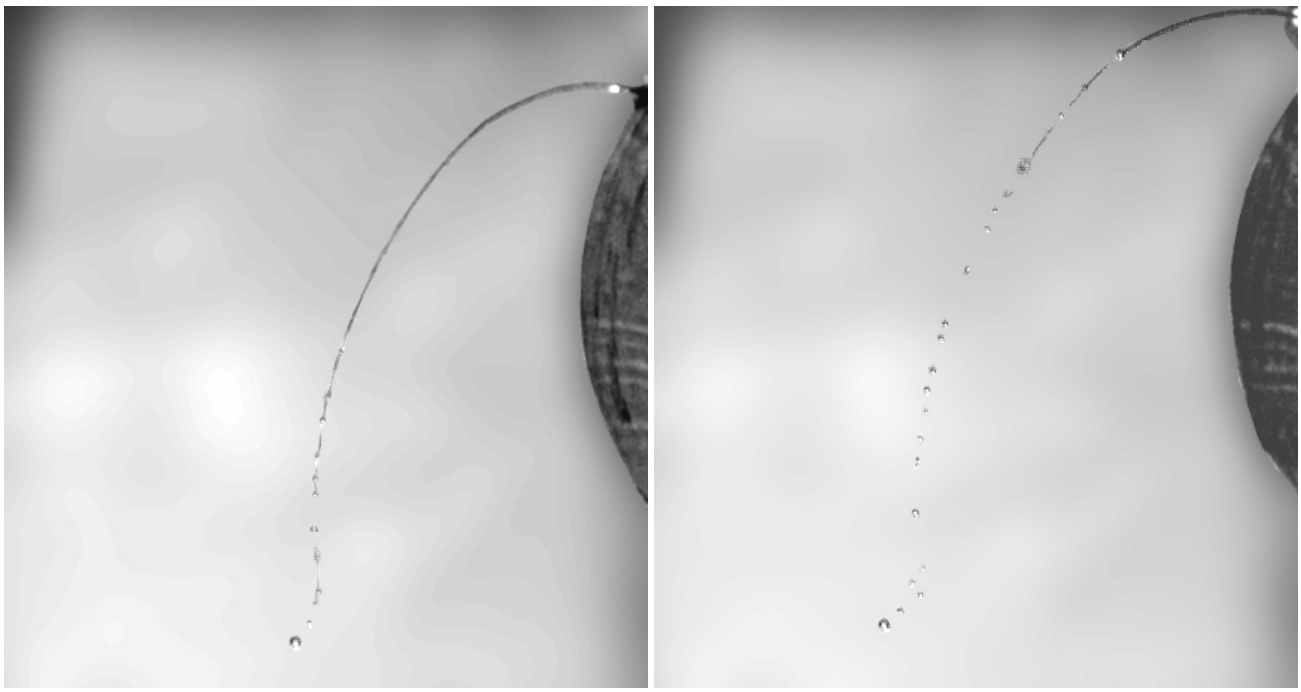

(c) (d)

Figure 6.6: Mode 4A: These photographs show the key features of a jet undergoing Mode 4A type break-up. Figure 6.6(a) shows a long viscous jet with a bulge at its tip causing the jet to move away from the can. As the jet grows further, disturbances are observed to propagate upstream and the bulge detaches itself from the jet (6.6(b)). Figures 6.6(c) and 6.6(d) show disturbances being convected upstream, causing the jet to shatter as they move up, leaving the remainder of the jet attached to the orifice.

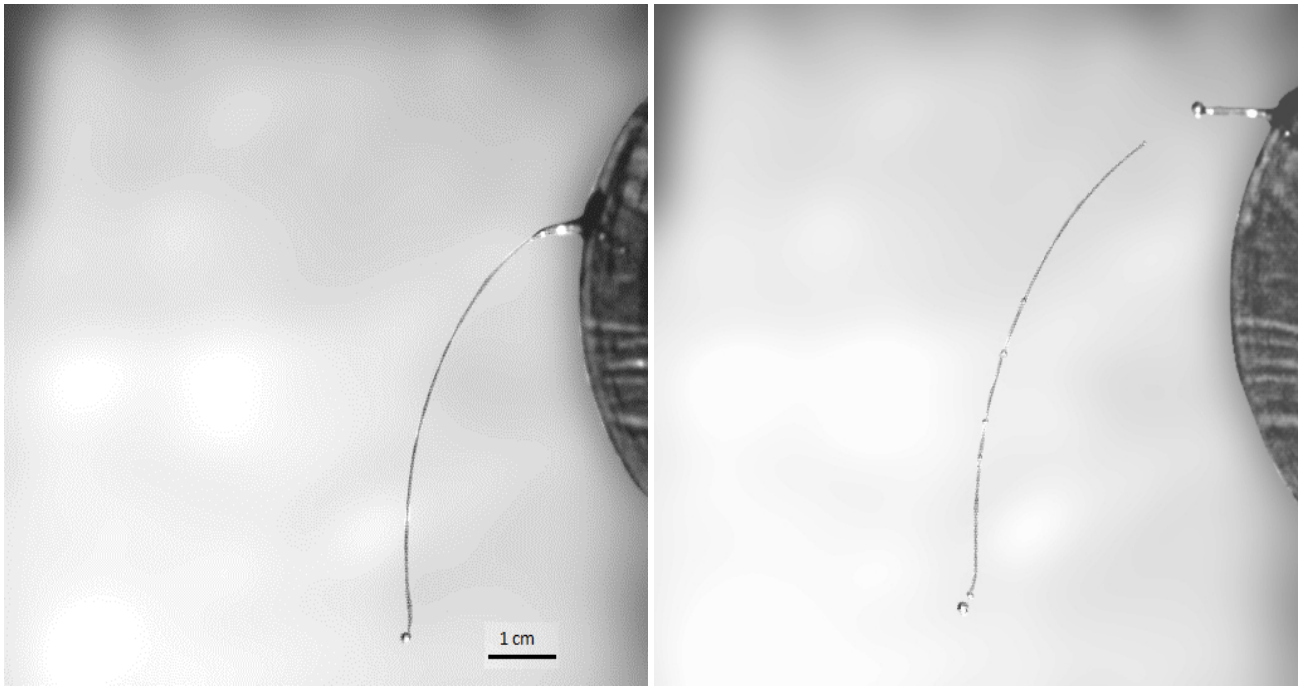

(a) (b)

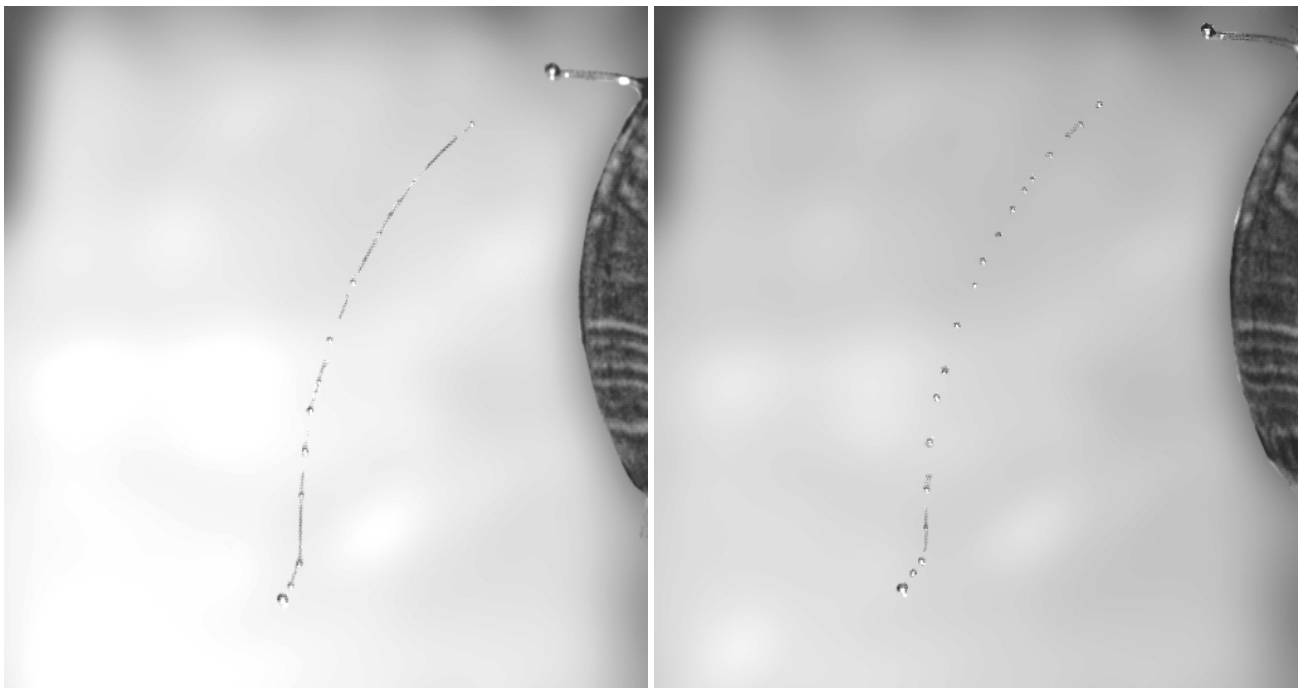

(c) (d)

Figure 6.7: Mode 4B: Here we show a series of images depicting the characteristic features of M4B. Figure 6.7(a) shows a long viscous jet with a bulge at its tip, just as in the M4A case. In Figure 6.7(b) we observe upstream propagation of disturbances and also note that the bulge detaches itself from the jet and a section of the jet breaks off close the orifice, leaving a shorter jet behind. Figures 6.7(c) and 6.7(d) depict the disconnected jet shattering to form satellite drops caused by the absolutely unstable disturbances travelling upstream towards the orifice.

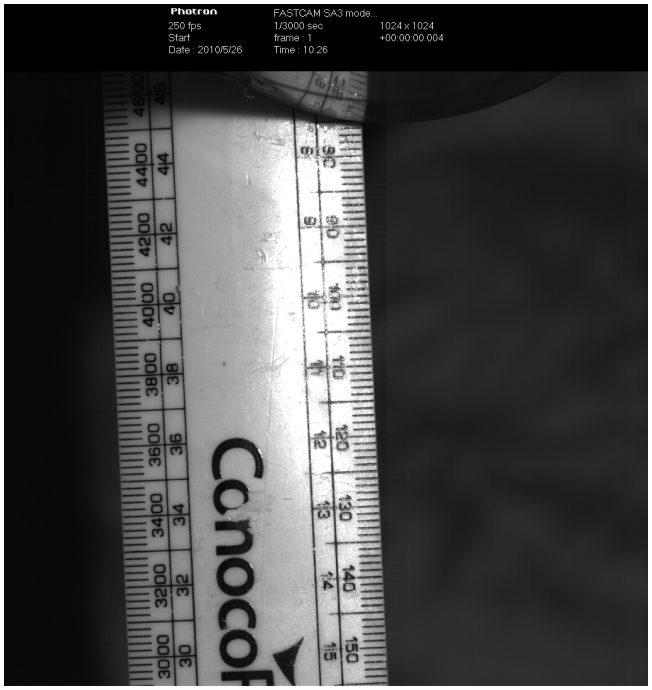

Figure 6.8: Calibration image giving reference length scales for Figures 6.9 and 6.10.

reduces the effect of surface tension driven instabilities. Therefore, as the liquid comes out of the can it forms a very thin, long, coherent jet. As the jet grows, it forms a big bulge at its tip and the inertia of this bulge allows the jet to move away from the can which in turn alters the trajectory of its centreline (as seen in M4A and M4B). The bulge eventually detaches itself from the jet forming a droplet while the remainder of jet breaks off completely from the orifice and disconnects itself from the can creating a No Jet scenario. This detached jet then shatters to form satellite drops and a whole new jet then emerges from the orifice. Figures 6.9(a)-6.9(d) show a sequence of images of a jet experiencing Long Mode 4/No Jet type break-up. Figure 6.8 provides a calibration image which gives reference length scales for Figures 6.9 and 6.10.

Short Mode 4/No Jet - Occurs at low exit velocities and low aspect ratios. Features of this mode are exactly the same as above, the only difference here is the length of the jet. In this case the jet does not grow as long as it does in the Long M4/No Jet case, owing to low exit velocities. As the bulge pinches itself off the tip of the jet, the jet detaches from the can and shatters into satellite drops. As the height of the liquid in the

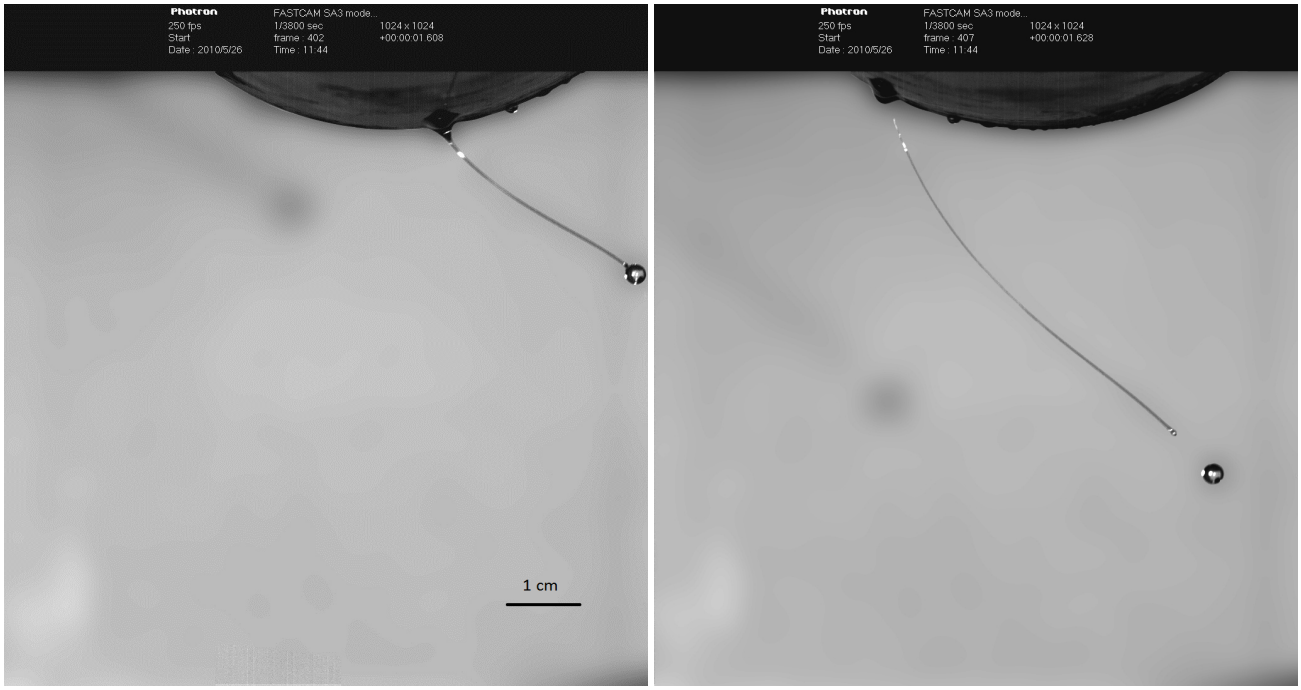

(a) (b)

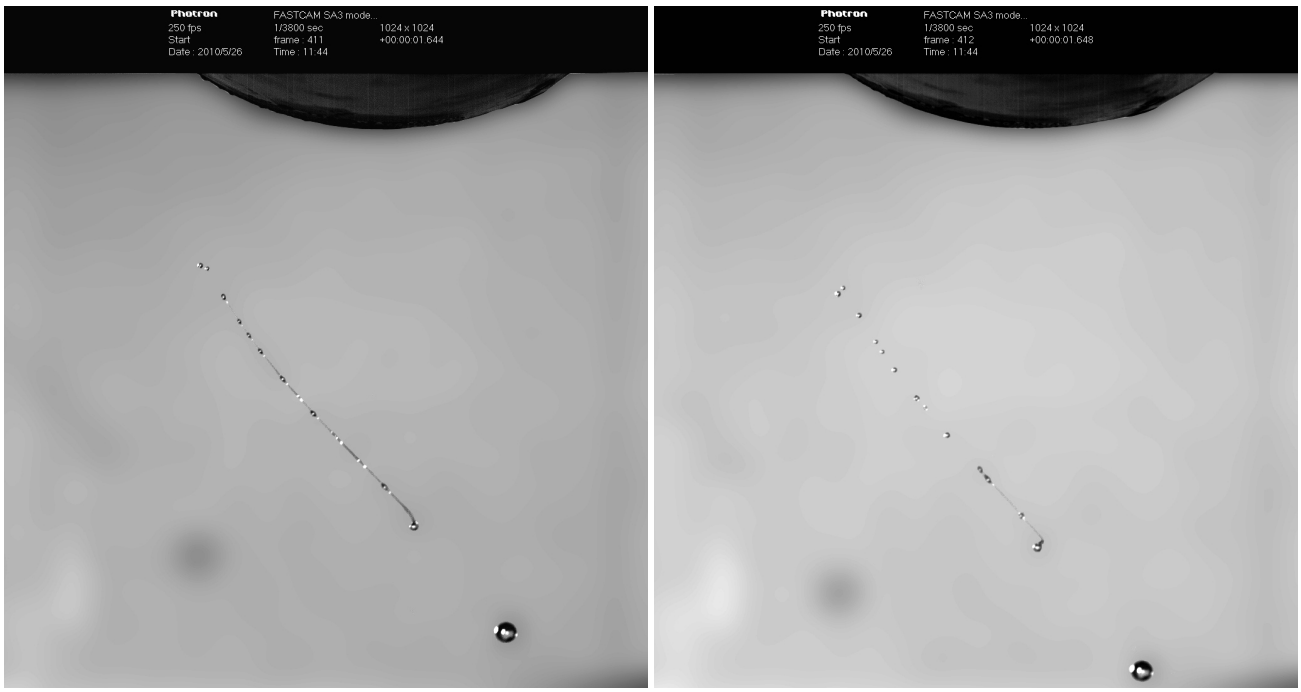

(c) (d)

Figure 6.9: Long Mode 4/No Jet: Series of photographs showing Long Mode 4/No Jet type break-up. Figure 6.9(a) shows a very slender jet with a big bulge formed at its tip. As the jet grows, the bulge detaches itself from the jet forming a droplet while the remainder of the jet completely disconnects from the orifice creating a No Jet scenario as seen in Figure 6.9(c). Figures 6.9(c) and 6.9(d) show the detached jet shattering to form satellite drops. This break-up mode occurs in very highly viscous jets.

can drops at the end of each experimental run, the hydrostatic pressure reduces as well. Low hydrostatic pressure results in low exit velocities at the orifice. Therefore, this mode occurs mainly as a transition mode between Mode 4 and the No Jet case as the height of the liquid in the can drops at each step of the experimental run after Mode 4 type break-up is observed, thus reducing the exit velocity. Figures 6.10(a)-6.10(d) show the primary features of a jet evolving and breaking up in this manner.

Convective/Mode 4 - The jet grows with convectively unstable disturbances travelling downstream on its surface. But at a certain point along its length, disturbances are seen to be convected upstream which causes a section of the jet to shatter. The absence of a bulge at the tip of the jet, which leads to a change in direction of the trajectory of the jet in M4A and M4B type break-up, distinguishes this break-up situation from those two modes. Figures 6.12(a)-6.12(d) demonstrate the fundamental features of this mode. Also, as seen in Figure 6.12(c) there are signs of Mode 3 type break-up with short ligaments being formed between droplets and the jet shattering simultaneously leading to the formation of satellite droplets. Figure 6.11 provides a calibration image giving reference length scales for Figures 6.12, 6.13 and 6.14.

Borderline Mode 4/Convective - In this case, the jet undergoes Mode 4A type break-up caused by absolutely unstable disturbances, followed by Mode 2 type break-up observed after a couple of rotations of the can in the same run of the experiment. After the jet undergoes a Mode 4A type break-up, the part of the continuous jet from the orifice to the first rupture point grows with convectively unstable disturbances causing Mode 2 like break-up gradually over successive rotations of the can until transition from Mode 2 to Mode 4 occurs. These type of jets form a borderline case between convectively unstable jets and those experiencing Mode 4 type break-up making them quite difficult to classify and designate specifically into one of the above categories. This sort of scenario mainly arises at high rotation rates and high aspect ratios. Figures 6.13(a)-6.13(d) show a sequence of images of a jet undergoing M4A type break-up and Figures 6.14(a)-6.14(d) show the same jet undergoing Mode 2 type break-up after a few rotations of the can.

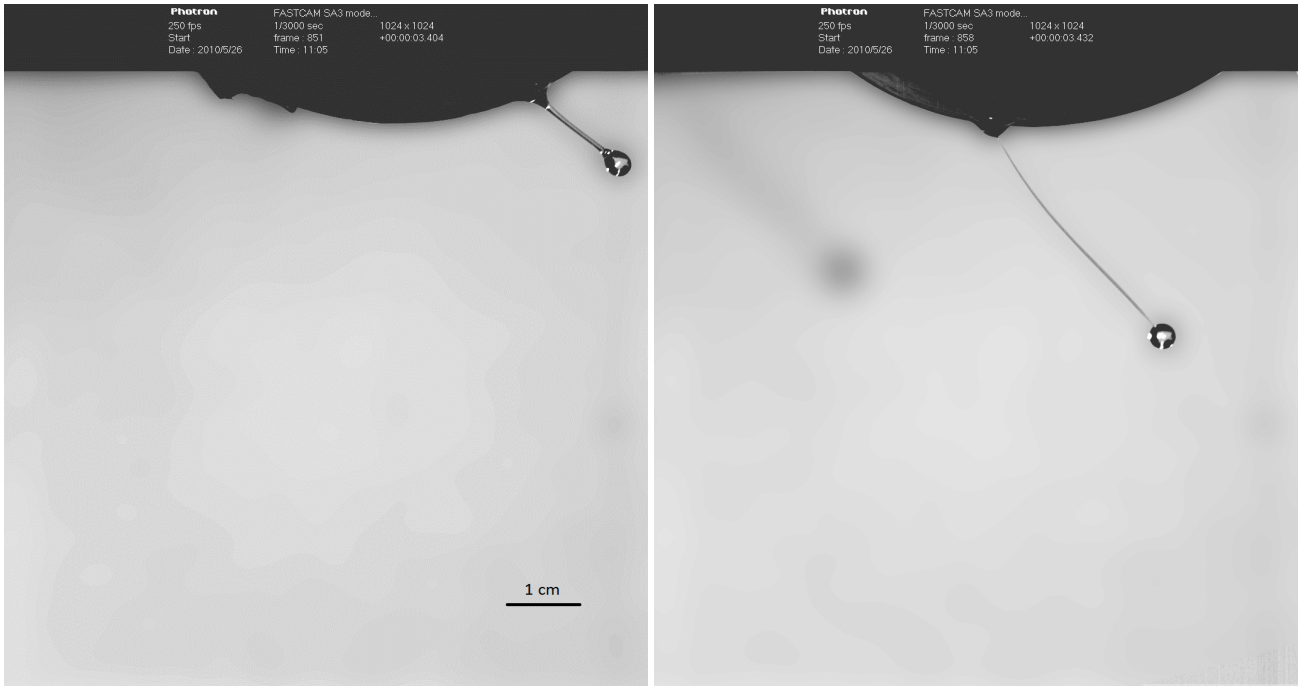

(a) (b)

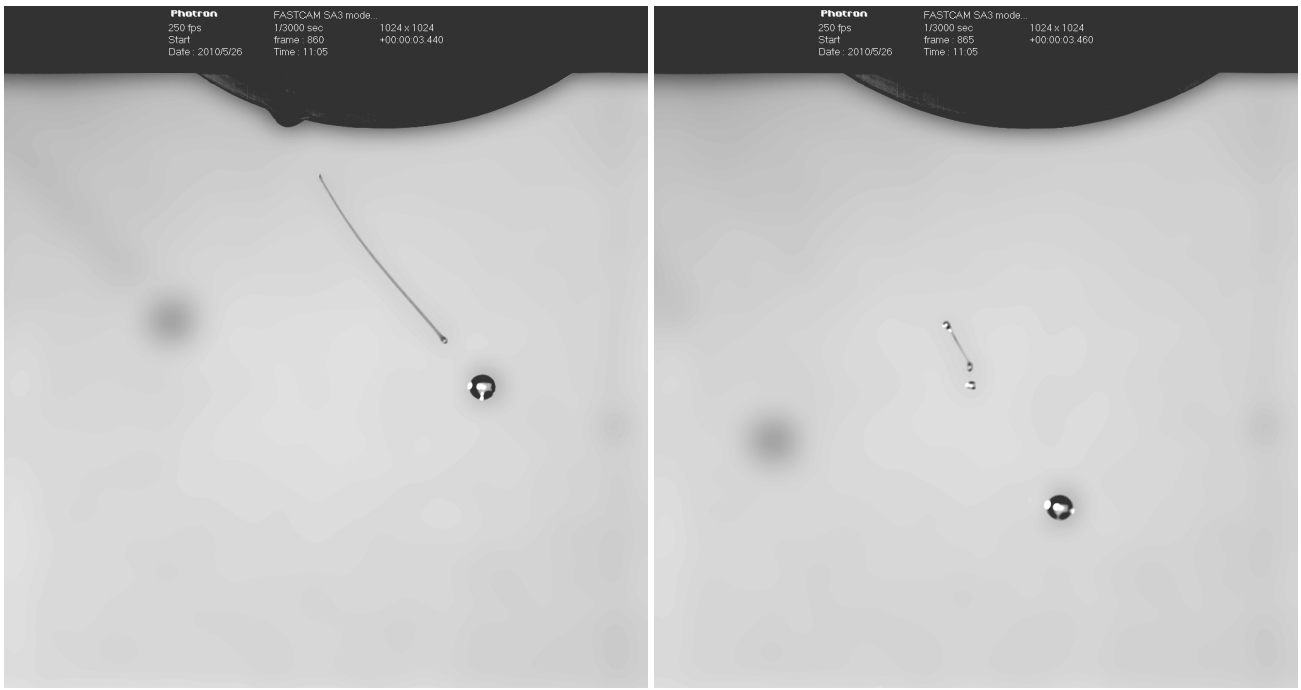

(c) (d)

Figure 6.10: Short Mode 4/No Jet: Photographs showing the features of a jet undergoing Short Mode 4/No Jet type break-up. Figure 6.10(a) shows a very thin viscous jet emerging from the orifice with a big bulge at its tip. Figure 6.10(c) shows the bulge detaching itself from the tip and the jet disconnecting completely from the orifice. In Figure 6.10(d) the disconnected jet recoils and shatters to form satellite drops.

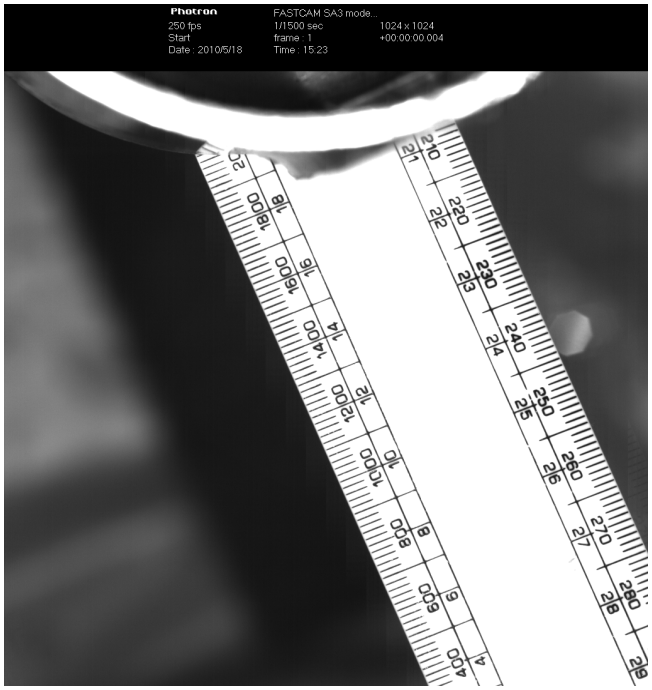

Figure 6.11: Calibration image giving reference length scales for Figures 6.12, 6.13 and 6.14.

6.2.3 Results

We now present results by plotting the experimental values of the Reynolds and Weber numbers along with the critical curve in the Re-We space. Figures 6.15-6.42 show the graphs of the experimental parameter values of jets produced by a particular fluid. Figures 6.15, 6.18, 6.21, 6.24, 6.27, 6.30, 6.33, 6.36, 6.39 and 6.42 show the experimental values of the Reynolds and Weber numbers of jets plotted in the critical region of the Re-We plane. Data points for each break-up mode are denoted by a different symbol and plotted in the critical region. The area between the critical curve and the solid black line marks the Mode 4 region. Theoretically, all jets having Reynolds and Weber numbers lying in this region have their Re_{local}-We_{local} trajectories starting in the convective instability region above the critical curve and cross it at a certain point along the length of the jet as it grows. Therefore, in order to compare experimental results with theory, we plot experimental Re and We data points in the Re-We space and examine their position in the critical region. Figures 6.16, 6.19, 6.22, 6.25, 6.28, 6.31, 6.34, 6.37, 6.40 and 6.43

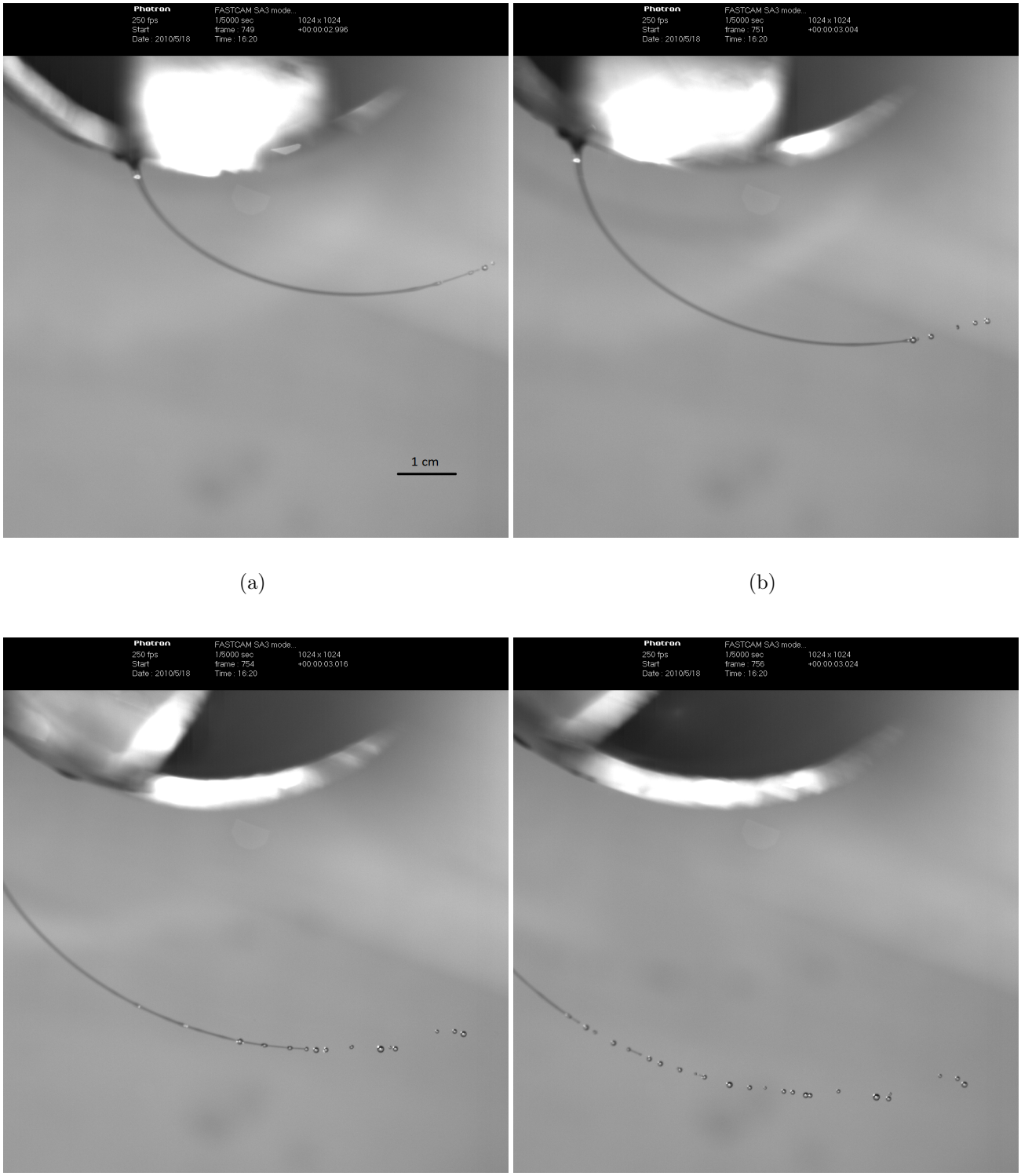

(a) (b)

(c) (d)

Figure 6.12: Convective/Mode 4: Series of images showing the key features of a jet undergoing Convective/Mode 4. Figures 6.12(a) and 6.12(b) show a jet with convectively unstable disturbances travelling downstream causing break-up at the end of the jet. Figure 6.12(c) shows disturbances travelling upstream that cause the jet to shatter in Figure 6.12(d).

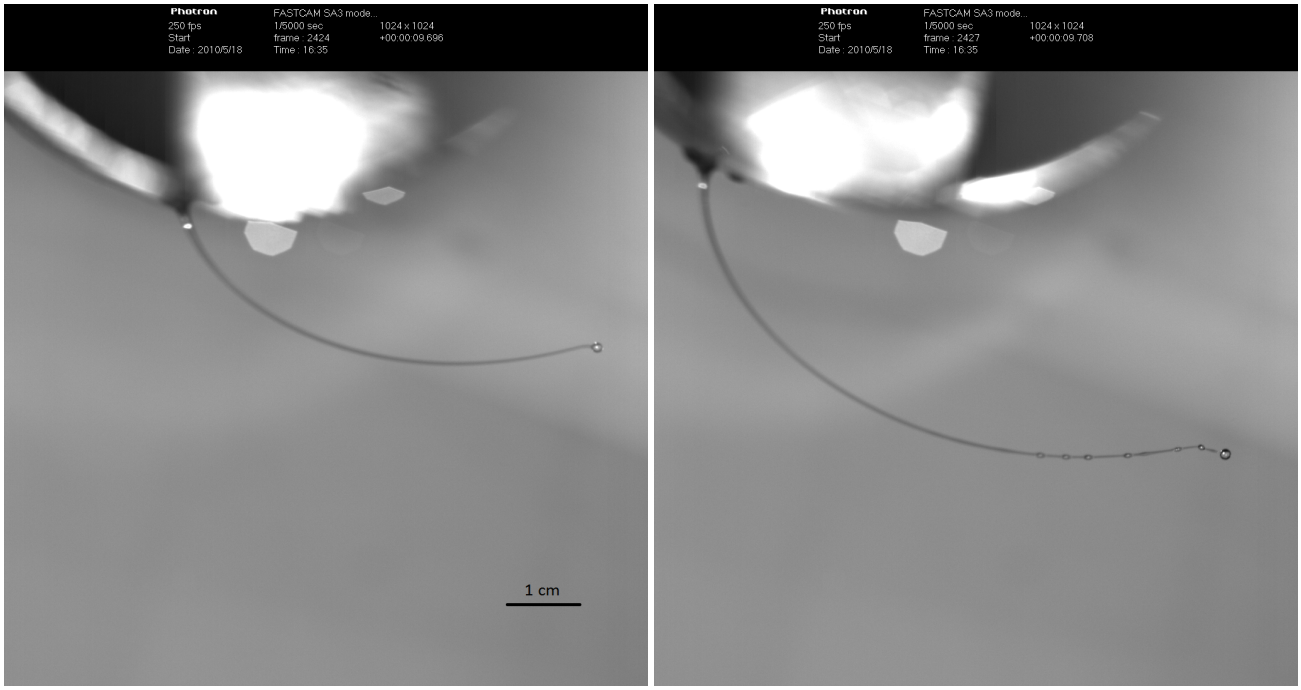

(a) (b)

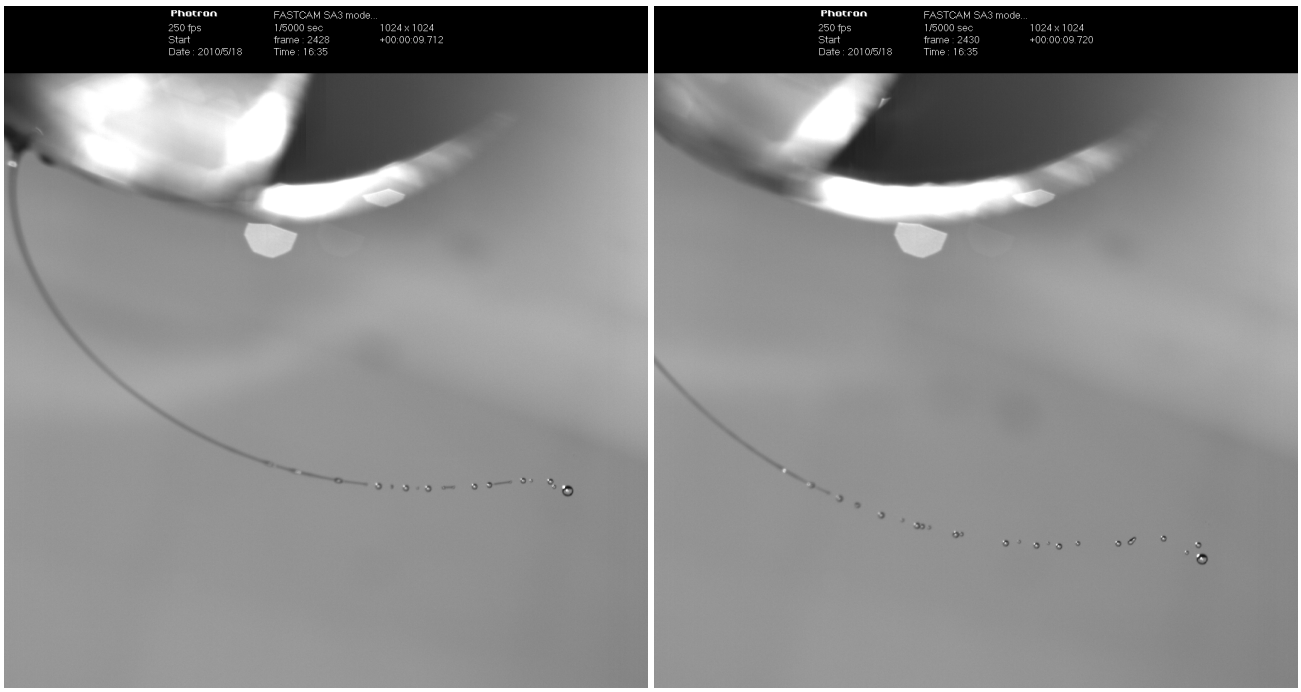

(c) (d)

Figure 6.13: Borderline Mode 4/Convective: This sequence of images depicts a jet undergoing typical Mode 4A type break-up with the jet growing initially and forming a bulge at its tip causing it to bend away from the can. Figure 6.13(b) shows disturbances travelling upstream which cause a section of the jet to shatter as a result of absolute instability. Images 6.13(a)-6.13(d) were captured between 09.696-09.72 s from the time the camera started recording.

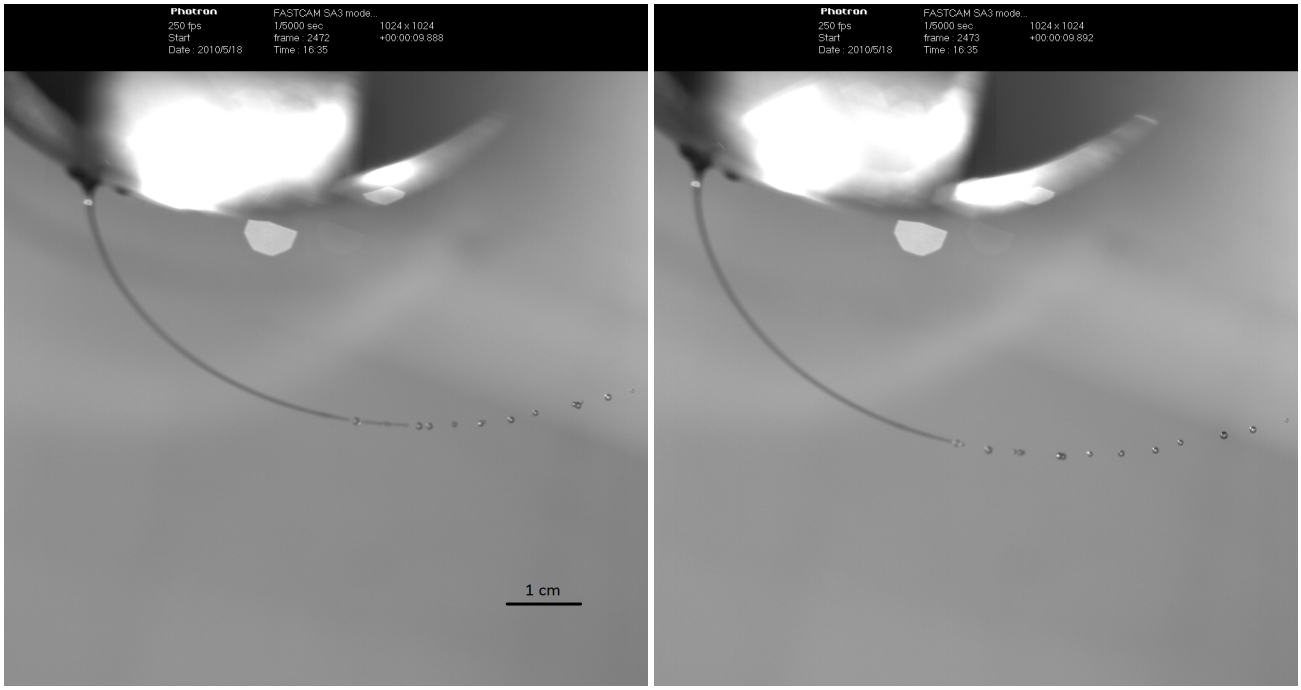

(a) (b)

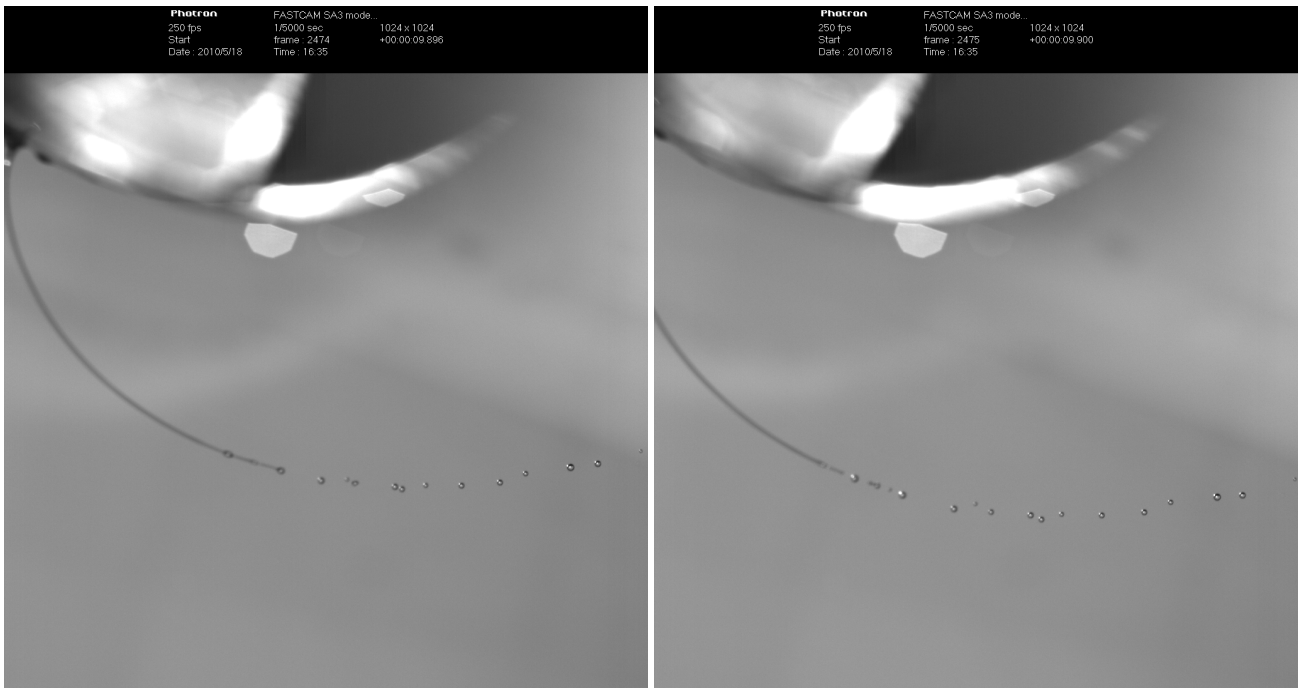

(c) (d)

Figure 6.14: Borderline Mode 4/Convective: This sequence of images depicts the same jet as in Figures 6.13(a)-6.13(d) after it has undergone a typical Mode 4A type break-up. Here the jet can be seen with convectively unstable disturbances travelling down its surface causing break-up. Images 6.14(a)-6.14(d) were captured between 09.888-09.900 s from the time the camera started recording.

show the corresponding experimental Froude number values plotted against the Reynolds number and Figures 6.17, 6.20, 6.23, 6.26, 6.29, 6.32, 6.35, 6.38, 6.41 and 6.44 show the corresponding Rossby number values plotted against Re.

Figure 6.15 shows data points corresponding to two experimental runs at different rotation rates (325rpm and 305rpm). The Convective/M4 type break-up was found to occur at a high rotation rate of 325rpm when the level of liquid in the can was relatively high. As the level of liquid drops in the can at the end of each step of the experimental run, the break-up mode switches to Mode 4. In Figure 6.15 we see Re and We values of jets experiencing M4A type break-up fall in the Mode 4 region which lies above the critical curve in convective instability region, with the upper boundary of the Mode 4 region marked with a solid black line. As the height of the liquid reduces further, we observe a transition to Short M4/No Jet type break-up (data points marked by crosses) which then finally switches to the No Jet scenario as the level of liquid drops further, reducing the hydrostatic pressure and hence dropping the exit velocity which leads to the failure of the formation of a coherent jet. Figures 6.16 and 6.17 show the corresponding Froude and Rossby number values plotted against Re.

Figure 6.18 shows Re and We of jets produced in a single experimental run. The rotation rate of the can was kept constant at 290rpm throughout the experimental run. We find the Re and We values of jets experiencing M4A and M4B type break-up fall correctly in the Mode 4 region. The Short M4/No Jet type break-up, represented by a cross is found to occur towards the end of the experimental run when the experiment is started at a low liquid level, while M4A and M4B are found to occur when the height of the liquid in the can is relatively much higher. Figures 6.19 and 6.20 show the corresponding Froude and Rossby number values plotted against Re.

Figure 6.21 shows experimental data in the Re-We plane from five different experimental runs at rotation rates of 290rpm, 320rpm, 330rpm, 285rpm and 295rpm. Convective/M4 type break-up was observed when the level of liquid was high in the can and the rotation rate was 320rpm. M4A and M4B type break-up modes were observed in

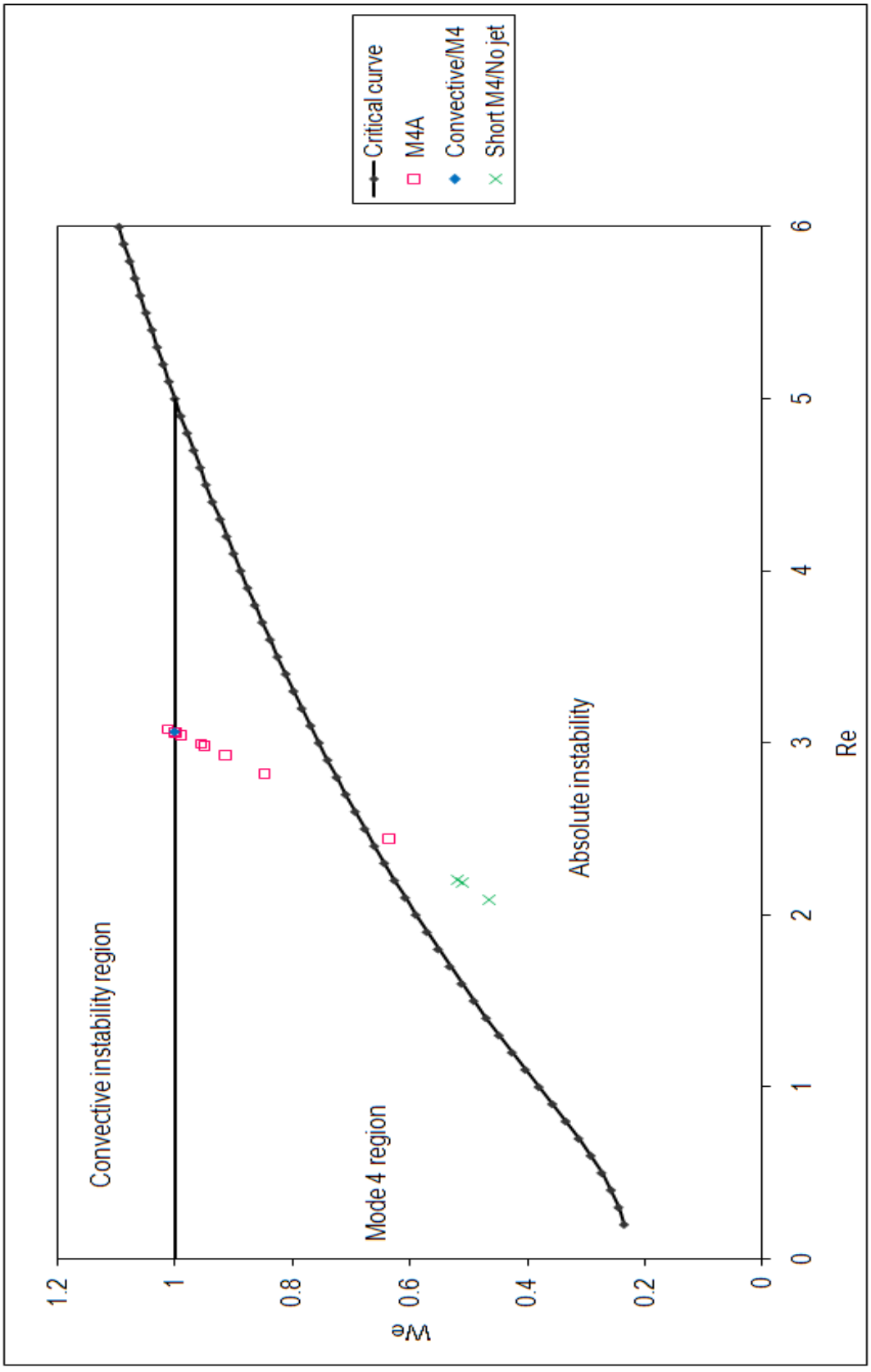

Figure 6.15: Graph showing the experimental Re and We values of jets formed from a water-glycerol solution having $\eta = 0.06506$Pas, $\rho = 1245.306$kgm^{-3}, $\sigma = 0.06375$Nm^{-1} at rotation rates of 325rpm and 305rpm. The critical curve is marked by the dotted line and the solid black line marks the upper boundary of the Mode 4 region.

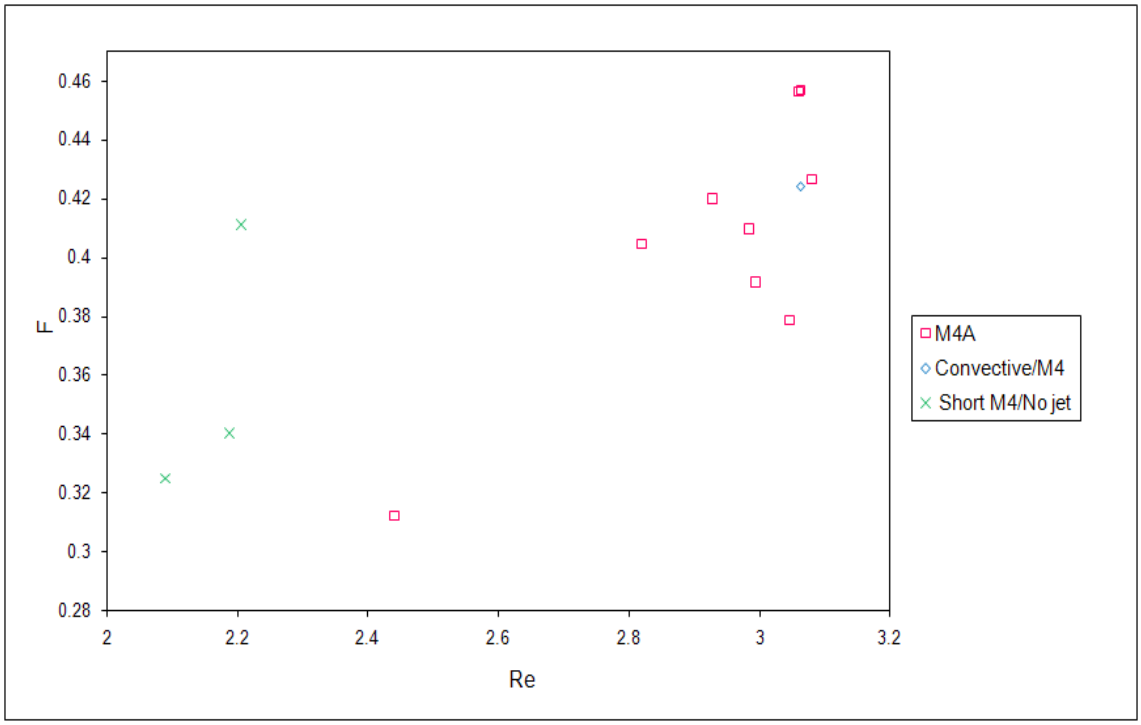

Figure 6.16: Corresponding F values of data points in Figure 6.15 plotted against Re.

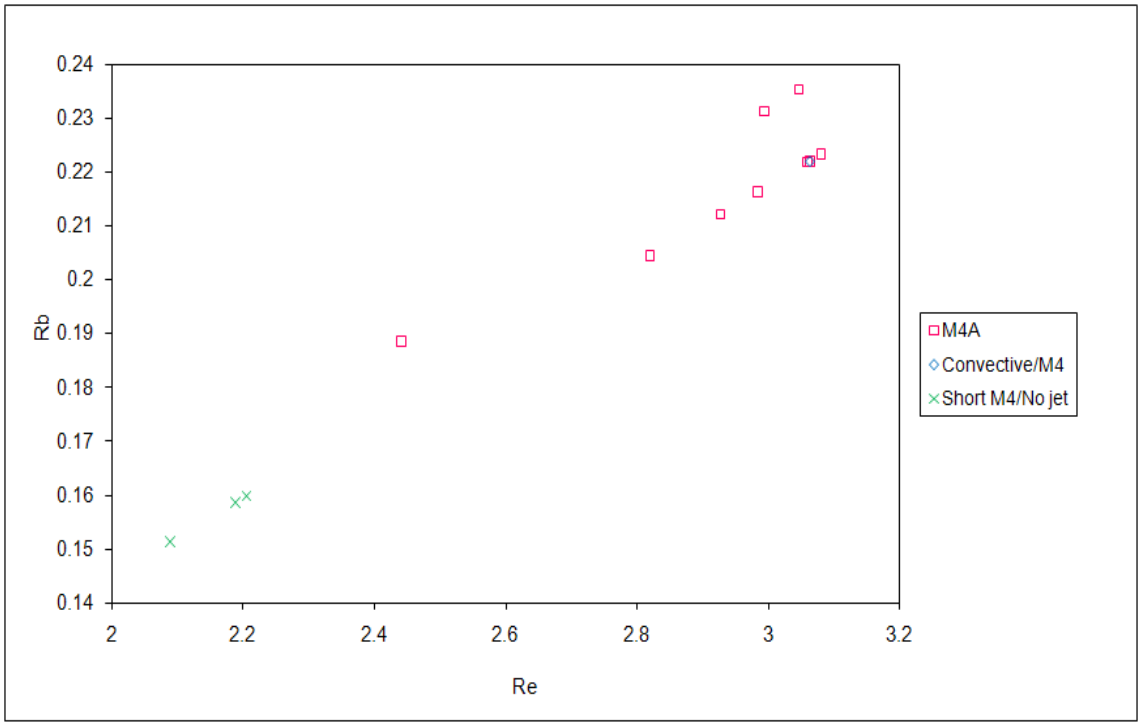

Figure 6.17: Corresponding Rb values of data points in Figure 6.15 plotted against Re.

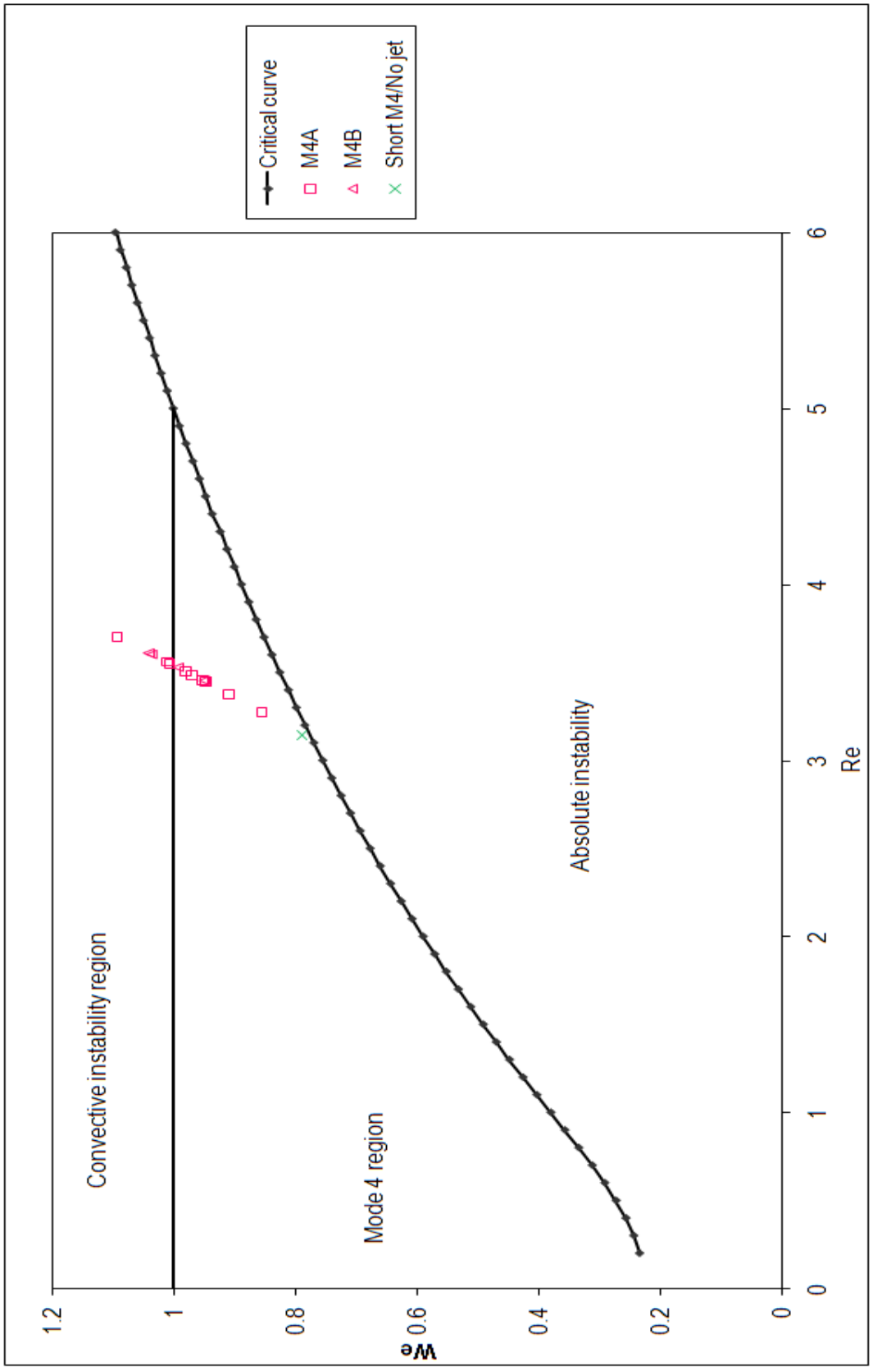

Figure 6.18: Graph showing the experimental Re and We values of jets formed from a water-glycerol solution having $\eta = 0.04575$Pas, $\rho = 1238.152$kgm^{-3}, $\sigma = 0.063$Nm^{-1} with rotation rate 290rpm. The critical curve is marked by the dotted line and the solid black line marks the upper boundary of the Mode 4 region.

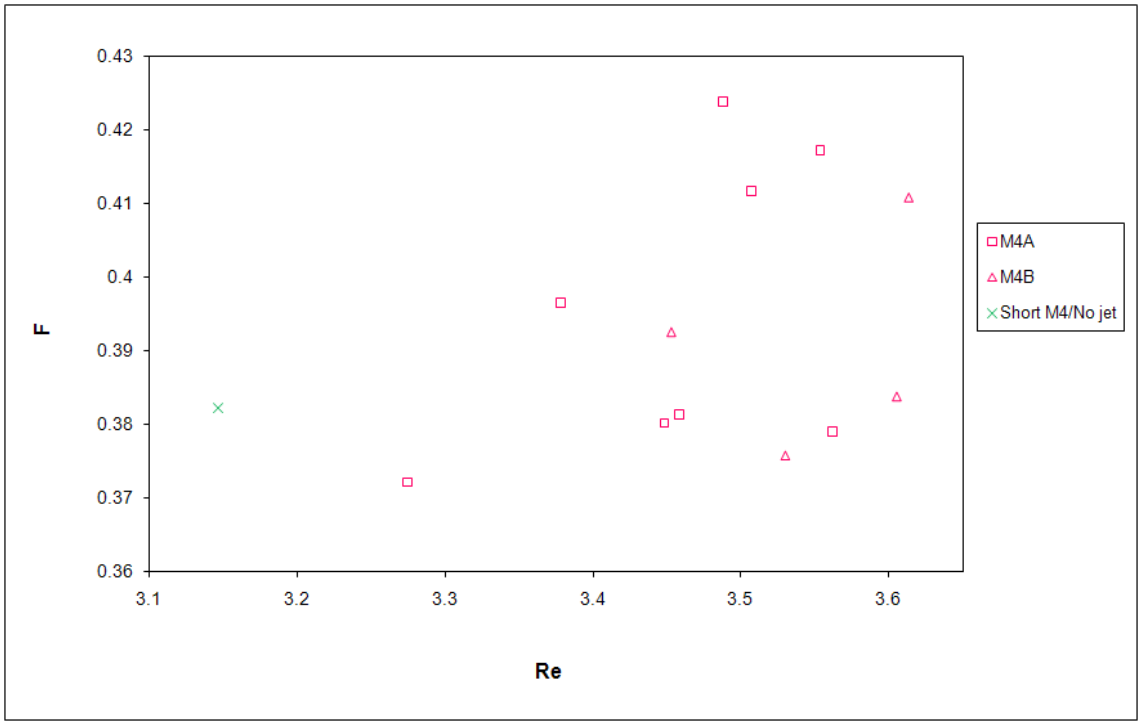

Figure 6.19: Corresponding F values of data points in Figure 6.18 plotted against Re.

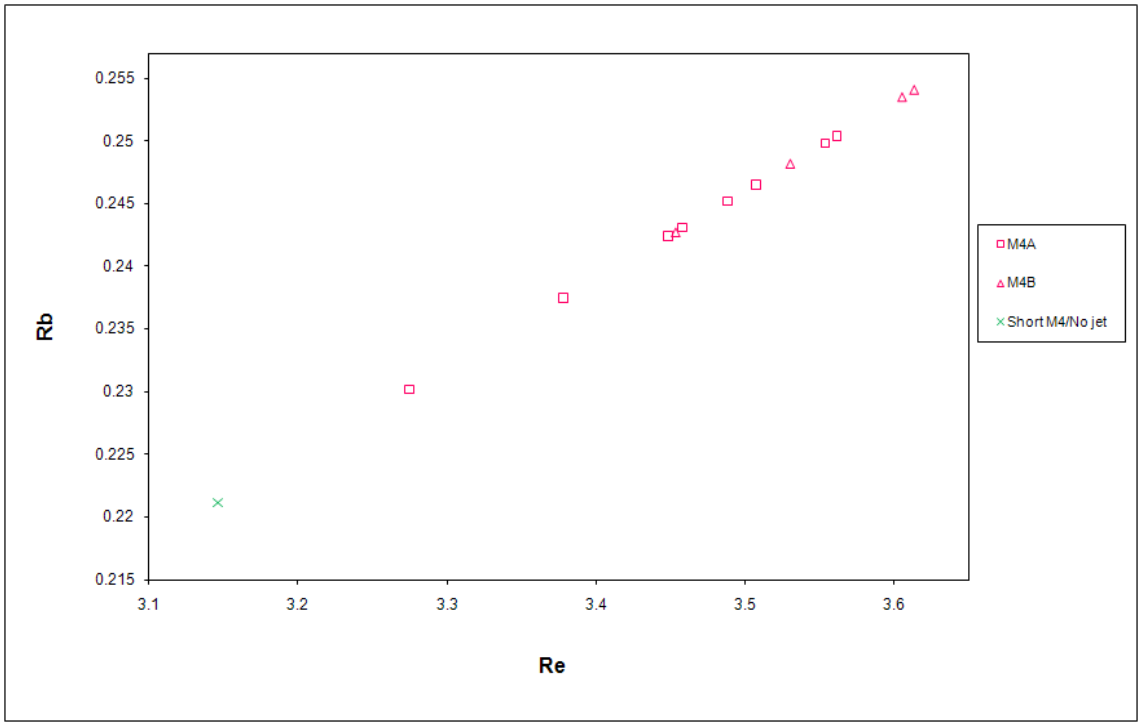

Figure 6.20: Corresponding Rb values of data points in Figure 6.18 plotted against Re.

succeeding steps of the experimental run as the height of the liquid in the can reduced at the end of each experiment. The break-up mode then switches to Short M4/No Jet as the level of liquid drops further. Data points labelled M4A/B correspond to jets where M4A and M4B type break-up were observed in successive rotations of the can in a single experiment. Figures 6.22 and 6.23 show the corresponding Froude and Rossby number values plotted against Re. Figure 6.24 shows data points plotted in the critical Re-We region from two experimental runs at rotation rates of 295rpm and 320rpm. Again, convective and Borderline M4/Convective type break-up is observed at high rotation rates when the height of the liquid in the can is high which then switches to M4A and as the level of liquid in the can drops the break-up mode subsequently changes to the Short M4/No Jet case. Figures 6.25 and 6.26 show the corresponding Froude and Rossby number values plotted against Re.

Figure 6.27 shows parameters of experiments carried out at 305rpm and 345rpm and Figures 6.28 and 6.29 show the corresponding plots of F and Rb plotted against Re. Figure 6.30 show experimental parameters corresponding to jets emerging from the can at rotation rates of 270rpm and 285rpm. The data points denoting M4 correspond to cases where the images of the jet do not capture the break-up point or the length of the jet left attached to the can, due to incorrect positioning of the camera. But the photographs depict all the typical features of M4 type break-up where a bulge develops at the end of the jet and causes the centreline to bend, with upstream propagation of disturbances causing the jet to shatter behind them as they travel upstream. Figures 6.31 and 6.32 show the corresponding F and Rb plotted against Re.

Figure 6.33 shows data points corresponding to jets emanating at rotation rates 285rpm and 310rpm with Figures 6.34 and 6.35 showing the corresponding F and Rb plotted against Re. Figure 6.36 shows data points corresponding to two experimental runs at rotation rates 280rpm and 320rpm and Figures 6.37 and 6.38 show the corresponding F and Rb plotted against Re. Figures 6.39 and 6.42 show Re and We values of jets from experiments performed using very viscous fluids. Only Long M4/No Jet type

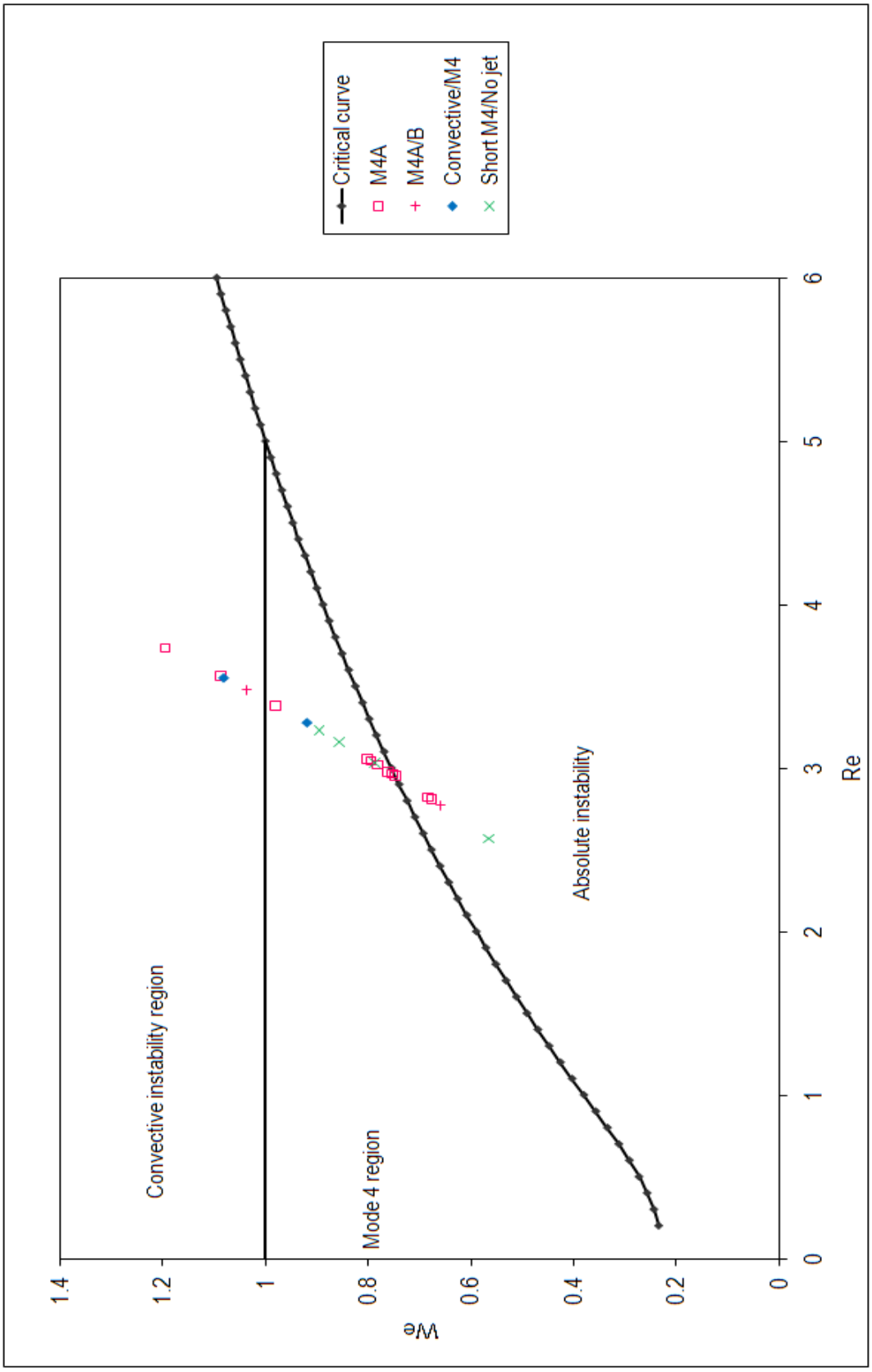

Figure 6.21: Graphs showing the experimental Re and We values of jets formed from a water-glycerol solution having $\eta = 0.0684$ Pa s, $\rho = 1242.340\text{kgm}^{-3}$, $\sigma = 0.0635\text{Nm}^{-1}$ at rotation rates of 290rpm, 320rpm, 330rpm, 285rpm and 295rpm. The critical curve is marked by the dotted line and the solid black line marks the upper boundary of the Mode 4 region.

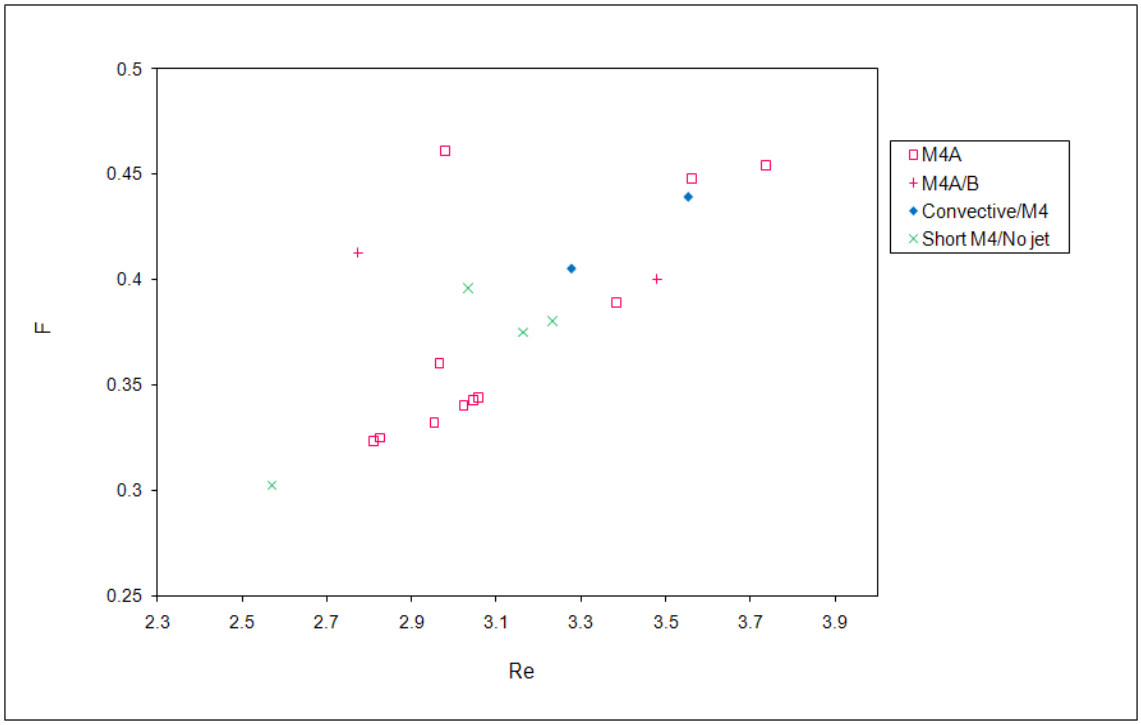

Figure 6.22: Corresponding F values of data points in Figure 6.21 plotted against Re.

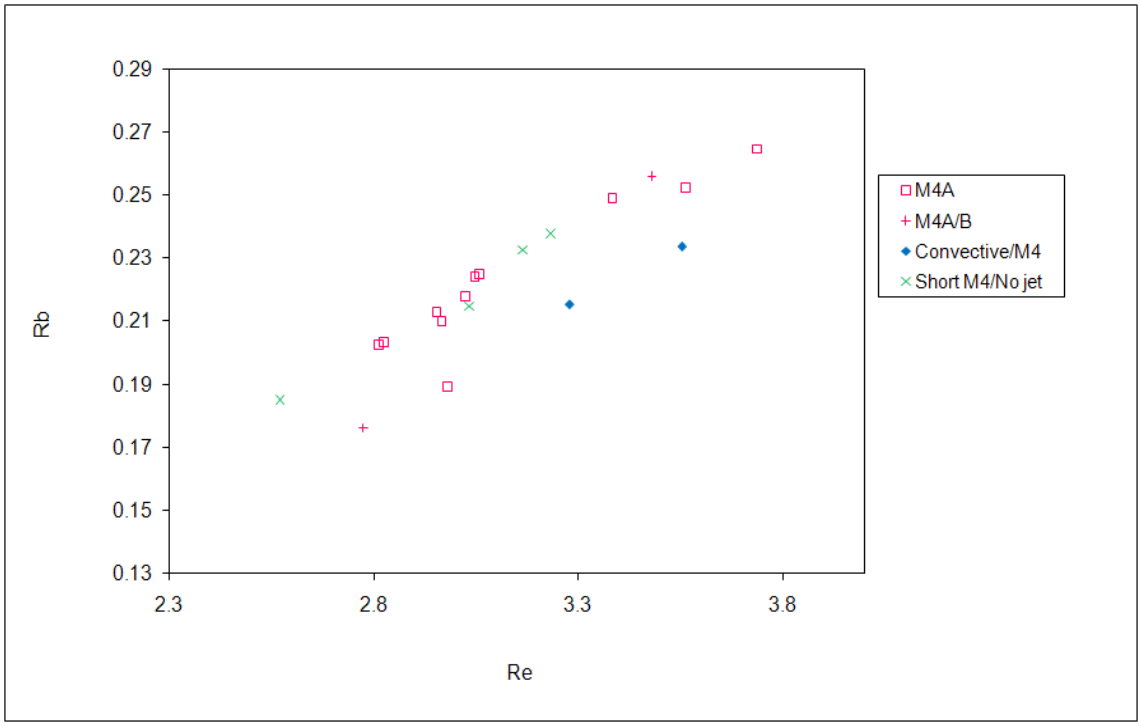

Figure 6.23: Corresponding Rb values of data points in Figure 6.21 plotted against Re.

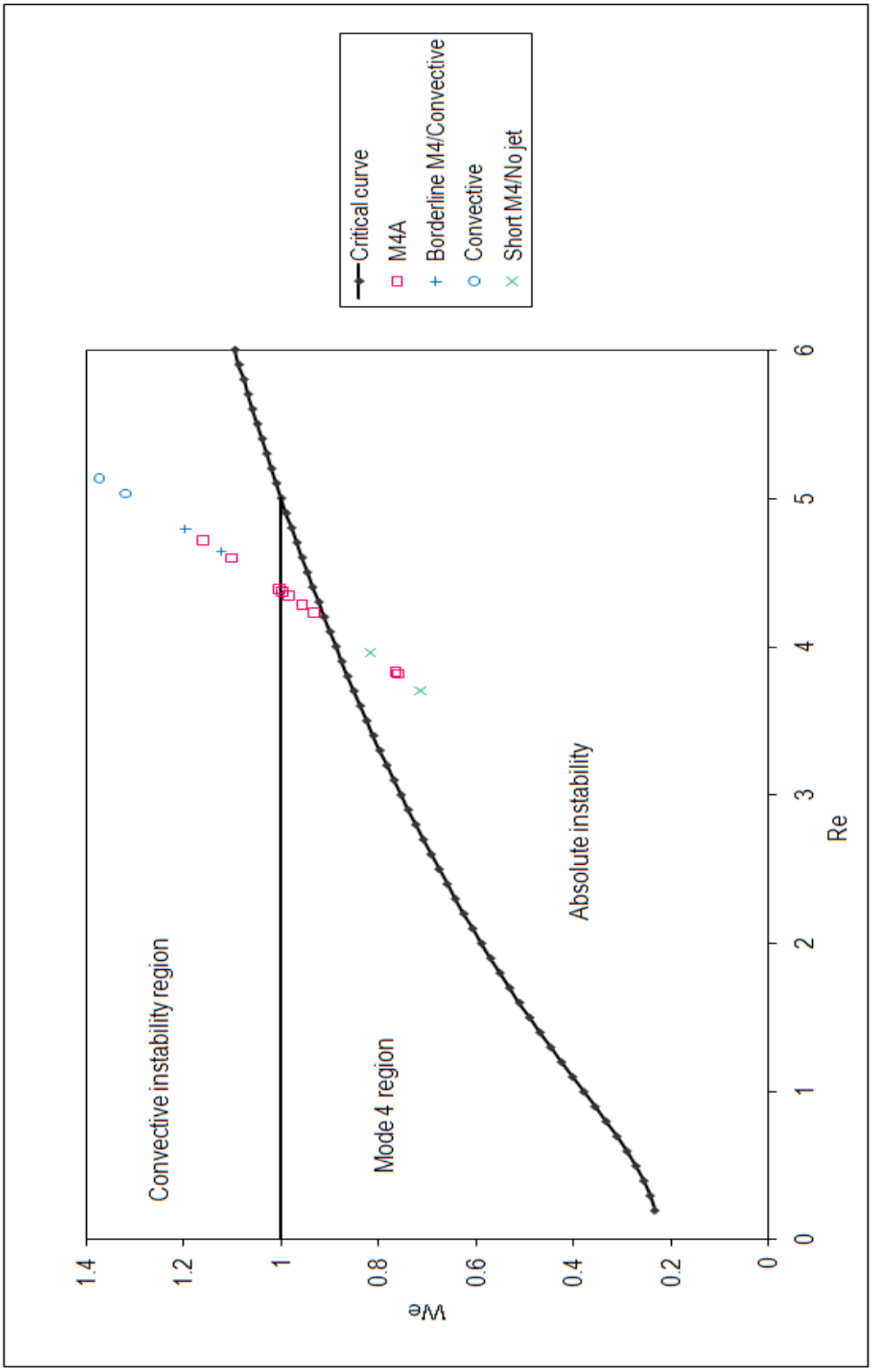

Figure 6.24: Graphs showing the experimental Re and We values of jets formed from a water-glycerol solution having $\eta = 0.045205$Pas, $\rho = 1235.624$kgm^{-3}, $\sigma = 0.0635$Nm^{-1} at rotation rates of 295rpm and 320rpm. The critical curve is marked by the dotted line and the solid black line marks the upper boundary of the Mode 4 region.

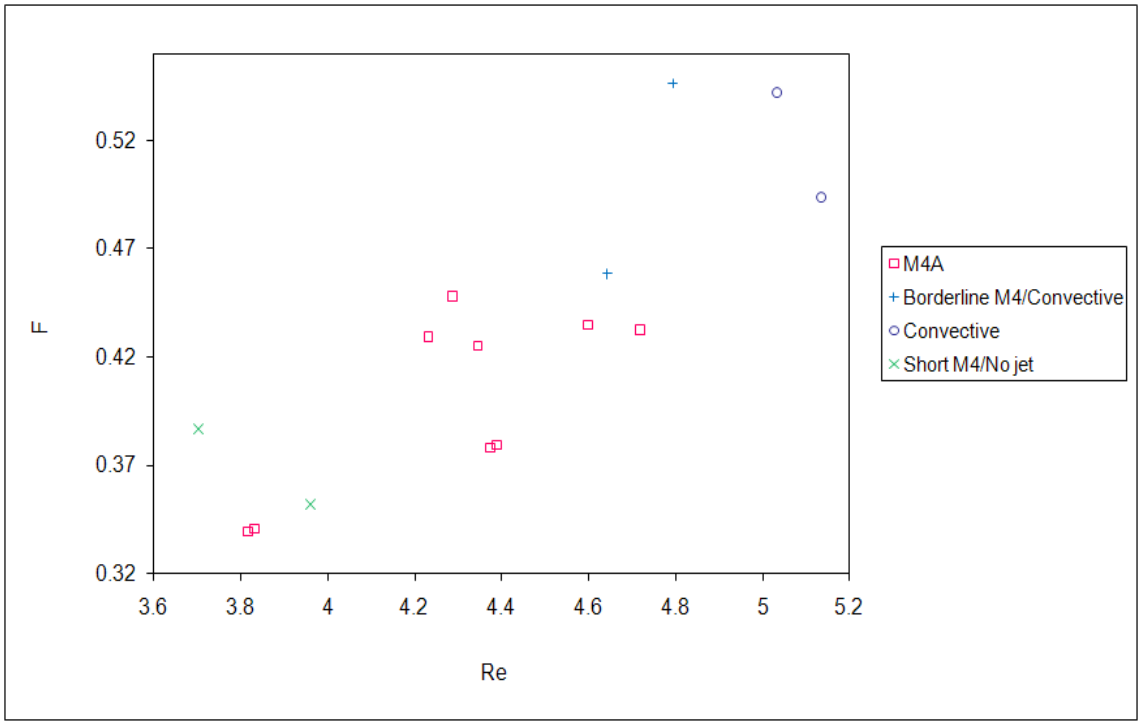

Figure 6.25: Corresponding F values of data points in Figure 6.24 plotted against Re.

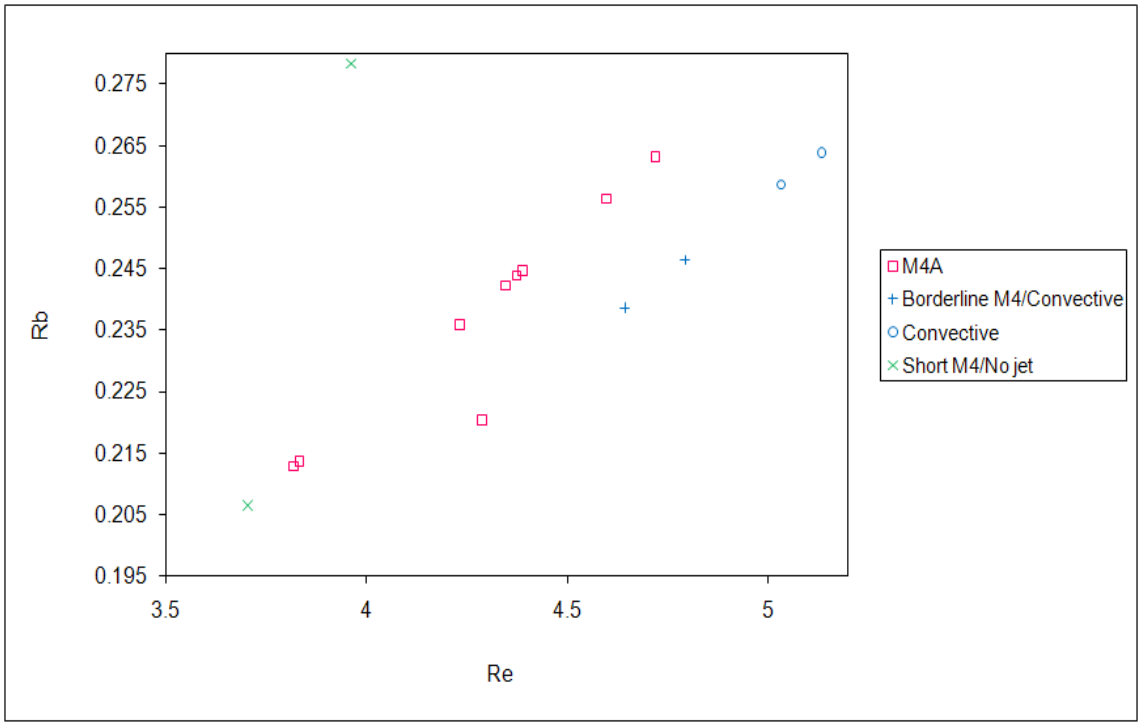

Figure 6.26: Corresponding Rb values of data points in Figure 6.24 plotted against Re.

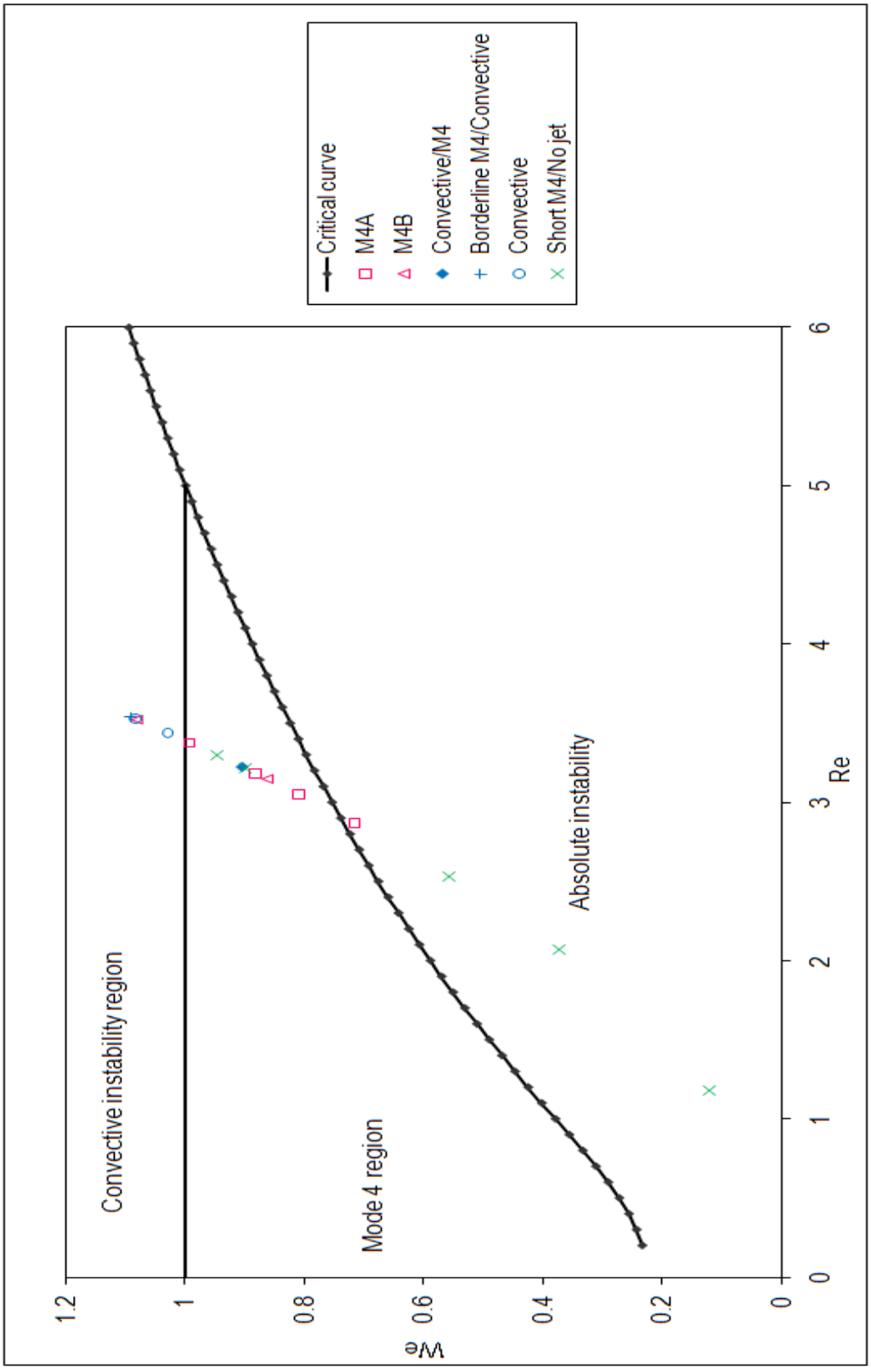

Figure 6.27: Graphs showing the experimental Re and We values of jets formed from a water-glycerol solution having $\eta = 0.05941$Pas, $\rho = 1241.558$kgm^{-3}, $\sigma = 0.06525$Nm^{-1} at rotation rates of 305rpm and 345rpm. The critical curve is marked by the dotted line and the solid black line marks the upper boundary of the Mode 4 region.

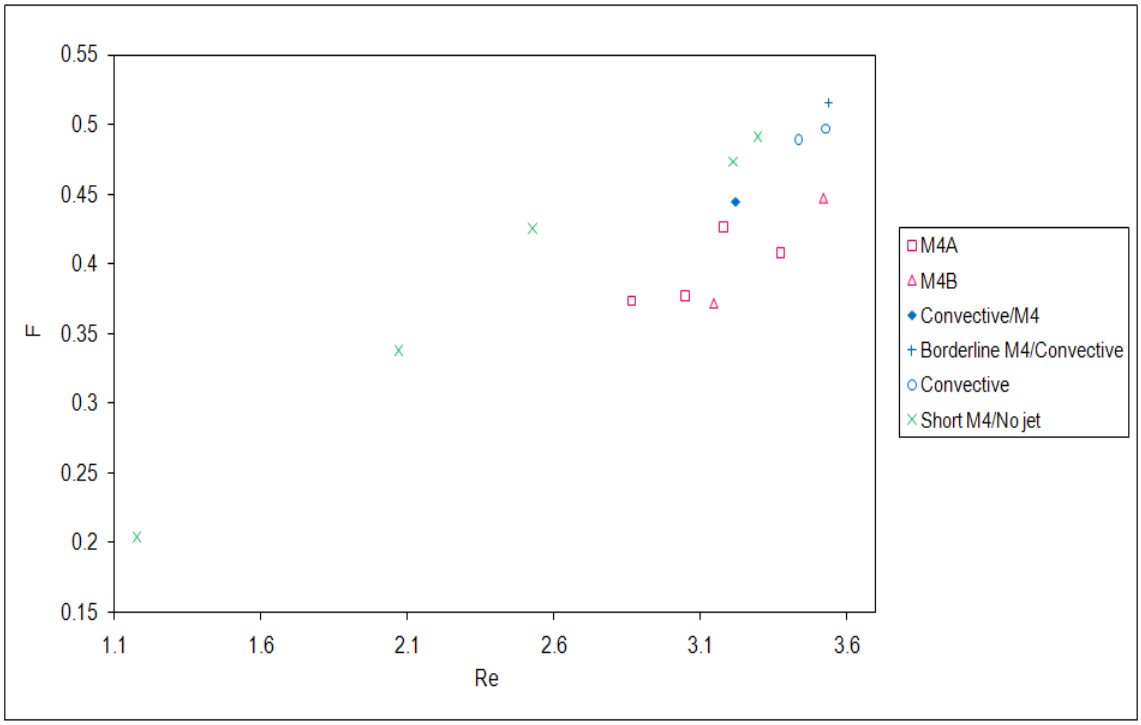

Figure 6.28: Corresponding F values of data points in Figure 6.27 plotted against Re.

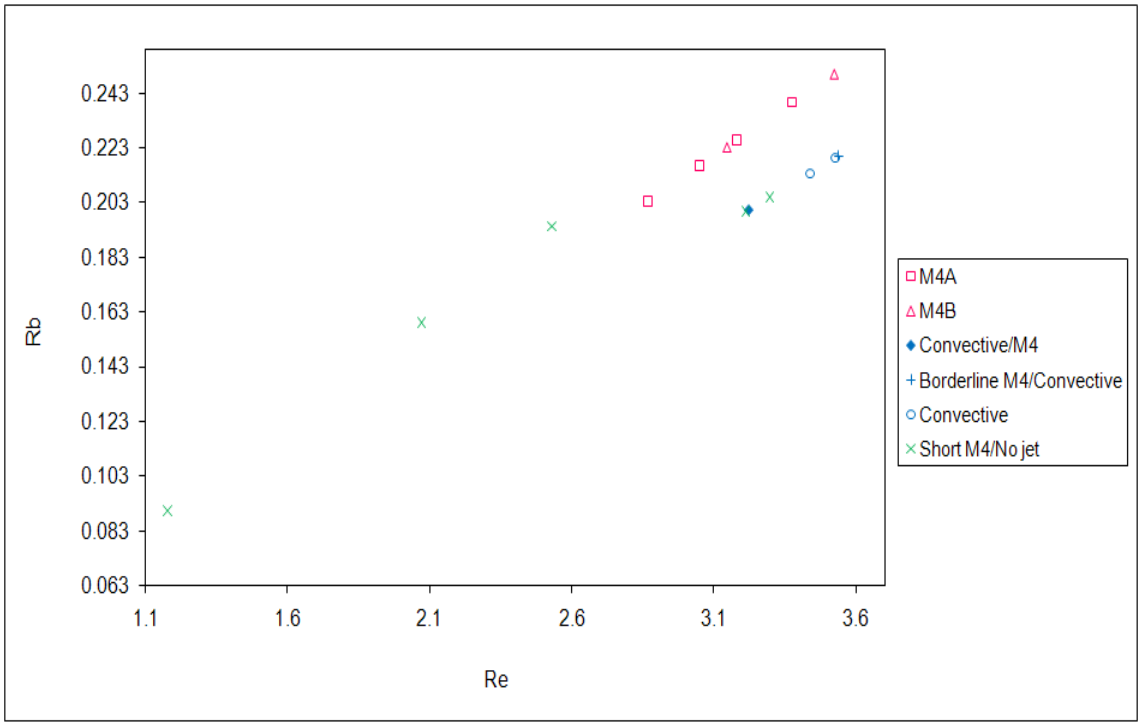

Figure 6.29: Corresponding Rb values of data points in Figure 6.27 plotted against Re.

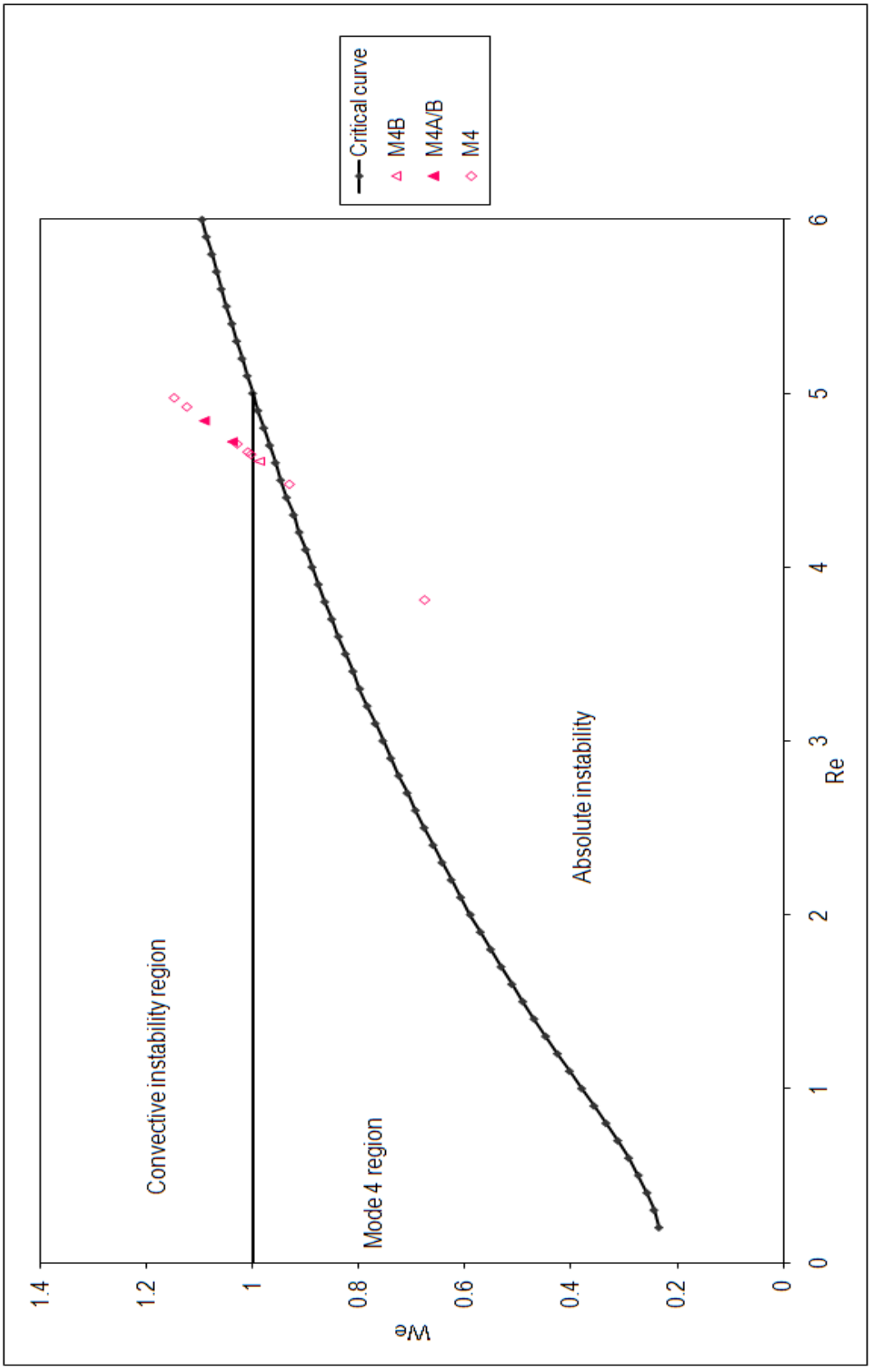

Figure 6.30: Graphs showing the experimental Re and We values of jets formed from a water-glycerol solution having $\eta = 0.05941$Pas, $\rho = 1241.558$kgm^{-3}, $\sigma = 0.06525$Nm^{-1} at rotation rates of 270rpm and 285rpm. The critical curve is marked by the dotted line and the solid black line marks the upper boundary of the Mode 4 region.

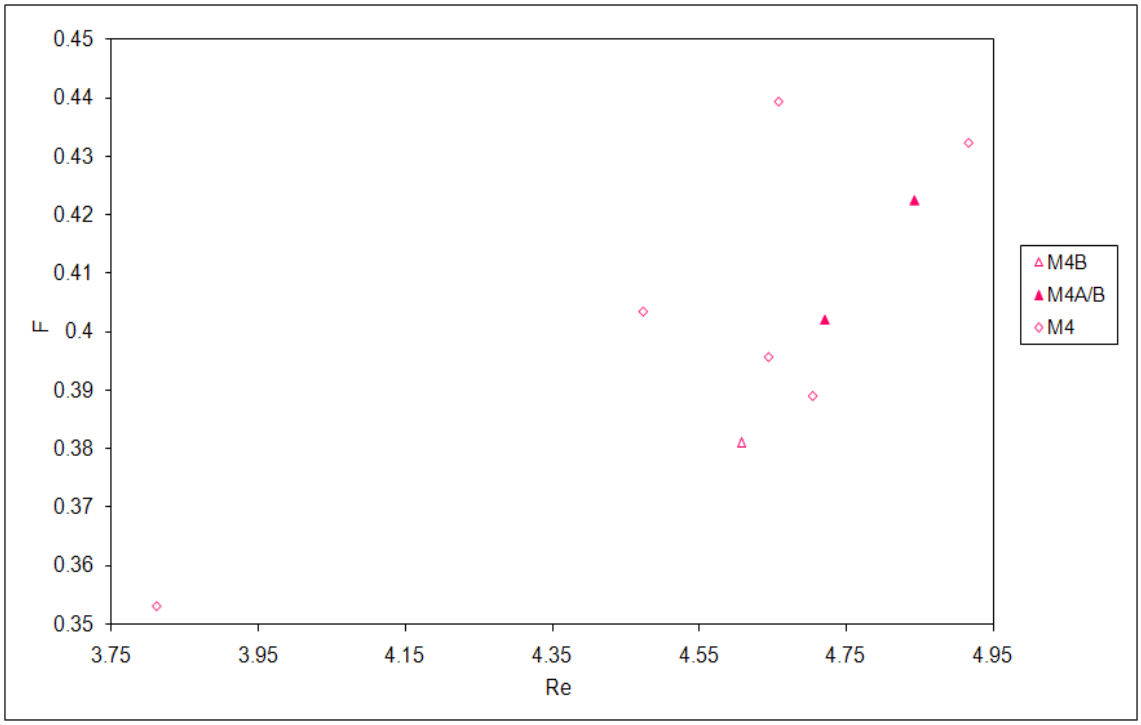

Figure 6.31: Corresponding F values of data points in Figure 6.30 plotted against Re.

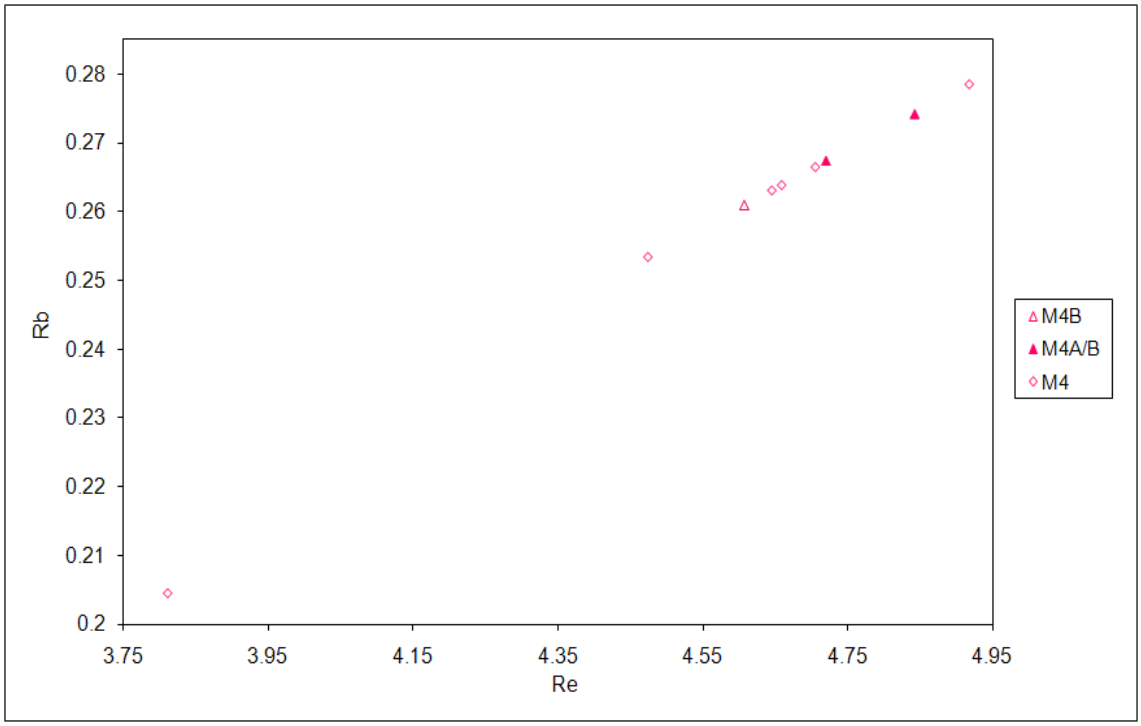

Figure 6.32: Corresponding Rb values of data points in Figure 6.30 plotted against Re.

break-up was observed for these liquids. Jets in this case have very low exit velocities and thus very low Weber numbers. Therefore, in Figures 6.39 and 6.42 data points corresponding to Long M4/No Jet lie below the critical curve close to the origin. Figures 6.40 and 6.41 show the F and Rb plotted against Re corresponding to Figure 6.39 and Figures 6.43 and 6.44 show the F and Rb plotted against Re corresponding to Figure 6.42.

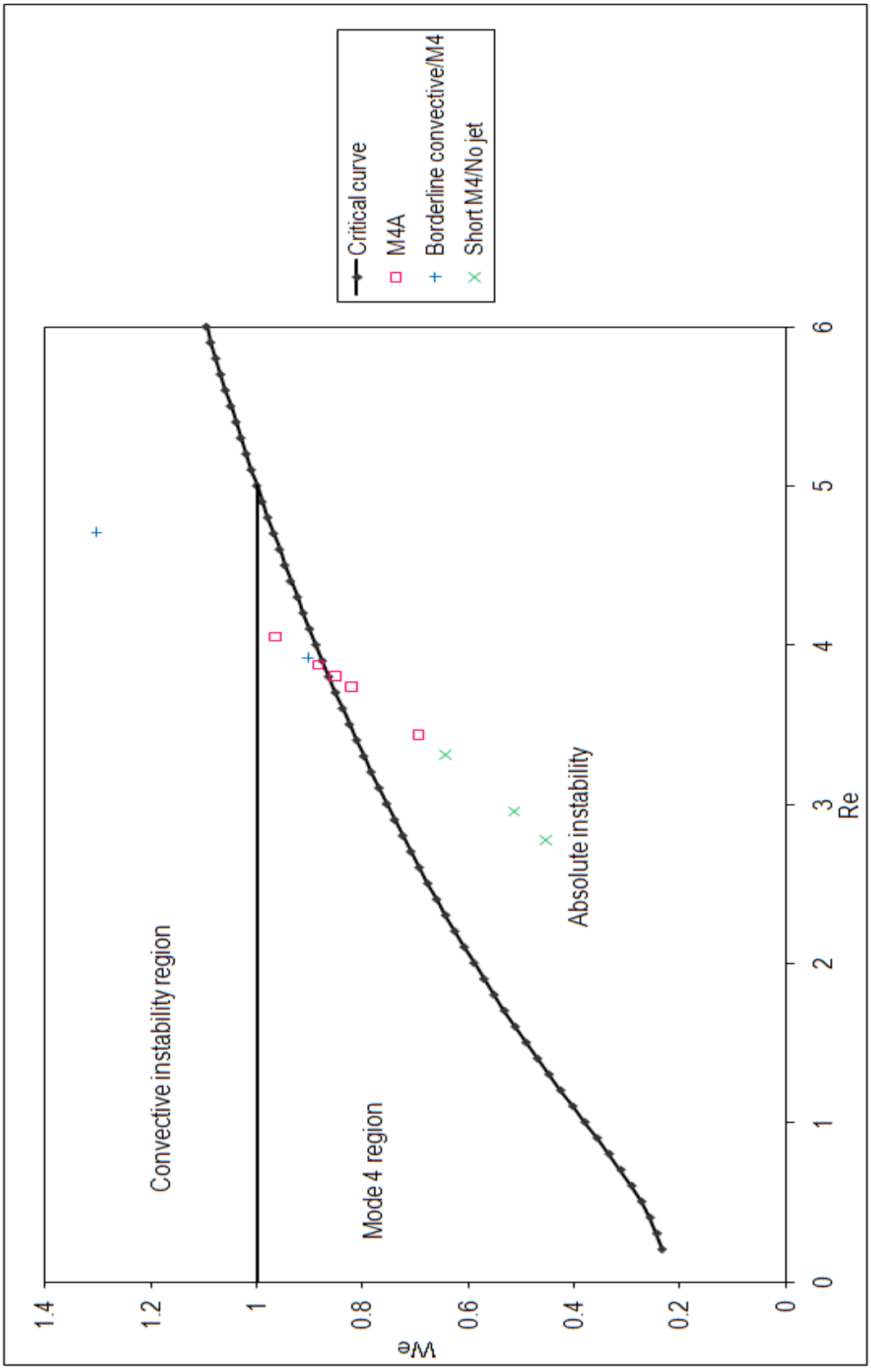

Figure 6.33: Graphs showing the experimental Re and We values of jets formed from a water-glycerol solution having $\eta = 0.04844$Pas, $\rho = 1242.54$kgm^{-3}, $\sigma = 0.06425$Nm^{-1} at rotation rates of 285rpm and 310rpm. The critical curve is marked by the dotted line and the solid black line marks the upper boundary of the Mode 4 region.

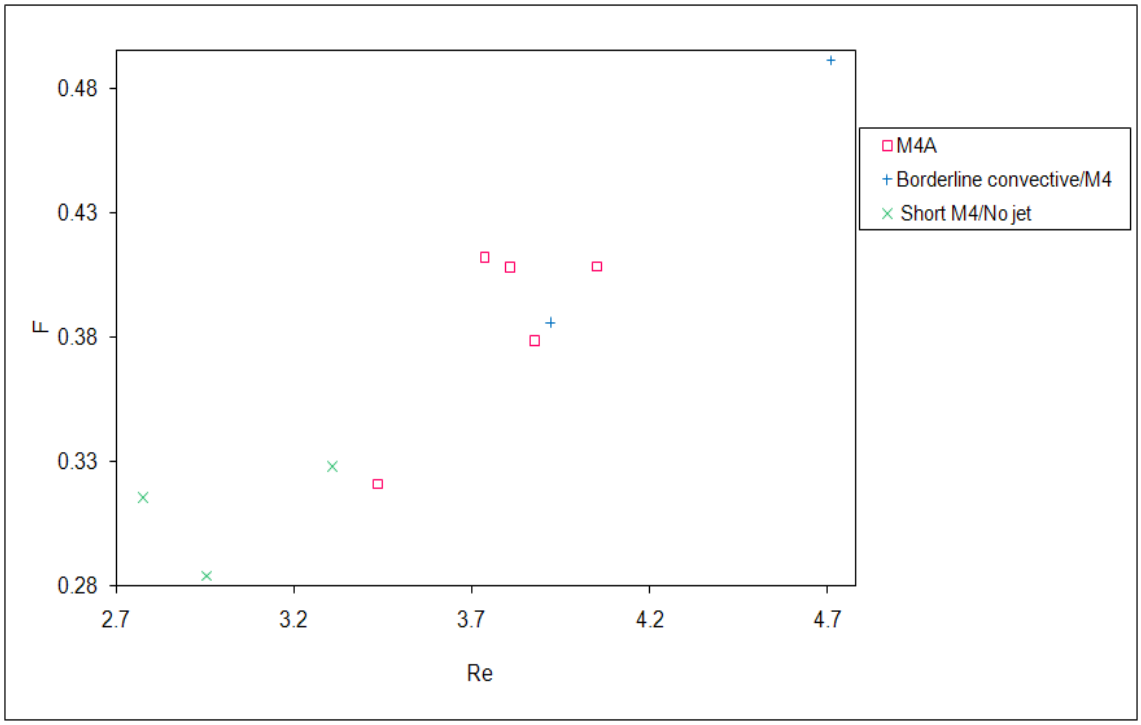

Figure 6.34: Corresponding F values of data points in Figure 6.33 plotted against Re.

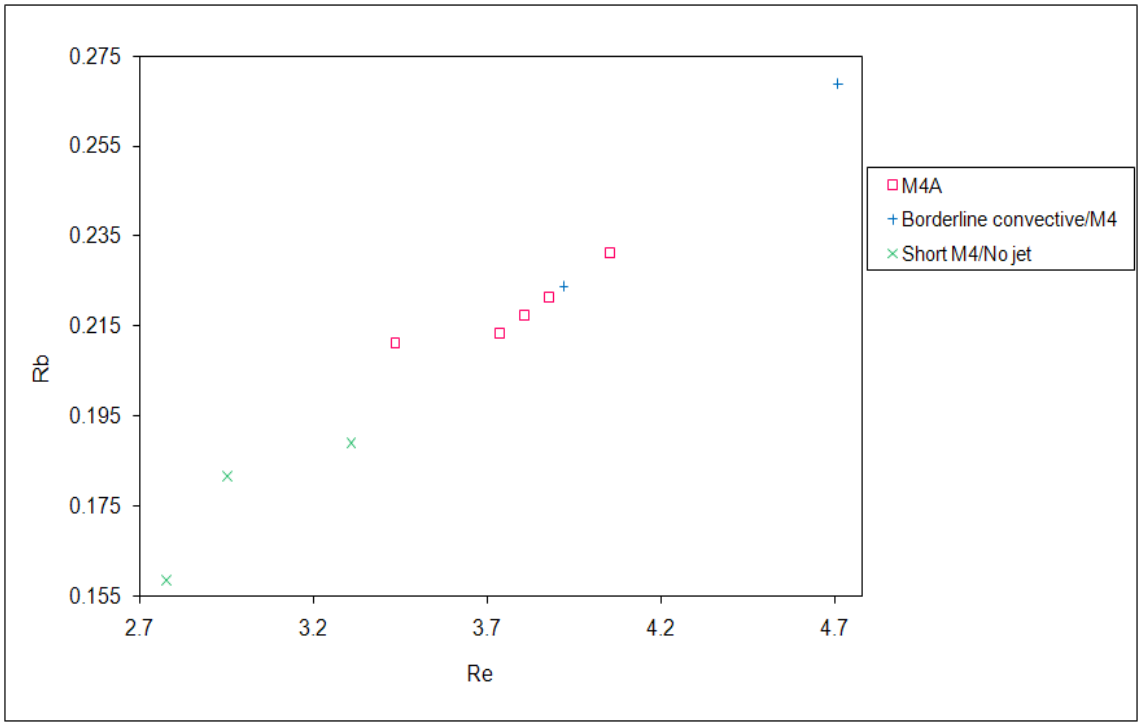

Figure 6.35: Corresponding Rb values of data points in Figure 6.33 plotted against Re.

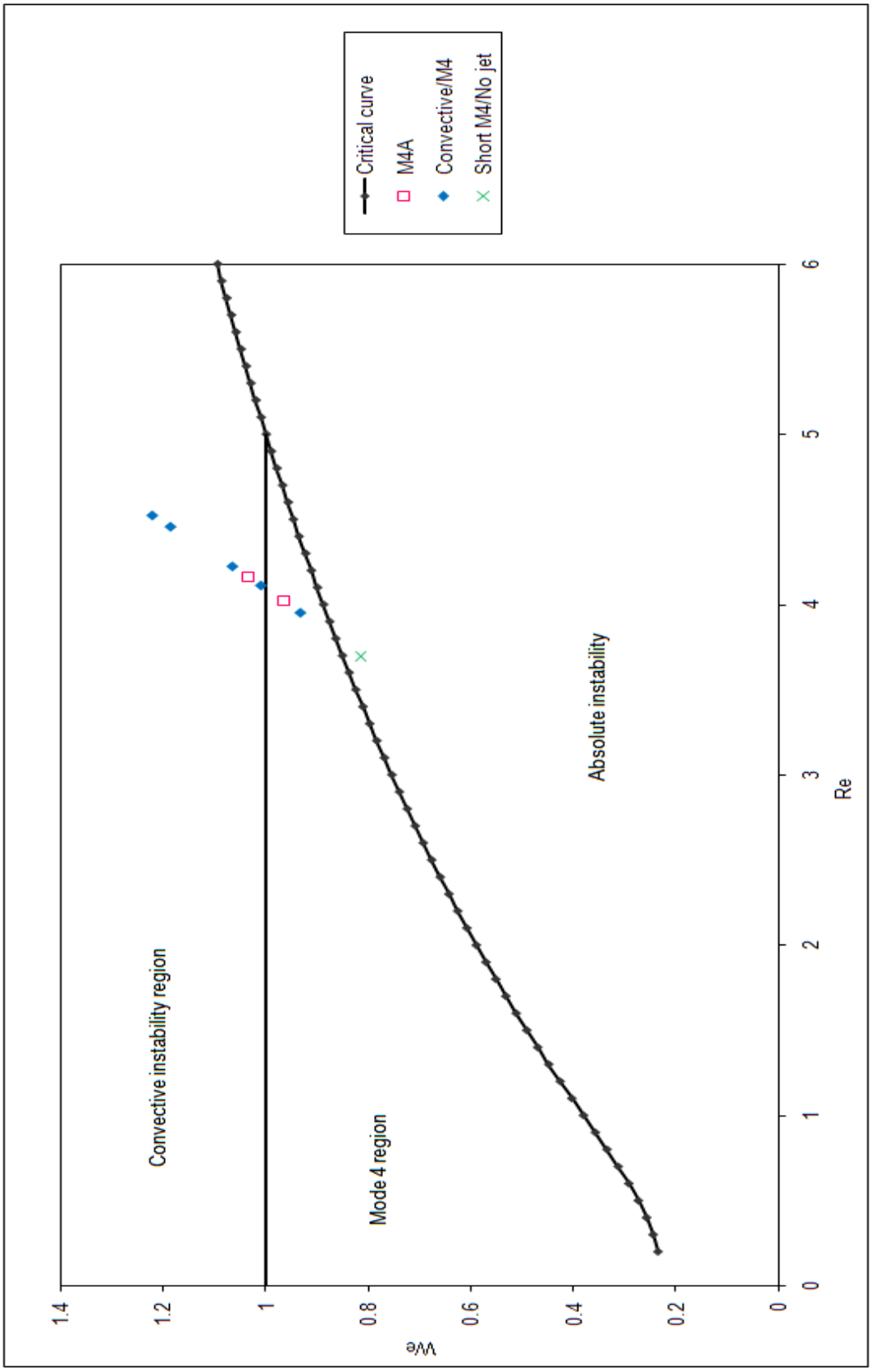

Figure 6.36: Graphs showing the experimental Re and We values of jets formed from a water-glycerol solution having $\eta = 0.04873$Pas, $\rho = 1235.018$kgm^{-3}, $\sigma = 0.0645$Nm^{-1} at rotation rates of 280rpm and 320rpm. The critical curve is marked by the dotted line and the solid black line marks the upper boundary of the Mode 4 region.

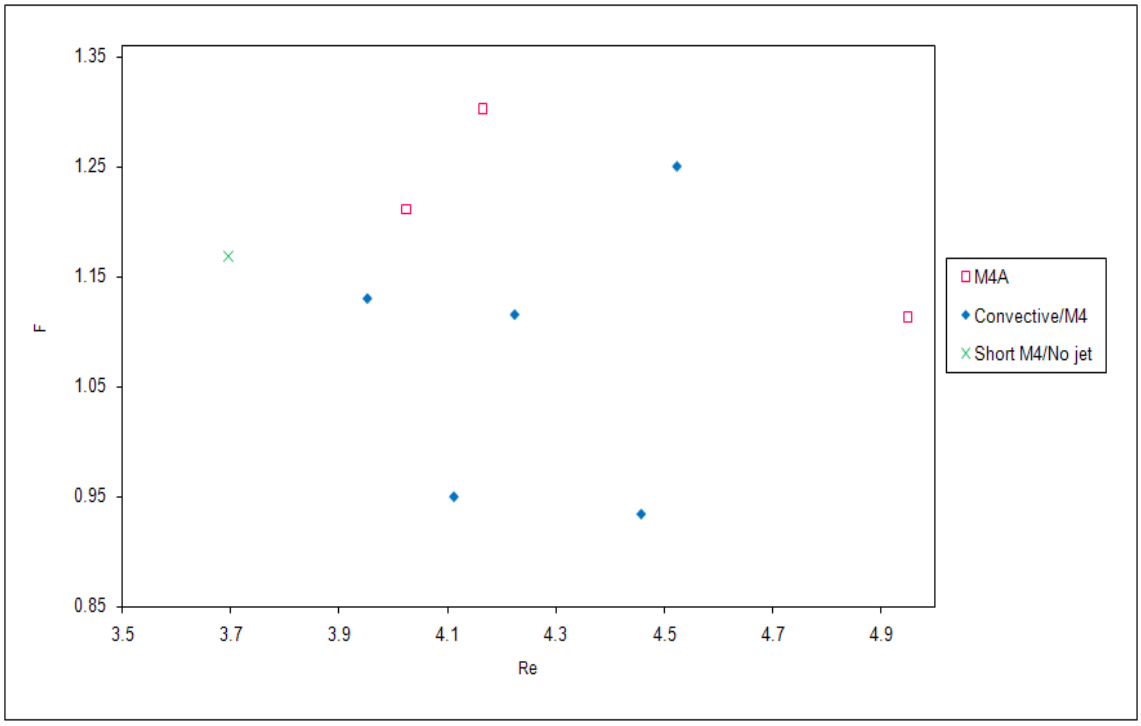

Figure 6.37: Corresponding F values of data points in Figure 6.36 plotted against Re.

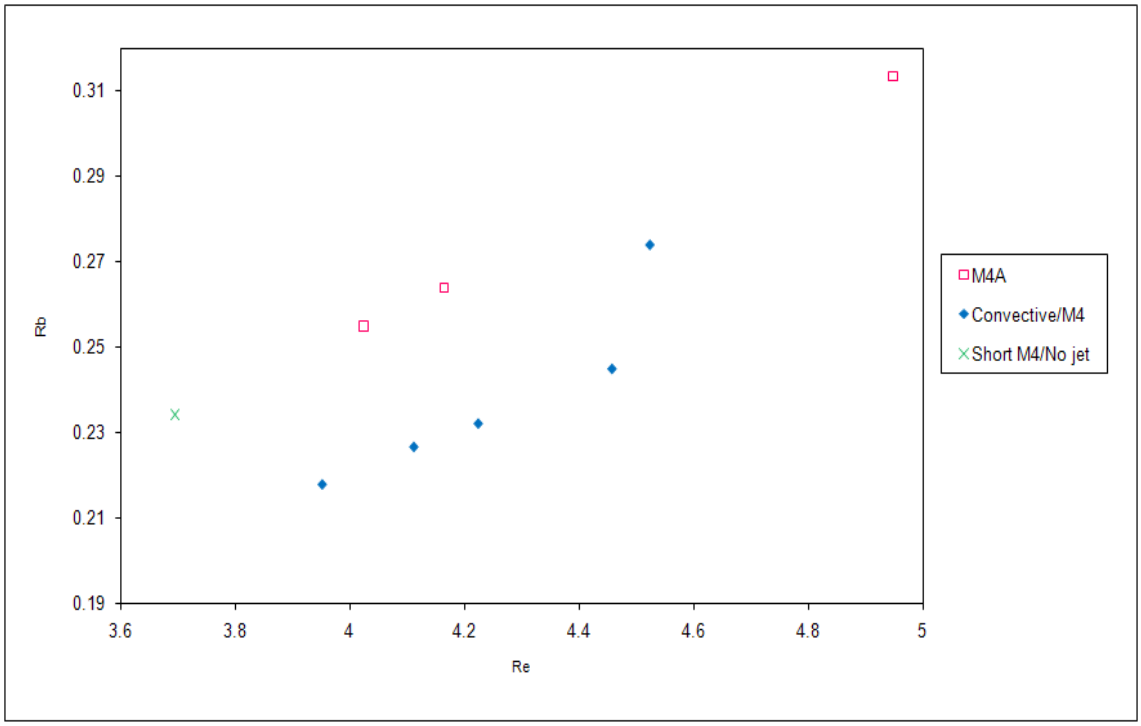

Figure 6.38: Corresponding Rb values of data points in Figure 6.36 plotted against Re.

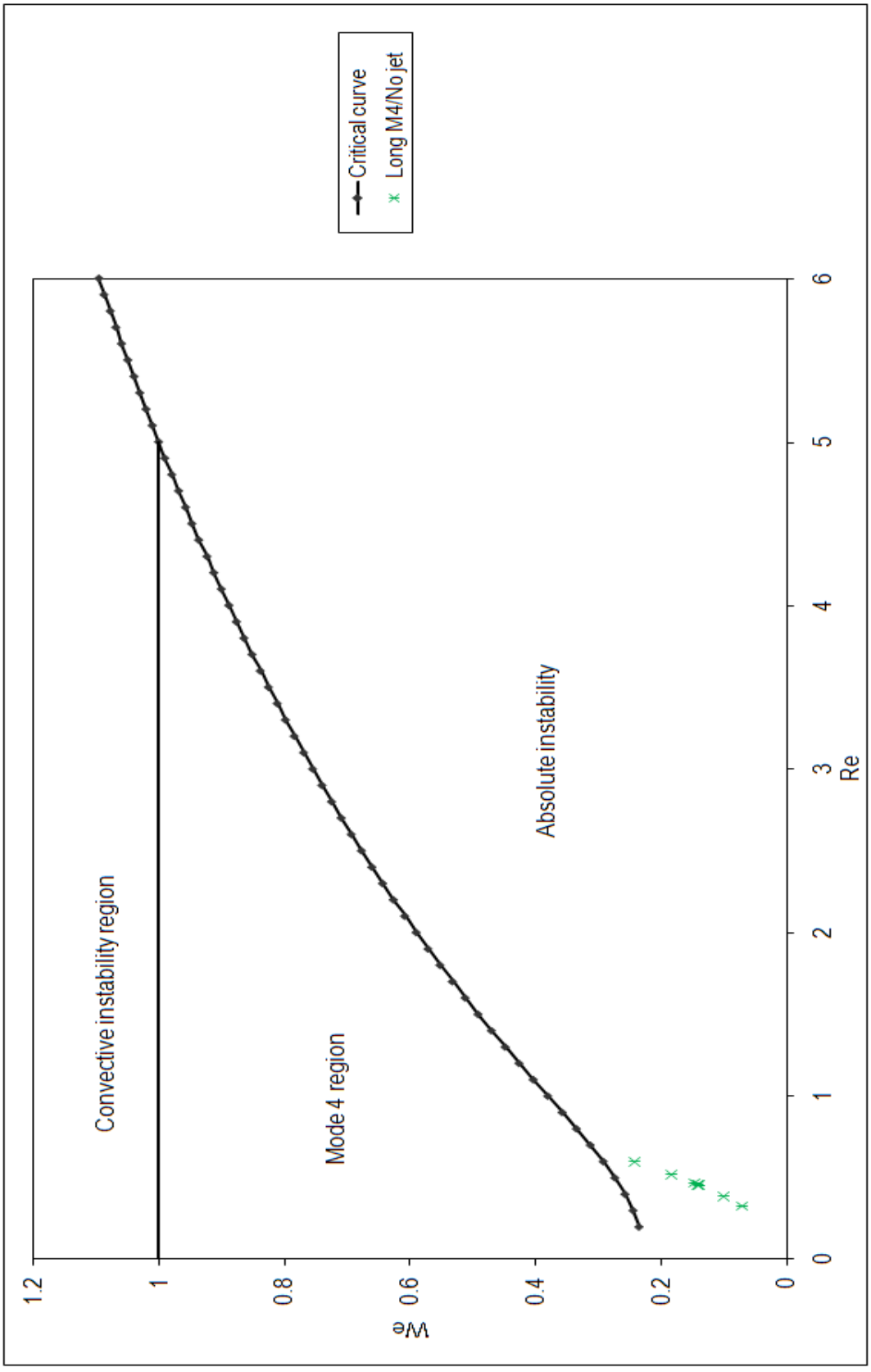

Figure 6.39: Graphs showing the experimental Re and We values of jets formed from a water-glycerol solution having $\eta = 0.1675$Pas, $\rho = 1264.672$kgm^{-3}, $\sigma = 0.065275$Nm^{-1} at rotation rates of 280rpm and 310rpm. The critical curve is marked by the dotted line and the solid black line marks the upper boundary of the Mode 4 region.

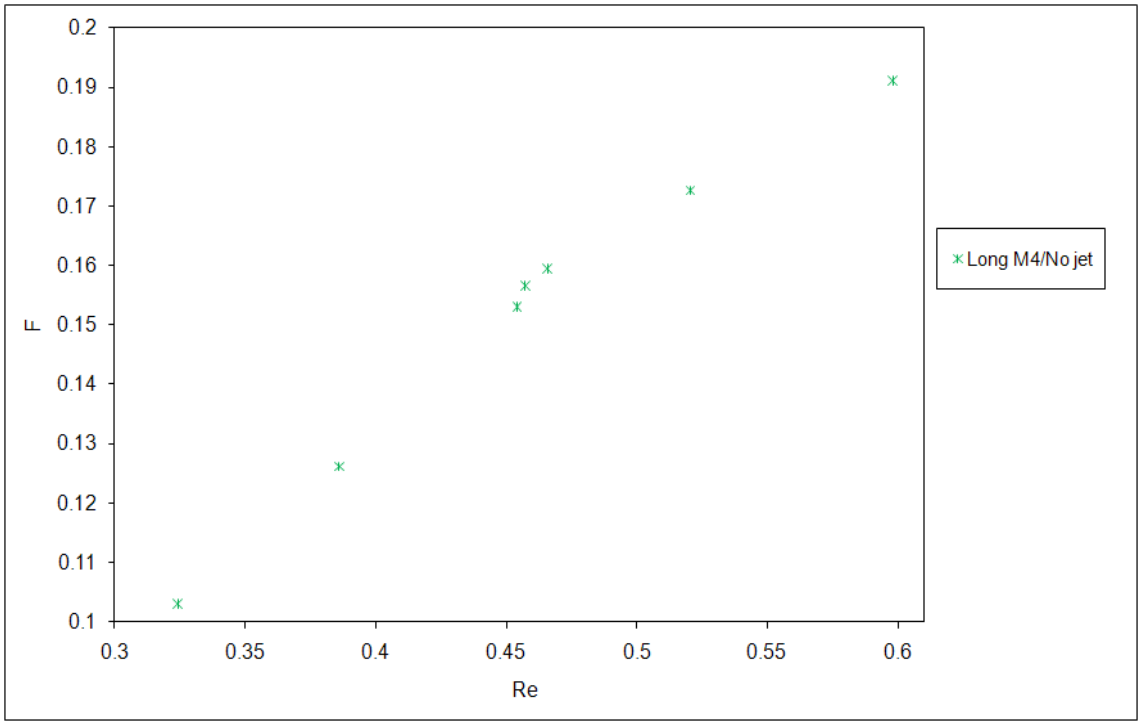

Figure 6.40: Corresponding F values of data points in Figure 6.39 plotted against Re.

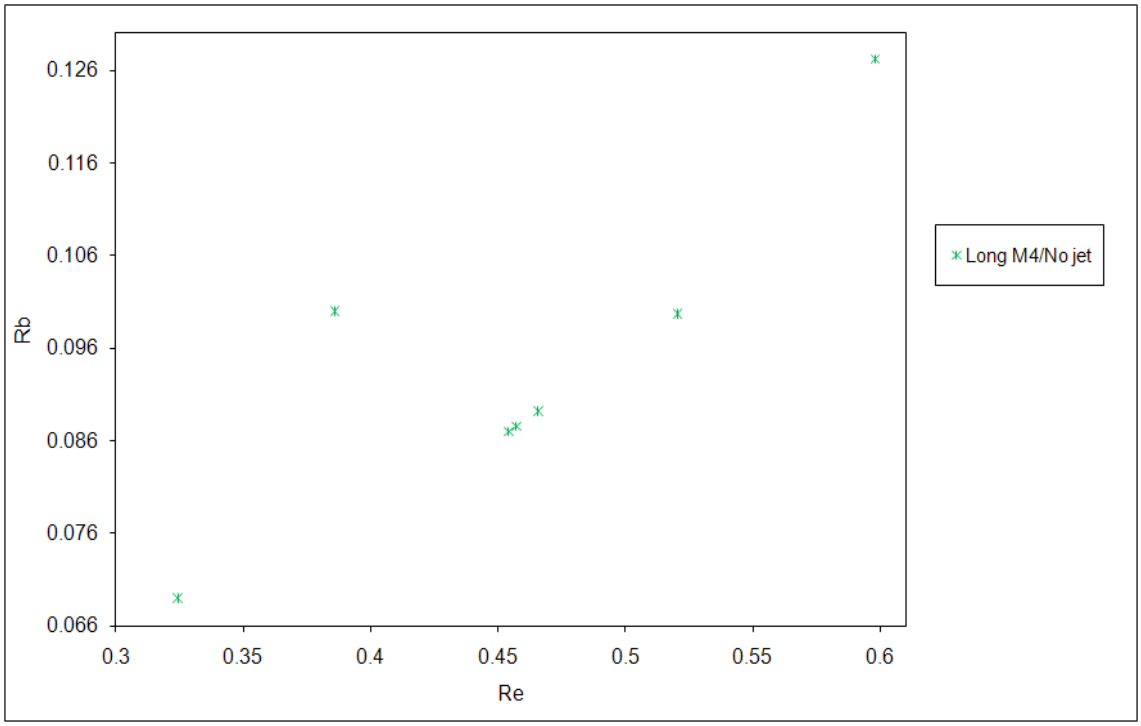

Figure 6.41: Corresponding Rb values of data points in Figure 6.39 plotted against Re.

Figures 6.45, 6.46 and 6.47 show the experimental data points plotted in the *Re-We* plane along with the critical and Mode 4 curves. In Figure 6.45, all the data points correspond to M4A, M4B and M4A/B (cases which exhibit M4 type break-up). Most of the points on this graph lie in the Mode 4 region. Figure 6.46 gives a plot of all the data points corresponding to the Convective/M4, Borderline M4/Convective and convective break-up modes (break-up modes which are convectively unstable or form borderline cases between convective and M4 type break-up). The data points in this graph lie in the region above the critical curve and the Mode 4 region in the convective instability area. Figure 6.47 presents a plot of data points corresponding to Short M4/No Jet, Long M4/No Jet and the No Jet cases (break-up modes which demonstrate some form of absolute instability in their break-up dynamics). Data points in this graph lie below the critical curve in the absolute instability region. Figure 6.48 shows a graph of all the aggregated data points from Figures 6.15-6.42 plotted in the *Re-We* plane. Very good agreement is found between theory and experiments. Figures 6.45, 6.46, 6.47 and 6.48 show that 74% of the M4 data points lie in the Mode 4 region while 78% of the convective data points lie above the Mode 4 boundary in the convective instability region and 83% of the Long M4/No Jet, Short M4/No Jet and No jet data points lie below the critical curve in the absolute instability region. The data points corresponding to the Short M4/No Jet case, which forms a transition mode between M4 and No Jet, lie in the Mode 4 and absolute instability regions. Thus, the height of the liquid in the can needs to be maintained at a sufficiently high level so as to acquire a high enough exit velocity at the orifice in order to avoid the Short M4/No Jet case, where it becomes hard to predict the behaviour of jet break-up. Thus from Figures 6.45, 6.46, 6.47 and 6.48, we observe that the experimental results clearly pick up the Mode 4 region and the critical boundary as there is some form of transition occurring around these two boundaries.

Note that there is an area in the Mode 4 region where no data was found. For viscous liquids that have Reynolds numbers that are small enough to lie in this part of the critical *Re-We* space, the high viscosity of the fluid leads to very low exit velocities at the orifice

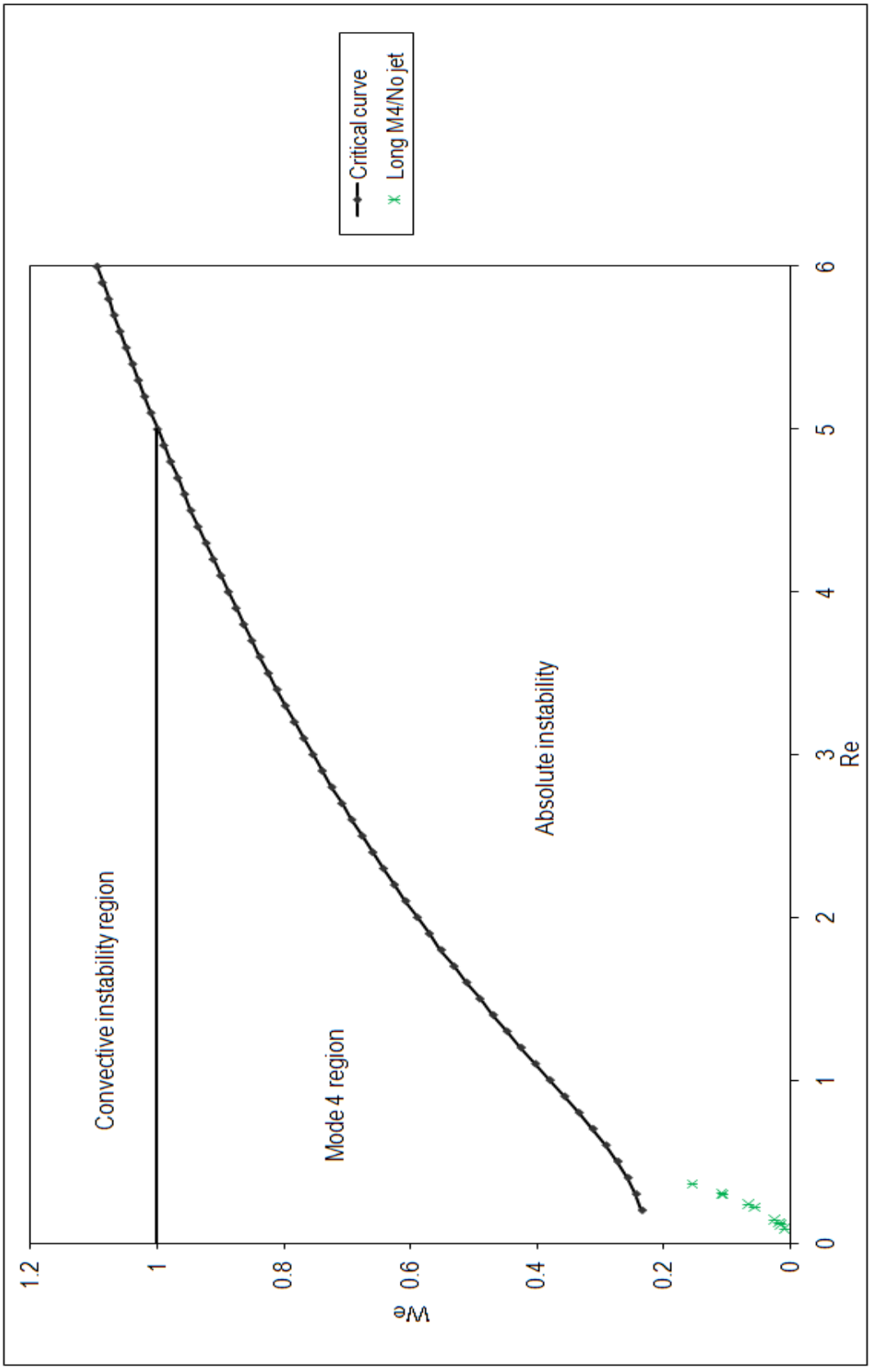

Figure 6.42: Graphs showing the experimental Re and We values of jets formed from a water-glycerol solution having $\eta = 0.218801$Pas, $\rho = 1268.026$kgm^{-3}, $\sigma = 0.064$Nm^{-1} at rotation rates of 200rpm, 260rpm, 300rpm and 330rpm. The critical curve is marked by the dotted line and the solid black line marks the upper boundary of the Mode 4 region.

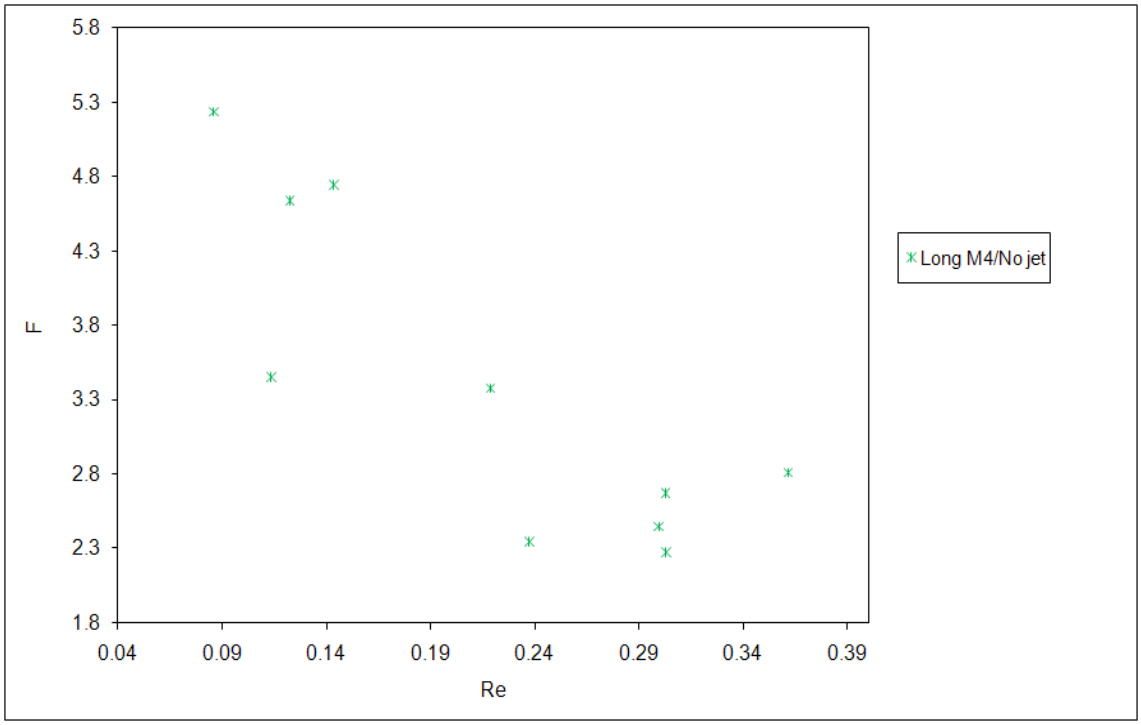

Figure 6.43: Corresponding F values of data points in Figure 6.42 plotted against Re.

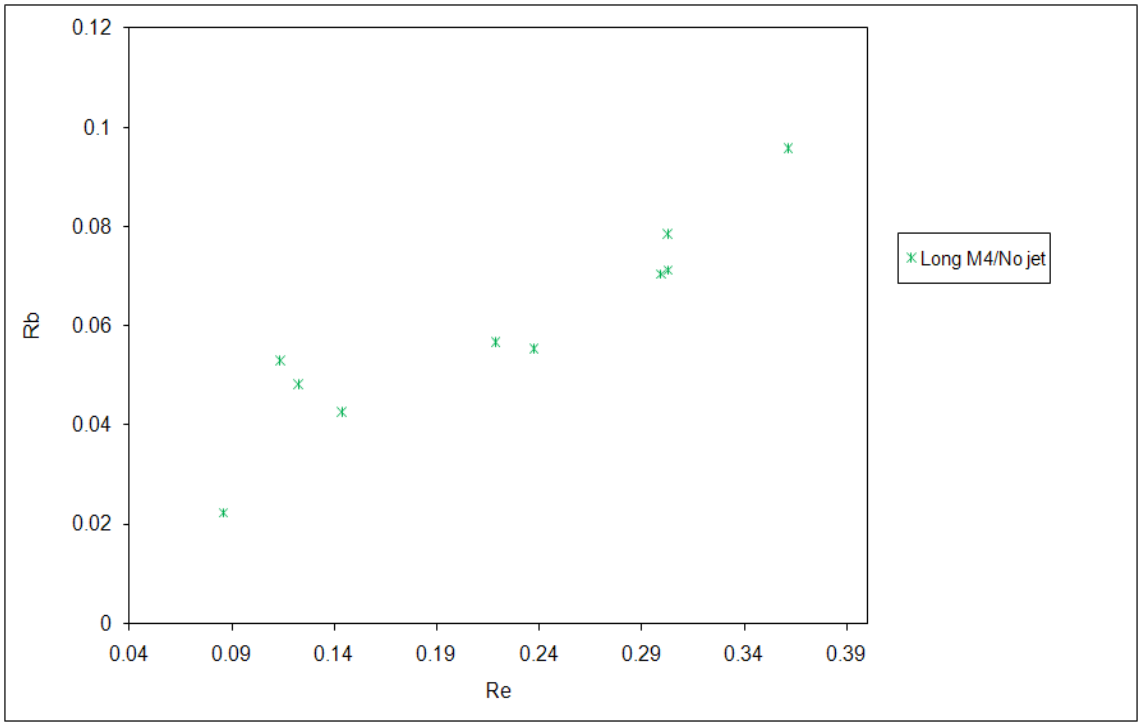

Figure 6.44: Corresponding Rb values of data points in Figure 6.42 plotted against Re.

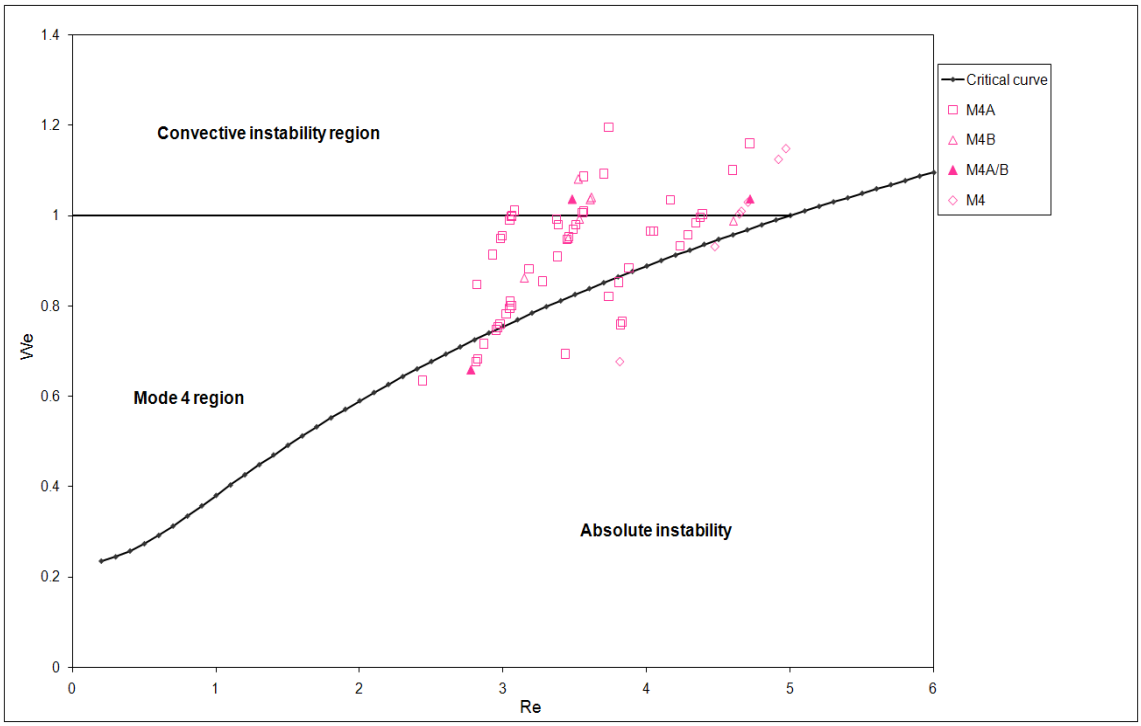

Figure 6.45: Graph showing the experimental data points corresponding to M4A, M4B and M4A/B from Figures 6.15-6.42.

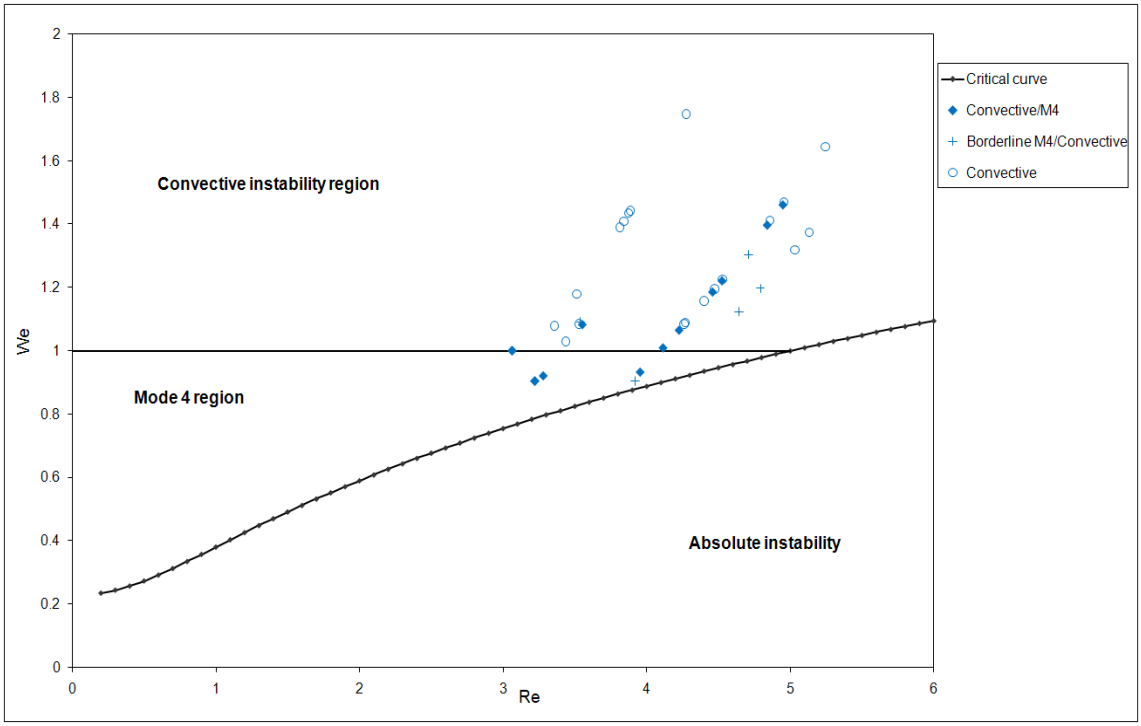

Figure 6.46: Graph showing the experimental data points corresponding to the Convective/M4, Borderline M4/Convective and convective break-up modes from Figures 6.15-6.42.

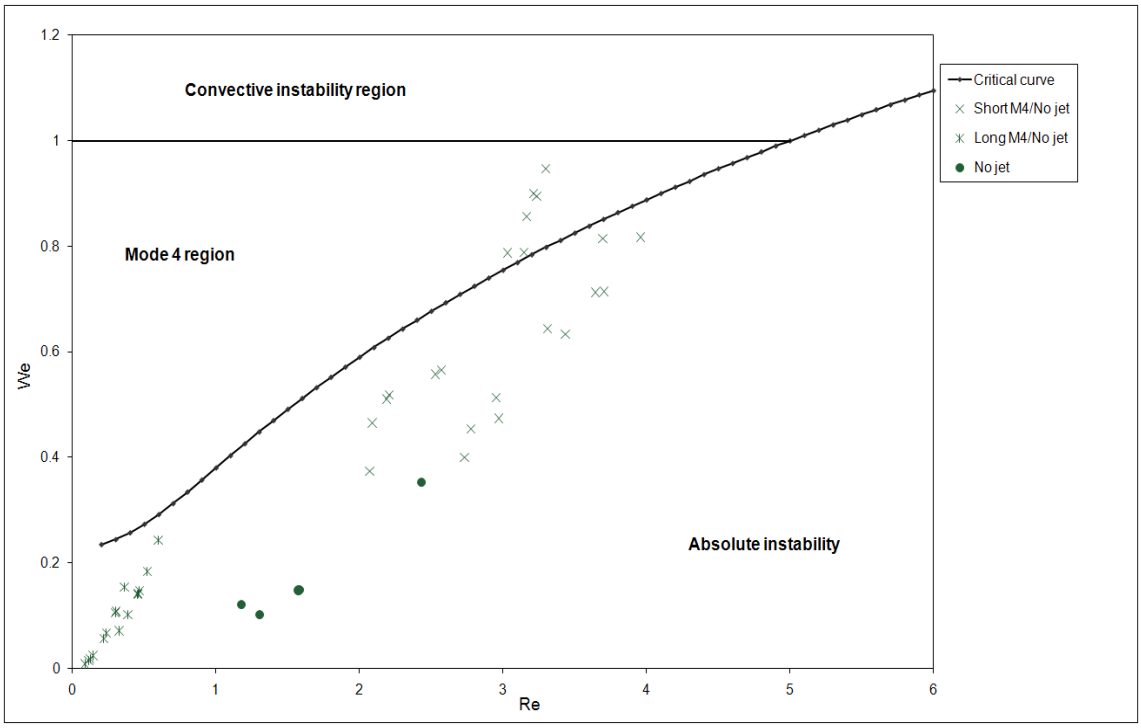

Figure 6.47: Graph showing the experimental data points corresponding to the Short M4/No Jet, Long M4/No Jet and the No Jet cases from Figures 6.15-6.42.

in experiments and thus very low Weber numbers. Therefore, data points corresponding to Long M4/No Jet type break-up (which have Re lying in the no data area of the Mode 4 region) lie below the critical curve in the absolute instability region.

Our theory predicts three different results - convective, Mode 4 and absolute instability regions; i.e. convectively unstable jets (Modes 1, 2 and 3) which have Re and We values lying above the critical curve in the convective instability region, jets that are initially convectively unstable and become absolutely unstable as they grow have their Re and We values lying above the critical curve in the convective instability region above the critical curve which we have called the Mode 4 area and, finally, the No Jet situation where the flow is absolutely unstable at the orifice and thus the fluid fails to take the shape of a coherent jet, have Re and We values lying below the critical curve in the absolute instability region. Along with these three scenarios, we have also detected the presence of interesting borderline break-up modes which exhibit some form of absolute instability in their dynamics. It was not the aim of our experimental study to capture these break-up

modes as they fall beyond the scope of our theoretical model. In order to examine them further, a more complicated model describing curved jets is required. Our experimental comparison confirms the hypothesis we formulated in Chapter 4

6.3 Conclusion

In Section 6.1, we compared the experimental results in [70] to our theoretical results and obtained good agreement between the two. The Re_{local}-We_{local} trajectories starting at values of We and Re corresponding to Mode 4 in experiments, start above the critical curve in the convective instability region and cross the critical boundary between convective and absolute instability, into the absolute instability region (jets corresponding to this case are shown in Figures 3.9 and 3.10); while trajectories with experimental We and Re values lying below the critical curve in the absolute instability region represent the No Jet situation (here jets appear as in Figure 3.11). We have also compared experimental data points for Modes 1, 2 and 3. In this case the Re_{local}-We_{local} trajectory has the initial experimental Re and We values lying above the critical curve in the convective instability region and as s increases we find that the trajectory remains above the critical curve. Hence jets in this case correspond to the photographs in Figures 3.3-3.8. This confirms the hypothesis we formulated in Chapter 4.

We have extended the work of Wong *et al.* [70] with an increased focus on the Mode 4 region. In Section 6.2.2 we describe the break-up modes discovered, along with the standard Mode 4, which are mainly slight variations of Mode 4 or borderline cases where jets experience absolute instability leading up to their break-up. Very good agreement is found between experiments and theory with 74% of the Re and We data points for Mode 4 and its variations lying in the M4 region while 78% of those corresponding to the convective modes (Modes 1, 2 and 3) lie in the convective instability region above the critical curve and the M4 region and 83% of the Re and We data points corresponding to the No Jet, Short M4/No Jet and Long M4/No Jet cases, where absolute instability plays a stronger role in the break-up dynamics, lie below the critical curve in the absolute

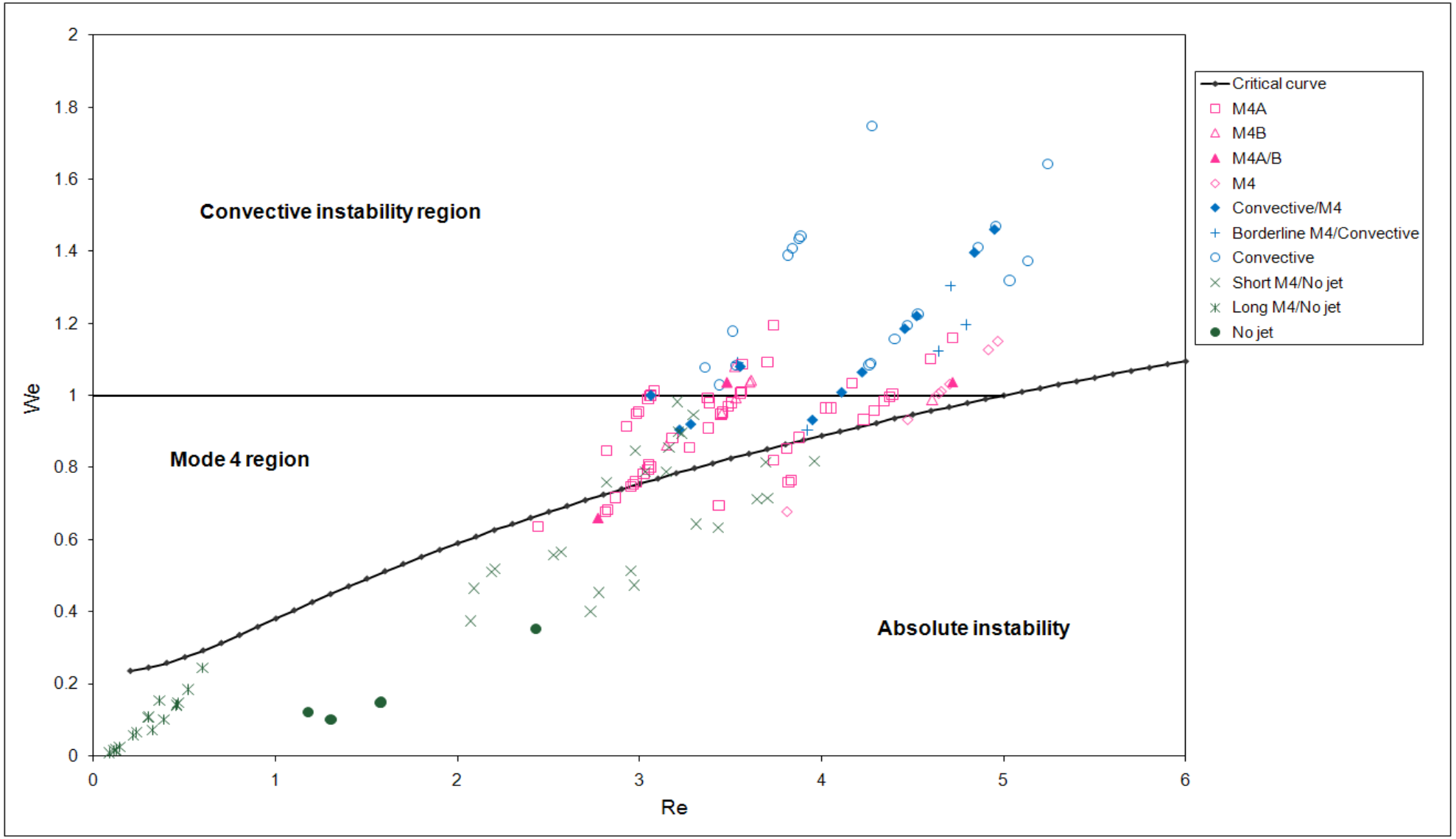

Figure 6.48: Graph showing experimental data points from Figures 6.15-6.42 plotted in the Re-We plane.

instability region. Overall, 77% of the experimental Re and We values lie correctly in the respective regions in Figure 6.48, implying very good agreement with theory.

Chapter 7

Absolute Instability in Ligaments

So far, we have considered a model based on linear theory. It assumes that the size of droplets formed as a result of jet break-up is almost equal to the wavelength of the disturbance that causes it. It is possible to calculate the trajectory of the centreline of the jet and its stability accurately through linear theory, however it fails to predict the formation of satellite drops. In this chapter, we extend the nonlinear model derived by Parau *et al.* [51] to study absolute instability in ligaments that are formed as the jet approaches break-up.

Figures 7.1, 7.2 and 7.3 show a series of photographs, captured using a high speed Photron Fastcam SA3 digital camera, which depict the evolution of a jet and the propagation of disturbances on its surface, eventually leading to its break-up. Figure 7.4 gives a calibration image which provides reference length scales for Figures 7.1, 7.2 and 7.3. As the jet breaks up (see Figures 7.1(c) and 7.1(d)), we observe the formation of thin ligaments between the main primary drops. These ligaments then break-up to form satellite drops. Some of the satellite drops are observed to merge with each other to form secondary intermediate drops. The size of these secondary drops is quite random, as they can either be produced through the merging of two small satellite drops to form an intermediate drop which is bigger than the satellite drop but smaller than the main drop, or by the coalescence of a satellite and a primary drop to form a drop which is bigger in size than the main primary drop. Thus, as pinch-off is approached, the big main primary drops on

either side of the ligament are produced from the convectively unstable waves travelling downstream along the jet while the smaller satellite drops seem to come to existence as a result of a local absolute instability that occurs near break-up.

To study these ligaments and the effect of absolute instability on them, we start by describing the model and reviewing previous work on curved liquid jets using the nonlinear model. We then use our multiple scales approach and compute Re_{local} and We_{local}, allowing us to examine absolute instability in ligaments.

7.1 Review of Viscous Nonlinear Model

In this section we describe the one-dimensional model for a non-linear disturbance on a curved jet. Parau *et al.* [51] considered a slender jet with small ϵ and derived the model using a long length-scale over which the jet curves and a short length scale which represents the wavelength of the perturbations on the surface of the jet which cause break-up.

Here we present the problem considered by Parau *et al.* [52] and the full set of viscous equations derived in Wallwork *et al.* [68]. The equations are non-dimensionalised using the scalings (3.16). The continuity equation after non-dimensionalisation is given by

$$\epsilon n\frac{\partial u}{\partial s} + (1+\epsilon n\cos\phi(X_sZ_{ss}-X_{ss}Z_s))\left(v+n\frac{\partial v}{\partial n}+\frac{\partial w}{\partial \phi}\right)+\epsilon n(X_sZ_{ss}-X_{ss}Z_s)(v\cos\phi - w\sin\phi)=0. \tag{7.1}$$

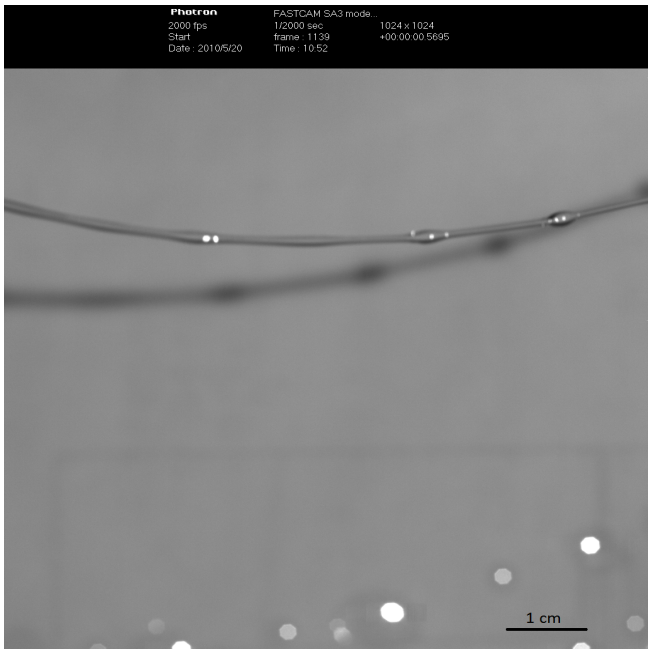

(a) Image captured 0.5695s after the camera started recording.

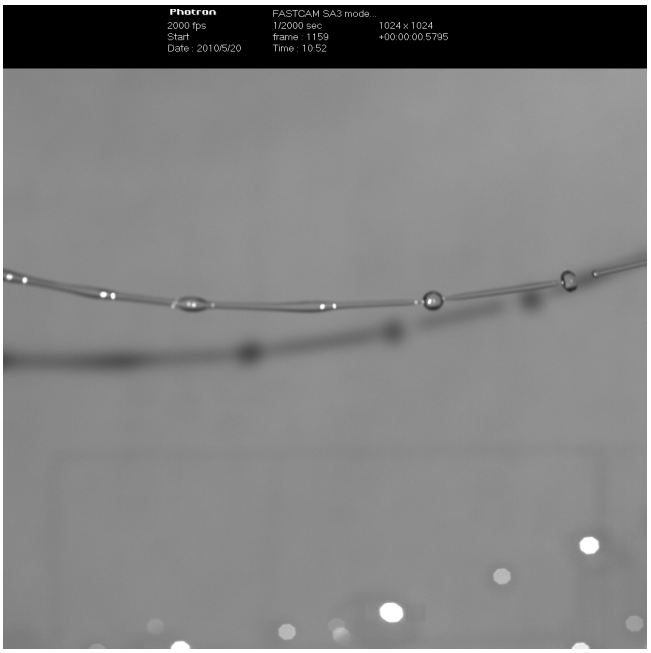

(b) Image captured 0.5795s after the camera started recording.

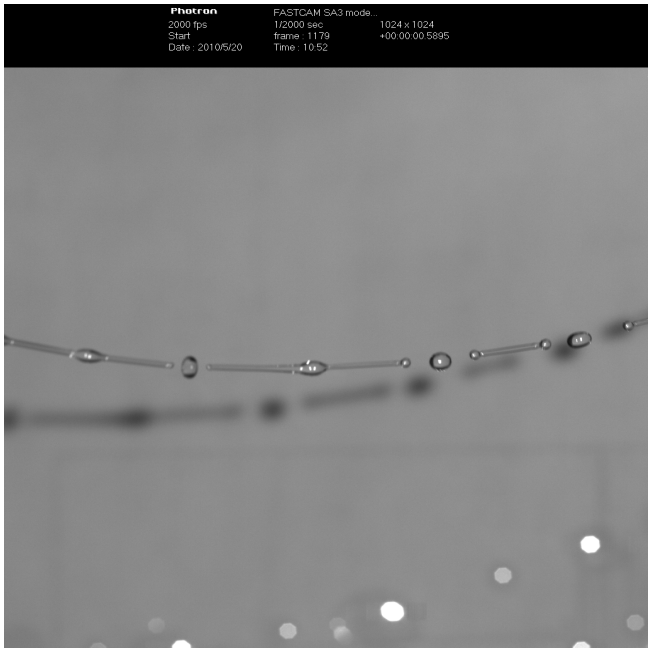

(c) Image captured 0.5895s after the camera started recording.

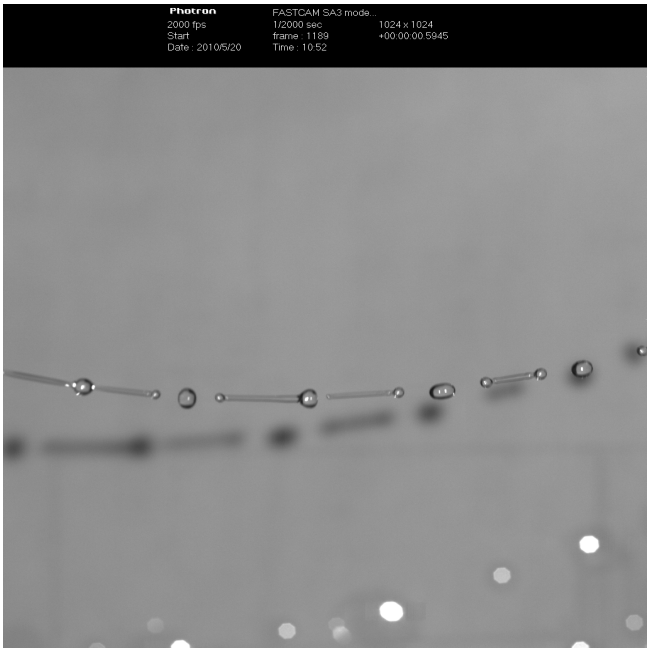

(d) Image captured 0.5945s after the camera started recording.

Figure 7.1: Series of photographs showing a jet of a fluid having viscosity=0.04873Pas, surface tension=0.0645Nm^{-1} and density=1235.018kgm^{-3} emerging from a container rotating at a speed of 250rpm through an orifice of radius 3mm.

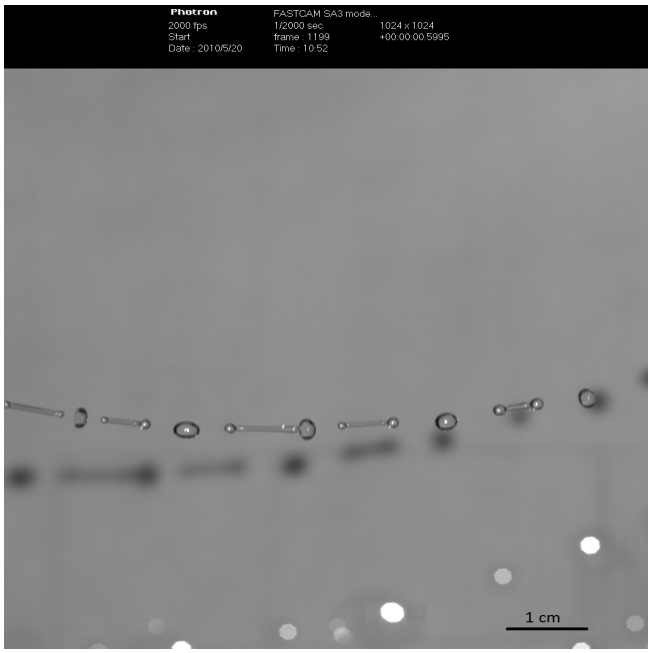

(a) Image captured 0.5995s after the camera started recording.

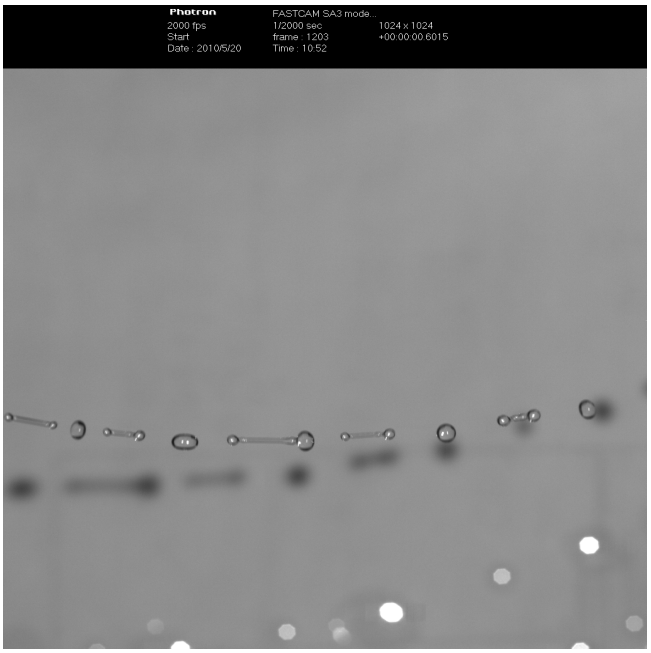

(b) Image captured 0.6015s after the camera started recording.

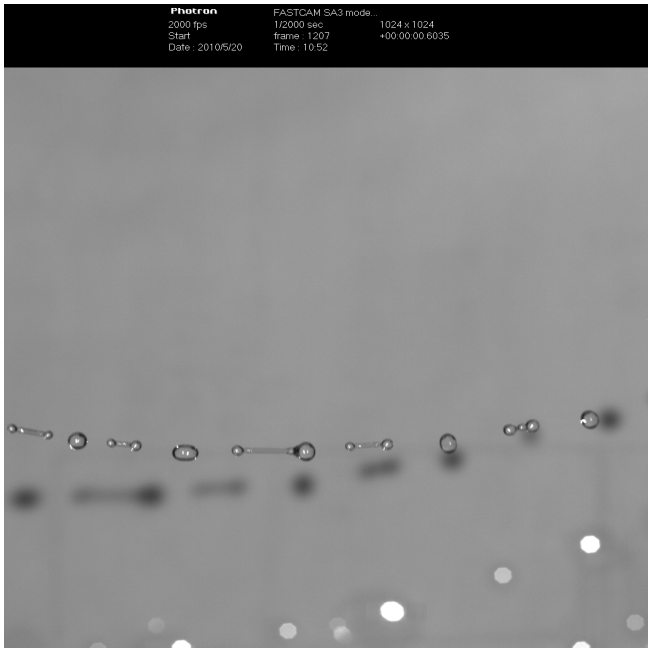

(c) Image captured 0.6035s after the camera started recording.

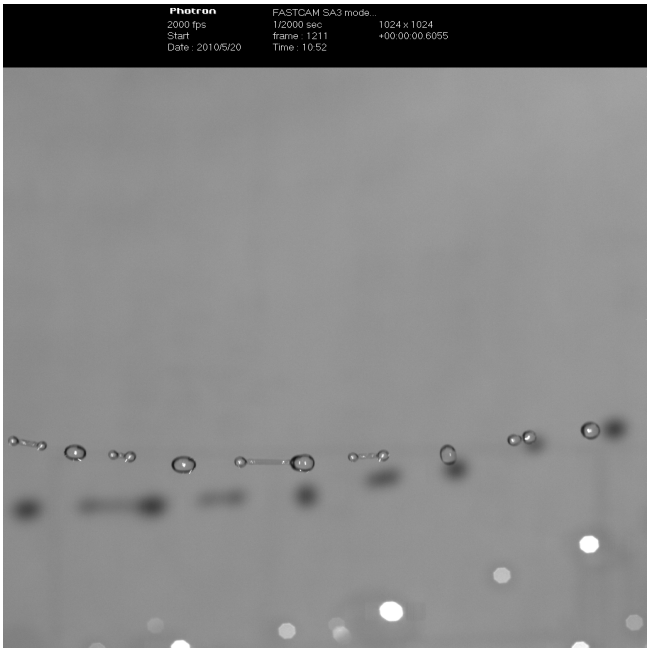

(d) Image captured 0.6055s after the camera started recording.

Figure 7.2: Series of photographs showing the same jet as in Figure 7.1 having viscosity=0.04873Pas, surface tension=0.0645Nm^{-1} and density=1235.018kgm^{-3} emerging from a container rotating at a speed of 250rpm through an orifice of radius 3mm.

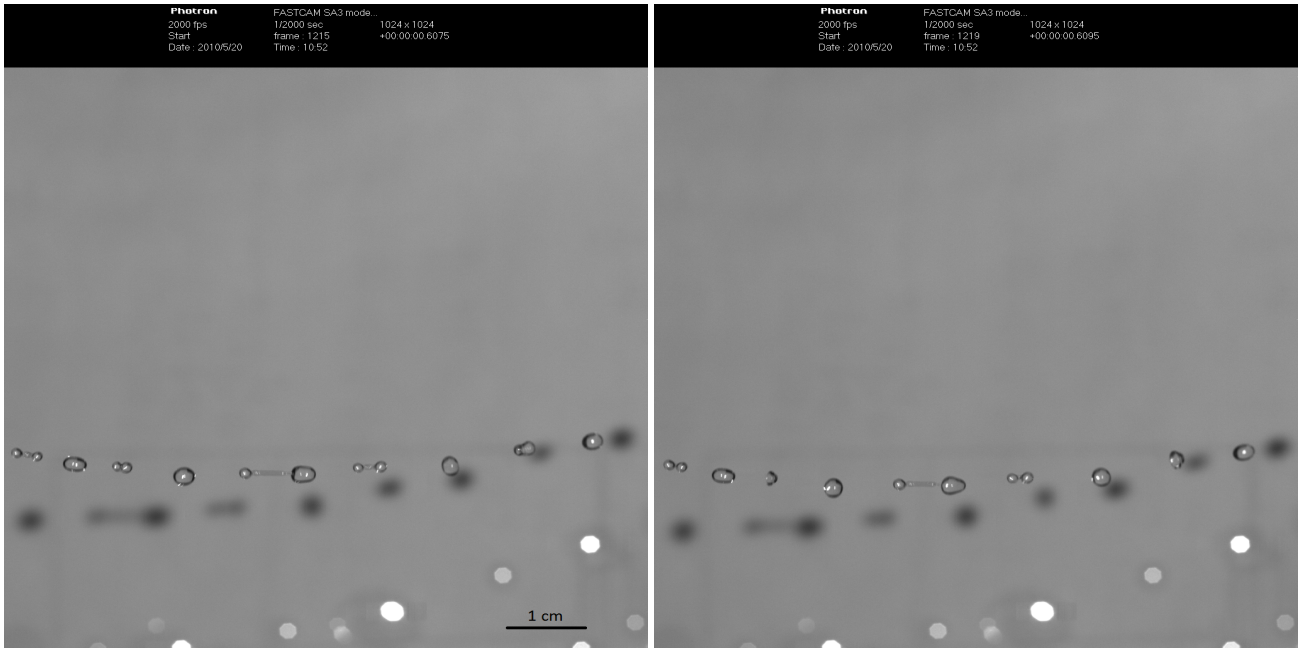

(a) Image captured 0.6075s after the camera started recording.

(b) Image captured 0.6095s after the camera started recording.

Figure 7.3: Series of photographs showing the same jet as in Figure 7.1 having viscosity=0.04873Pas, surface tension=0.064Nm^{-1} and density=1235.018kgm^{-3} emerging from a container rotating at a speed of 250rpm through an orifice of radius 3mm.

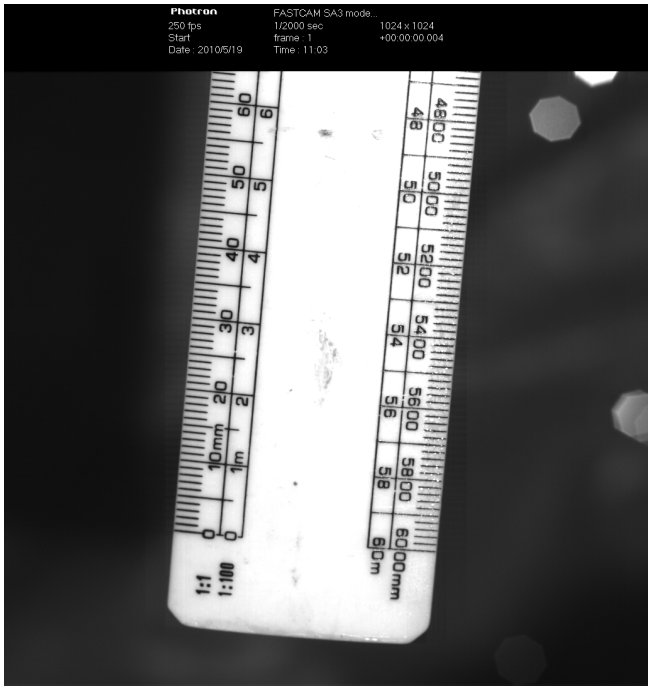

Figure 7.4: Calibration image giving reference length scales for Figures 7.1, 7.2 and 7.3.

The Navier-Stokes equations are given by

$$
\begin{aligned}
&h_s\left(\epsilon\frac{\partial u}{\partial t}+\epsilon(v\cos\phi-w\sin\phi)(Z_{st}X_s-X_{st}Z_s)+v\frac{\partial u}{\partial n}+\frac{w}{n}\frac{\partial u}{\partial\phi}\right)+\epsilon u\frac{\partial u}{\partial s}\\
&+\epsilon u(X_sZ_{ss}-X_{ss}Z_s)(v\cos\phi-w\sin\phi)=\\
&-\epsilon\frac{\partial p}{\partial s}+h_s\left(\frac{2\epsilon}{Rb}(v\cos\phi-w\sin\phi)+\frac{\epsilon}{Rb^2}((X+1)X_s+ZZ_s)\right)\\
&+\frac{1}{\epsilon Ren}\left[\frac{-\epsilon^3n^2\cos\phi(X_sZ_{sss}-Z_sX_{sss})}{h_s^2}\left(\frac{\partial u}{\partial s}+v\cos\phi(X_sZ_{ss}-Z_sX_{ss})\right.\right.\\
&-w\sin\phi(X_sZ_{ss}-Z_sX_{ss}))\,\frac{\epsilon^2n}{h_s}\left(-u(X_sZ_{ss}-Z_sX_{ss})^2+\frac{\partial^2u}{\partial s^2}\right.\\
&+2\frac{\partial v}{\partial s}\cos\phi(X_sZ_{ss}-Z_sX_{ss})+(v\cos\phi-w\sin\phi)(X_sZ_{sss}-Z_sX_{sss})\\
&\left.\left.-2\frac{\partial w}{\partial s}\sin\phi(X_sZ_{ss}-X_{ss}Z_s)\right)+(1+2\epsilon n\cos\phi(X_sZ_{ss}-X_{ss}Z_s))\frac{\partial u}{\partial n}+nh_s\frac{\partial^2u}{\partial n^2}\right.\\
&\left.-\epsilon\frac{\partial u}{\partial\phi}\sin\phi(X_sZ_{ss}-Z_sX_{ss})+\frac{h_s}{n}\frac{\partial^2u}{\partial\phi^2}\right],
\end{aligned}
\tag{7.2}
$$

$$
\begin{aligned}
&h_s\left(\epsilon\frac{\partial v}{\partial t}+\epsilon u\cos\phi(X_{st}Z_s-Z_{st}X_s)+v\frac{\partial v}{\partial n}+\frac{w}{n}\frac{\partial v}{\partial\phi}-\frac{w^2}{n}\right)\\
&+\epsilon u\frac{\partial v}{\partial s}-\epsilon\cos\phi(X_sZ_{ss}-Z_sX_{ss})u^2\\
&=\left(-\frac{\partial p}{\partial n}-\frac{2\epsilon}{Rb}u\cos\phi+\frac{h_s\epsilon\cos\phi}{Rb^2}((X+1)Z_s-ZX_s+\epsilon n\cos\phi)\right)+\\
&\frac{1}{\epsilon Ren}\left[\frac{-\epsilon^3n^2\cos\phi(X_sZ_{sss}-Z_sX_{sss})}{h_s^2}\left(\frac{\partial v}{\partial s}-u\cos\phi(X_sZ_{ss}-Z_sX_{ss})\right)\right.\\
&+\frac{\epsilon^2n}{h_s}\left(-v\cos^2\phi(X_sZ_{ss}-Z_sX_{ss})^2+\frac{\partial^2v}{\partial s^2}-2\frac{\partial u}{\partial s}\cos\phi(X_sZ_{ss}-Z_sX_{ss})\right.\\
&\left.-u\cos\phi(X_sZ_{sss}-Z_sX_{sss})+w\sin\phi\cos\phi(X_sZ_{ss}-Z_sX_{ss})^2\right)\\
&+(1+2\epsilon n\cos\phi(X_sZ_{ss}-Z_sX_{ss}))\frac{\partial v}{\partial n}+nh_s\frac{\partial^2v}{\partial n^2}\\
&\left.-\epsilon\left(\frac{\partial v}{\partial\phi}-w\right)\sin\phi(X_sZ_{ss}-Z_sX_{ss})+\frac{h_s}{n}\left(\frac{\partial^2v}{\partial\phi^2}-v-2\frac{\partial w}{\partial\phi}\right)\right]
\end{aligned}
\tag{7.3}
$$

and

$$
\begin{aligned}
&h_s\left(\epsilon\frac{\partial w}{\partial t}+\epsilon u\sin\phi(Z_{st}X_s-X_{st}Z_s)+v\frac{\partial w}{\partial n}+\frac{w}{n}\frac{\partial w}{\partial\phi}+\frac{wv}{n}\right)\\
&\quad+\epsilon u\frac{\partial w}{\partial s}+\epsilon\sin\phi(X_sZ_{ss}-X_{ss}Z_s)u^2\\
&=h_s\left(-\frac{1}{n}\frac{\partial p}{\partial\phi}+\frac{2\epsilon}{Rb}u\sin\phi+\frac{\epsilon\sin\phi}{Rb^2}(ZX_s-(X+1)Z_s-\epsilon n\cos\phi)\right)\\
&\quad+\frac{1}{\epsilon nRe}\left[\frac{-\epsilon^3n^2\cos\phi(X_sZ_{sss}-Z_sX_{sss})}{h_s^2}\left(\frac{\partial w}{\partial s}\right.\right.\\
&\quad\left.+u\sin\phi(X_sZ_{ss}-X_{ss}Z_s)\right)+\frac{\epsilon^2n}{h_s}\left(-w\sin^2\phi(X_sZ_{ss}-X_{ss}Z_s)^2+\frac{\partial^2w}{\partial s^2}\right.\\
&\quad+2\frac{\partial u}{\partial s}\sin\phi(X_sZ_{ss}-X_{ss}Z_s)+u\sin\phi(X_sZ_{sss}-Z_sX_{sss})\\
&\quad\left.+v\sin\phi\cos\phi(X_sZ_{ss}-Z_sX_{ss})^2\right)+(1+2\epsilon n\cos\phi(X_sZ_{ss}-Z_sX_{ss}))\frac{\partial w}{\partial n}\\
&\quad\left.+nh_s\frac{\partial^2w}{\partial n^2}-\epsilon\left(\frac{\partial w}{\partial\phi}+v\right)\sin\phi(X_sZ_{ss}-Z_sX_{ss})+\frac{h_s}{n}\left(\frac{\partial^2w}{\partial\phi^2}-w+2\frac{\partial v}{\partial\phi}\right)\right].
\end{aligned}
\tag{7.4}
$$

The boundary conditions on $n = R(s,\phi,t)$ are non-dimensionalised and the kinematic condition is given by

$$
\begin{aligned}
&h_s\left(\epsilon\frac{\partial R}{\partial t}+\cos\phi(X_tZ_s-X_sZ_t)-v+\frac{w}{n}\frac{\partial R}{\partial\phi}+\frac{1}{n}\frac{\partial R}{\partial\phi}\sin\phi(X_tZ_s-X_sZ_t)\right)\\
&\quad+\epsilon u\frac{\partial R}{\partial s}-\epsilon\frac{\partial R}{\partial s}(X_tZ_s+Z_tX_s+\epsilon n\cos\phi(X_sZ_{st}-X_{st}Z_s))=0.
\end{aligned}
\tag{7.5}
$$

The tangential stress conditions are written as

$$
\begin{aligned}
&\left(1-\frac{\epsilon^2}{h_s^2}\left(\frac{\partial R}{\partial s}\right)^2\right)\left(\epsilon\frac{\partial v}{\partial s}+h_s\frac{\partial u}{\partial n}-\epsilon u\cos\phi(X_sZ_{ss}-X_{ss}Z_s)\right)+2\epsilon\frac{\partial R}{\partial s}\left(\frac{\partial v}{\partial n}\right.\\
&\quad\left.-\frac{\epsilon}{h_s}\frac{\partial u}{\partial s}-\frac{\epsilon(v\cos\phi-w\sin\phi)}{h_s}(X_sZ_{ss}-X_{ss}Z_s)\right)=0,
\end{aligned}
\tag{7.6}
$$

and

$$
\left(1-\frac{1}{n^2}\left(\frac{\partial R}{\partial\phi}\right)^2\right)\left(\frac{\partial w}{\partial n}-\frac{w}{n}+\frac{1}{n}\frac{\partial v}{\partial\phi}\right)+\frac{2}{n}\frac{\partial R}{\partial\phi}\left(\frac{\partial v}{\partial n}-\frac{1}{n}\left(\frac{\partial w}{\partial\phi}+v\right)\right)=0,
\tag{7.7}
$$

and the normal stress condition

$$p - \frac{2}{ReE^2}\left(\frac{\epsilon^2}{h_s^3}\left(\frac{\partial R}{\partial s}\right)^2\left(\frac{\partial u}{\partial s} + (v\cos\phi - w\sin\phi)(X_sZ_{ss} - X_{ss}Z_s)\right)\right.$$
$$+\frac{1}{\epsilon}\frac{\partial v}{\partial n} + \frac{1}{\epsilon n^3}\left(\frac{\partial R}{\partial \phi}\right)^2\left(\frac{\partial w}{\partial \phi} + v\right) - \frac{\epsilon}{h_s}\frac{\partial R}{\partial s}\left(\frac{\partial v}{\partial s} + \frac{1}{\epsilon}\frac{\partial u}{\partial n} - \frac{u}{h_s}\cos\phi(X_sZ_{ss} - X_{ss}Z_s)\right)$$
$$-\frac{1}{\epsilon n}\frac{\partial R}{\partial \phi}\left(\frac{\partial w}{\partial n} - \frac{w}{n} + \frac{1}{n}\frac{\partial v}{\partial \phi}\right) + \frac{\epsilon}{h_s n}\frac{\partial R}{\partial s}\frac{\partial R}{\partial \phi}\left(\frac{1}{\epsilon n}\frac{\partial u}{\partial \phi} + \frac{u}{h_s}\sin\phi(X_sZ_{ss} - X_{ss}Z_s)\right.$$
$$\left.\left.+\frac{1}{h_s}\frac{\partial u}{\partial s}\right)\right) = \frac{\kappa}{We}, \tag{7.8}$$

where

$$\kappa = \frac{1}{h_s}\left(\epsilon^2\frac{\partial}{\partial s}\left(-\frac{1}{h_sE}\frac{\partial R}{\partial s}\right) + \frac{1}{n}\frac{\partial}{\partial n}\left(\frac{nh_s}{E}\right) + \frac{\partial}{\partial \phi}\left(-\frac{h_s}{n^2E}\frac{\partial R}{\partial \phi}\right)\right),$$

$$h_s = (1 + \epsilon n\cos\phi(X_sZ_{ss} - X_{ss}Z_s)),$$

and

$$E = \left(1 + \frac{\epsilon^2}{h_s^2}\left(\frac{\partial R}{\partial s}\right)^2 + \frac{1}{n^2}\left(\frac{\partial R}{\partial \phi}\right)^2\right)^{1/2}.$$

We also have the arc length condition given by

$$X_s^2 + Z_s^2 = 1, \tag{7.9}$$

and centreline conditions

$$v = w = 0 \ \text{ on } \ n = 0.$$

7.1.1 Asymptotic Form of Nonlinear Unsteady Equations

We introduce the following expansions where we perturb our variables by a small parameter δ, assuming that $0 < \delta << \epsilon << 1$

$$\left.\begin{aligned} u &= \hat{u}(s,t,n,\phi,\epsilon) + \delta\tilde{u}(s,\bar{s},n,\phi,t,\bar{t}),\\ v &= \hat{v}(s,t,n,\phi,\epsilon) + \delta\tilde{v}(s,\bar{s},n,\phi,t,\bar{t}),\\ w &= \hat{w}(s,t,n,\phi,\epsilon) + \delta\tilde{w}(s,\bar{s},n,\phi,t,\bar{t}),\\ p &= \hat{p}(s,t,n,\phi,\epsilon) + \delta\tilde{p}(s,\bar{s},n,\phi,t,\bar{t}),\\ R &= \hat{R}(s,t,\phi,\epsilon) + \delta\tilde{R}(s,\bar{s},\phi,t,\bar{t}),\\ X &= \hat{X}(s,t,\epsilon) + \delta\epsilon\tilde{X}(s,\bar{s},t,\bar{t}),\\ Z &= \hat{Z}(s,t,\epsilon) + \delta\epsilon\tilde{Z}(s,\bar{s},t,\bar{t}). \end{aligned}\right\} \tag{7.10}$$

The hat variables denote solution to the leading order nonlinear equations and those with a tilde describe the unsteady linear disturbances. Like in Chapter 4, a multiple scales approach is used and new length and time scales $\bar{s}$ and $\bar{t}$ (where $\bar{s} = s/\epsilon$ and $\bar{t} = t/\epsilon$, respectively) to describe short wave disturbances of order ϵ are defined.

We now assume a slender jet and substitute $O(1)$ equations in δ and introduce the following expansions into the governing equations and boundary conditions

$$\hat{u} = u_0(s,t) + (\epsilon n)u_1(s,\phi,t) + (\epsilon n)^2 u_2(s,\phi,t) + \dots$$

$$\hat{v} = (\epsilon n)v_1(s,\phi,t) + (\epsilon n)^2 v_2(s,\phi,t) + \dots$$

$$\hat{w} = (\epsilon n)w_1(s,\phi,t) + (\epsilon n)^2 w_2(s,\phi,t) + \dots$$

$$\hat{p} = p_0(s,\phi,t) + (\epsilon n)p_1(s,\phi,t) + (\epsilon n)^2 u_2(s,\phi,t) + \dots$$

$$\hat{R} = R_0(s,t) + \epsilon R_1(s,\phi,t) + \dots$$

$$\hat{X} = X_0(s) + \epsilon X_1(s,t) + \dots$$

$$\hat{Z} = Z_0(s) + \epsilon Z_1(s,t) + \dots.$$

The radius of the jet R and the axial component of velocity u are taken to be independent of ϕ at leading order and we assume the position of the centreline remains unaffected by small perturbations and is independent of time at leading order. For simplicity, X_0 and Z_0 are replaced with X and Z, respectively, and $S = X_s Z_{ss} - Z_s X_{ss}$. Applying these expansions to the continuity equation (7.1) produces

$$O(\epsilon n) : u_{0s} + 2v_1 + w_{1\phi} = 0, \tag{7.11}$$

and

$$O\left((\epsilon n)^2\right) : u_{1s} + 3v_2 + w_{2\phi} + (3v_1 + w_{1\phi})S\cos\phi - w_1 S\sin\phi = 0. \tag{7.12}$$

Substituting these expansions into the first Navier-Stokes equation (7.2) produces the following equation at

$$\begin{aligned} O(\epsilon n) : u_{0t} + u_0 u_{0s} = -p_{0s} + \frac{1}{Rb^2}((X+1)X_s + ZZ_s) \\ + \frac{1}{Re}\bigg(- u_0 S^2 + u_{0ss} 4u_2 + u_{2\phi\phi} + (2u_1 + u_{1\phi\phi})S\cos\phi - u_{1\phi} S\sin\phi\bigg). \end{aligned} \tag{7.13}$$

The second Navier-Stokes equation (7.3) gives

$$\begin{aligned} O(\epsilon) : -u_0^2 S\cos\phi = -p_1 - \frac{2}{Rb}u_0\cos\phi + \frac{\cos\phi}{Rb^2}((X+1)Z_s + ZX_s) \\ + \frac{1}{Re}\bigg(3v_2 + v_{2\phi\phi} - 2w_{2\phi}((-2u_{0s} + v_1 + v_{1\phi\phi} - 2w_{1\phi})S - u_0 S_S)\cos\phi \\ -(w_1 - v_{1\phi})S\sin\phi\bigg), \end{aligned} \tag{7.14}$$

and the third Navier-Stokes equation produces

$$O(1) : p_{0\phi} = 0, \tag{7.15}$$

and

$$O(\epsilon) : u_0^2 S \sin\phi = -p_{1\phi} + \frac{2}{Rb} u_0 \sin\phi - \frac{\sin\phi}{Rb^2}((X+1)Z_s + ZX_s) + \frac{1}{Re}\Big(3w_2 + w_{2\phi\phi} + 2v_{2\phi}(w_1 + w_{1\phi\phi} + 2v_{1\phi})S\cos\phi + ((2u_{0s} + v_1 - w_{1\phi\phi})S + u_0 S_S)\sin\phi\Big). \tag{7.16}$$

The kinematic condition gives

$$O(\epsilon) : R_{0t} - R_0 v_1 + u_0 R_{0s} = 0. \tag{7.17}$$

The first tangential stress condition produces

$$O(\epsilon) : u_1 = u_0 S\cos\phi, \tag{7.18}$$

and

$$O\left(\epsilon^2\right) : R_0 v_{1s} + 2R_0 u_2 + R_{0s}(v_1 - u_{0s}) = 0, \tag{7.19}$$

and the second tangential stress condition gives

$$O(\epsilon) : v_{1\phi} = 0, \tag{7.20}$$

and

$$O\left(\epsilon^2\right) : R_0 w_2 + R_0 v_{2\phi} + \frac{2}{R_0} R_{1\phi} w_{1\phi} = 0. \tag{7.21}$$

The normal stress condition

$$O(1) : p_0 - \frac{2}{Re} v_1 = \frac{1}{We R_0}, \tag{7.22}$$

and

$$\begin{aligned} O(\epsilon) : R_0 p_1 &- \frac{2}{Re}\left(2R_0 v_2 - \frac{1}{R_0}R_{1\phi}v_{1\phi} - R_{0s}(u_1 - u_0 S\cos\phi)\right) \\ &= \frac{1}{We}\left(S\cos\phi - \frac{R_1 + R_{1\phi\phi}}{R_0^2}\right). \end{aligned} \tag{7.23}$$

The arc length condition at leading order is given by

$$X_s^2 + Z_s^2 = 1. \tag{7.24}$$

After some algebraic manipulation we have

$$u_0^2(X_s Z_{ss} - X_{ss}Z_s) - \frac{2}{Rb}u_0 + \frac{(X+1)Z_s - ZX_s}{Rb^2} - \frac{3}{Re}u_{0s}(X_s Z_{ss} - X_{ss}Z_s) - \frac{(X_s Z_{ss} - X_{ss}Z_s)}{WeR_0} = 0, \tag{7.25}$$

$$R_{0t} + \frac{u_{0s}}{2}R_0 + u_0 R_{0s} = 0, \tag{7.26}$$

$$u_{0t} + u_0 u_{0s} = -\frac{1}{We}\left(\frac{1}{R_0}\right)_s + \frac{(X+1)X + ZZ_s}{Rb^2} + \frac{3}{Re}\frac{(R_0^2 u_{0s})_s}{R_0^2}, \tag{7.27}$$

$$X_s^2 + Z_s^2 = 1. \tag{7.28}$$

These equations can be solved to determine the steady state solutions by considering all the variables to be functions of s only. The equations in the steady case are given by

$$(X_s Z_{ss} - X_{ss}Z_s)\left(u_0^2 - \frac{3}{Re}u_{0s} - \frac{\sqrt{u_0}}{We}\right) - \frac{2}{Rb}u_0 + \frac{(X+1)Z_s + ZX_s}{Rb^2} = 0 \tag{7.29}$$

$$u_0 u_{0s} = -\frac{1}{We}\frac{u_{0s}}{2\sqrt{u_0}} + \frac{(X+1)X + ZZ_s}{Rb^2} + \frac{3}{Re}\left(u_{0ss} - \frac{u_{0s}^2}{u_0}\right) \tag{7.30}$$

$$X_s^2 + Z_s^2 = 1 \tag{7.31}$$

where $u_0 R_0^2 = 1$ (from the steady version of (7.26)). The boundary conditions at the nozzle at $s = 0$ are $X(0) = Z(0) = Z_s(0) = 0, u_0(0) = R_0(0) = X_s(0) = 1$. The solution

to this system of ODEs serves as the initial condition at $t = 0$. To solve these equations Parau *et al.* developed a scheme which uses a second-order centred finite difference discretization of the equations. The nonlinear equations are solved for X_s, Z_s and u_0 using Newton's method and X and Z are then determined using trapezoidal-rule integration. Quadratic extrapolation of the last internal mesh points is used to determine the downstream boundary conditions.

Parau *et al.* [52] also examined the nonlinear temporal solutions of equations (7.26) and (7.27) by modifying the leading order pressure term arising in the normal stress condition (i.e. $p_0 = 1/(WeR_0)$) to include the full expression for curvature given by

$$p_0 = \frac{1}{We}\left[\frac{1}{R_0(1+\epsilon^2 R_{0_s}^2)^{1/2}} - \frac{\epsilon^2 R_{0_{ss}}}{(1+\epsilon^2 R_{0_s}^2)^{3/2}}\right]. \tag{7.32}$$

If $A = R_0^2$ and $u = u_0$, then (7.26) and (7.27) can be written as

$$A_t + (Au)_s = 0 \tag{7.33}$$

$$u_t + \left(\frac{u^2}{2}\right)_s = -\frac{1}{We}\frac{\partial}{\partial s}\left(\frac{4(2A + (\epsilon A_s)^2 - \epsilon^2 A A_{ss})}{(4A + (\epsilon A_s)^2)^{3/2}}\right) + \frac{(X+1)X_s + ZZ_s}{Rb^2} + \frac{3}{Re}\frac{(Au_s)_s}{A}. \tag{7.34}$$

These equations are solved numerically for $s \in [0, l]$ where l is the numerical length of the jet. A finite difference method is used to solve equations (7.33)-(7.34) by defining a uniform and fixed spatial grid with M equally spaced points with $s_0 = 0$ at the nozzle. Also, $s_i = s_0 + ids$, where $i = 1, ...M$ and ds is the spatial grid interval. The time integration method used is an explicit scheme based on the two stage Lax-Wendroff method. The solution to the steady state equations (7.29)-(7.31) serve as initial conditions at $t = 0$

$$A(s, 0) = R_0^2(s) \quad \text{and} \quad u(s, 0) = u_0(s). \tag{7.35}$$

Similarly, X and Z in (7.34) are also obtained from the solution to (7.29)-(7.31). The

upstream boundary conditions imposed at the nozzle are

$$A(0,t) = 1 \quad \text{and} \quad u(0,t) = 1 + \delta \sin(Kt/\epsilon) \tag{7.36}$$

where δ and K are the amplitude and frequency of the disturbance. We now describe the Lax-Wendroff scheme.

7.1.2 Lax-Wendroff Scheme

The Lax-Wendroff scheme is used to solve equations of the form

$$\frac{\partial \mathbf{u}}{\partial t} = -\frac{\partial \mathbf{F}(\mathbf{u})}{\partial s} \tag{7.37}$$

where $\mathbf{u} = (A, u)^T$ and $\mathbf{F}(\mathbf{u}) = \left(Au, \frac{u^2}{2}\right)^T$. The time derivative is denoted by

$$\frac{\partial \mathbf{u}}{\partial t} = \frac{\mathbf{u}_j^{n+1} - \mathbf{u}_j^n}{dt} + \dots \tag{7.38}$$

and the space derivatives can be written as

$$\frac{\partial \mathbf{F}}{\partial s} = \frac{\mathbf{F}_{j+1}^n - \mathbf{F}_{j-1}^n}{2ds} + \dots \tag{7.39}$$

where $\mathbf{u}_j^n = \mathbf{u}(s_0 + jds, t_0 + ndt)$, $\mathbf{F}_j^n = \mathbf{F}(s_0 + jds, t_0 + ndt)$, s_0 and t_0 are the initial s and t values and ds and dt are the space and time intervals, respectively. The resulting finite approximation is given by

$$\frac{\mathbf{u}_j^{n+1} - \mathbf{u}_j^n}{dt} = \frac{\mathbf{F}_{j+1}^n - \mathbf{F}_{j-1}^n}{2ds} \tag{7.40}$$

The above system can be unstable, so the following approximation is used

$$\mathbf{u}_j^n \to \frac{1}{2}\left(\mathbf{u}_{j+1}^n + \mathbf{u}_{j-1}^n\right). \tag{7.41}$$

The finite difference approximation then becomes

$$\mathbf{u}_j^{n+1} = \frac{1}{2}(\mathbf{u}_{j+1}^n + \mathbf{u}_{j-1}^n) + \frac{dt}{2ds}(\mathbf{F}_{j+1}^n - \mathbf{F}_{j-1}^n). \tag{7.42}$$

We now define intermediate points at half time steps $t_{n+1/2}$ and half mesh points $s_{i+1/2}$ to produce two steps of the Lax-Wendroff method as

$$\mathbf{u}_{j+1/2}^{n+1/2} = \frac{1}{2}(\mathbf{u}_{j+1}^n + \mathbf{u}_j^n) - \frac{dt}{2ds}(\mathbf{F}_{j+1}^n - \mathbf{F}_j^n) \tag{7.43}$$

$$\mathbf{u}_j^{n+1} = u_j^n - \frac{dt}{ds}(\mathbf{F}_{j+1/2}^{n+1/2} - \mathbf{F}_{j-1/2}^{n+1/2}). \tag{7.44}$$

$\mathbf{F}_{j+1/2}^{n+1/2}$ are computed from the values of $\mathbf{u}_{j+1/2}^{n+1/2}$. This system is solved for all points on the jet and break-up is chosen to occur when the radius of the jet becomes less than an arbitrarily chosen small value (usually 5% of the initial radius). Figure 7.5 shows the profile of a jet having $We = 90, Re = 94.868, Rb = 2, \delta = 0.01$ and $K = 0.642258$ computed by solving equations (7.29)-(7.31) along with (7.33) and (7.34). Figure 7.6 shows the graph of R_0 plotted against s. The point where the jet breaks up is marked on both the graphs.

7.2 Absolute Instability in Ligaments

We now look at absolute instability in ligaments formed as break-up is approached. Our methodology involves calculating the local Reynolds and local Weber numbers given by

$$Re_{local}(s,t) = Re\ u_0(s,t)R_0(s,t), \tag{7.45}$$

$$We_{local}(s,t) = We\ u_0(s,t)^2 R_0(s,t).$$

The nonlinear unsteady viscous dispersion relation, calculated in Gurney [26], is found to be identical to the linear viscous dispersion relation derived by Wallwork [68], but with $R_0(s)$ and $u_0(s)$ now replaced with $R_0(s,t)$ and $u_0(s,t)$, respectively. Thus, the critical curve in the Re-We plane remains the same as in Figure 2.7. To calculate Re_{local} and

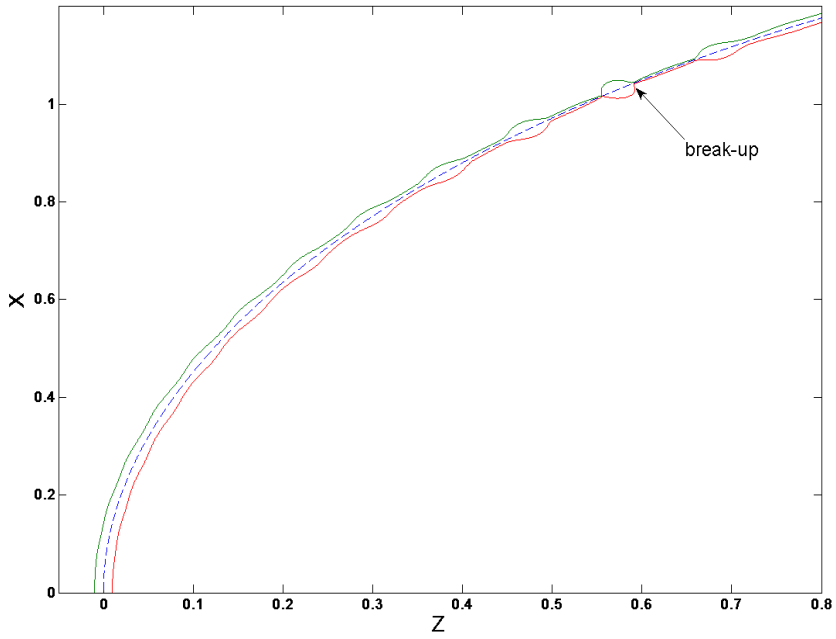

Figure 7.5: Graph showing the profile of a jet having $We = 90, Re = 94.868, Rb = 2, \delta = 0.01$ and $K = 0.642258$.

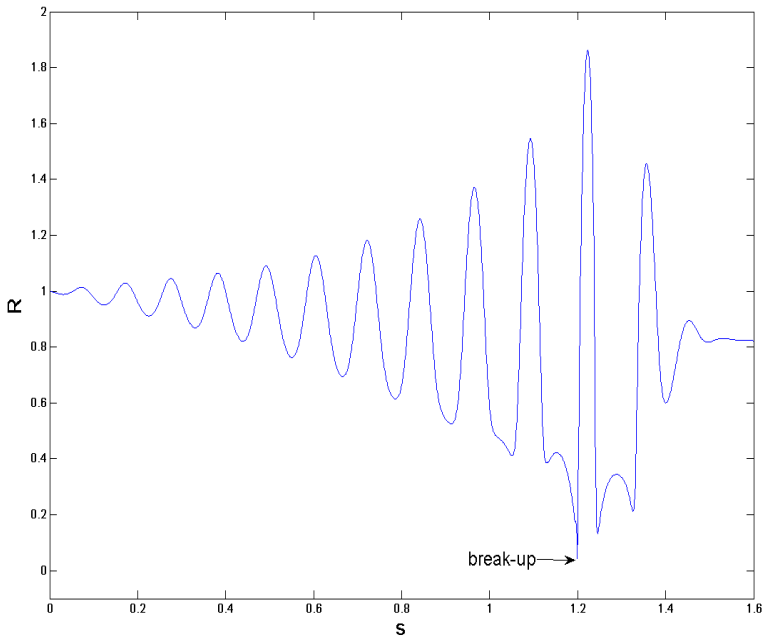

Figure 7.6: Graph showing the plot of R_0 against s for the jet in Figure 7.5.

We_{local} numerically, values for $u_0(s,t)$ and $R_0(s,t)$ are fed into the above expressions by solving the nonlinear equations (7.33) and (7.34) numerically. These Re_{local} and We_{local} values are then plotted in the *Re*-We plane along with the critical curve and their position is analysed with respect to the critical curve.

Figure 7.7 shows three different profiles of a jet having $We = 5$, $Rb = 2$, $Re = 223.607$, $\delta = 0.01$ and $K = 0.699724035$ as it evolves with time; Jet 1(i) is at $t = 0.28$, Jet 1(ii) at $t = 0.3$ and Jet 1(iii) is at $t = 0.346$ when the numerical simulation has ceased and jet break-up (according to convective theory) is assumed to have occurred. As time progresses, droplet formation becomes more clear. Ligaments can also be seen to form on either side of the droplet as the jet thins. We mark Sections 1, 2 and 3 (indicated by dash-dots, dots and dashes, respectively) on the surface of the jet in Figure 7.7; Section 1 lies between α_1 and α_2, Section 2 between β_1 and β_2 and Section 3 between γ_1 and γ_2. Note that we do not consider Section 3 in Jet (iii) as it would appear along the segment of the jet beyond the point of break-up after which the solution becomes invalid. The R_0 and u_0 values for each section, obtained through the numerical solution of (7.33) and (7.34) and illustrated in Figures 7.8 and 7.9, are used to calculate the $Re_{local}(s,t)$ and $We_{local}(s,t)$ for Jets (i)-(iii). By plotting Re_{local} and We_{local} for Jets (i)-(iii) in the *Re*-We plane and examining their position with respect to the critical curve, the onset of absolute instability at different times can be examined.

Figure 7.10 shows the Re_{local} and We_{local} data points representing Sections 1, 2 and 3 for Jet 1(i) in Figure 7.7 which are calculated from Figures 7.8 and 7.9. The path from α_1 to α_2 in the *Re*-We plane in Figure 7.10 represents data points taken along Section 1. Similarly β_1 and β_2 for Section 2 and γ_1 and γ_2 for Section 3. From Figure 7.10 we observe that Re_{local} and We_{local} values representing all three sections lie above the critical curve in the convective instability region, indicating that the jet is convectively unstable at $t = 0.28$.

Figures 7.11, 7.12 and 7.13 show results for Jet 1(ii). In this case we see that the Re_{local} and We_{local} data points corresponding to Section 2 cross the critical curve, demonstrating

the existence of absolute instability as the jet heads towards break-up at $t = 0.3$.

Figures 7.14, 7.15 and 7.16 show results for Jet 1(iii). In Figure 7.16, the Re_{local} and We_{local} values of Section 2 (which represent the ligament formed in Jet 1(iii)) lie below the critical curve in the absolute instability region, thus making it evident that the jet is absolutely unstable at break-up. Note that we have negative velocity in Section 2 in Figure 7.15 close to break-up. This corresponds to waves travelling back towards the orifice as found in the local stability analysis carried out in [26]. For points where u_0 is negative, we take its absolute value to calculate the Reynolds number.

We now examine another jet by changing the Reynolds number and K. Figure 7.17 shows the profiles of a jet with $We = 5$, $Rb = 2$, $Re = 477.2136$, $\delta = 0.01$ and $K = 0.703386351$ at $t = 0.28, 0.3$ and 0.34195. Jet break-up occurs at $t = 0.34195$ with Sections 1, 2 and 3 marked in a similar fashion as for Jet 1. Figures 7.20, 7.23 and 7.26 show the Re_{local} and We_{local} for Sections 1, 2 and 3 plotted in the Re-We plane for Jets 2(i), 2(ii) and 2(iii), respectively. Only Sections 1 and 2 are shown for Jet 2(iii) since Section 3 on this jet appears beyond the break-up point. We see similar behaviour to Jet 1; in Figure 7.20 all points lie above the critical curve and as time progresses in Figure 7.23, Section 2 heads towards absolute instability with some of the Re_{local} and We_{local} data points for Section 2 crossing the critical curve into the absolute instability region. Section 2 (corresponding to the ligament formed in Jet 2(iii)) in Figure 7.26, becomes fully absolutely unstable with Re_{local} and We_{local} data points belonging to this section lying below the critical curve in the absolute instability region. Section 1 remains above the critical curve and thus convectively unstable throughout. Figures 7.18, 7.19, 7.21, 7.22, 7.24 and 7.25 show the graphs of R_0 and u_0 plotted against s for Jets 2(i), 2(ii) and 2(iii), respectively.

We repeat the same process by changing the Reynolds number and K for Jets 3(i), 3(ii) and 3(iii) shown in Figure 7.27 where $We = 5$, $Rb = 2$, $Re = 44.7$, $\delta = 0.01$ and $K = 0.672348558$ for $t = 0.3, 0.35$ and 0.37912. The Re_{local} and We_{local} data points for Jets 3(i), 3(ii) and 3(iii) are given in Figures 7.30, 7.33 and 7.36, respectively. Figures

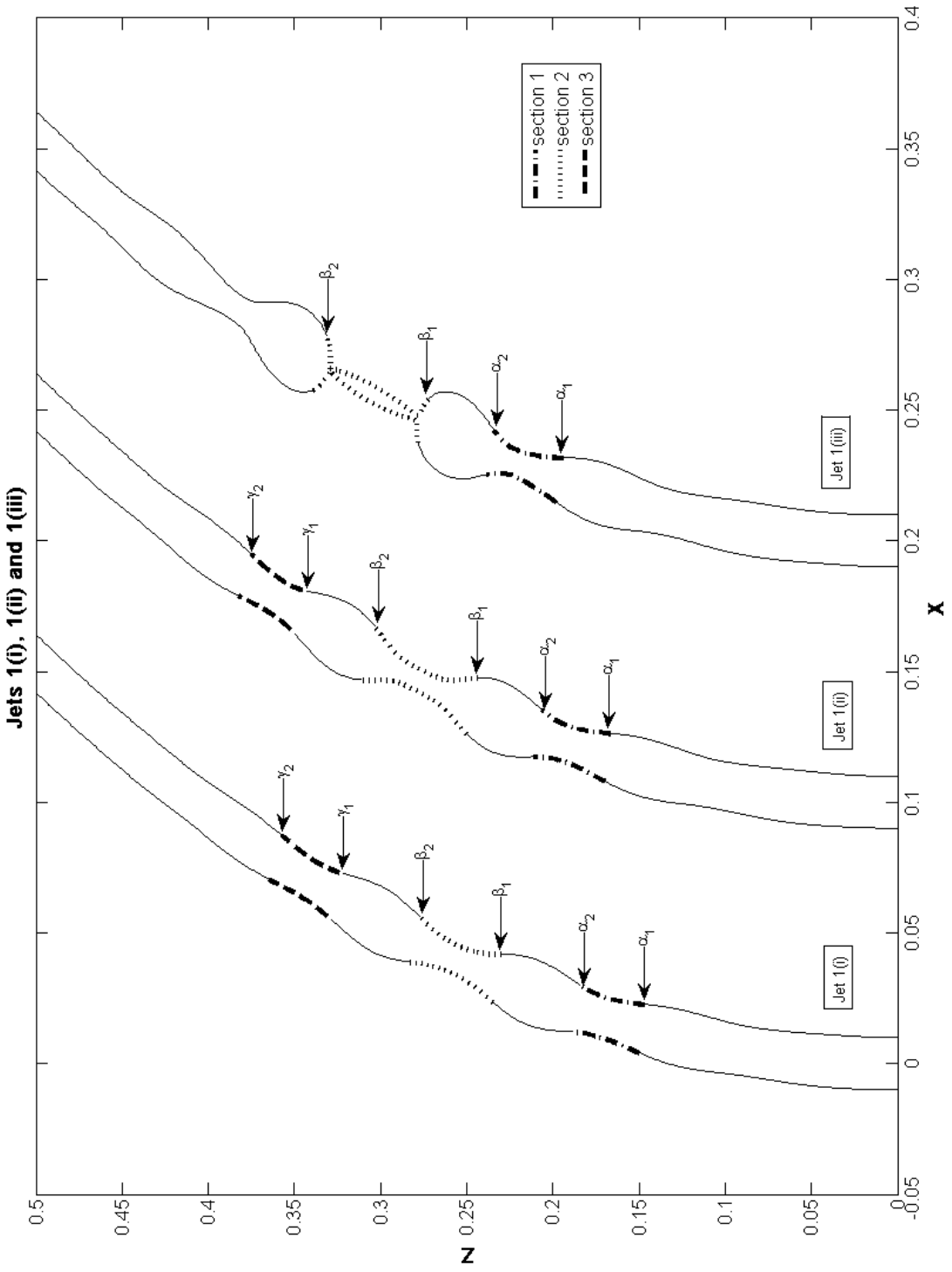

Figure 7.7: Graph showing three different profiles of a jet having $We = 5$, $Rb = 2$, $Re = 223.607$, $\delta = 0.01$ and $K = 0.699724035$ as it evolves with time. Jet 1(i) is at $t = 0.28$, Jet 1(ii) at $t = 0.3$ and Jet 1(iii) is at $t = 0.346$. Jet 1(iii) shows break-up.

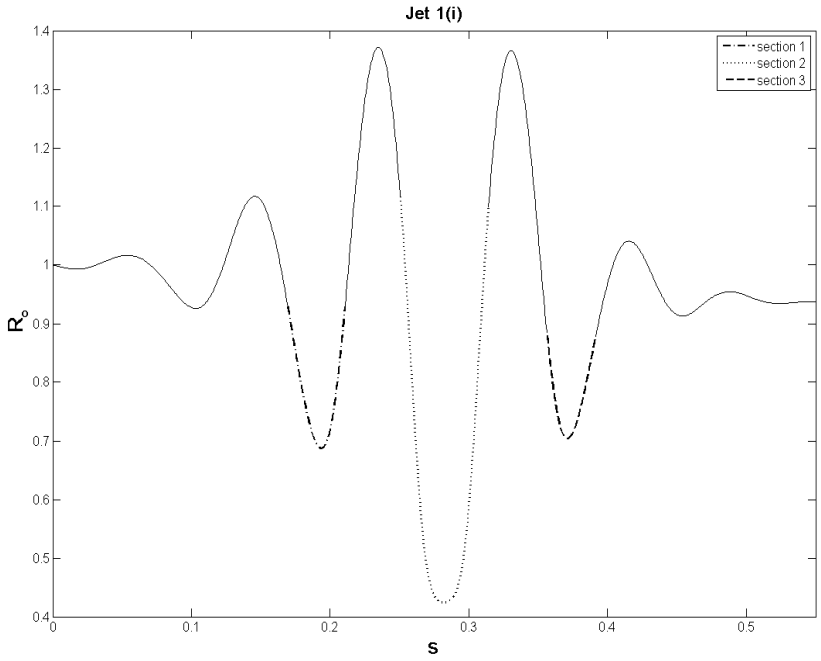

Figure 7.8: Graph showing the plot of R_0 against s for Jet 1(i). The R_0 values corresponding to Sections 1, 2 and 3 in Figure 7.7 are marked on the graph.

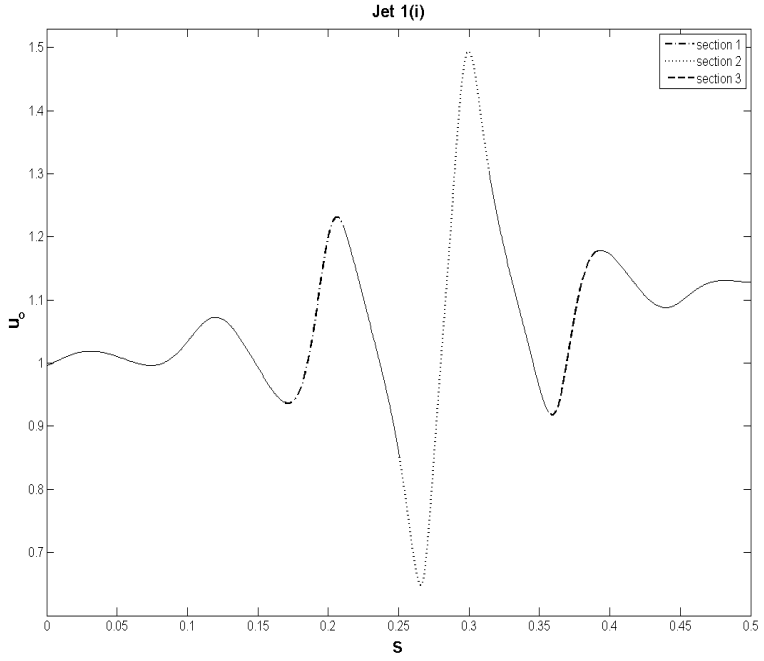

Figure 7.9: Graph showing the plot of u_0 against s for Jet 1(i). The u_0 values corresponding to Sections 1, 2 and 3 in Figure 7.7 are marked on the graph.

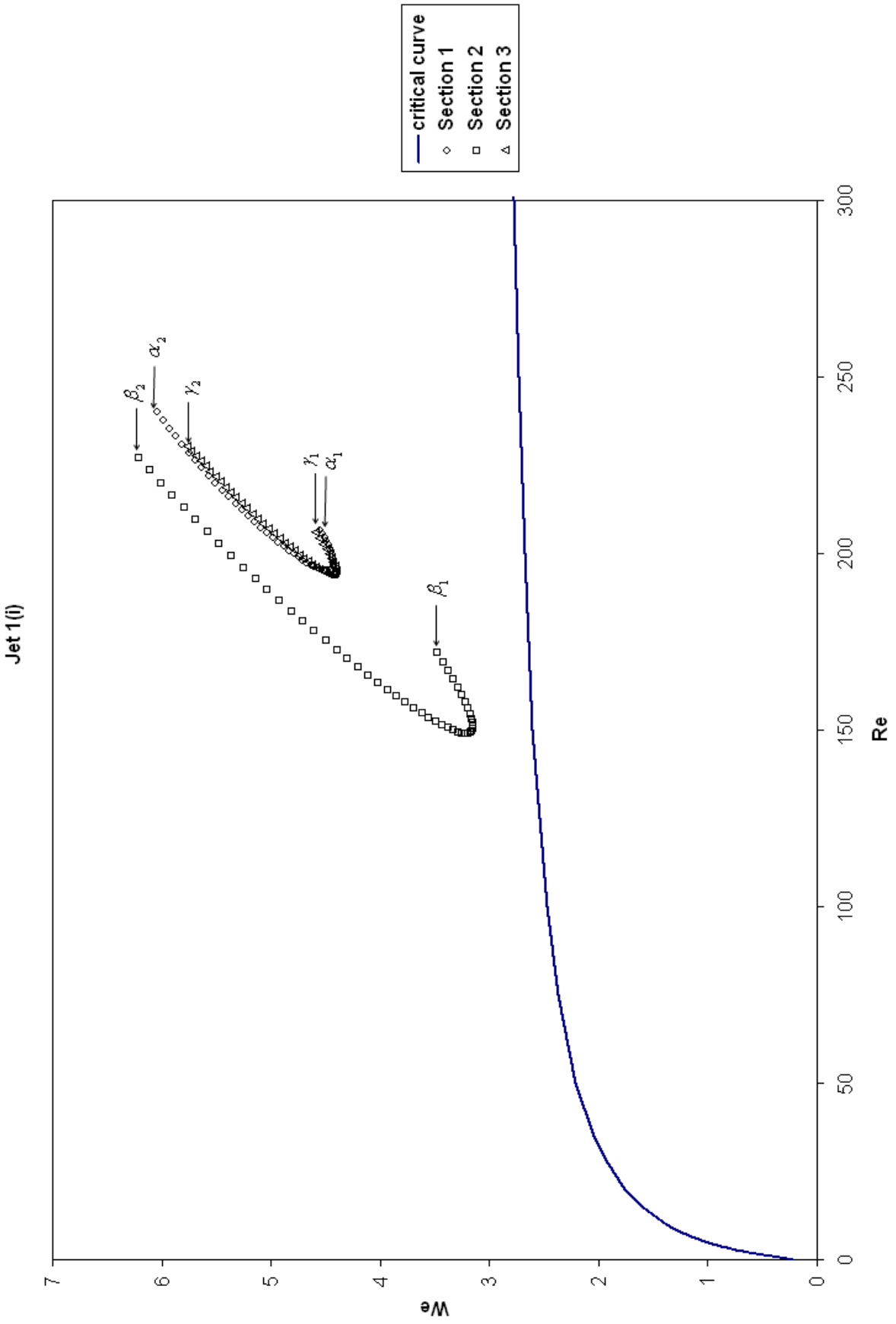

Figure 7.10: Graph showing the Re_{local} and We_{local} data points representing Sections 1, 2 and 3 for Jet 1(i). Note that all the data points, at this stage, lie above the critical curve, in the convective instability region.

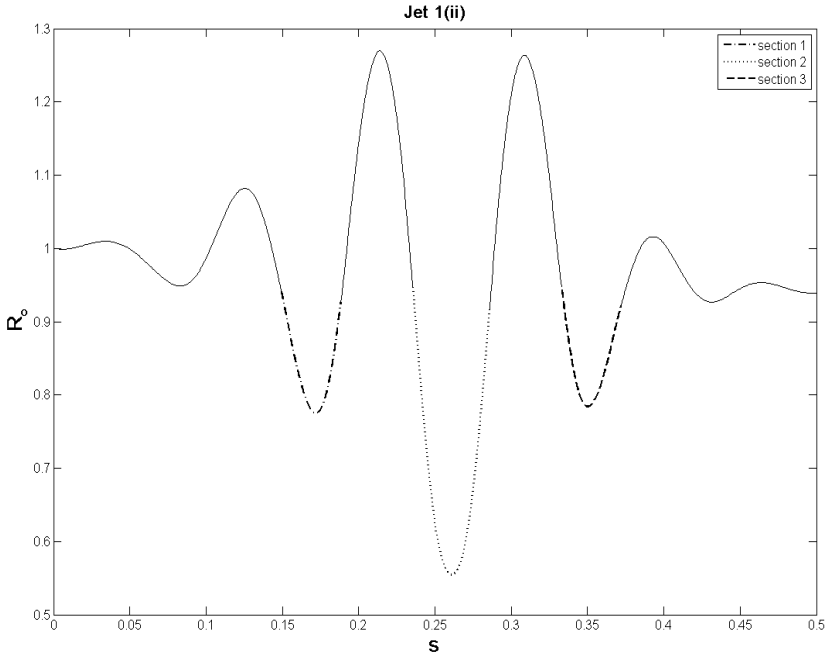

Figure 7.11: Graph showing the plot of R_0 against s for Jet 1(ii). The R_0 values corresponding to Sections 1, 2 and 3 in Figure 7.7 are marked on the graph.

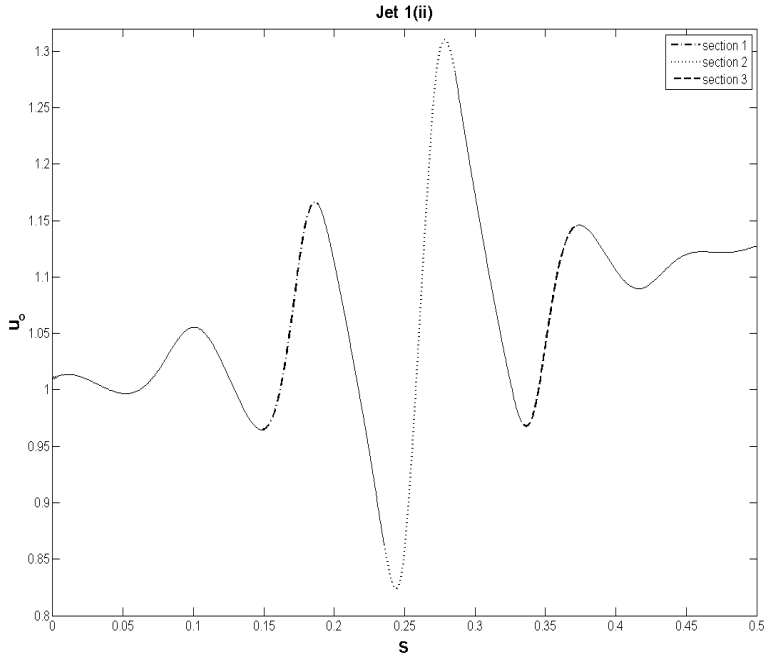

Figure 7.12: Graph showing the plot of u_0 against s for Jet 1(ii). The u_0 values corresponding to Sections 1, 2 and 3 in Figure 7.7 are marked on the graph.

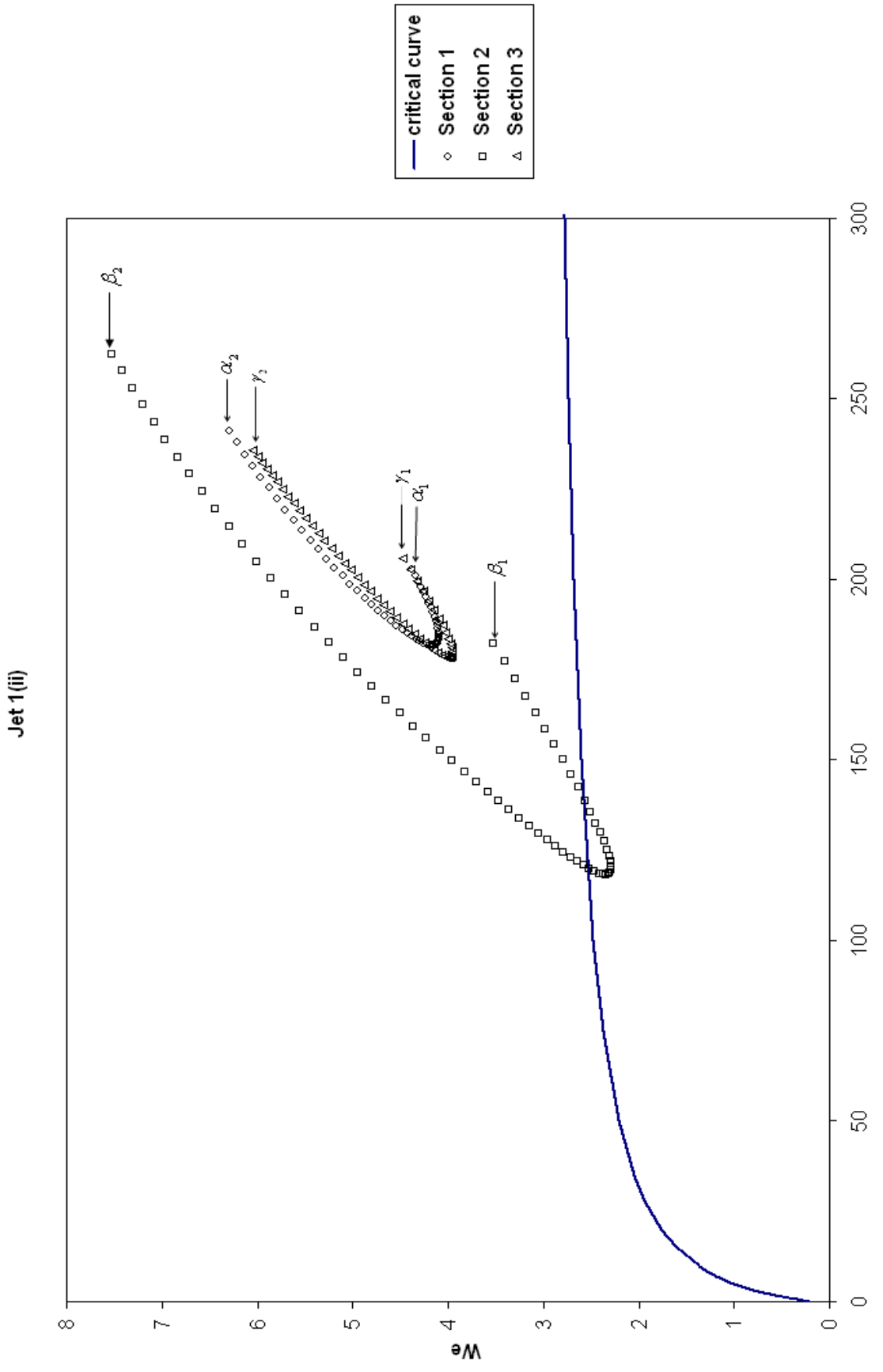

Figure 7.13: Graph showing the Re_{local} and We_{local} data points representing Sections 1, 2 and 3 for Jet 1(ii). Note that some of the Re_{local} and We_{local} data points corresponding to Section 2 cross the critical curve and lie in the absolute instability region, thus indicating the onset of absolute instability.

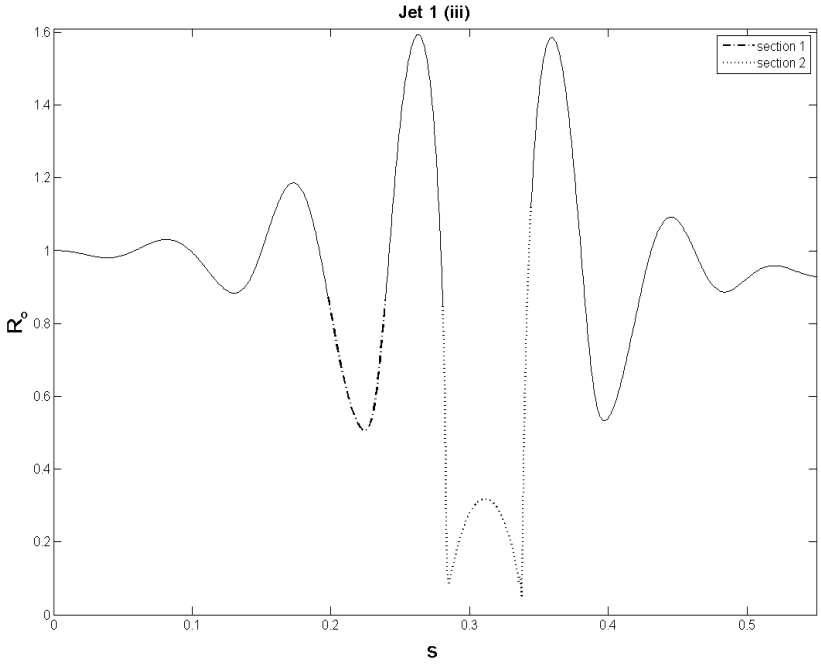

Figure 7.14: Graph showing the plot of R_0 against s for Jet 1(iii). The R_0 values corresponding to Sections 1 and 2 in Figure 7.7 are marked on the graph.

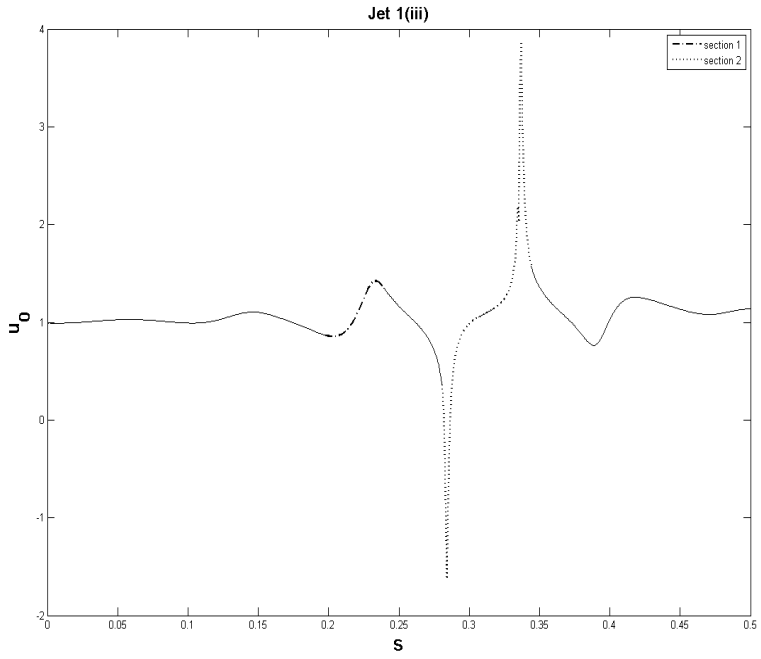

Figure 7.15: Graph showing the plot of u_0 against s for Jet 1(iii). The u_0 values corresponding to Sections 1 and 2 in Figure 7.7 are marked on the graph.

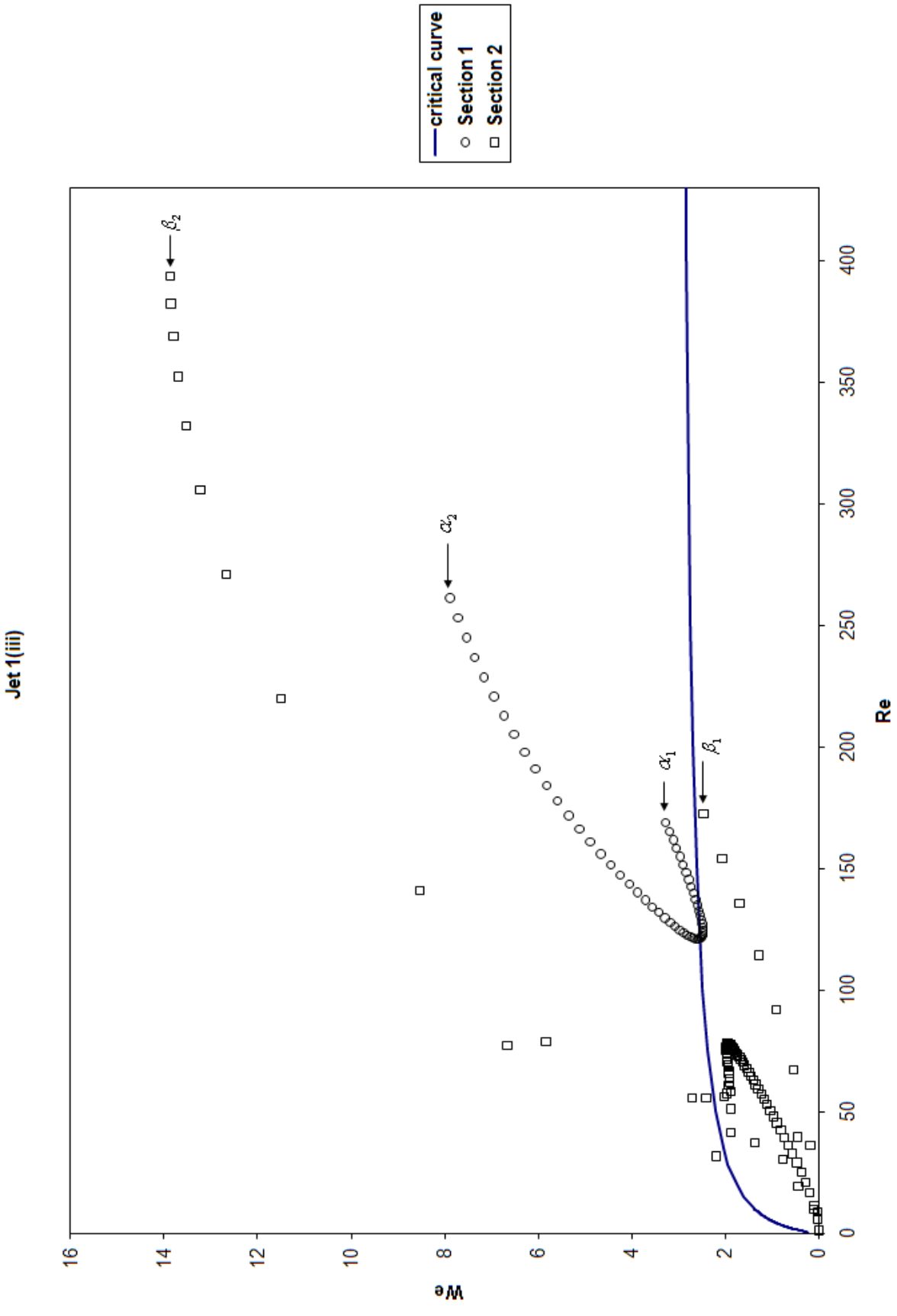

Figure 7.16: Graph showing the Re_{local} and We_{local} data points representing Sections 1 and 2 for Jet 1(iii). In this case, Re_{local} and We_{local} data points corresponding to Section 2 lie below the critical curve, confirming the existence of absolute instability at break-up.

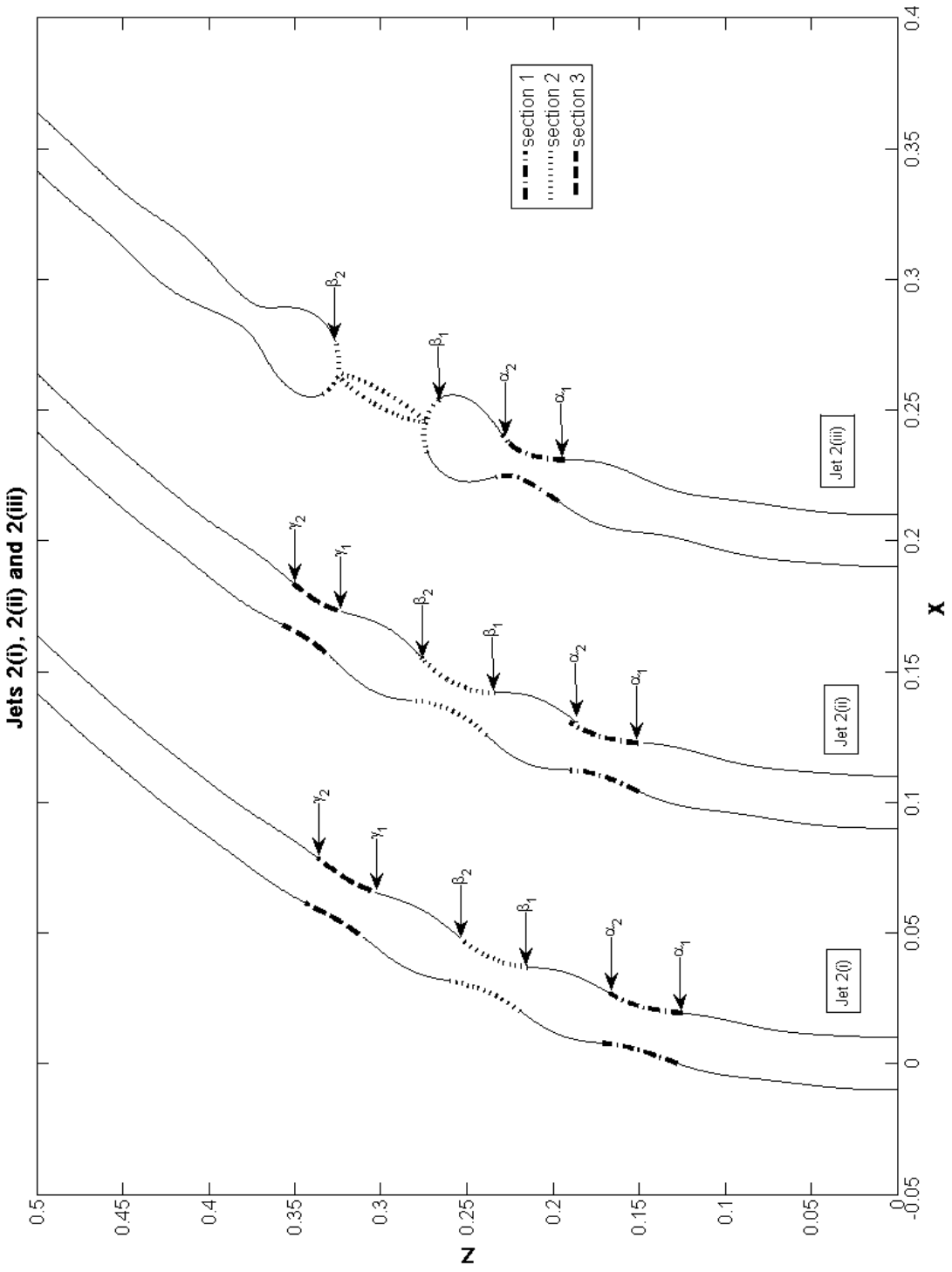

Figure 7.17: Graph showing three different profiles of a jet having $We = 5$, $Rb = 2$, $Re = 477.2136$, $\delta = 0.01$ and $K = 0.703386351$ at $t = 0.28, 0.3$ and 0.34195. Break-up occurs at $t = 0.34195$ in Jet 2(iii).

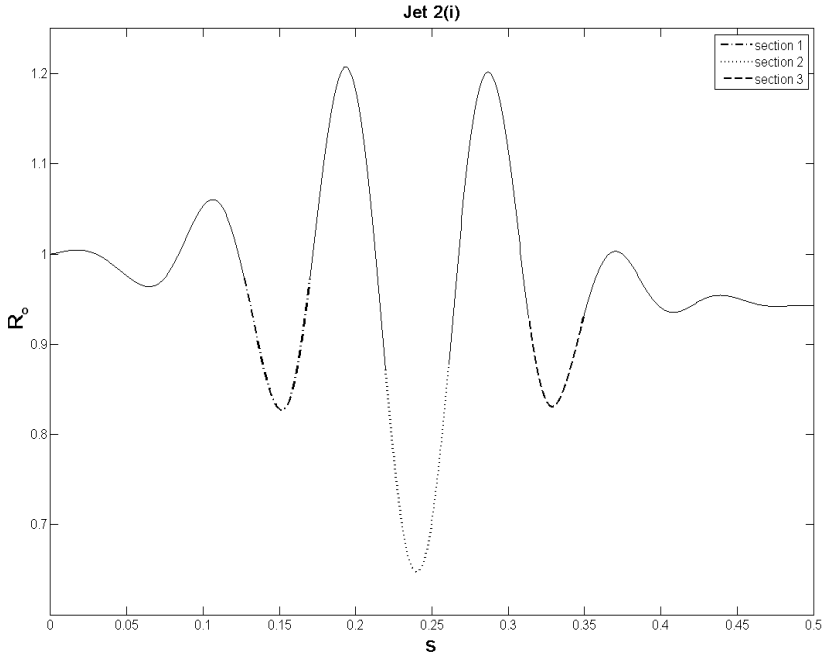

Figure 7.18: Graph showing the plot of R_0 against s for Jet 2(i). The R_0 values corresponding to Sections 1, 2 and 3 in Figure 7.17 are marked on the graph.

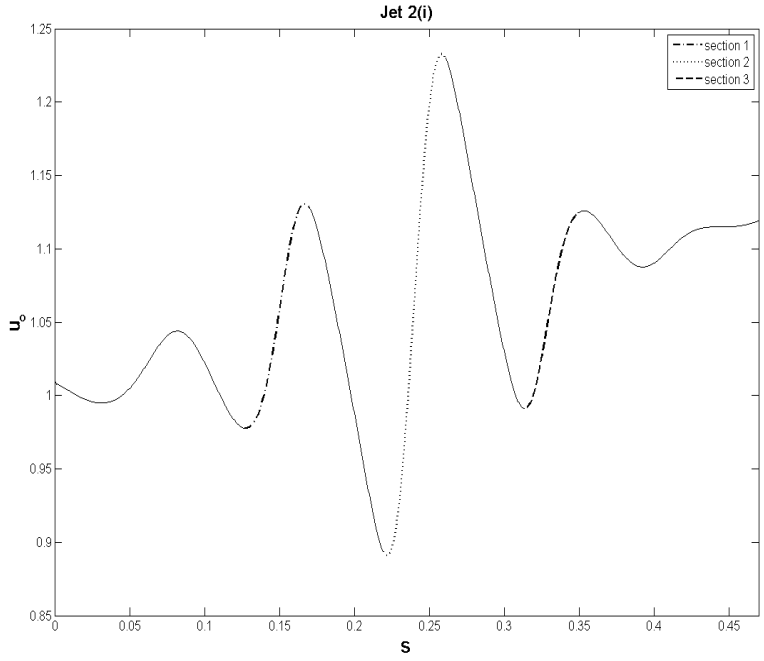

Figure 7.19: Graph showing the plot of u_0 against s for Jet 2(i). The u_0 values corresponding to Sections 1, 2 and 3 in Figure 7.17 are marked on the graph.

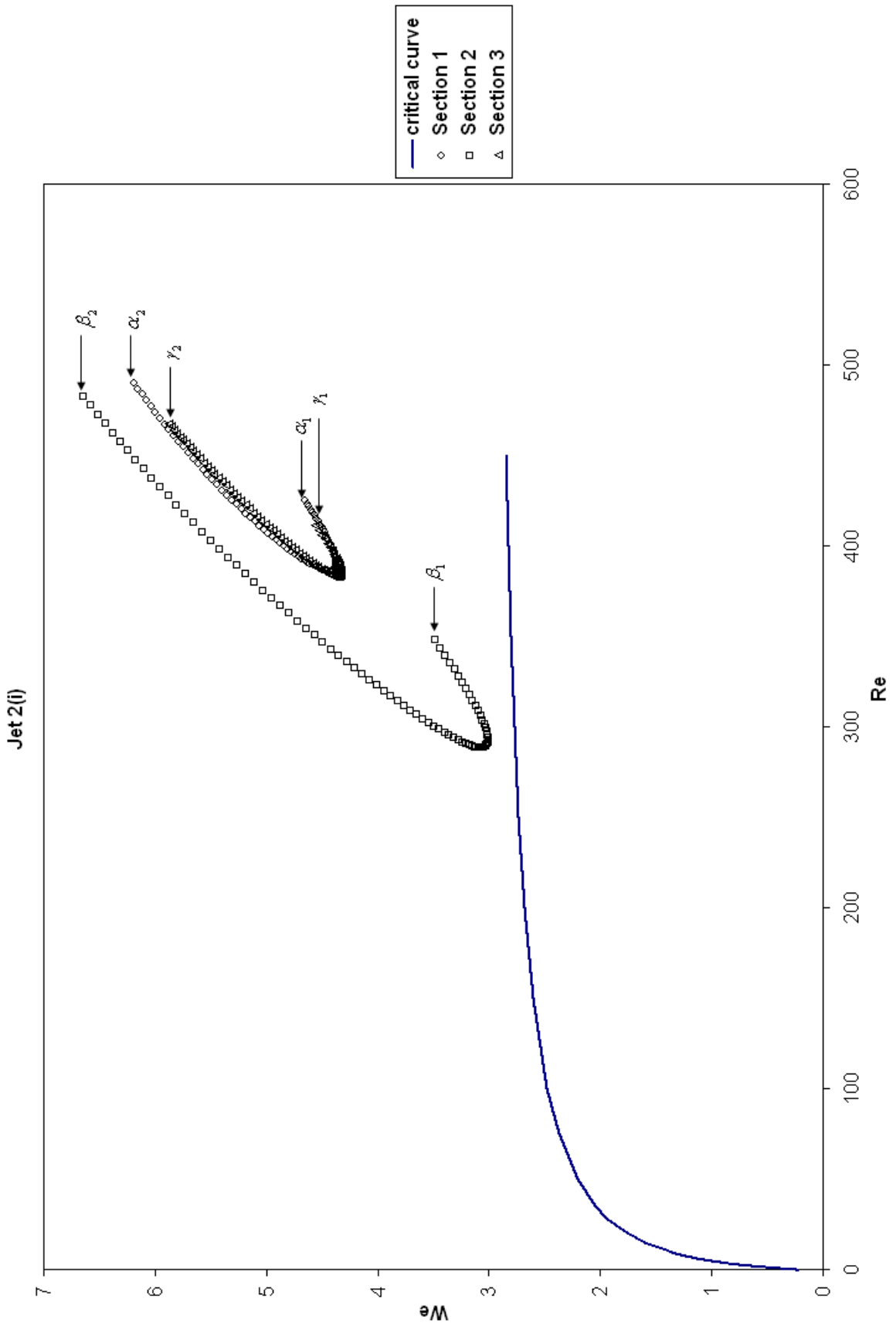

Figure 7.20: Graph showing the Re_{local} and We_{local} data points representing Sections 1, 2 and 3 for Jet 2(i). Note that all the data points, at this stage, lie above the critical curve, in the convective instability region.

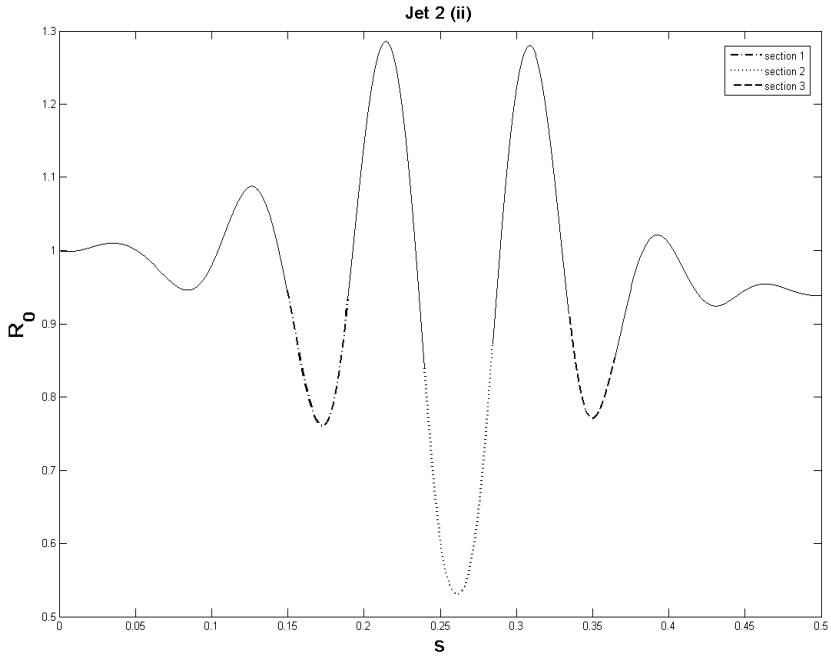

Figure 7.21: Graph showing the plot of R_0 against s for Jet 2(ii). The R_0 values corresponding to Sections 1, 2 and 3 in Figure 7.17 are marked on the graph.

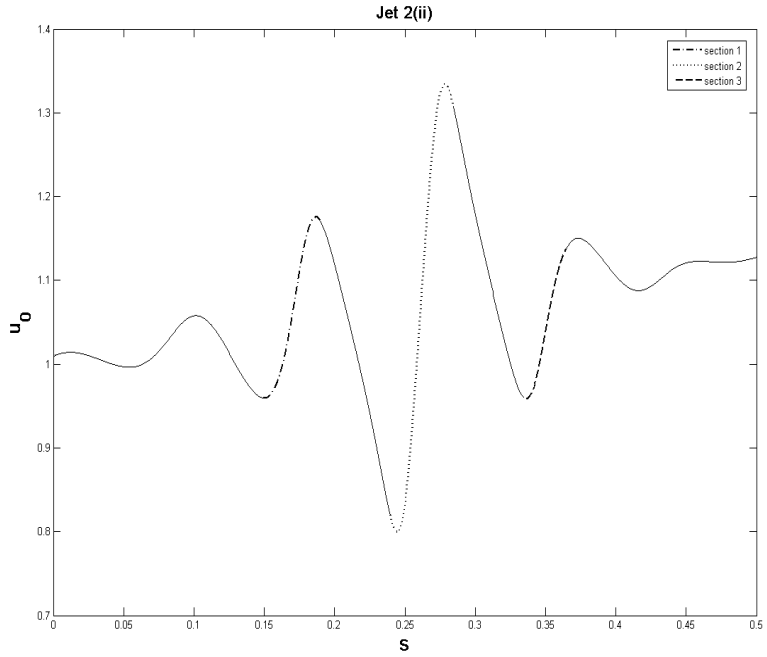

Figure 7.22: Graph showing the plot of u_0 against s for Jet 2(ii). The u_0 values corresponding to Sections 1, 2 and 3 in Figure 7.17 are marked on the graph.

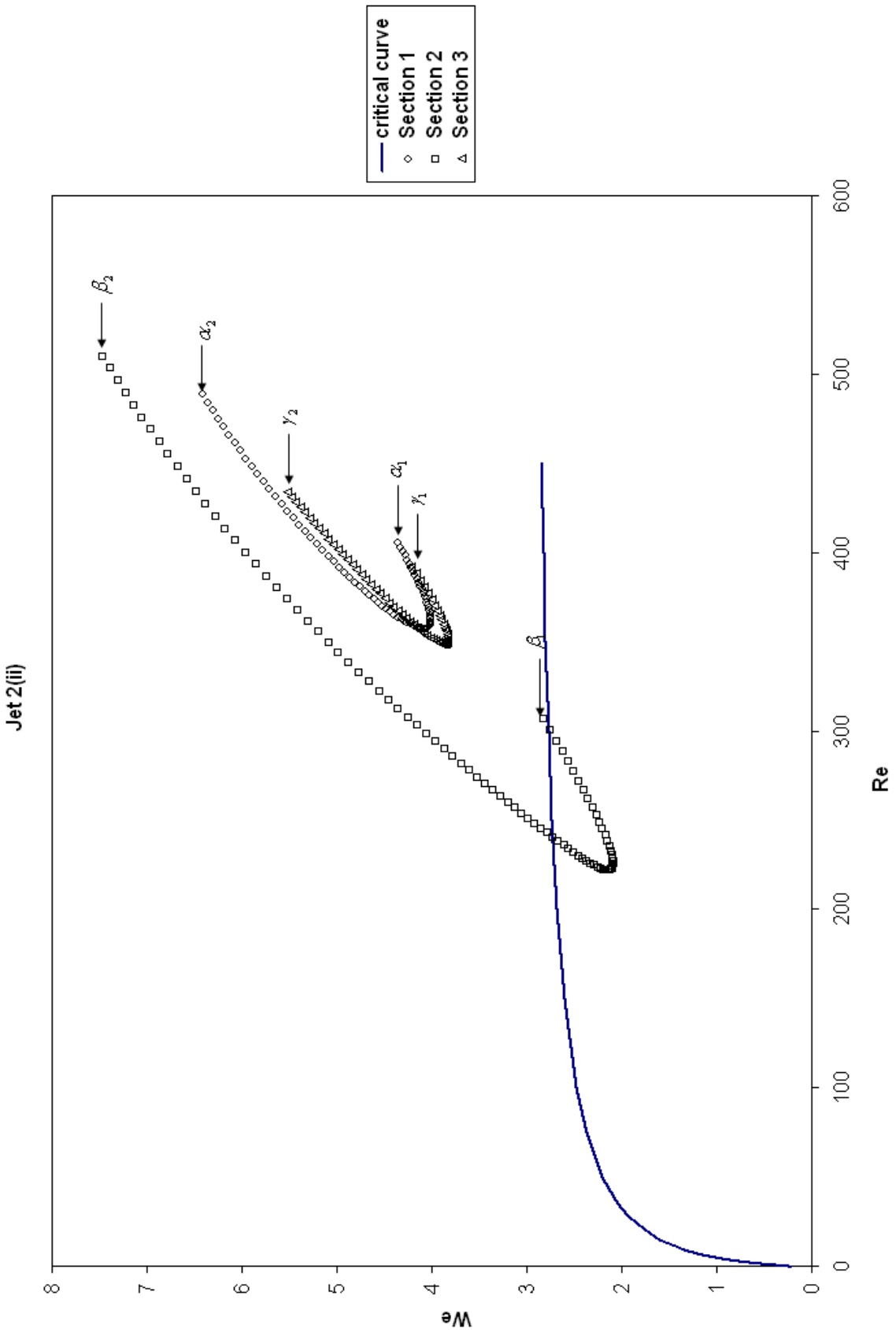

Figure 7.23: Graph showing the Re_{local} and We_{local} data points representing Sections 1, 2 and 3 for Jet 2(ii). Note that some of the Re_{local} and We_{local} data points corresponding to Section 2 cross the critical curve and lie in the absolute instability region, thus indicating the onset of absolute instability.

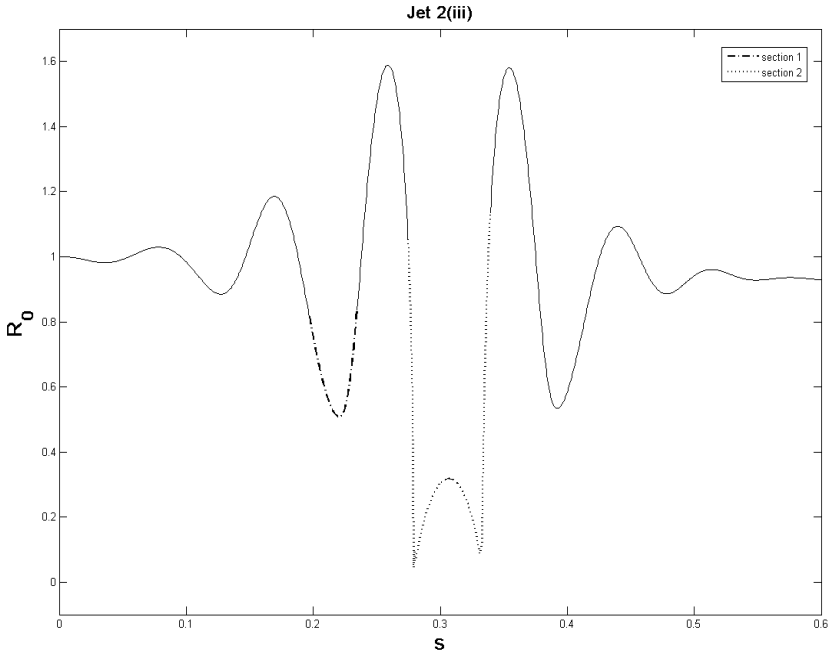

Figure 7.24: Graph showing the plot of R_0 against s for Jet 2(iii). The R_0 values corresponding to Sections 1 and 2 in Figure 7.17 are marked on the graph.

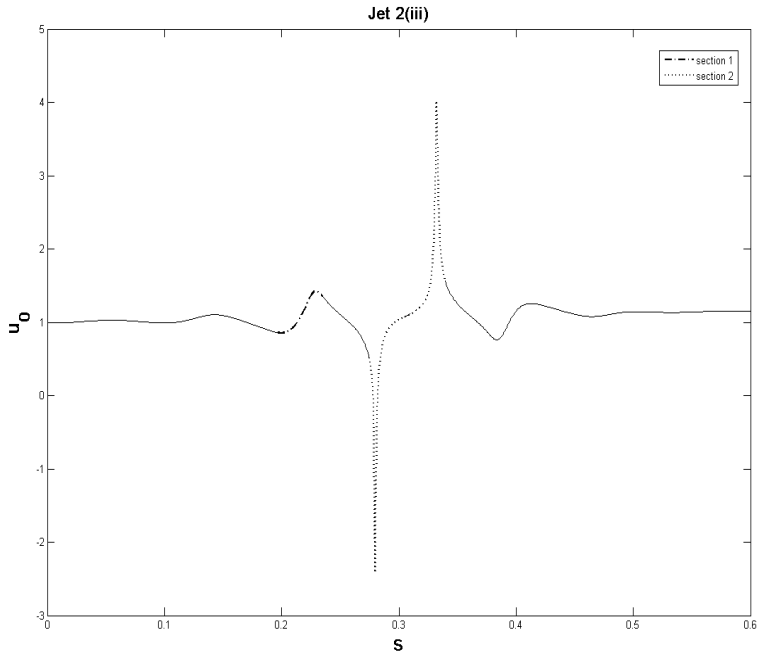

Figure 7.25: Graph showing the plot of u_0 against s for Jet 2(iii). The u_0 values corresponding to Sections 1 and 2 in Figure 7.17 are marked on the graph.

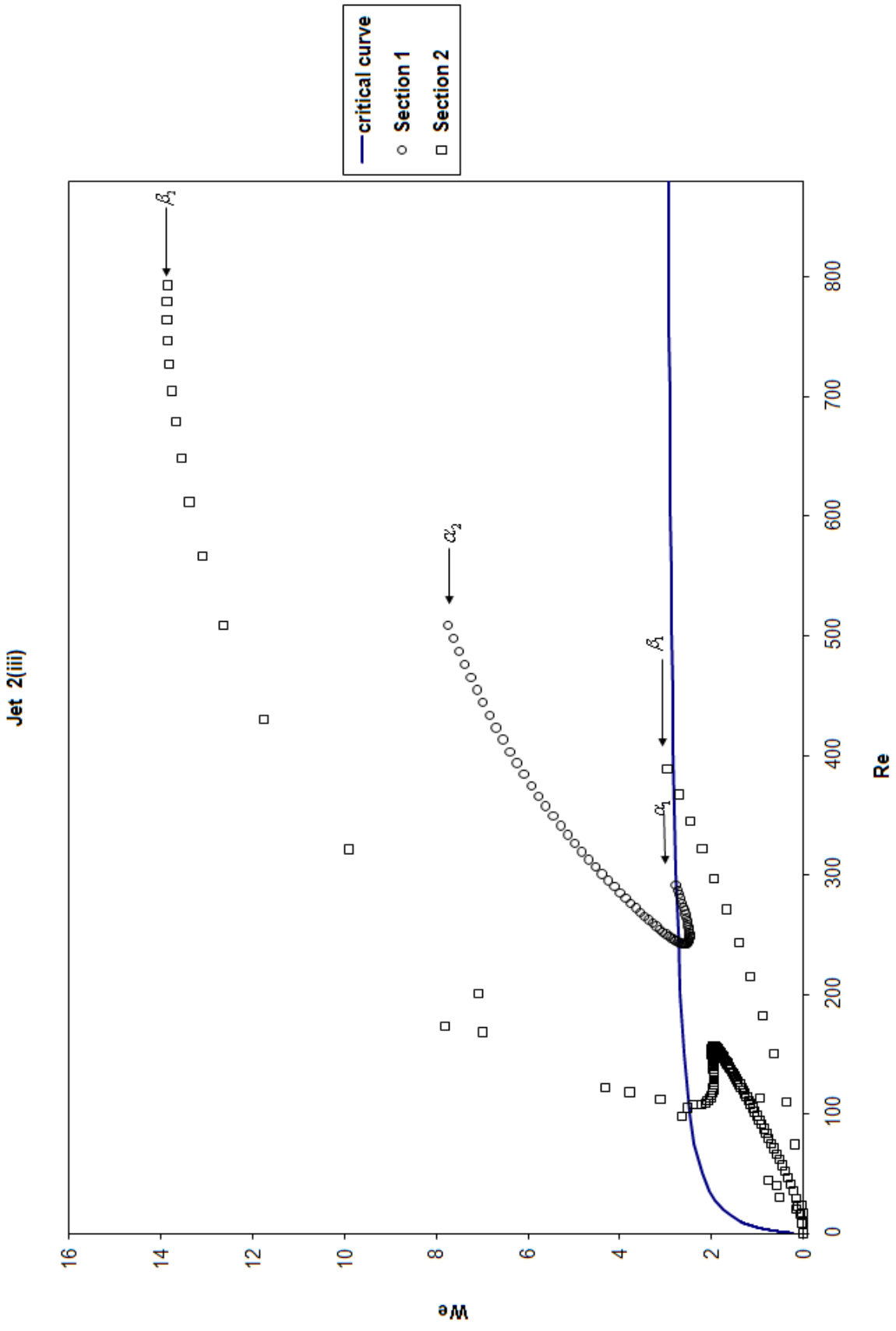

Figure 7.26: Graph showing the Re_{local} and We_{local} data points representing Sections 1 and 2 for Jet 2(iii). In this case, Re_{local} and We_{local} data points corresponding to Section 2 lie below the critical curve, confirming the existence of absolute instability at break-up.

7.28, 7.29, 7.31, 7.32, 7.34 and 7.35 show the graphs of R_0 and u_0 plotted against s for Jets 3(i), 3(ii) and 3(iii), respectively. Similar results as for Jet 1 and 2 are seen here.

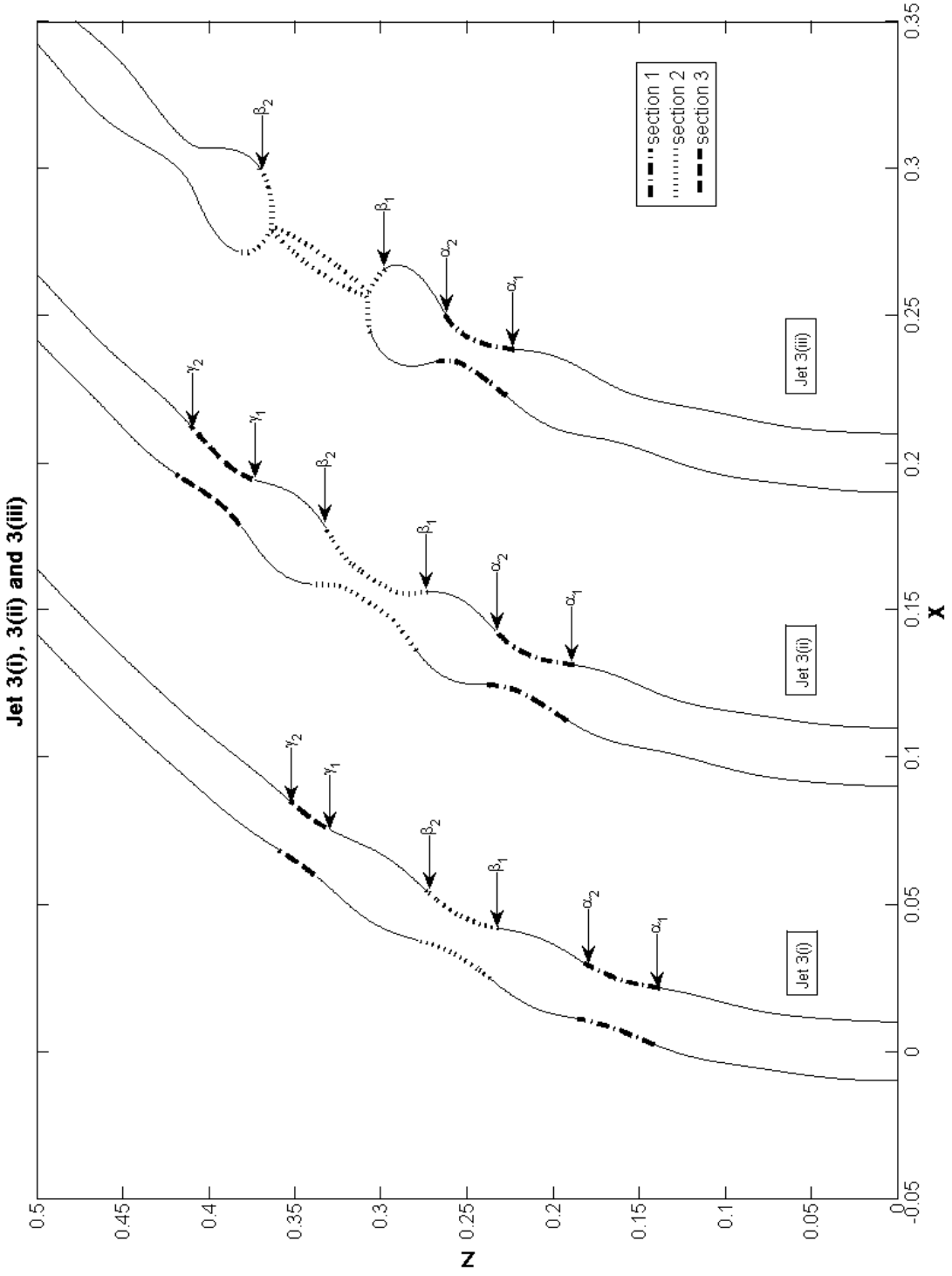

Figure 7.27: Graph showing three different profiles of a jet having $We = 5$, $Rb = 2$, $Re = 44.7$, $\delta = 0.01$ and $K = 0.672348558$ for $t = 0.3, 0.35$ and 0.37912. Break-up occurs at $t = 0.37912$ in Jet 3(iii).

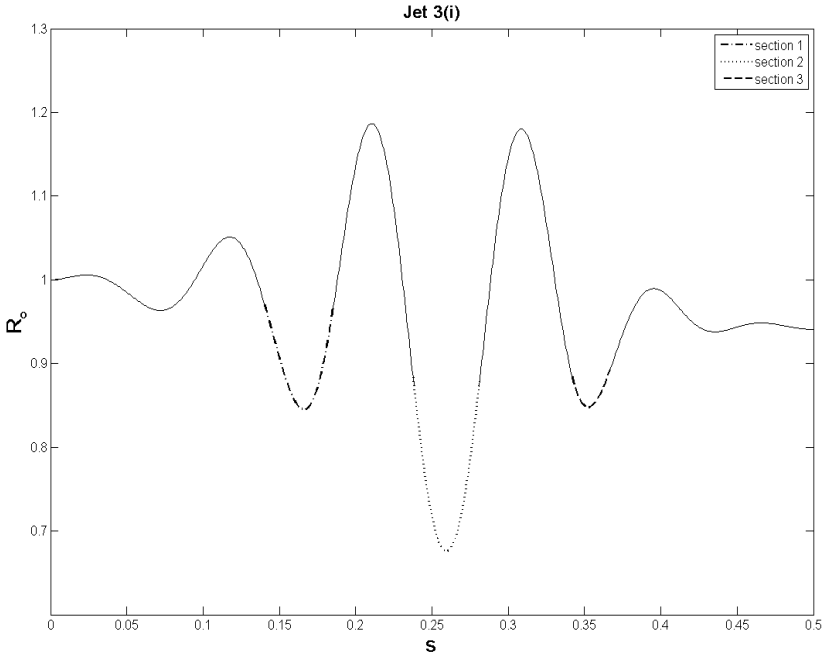

Figure 7.28: Graph showing the plot of R_0 against s for Jet 3(i). The R_0 values corresponding to Sections 1, 2 and 3 in Figure 7.27 are marked on the graph.

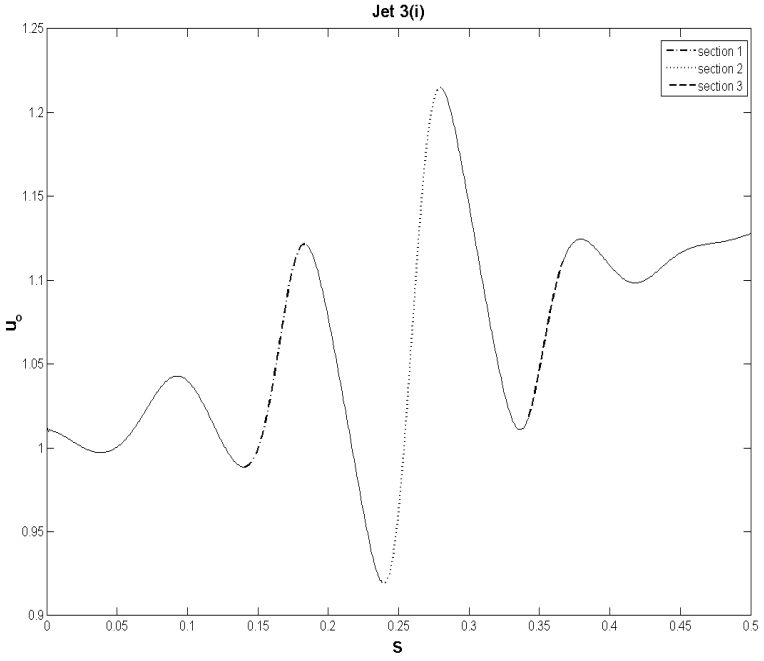

Figure 7.29: Graph showing the plot of u_0 against s for Jet 3(i). The u_0 values corresponding to Sections 1, 2 and 3 in Figure 7.27 are marked on the graph.

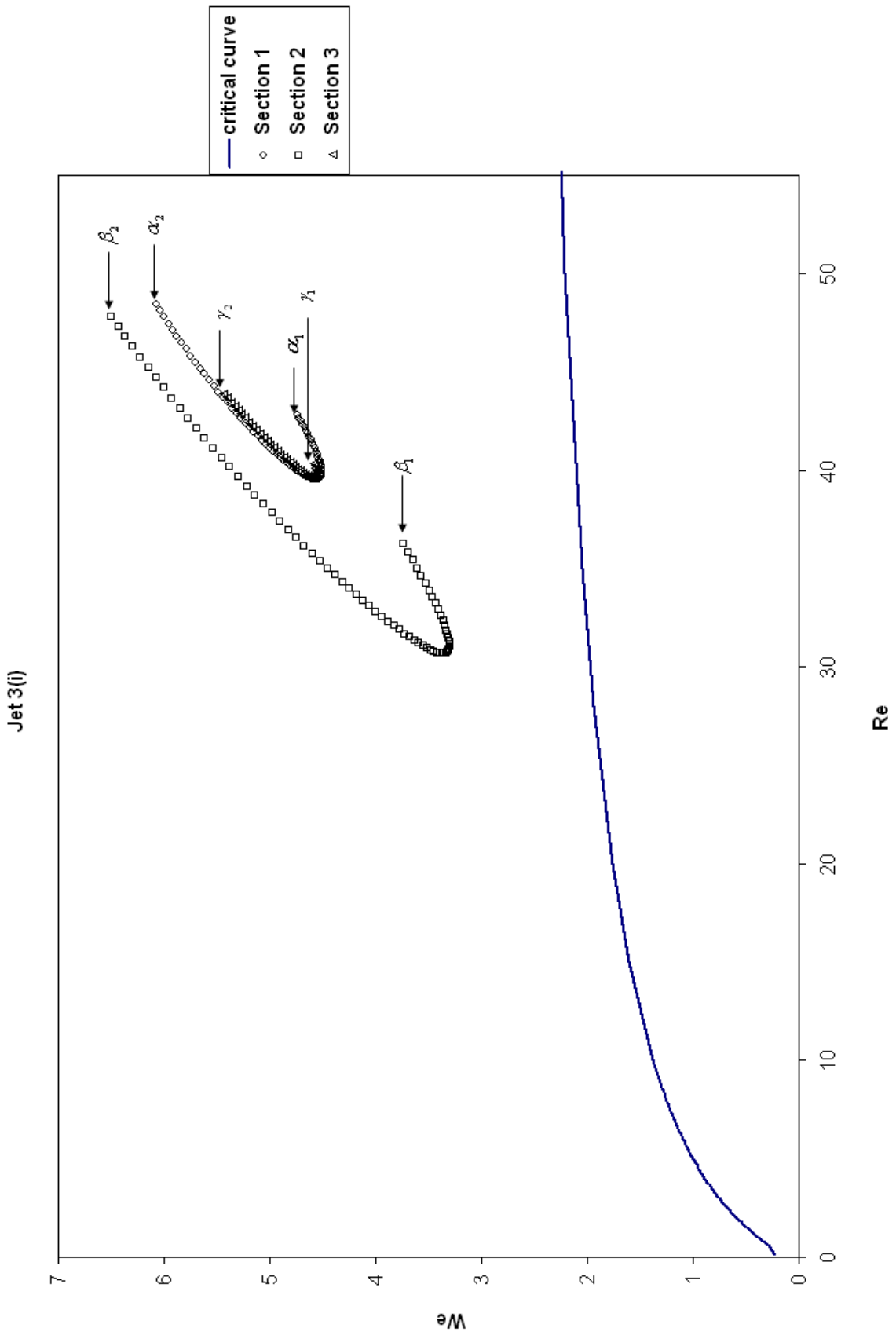

Figure 7.30: Graph showing the Re_{local} and We_{local} data points representing Sections 1, 2 and 3 for Jet 3(i). Note that all the data points, at this stage, lie above the critical curve, in the convective instability region.

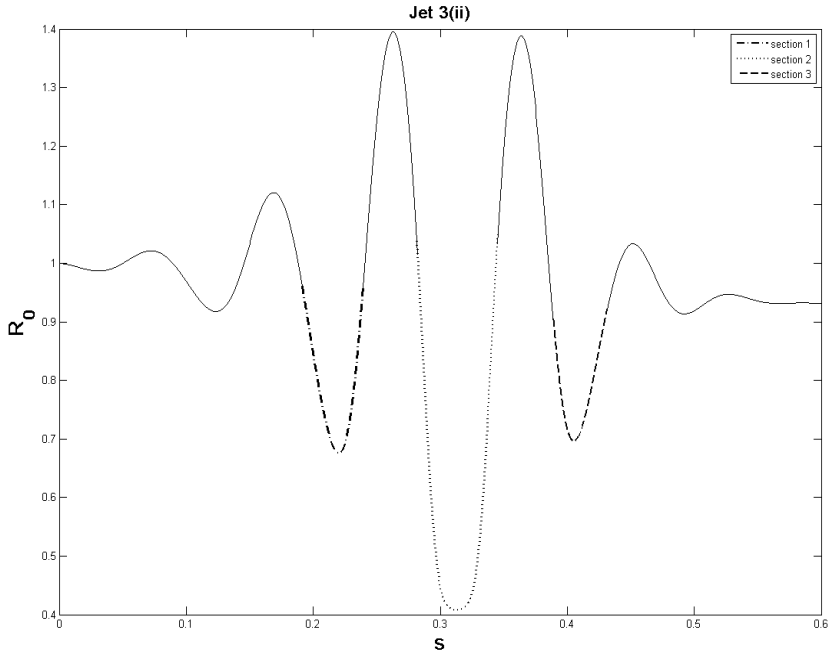

Figure 7.31: Graph showing the plot of R_0 against s for Jet 3(ii). The R_0 values corresponding to Sections 1, 2 and 3 in Figure 7.27 are marked on the graph.

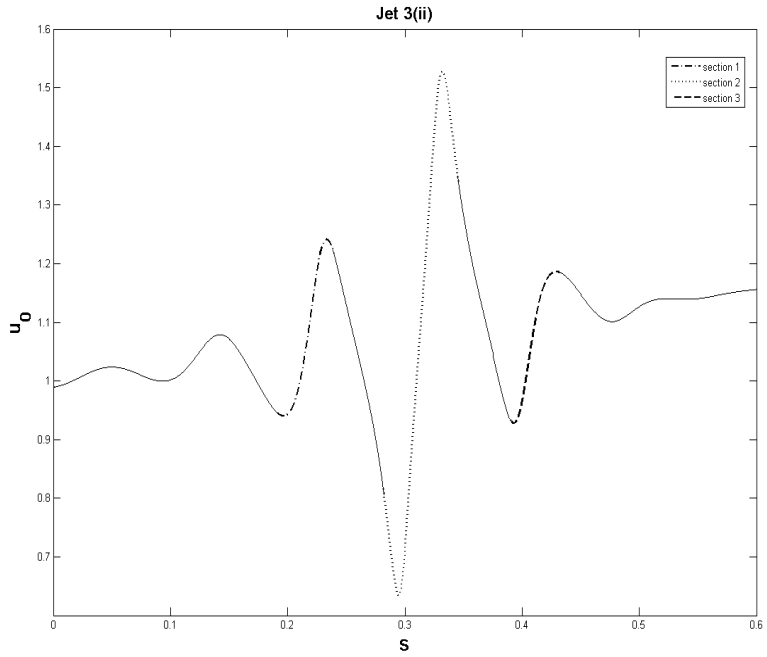

Figure 7.32: Graph showing the plot of u_0 against s for Jet 3(ii). The u_0 values corresponding to Sections 1, 2 and 3 in Figure 7.27 are marked on the graph.

7.3 Conclusion

In this chapter we have looked as absolute instability using the model derived in Parau *et al.* [52]. As the jet evolves with time and approaches pinch off, it thins to form ligaments at break-up. As the jet grows with time, we used our multiple scales approach to calculate Re_{local} and We_{local} and examined their position in the critical Re-We plane. Our results demonstrate that for Jets 1(i), 2(i) and 3(i), the Re_{local} and We_{local} values lie above the critical curve in the convective instability region, suggesting that the jet is convectively unstable for times approaching break-up. As the jet heads towards pinch-off, the first part to become absolutely unstable is always Section 2 in Jets 1(ii), 2(ii) and 3(ii) due to the small u_0 and R_0 in Re_{local} and We_{local}. Section 2 corresponds to the part of the jet which later thins and forms a ligament when the jet breaks up. Shortly after we observe the presence of absolute instability in Jets 1(ii), 2(ii) and 3(ii), break-up occurs in Jets 1(iii), 2(iii) and 3(iii). Here a large part of Section 2, corresponding to the ligament formed, lies below the critical curve in the absolute instability region implying that the jet is absolutely unstable around the break-up point.

The fact that the jet breaks shortly after a local absolute instability forms around pinch-off suggests that it plays a key feature in jet break-up, as shown in the experimental photographs in Figures 7.1-7.3 at the beginning of this chapter. However, the effect of this instability and subsequent ligament behaviour, can not be ascertained as the numerical model breaks down at pinch-off. The break down of the numerical model also caused problems when we tried to examine ligaments that form in Mode 3 break-up; u_0 becomes too large at break-up. Hence values of Re_{local} and We_{local} were not close to the critical curve. Thus, the onset of absolute instability in cases of high rotation and high viscosity could not be examined. Although, we have carried out a qualitative experimental comparison, there is need for a quantitative comparison with experiments. Thus, experiments looking particularly at the break-up of ligaments need to be performed so a better understanding of ligament break-up can be gained.

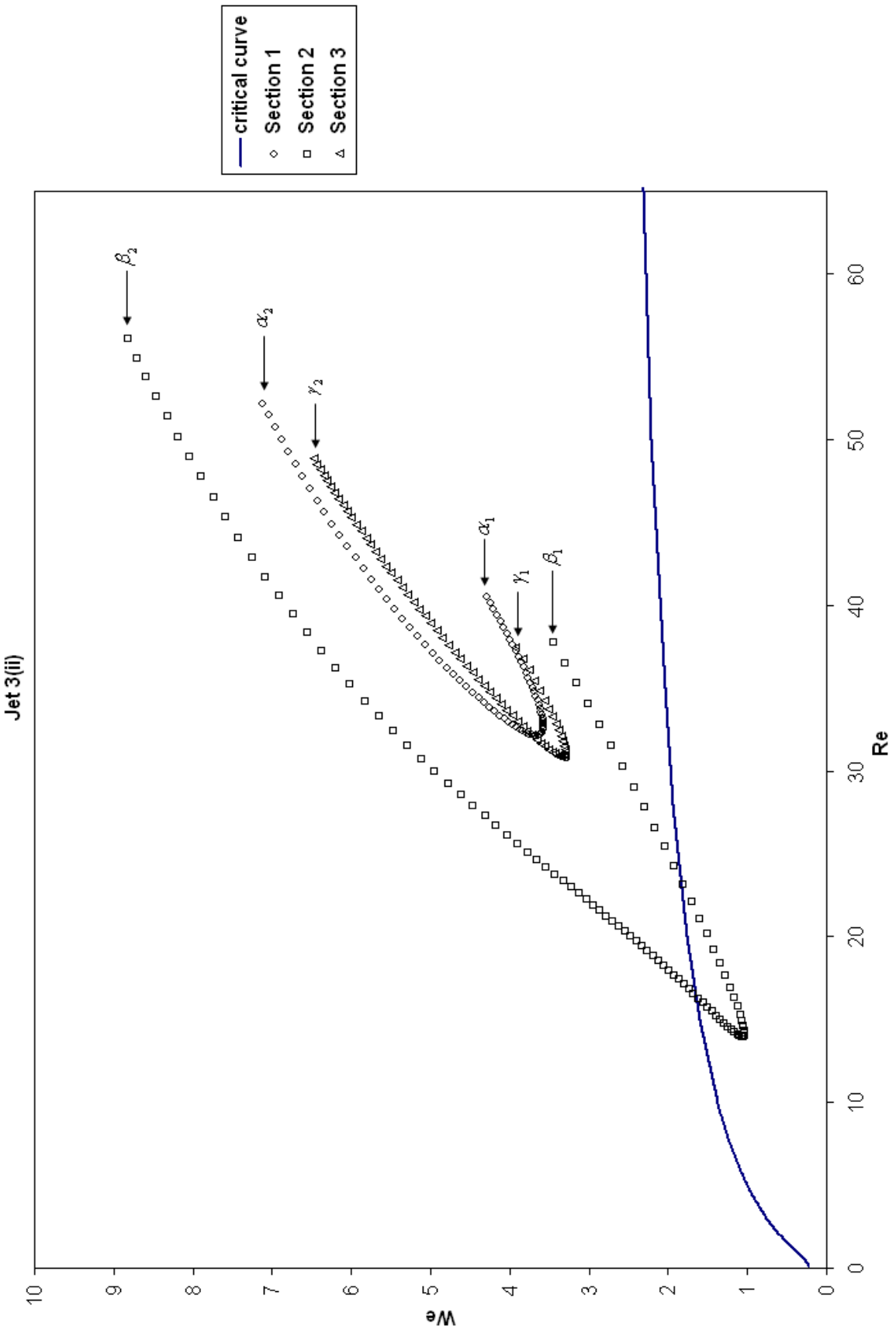

Figure 7.33: Graph showing the Re_{local} and We_{local} data points representing Sections 1, 2 and 3 for Jet 3(ii). Note that some of the Re_{local} and We_{local} data points corresponding to Section 2 cross the critical curve and lie in the absolute instability region, thus indicating the onset of absolute instability.

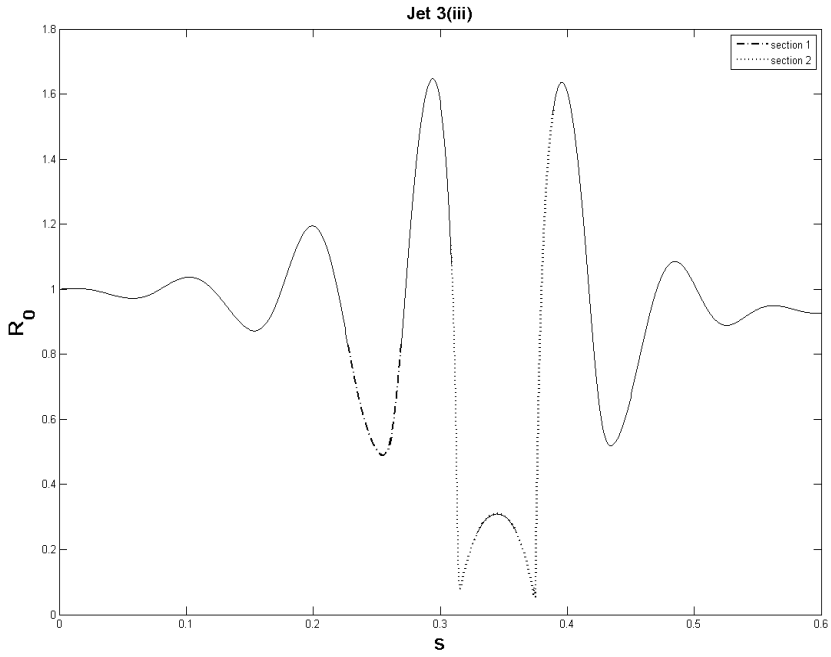

Figure 7.34: Graph showing the plot of R_0 against s for Jet 3(iii). The R_0 values corresponding to Sections 1 and 2 in Figure 7.27 are marked on the graph.

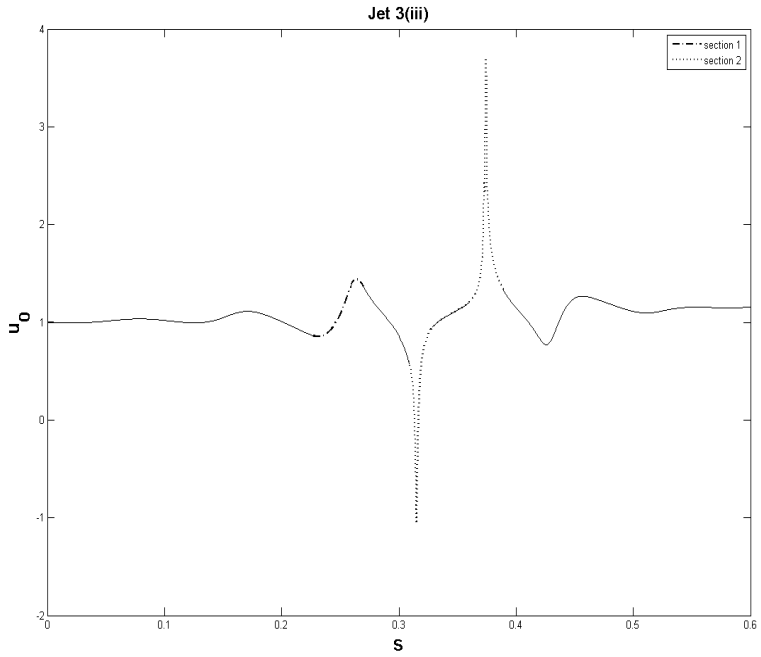

Figure 7.35: Graph showing the plot of u_0 against s for Jet 3(iii). The u_0 values corresponding to Sections 1 and 2 in Figure 7.27 are marked on the graph.

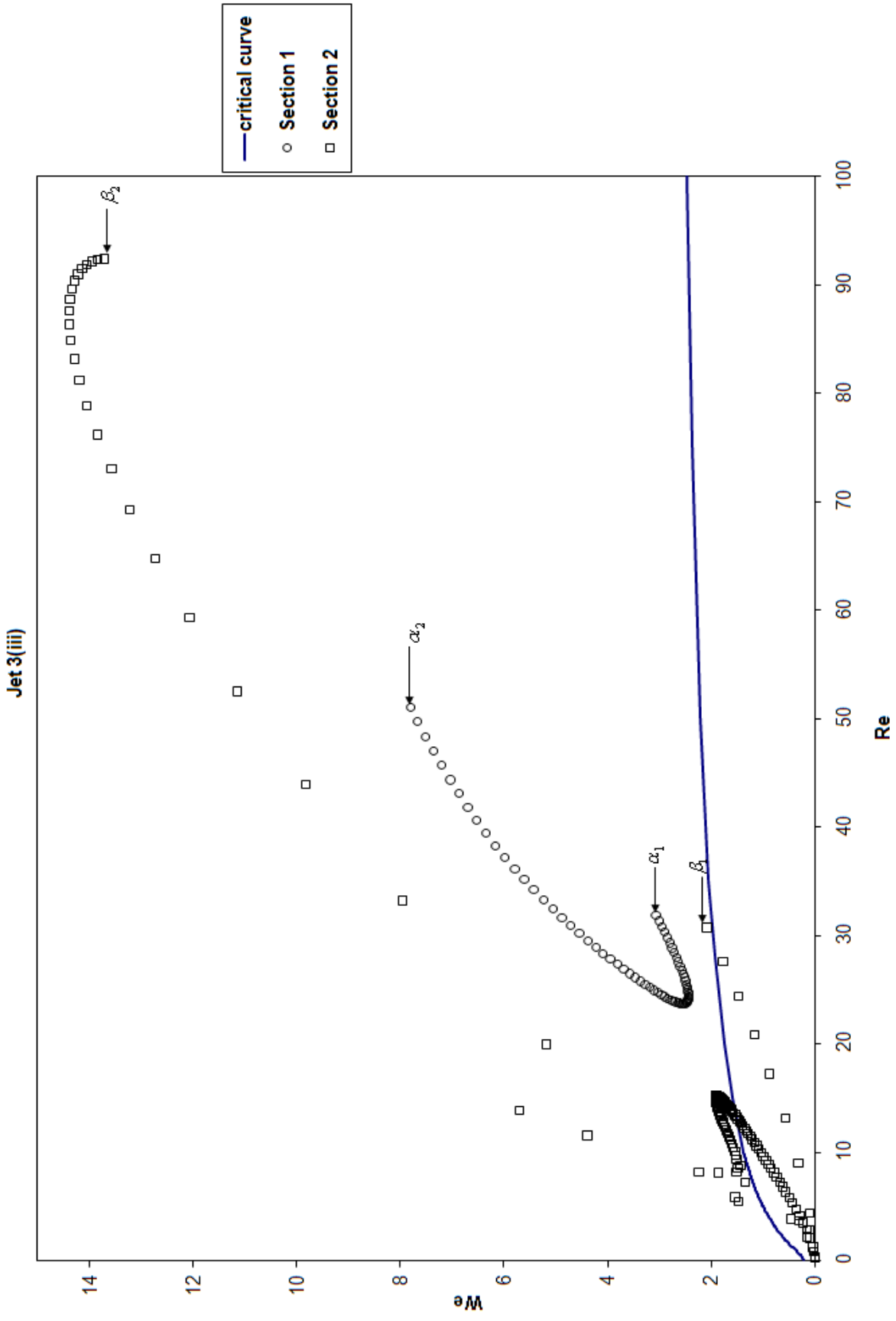

Figure 7.36: Graph showing the Re_{local} and We_{local} data points representing Sections 1 and 2 for Jet 3(iii). In this case, Re_{local} and We_{local} data points corresponding to Section 2 lie below the critical curve, confirming the existence of absolute instability at break-up.

Chapter 8

Absolute Instability in Non-Newtonian Curved Liquid Jets

In this chapter we introduce the concept of non-Newtonian liquids. Unlike Newtonian fluids, these fluids do not have a linear relationship between stress and strain, forcing them to behave in a different manner to Newtonian fluids when subjected to external forces. They can be classified into two types: inelastic or generalised Newtonian fluids and viscoelastic fluids. Viscoelastic or elastic fluids demonstrate viscous liquid like behaviour with a blend of elastic solid like behaviour. We shall be studying inelastic fluids which can be further grouped as shear-thinning or shear-thickening fluids. If a liquid's viscosity decreases with the rate of shear applied, it is known as a shear-thinning fluid. Fluids which thicken as stress is applied to them are known as shear-thickening fluids. Examples of shear-thickening fluids are solutions of corn starch, surfactants, clay slurries and many more. The wide applications of non-Newtonian liquids in industry has created a need for a better understanding in this area.

Mathematically, the main difference between a Newtonian and a non-Newtonian liquid lies in the fact that the stress and the rate of strain are not linearly related in the constitutive equation for a non-Newtonian liquid. Non-Newtonian liquids have variable viscosity which changes as stress is applied. There are numerous models which are used to describe non-Newtonian liquids, but since our main interest lies in inelastic fluids, we

will explain the two most common models used to describe them.

8.1 Power-Law Model

This is the most basic model used to characterise an inelastic non-Newtonian fluid. For a power law fluid the constitutive equation is given by

$$\boldsymbol{\tau} = \eta(\nabla \boldsymbol{u} + (\nabla \boldsymbol{u})^T) = \eta \boldsymbol{\gamma} \tag{8.1}$$

where $\boldsymbol{\tau}$ is the stress tensor, $\boldsymbol{u}$ is the velocity vector, $\boldsymbol{\gamma}$ is the rate of strain tensor and η is the apparent (effective) viscosity (which is replaced by the dynamic viscosity in the Newtonian case). The relationship between the apparent viscosity and the shear rate is given by

$$\eta = m\dot{\gamma}^{\alpha-1} \tag{8.2}$$

where α is the dimensionless flow index number, m is the fluid consistency number having dimensions $Pa.s^{\alpha}$ and $\dot{\gamma}$ is the shear rate which is given by the second invariant of the rate of strain tensor γ

$$\dot{\gamma} = \sqrt{\frac{\boldsymbol{\gamma} : \boldsymbol{\gamma}}{2}}. \tag{8.3}$$

The flow index number α and the fluid consistency number m are determined experimentally. The value of α establishes the degree of non-Newtonian behaviour of a material. For $\alpha < 1$, the fluid is shear-thinning and for $\alpha > 1$ the fluid is shear-thickening. The special case when $\alpha = 1$ corresponds to the liquid being Newtonian. Shear thinning fluids at low shear rates and shear thickening fluids at high shear rates can not be described using the Power-Law model since at zero shear rates this model predicts infinite viscosity and at high shear rates it predicts zero viscosity, but this is not the case for a real fluid. The power law rheology also fails to model a straight non-Newtonian liquid jet as the rate

of strain tensor goes to infinity in this case.

8.2 Carreau Model

This model overcomes the limitations of the Power-Law model and can be used to describe a straight liquid jet. The apparent viscosity in this case is given by

$$\eta = \eta_0[(1-\lambda)(1+(h\dot{\gamma})^2)^{\frac{f-1}{2}} + \lambda] \tag{8.4}$$

where h is a time constant, $\lambda\eta_0$ is the dimensionless infinite shear viscosity and η_0 is the zero shear rate viscosity. For this model, f is defined to be less than or equal to one which means the Carreau model takes into account only the shear thinning properties of a fluid. For zero shear rates, the effective viscosity tends to η_0 and for infinite shear rates the effective viscosity tends to $\lambda\eta_0$.

We are now in a position to look at absolute instability in non-Newtonian liquid jets and start by reviewing work done previously on non-Newtonian curved liquid jets.

8.3 Review of Previous Work

We start by describing the model used in Uddin [65]. We consider a non-Newtonian shear thinning liquid jet described by the Carreau constitutive equation

$$\eta = \tilde{\eta_0}\tilde{\eta} = \tilde{\eta_0}(1-\xi)[1+(h\dot{\gamma})^2]^{\frac{f-1}{2}} + \tilde{\eta_0}\xi \tag{8.5}$$

where η is the shear rate dependent viscosity, $\dot{\gamma} = \sqrt{\frac{\varepsilon:\varepsilon}{2}}$ is the second invariant of the deformation tensor $\varepsilon = \nabla\boldsymbol{u} + (\nabla\boldsymbol{u})^T$, $\tilde{\eta_0}$ is the zero shear rate viscosity, $\tilde{\eta}$ is the dimensionless viscosity, h is a time constant, ξ is the viscosity in the limit of infinite shear and f is the flow index number such that $0 \leq f \leq 1$. In the case where $f = 1$, we have a constant viscosity and the model reduces to the Newtonian case. We now describe the equations governing the flow of a non-Newtonian jet by incorporating the variable viscosity given by (8.5). We use the same curved jet model as that used in the previous chapters but include

the variable viscosity terms in the governing equations and the boundary conditions. We ignore gravitational effects and consider a jet rotating in the XZ plane. In vector form the continuity and Navier-Stokes equations are given by

$$\nabla \cdot \boldsymbol{u} = 0 \tag{8.6}$$

$$\rho\left(\frac{\partial \boldsymbol{u}}{\partial t} + \boldsymbol{u}\cdot\nabla\boldsymbol{u}\right) = -\nabla p + \nabla\cdot\tau - 2\boldsymbol{\omega}\times\boldsymbol{u} - \boldsymbol{\omega}\times(\boldsymbol{\omega}\times\boldsymbol{r}) \tag{8.7}$$

where $\boldsymbol{u} = (u, v, w)$ is the velocity field, ρ density of the liquid, t is time, p is the pressure and $\boldsymbol{\omega} = (0, \omega, 0)$ is the angular velocity vector of the container and $\boldsymbol{r}$ is the position vector of any particle on the free-surface. These equations are non-dimensionalised using the same scalings (3.16) as in Chapter 4. The non-dimensional parameters in the following equations are the Weber number We, the Rossby number Rb, the aspect ratio ϵ and the Reynolds number based on the shear rate given by $Re = \rho U a/\tilde{\eta_0}$, where U is the exit velocity of the jet and a is the radius of the orifice. The non-dimensionalised continuity equation can be written as

$$\epsilon n\frac{\partial u}{\partial s} + (1+\epsilon n\cos\phi(X_sZ_{ss} - X_{ss}Z_s))\left(v + n\frac{\partial v}{\partial n} + \frac{\partial w}{\partial \phi}\right) + \epsilon n(X_sZ_{ss} - X_{ss}Z_s)(v\cos\phi - w\sin\phi) = 0. \tag{8.8}$$

The non-dimensionalised Navier-Stokes equations are given by

$$
\begin{aligned}
h_s\left(\epsilon\frac{\partial u}{\partial t}+\epsilon(v\cos\phi-w\sin\phi)(Z_{st}X_s-X_{st}Z_s)+v\frac{\partial u}{\partial n}+\frac{w}{n}\frac{\partial u}{\partial\phi}\right)+\epsilon u\frac{\partial u}{\partial s}\\
+\epsilon u(X_sZ_{ss}-X_{ss}Z_s)(v\cos\phi-w\sin\phi)=\\
-\epsilon\frac{\partial p}{\partial s}+h_s\left(\frac{2\epsilon}{Rb}(v\cos\phi-w\sin\phi)+\frac{\epsilon}{Rb^2}((X+1)X_s+ZZ_s)\right)\\
+\frac{\tilde{\eta}}{\epsilon Ren}\left[\frac{-\epsilon^3n^2\cos\phi(X_sZ_{sss}-Z_sX_{sss})}{h_s^2}\left(\frac{\partial u}{\partial s}+v\cos\phi(X_sZ_{ss}-Z_sX_{ss})\right.\right.\\
-w\sin\phi(X_sZ_{ss}-Z_sX_{ss}))+\frac{\epsilon^2n}{h_s}\left(-u(X_sZ_{ss}-Z_sX_{ss})^2+\frac{\partial^2u}{\partial s^2}\right.\\
+2\frac{\partial v}{\partial s}\cos\phi(X_sZ_{ss}-Z_sX_{ss})+(v\cos\phi-w\sin\phi)(X_sZ_{sss}-Z_sX_{sss})\\
\left.\left.-2\frac{\partial w}{\partial s}\sin\phi(X_sZ_{ss}-X_{ss}Z_s)\right)+(1+2\epsilon n\cos\phi(X_sZ_{ss}-X_{ss}Z_s))\frac{\partial u}{\partial n}+nh_s\frac{\partial^2u}{\partial n^2}\right.\\
\left.-\epsilon\frac{\partial u}{\partial\phi}\sin\phi(X_sZ_{ss}-Z_sX_{ss})+\frac{h_s}{n}\frac{\partial^2u}{\partial\phi^2}\right]+\frac{1}{\epsilon Re}\left[\frac{2\epsilon^2}{h_s}\frac{\partial\tilde{\eta}}{\partial s}\left(\frac{\partial u}{\partial s}+v\cos\phi(X_sZ_{ss}-Z_sX_{ss})\right.\right.\\
\left.-w\sin\phi(X_sZ_{ss}-Z_sX_{ss}))+\frac{1}{n}\frac{\partial\tilde{\eta}}{\partial\phi}\left(\epsilon u\sin\phi(X_sZ_{ss}-Z_sX_{ss})+\frac{h_s}{n}\frac{\partial u}{\partial\phi}+\epsilon\frac{\partial w}{\partial s}\right)\right.\\
\left.+\frac{\partial\tilde{\eta}}{\partial n}\left(\epsilon\frac{\partial v}{\partial s}-\epsilon y\cos\phi(X_sZ_{ss}-Z_sX_{ss})+h_s\frac{\partial u}{\partial n}\right)\right],
\end{aligned}
\tag{8.9}
$$

$$
\begin{aligned}
&h_s\left(\epsilon\frac{\partial v}{\partial t}+\epsilon u\cos\phi(X_{st}Z_s-Z_{st}X_s)+v\frac{\partial v}{\partial n}+\frac{w}{n}\frac{\partial v}{\partial\phi}-\frac{w^2}{n}\right)\\
&\qquad+\epsilon u\frac{\partial v}{\partial s}-\epsilon\cos\phi(X_sZ_{ss}-Z_sX_{ss})u^2\\
&=\left(-\frac{\partial p}{\partial n}-\frac{2\epsilon}{Rb}u\cos\phi+\frac{\epsilon\cos\phi}{Rb^2}((X+1)Z_s-ZX_s+\epsilon n\cos\phi)\right)h_s\\
&+\frac{\tilde{\eta}}{\epsilon Re}n\left[\frac{-\epsilon^3n^2\cos\phi(X_sZ_{sss}-Z_sX_{sss})}{h_s^2}\left(\frac{\partial v}{\partial s}-u\cos\phi(X_sZ_{ss}-Z_sX_{ss})\right)\right.\\
&+\frac{\epsilon^2n}{h_s}\left(-v\cos^2\phi(X_sZ_{ss}-Z_sX_{ss})^2+\frac{\partial^2v}{\partial s^2}-2\frac{\partial u}{\partial s}\cos\phi(X_sZ_{ss}-Z_sX_{ss})\right.\\
&\qquad\left.-u\cos\phi(X_sZ_{sss}-Z_sX_{sss})+w\sin\phi\cos\phi(X_sZ_{ss}-Z_sX_{ss})^2\right)\\
&\qquad+(1+2\epsilon n\cos\phi(X_sZ_{ss}-Z_sX_{ss}))\frac{\partial v}{\partial n}+nh_s\frac{\partial^2v}{\partial n^2}\\
&\qquad\left.-\epsilon\left(\frac{\partial v}{\partial\phi}-w\right)\sin\phi(X_sZ_{ss}-Z_sX_{ss})+\frac{h_s}{n}\left(\frac{\partial^2v}{\partial\phi^2}-v-2\frac{\partial w}{\partial\phi}\right)\right]\\
&\qquad+\frac{1}{\epsilon Re}\left[\frac{\epsilon}{h_s}\frac{\partial\tilde{\eta}}{\partial s}\left(\epsilon\frac{\partial v}{\partial s}-\epsilon u\cos\phi(X_sZ_{ss}-Z_sX_{ss})+h_s\frac{\partial u}{\partial n}\right)\right.\\
&\qquad\left.+\frac{\partial\tilde{\eta}}{\partial n}\left(2h_s\frac{\partial v}{\partial n}\right)+\frac{h_s}{n}\frac{\partial\tilde{\eta}}{\partial\phi}\left(\frac{\partial w}{\partial n}-\frac{w}{n}+\frac{1}{n}\frac{\partial v}{\partial\phi}\right)\right]
\end{aligned}
\tag{8.10}
$$

and

$$
\begin{aligned}
&h_s\left(\epsilon\frac{\partial w}{\partial t}+\epsilon u\sin\phi(Z_{st}X_s-X_{st}Z_s)+v\frac{\partial w}{\partial n}+\frac{w}{n}\frac{\partial w}{\partial\phi}+\frac{wv}{n}\right)\\
&+\epsilon u\frac{\partial w}{\partial s}+\epsilon\sin\phi(X_sZ_{ss}-X_{ss}Z_s)u^2\\
&=h_s\left(-\frac{1}{n}\frac{\partial p}{\partial\phi}+\frac{2\epsilon}{Rb}u\sin\phi+\frac{\epsilon\sin\phi}{Rb^2}(ZX_s-(X+1)Z_s-\epsilon n\cos\phi)\right)\\
&+\frac{\tilde{\eta}}{\epsilon nRe}\left[\frac{-\epsilon^3n^2\cos\phi(X_sZ_{sss}-Z_sX_{sss})}{h_s^2}\left(\frac{\partial w}{\partial s}\right.\right.\\
&\left.+u\sin\phi(X_sZ_{ss}-X_{ss}Z_s)\right)+\frac{\epsilon^2n}{h_s}\left(-w\sin^2\phi(X_sZ_{ss}-X_{ss}Z_s)^2+\frac{\partial^2w}{\partial s^2}\right.\\
&+2\frac{\partial u}{\partial s}\sin\phi(X_sZ_{ss}-X_{ss}Z_s)+u\sin\phi(X_sZ_{sss}-Z_sX_{sss})\\
&\left.+v\sin\phi\cos\phi(X_sZ_{ss}-Z_sX_{ss})^2\right)+(1+2\epsilon n\cos\phi(X_sZ_{ss}-Z_sX_{ss}))\frac{\partial w}{\partial n}\\
&\left.+nh_s\frac{\partial^2w}{\partial n^2}-\epsilon\left(\frac{\partial w}{\partial\phi}+v\right)\sin\phi(X_sZ_{ss}-Z_sX_{ss})+\frac{h_s}{n}\left(\frac{\partial^2w}{\partial\phi^2}-w+2\frac{\partial v}{\partial\phi}\right)\right]\\
&+\frac{1}{\epsilon Re}\left[\frac{\epsilon}{h_s}\frac{\partial\tilde{\eta}}{\partial s}\left(\epsilon\frac{\partial w}{\partial s}+\epsilon u\sin\phi(X_sZ_{ss}-Z_sX_{ss})+\frac{h_s}{n}\frac{\partial u}{\partial\phi}\right)\right.\\
&\left.+\frac{h_s}{n}\frac{\partial\tilde{\eta}}{\partial n}\left(\frac{\partial v}{\partial\phi}-w+n\frac{\partial w}{\partial n}\right)+\frac{\partial\tilde{\eta}}{\partial\phi}\frac{2h_s}{n^2}\left(\frac{\partial w}{\partial\phi}+v\right)\right].
\end{aligned}
\tag{8.11}
$$

The boundary conditions applied are the kinematic, normal and tangential stress conditions. The non-dimenstionalised kinematic stress condition can be written as

$$
\begin{aligned}
&h_s\left(\epsilon\frac{\partial R}{\partial t}+\cos\phi(X_tZ_s-X_sZ_t)-v+\frac{w}{n}\frac{\partial R}{\partial\phi}+\frac{1}{n}\frac{\partial R}{\partial\phi}\sin\phi(X_tZ_s-X_sZ_t)\right)\\
&+\epsilon u\frac{\partial R}{\partial s}-\epsilon\frac{\partial R}{\partial s}(X_tZ_s+Z_tX_s+\epsilon n\cos\phi(X_sZ_{st}-X_{st}Z_s))=0.
\end{aligned}
\tag{8.12}
$$

The tangential stress conditions are given by

$$
\begin{aligned}
&\left(1-\frac{\epsilon^2}{h_s^2}\left(\frac{\partial R}{\partial s}\right)^2\right)\left(\epsilon\frac{\partial v}{\partial s}+h_s\frac{\partial u}{\partial n}-\epsilon u\cos\phi(X_sZ_{ss}-X_{ss}Z_s)\right)+2\epsilon\frac{\partial R}{\partial s}\left(\frac{\partial v}{\partial n}\right.\\
&\left.-\frac{\epsilon}{h_s}\frac{\partial u}{\partial s}-\frac{\epsilon(v\cos\phi-w\sin\phi)}{h_s}(X_sZ_{ss}-X_{ss}Z_s)\right)=0,
\end{aligned}
\tag{8.13}
$$

and

$$\left(1-\frac{1}{n^2}\left(\frac{\partial R}{\partial \phi}\right)^2\right)\left(\frac{\partial w}{\partial n}-\frac{w}{n}+\frac{1}{n}\frac{\partial v}{\partial \phi}\right)+\frac{2}{n}\frac{\partial R}{\partial \phi}\left(\frac{\partial v}{\partial n}-\frac{1}{n}\left(\frac{\partial w}{\partial \phi}+v\right)\right)=0. \tag{8.14}$$

The normal stress condition is

$$\begin{aligned} p-\frac{2\tilde{\eta}}{Re}E^2\Bigg(&\frac{\epsilon^2}{h_s^3}\left(\frac{\partial R}{\partial s}\right)^2\left(\frac{\partial u}{\partial s}+(v\cos\phi-w\sin\phi)(X_sZ_{ss}-X_{ss}Z_s)\right)\\ &+\frac{1}{\epsilon}\frac{\partial v}{\partial n}+\frac{1}{\epsilon R^3}\left(\frac{\partial R}{\partial \phi}\right)^2\left(\frac{\partial w}{\partial \phi}+v\right)-\frac{\epsilon}{h_s}\frac{\partial R}{\partial s}\left(\frac{\partial v}{\partial s}+\frac{1}{\epsilon}\frac{\partial u}{\partial n}-\frac{u}{h_s}\cos\phi(X_sZ_{ss}-X_{ss}Z_s)\right)\\ &-\frac{1}{\epsilon R}\frac{\partial R}{\partial \phi}\left(\frac{\partial w}{\partial n}-\frac{w}{R}+\frac{1}{R}\frac{\partial v}{\partial \phi}\right)+\frac{\epsilon}{h_sR}\frac{\partial R}{\partial s}\frac{\partial R}{\partial \phi}\left(\frac{1}{\epsilon R}\frac{\partial u}{\partial \phi}+\frac{u}{h_s}\sin\phi(X_sZ_{ss}-X_{ss}Z_s)\right.\\ &\left.+\frac{1}{h_s}\frac{\partial u}{\partial s}\right)\Bigg)=\frac{\kappa}{We}, \end{aligned} \tag{8.15}$$

where

$$\kappa=\frac{1}{h_s}\left(\epsilon^2\frac{\partial}{\partial s}\left(-\frac{1}{h_sE}\frac{\partial R}{\partial s}\right)+\frac{1}{n}\frac{\partial}{\partial n}\left(\frac{nh_s}{E}\right)+\frac{\partial}{\partial \phi}\left(-\frac{h_s}{n^2E}\frac{\partial R}{\partial \phi}\right)\right),$$

$$h_s=(1+\epsilon n\cos\phi(X_sZ_{ss}-X_{ss}Z_s)),$$

and

$$E=\left(1+\frac{\epsilon^2}{h_s^2}\left(\frac{\partial R}{\partial s}\right)^2+\frac{1}{n^2}\left(\frac{\partial R}{\partial \phi}\right)^2\right)^{1/2}.$$

We also have the arc length condition given by

$$X_s^2+Z_s^2=1 \tag{8.16}$$

and centreline conditions

$$v=w=0 \ \text{ on } \ n=0.$$

8.3.1 Asymptotic Solution

We solve the above equations by introducing steady asymptotic expansions in ϵ for all our variables

$$\boldsymbol{u} = \boldsymbol{u_0}(s) + \epsilon \boldsymbol{u_1}(s, n, \phi) + O(\epsilon^2),$$
$$p = p_0(s, n, \phi) + \epsilon p_1(s, n, \phi) + O(\epsilon^2),$$
$$R = R_0(s) + \epsilon R_1(s, \phi) + O(\epsilon^2),$$
$$\boldsymbol{X} = \boldsymbol{X_0}(s) + \epsilon \boldsymbol{X_1}(s) + O(\epsilon^2),$$
$$\eta = \eta_0(s) + \epsilon \eta_1(s, n, \phi) + O(\epsilon^2),$$

where $\boldsymbol{u_i} = u_i \boldsymbol{e_s} + v_i \boldsymbol{e_n}, v_0 = 0$ and $\boldsymbol{X_i} = X_i \boldsymbol{i} + Z_i \boldsymbol{k}$ for $i = 0, 1, \ldots$. Substituting these expansions into the equation for the variable viscosity we have the following leading order viscosity term

$$\tilde{\eta} = (1 - \xi)[1 + (\sqrt{3}\tilde{h}u_{0s})^2]^{\frac{f-1}{2}} + \xi + \epsilon n M \cos\phi + O(\epsilon^2), \tag{8.17}$$

where $\tilde{h}$ is non-dimensionalised h and M is some function of s and ϕ which can be determined by going to next order. We denote the leading order component of viscosity by η_0 (where $\eta_0 = (1 - \xi)[1 + (\sqrt{3}\tilde{h}u_{0s})^2]^{\frac{f-1}{2}} + \xi$). The above expansions are substituted into the governing equations and the boundary conditions ((8.8)-(8.15)). After lengthy

algebra we arrive at

$$n\frac{du_0}{ds} + v_1 + n\frac{\partial v_1}{\partial n} = 0, \tag{8.18}$$

$$u_0\frac{du_0}{ds} = -\frac{\partial p_0}{\partial s} + \frac{1}{Rb^2}((X+1)X_s + ZZ_s) + \frac{\eta_0}{Re}\left(\frac{1}{n}\frac{\partial u_1}{\partial n} + \frac{\partial^2 u_1}{\partial n^2} + \frac{1}{n^2}\frac{\partial^2 u_1}{\partial \phi^2}\right), \tag{8.19}$$

$$\frac{p_0}{\partial n} = 0, \tag{8.20}$$

$$-\cos\phi(X_sZZ_{ss} - Z_sX_{ss}){u_0}^2 = -\frac{\partial p_1}{\partial n} - \frac{2u_0\cos\phi}{Rb} + \frac{\cos\phi}{Rb} + \frac{\cos\phi}{Rb^2}((X+1)Z_s - ZX_s) + \frac{\eta_0}{Re}\left(\frac{1}{n}\frac{\partial v_1}{\partial n} + \frac{\partial^2 v_1}{\partial n^2} + \frac{1}{n^2}\left(-v_1 + \frac{\partial^2 v_1}{\partial \phi^2}\right)\right), \tag{8.21}$$

$$\frac{p_0}{\partial \phi} = 0, \tag{8.22}$$

$$\sin\phi(X_sZ_{ss} - Z_sX_{ss}){u_0}^2 = -\frac{1}{n}\frac{\partial p_1}{\partial \phi} + \frac{2u_0\sin\phi}{Rb} + \frac{\sin\phi}{Rb^2}(ZX_s - (X+1)Z_s) + \frac{\eta_0}{Re}\left(\frac{2}{n^2}\frac{v_1}{\partial \phi}\right), \tag{8.23}$$

$$u_0\frac{dR_0}{ds} = v_1 \ \text{ on } \ n = R_0, \tag{8.24}$$

$$p_1 - \frac{2\eta_0}{Re}\frac{\partial v_1}{\partial n} = \frac{1}{We}\left(-\frac{1}{{R_0}^2}\left(R_1 + \frac{\partial^2 R_1}{\partial \phi^2}\right) + \cos\phi(X_sZ_{ss} - Z_sX_{ss})\right) \ \text{ on } \ n = R_0, \tag{8.25}$$

$$v_1 = 0 \ \text{ on } \ n = 0 \tag{8.26}$$

$$X_s^2 + Z_s^2 = 1. \tag{8.27}$$

For simplicity, we have replaced X_0 and Z_0 with X and Z, respectively. Even though these equations appear to be different to the inviscid leading order jet equations (3.42) derived by Wallwork [68], they compute the same solution at leading order as in the inviscid case. Effects of viscosity can be looked at higher order and for this a new scaling for the Reynolds number $\bar{Re} = \epsilon Re$ is required in order to obtain a distinguished limit in the linear stability analysis in the next section. But since viscosity does not affect the leading order solution, we can use the inviscid equations to compute X, Z, u_0 and R_0.

Simplifying these equations further gives us the following set of equations

$$p_0 = \frac{1}{R_0 We}, \tag{8.28}$$

$$u_0 = \left(1 + \frac{1}{Rb^2}\left(X^2 + 2X + Z^2\right) + \frac{2}{We}\left(1 - \frac{1}{R_0}\right)\right)^{\frac{1}{2}}, \tag{8.29}$$

$$v_1 = -\frac{n}{2}\frac{du_0}{ds}, \tag{8.30}$$

$$p_1 = \frac{n}{WeR_0}\cos\phi\left(X_s Z_{ss} - X_{ss} Z_s\right) + h_1(s) - \frac{\eta_0}{Re}\frac{du_0}{ds}, \tag{8.31}$$

$$Z_{ss} = \frac{X_s}{u_0^2 - \frac{1}{WeR_0}}\left(\frac{2u_0}{Rb} + \frac{ZX_s - (X+1)Z_s}{Rb^2}\right), \tag{8.32}$$

$$\frac{du_0}{ds} = \frac{2u_0}{R_0}\frac{dR_0}{ds}, \tag{8.33}$$

$$\text{and} \quad \frac{dR_0}{ds} = -\frac{R_0\left((X+1)X_s + ZZ_s\right)}{2Rb^2\left(u_0^2 + \frac{1}{2WeR_0}\right)}. \tag{8.34}$$

The apparent viscosity term only appears in the equation for p_1 which does not affect the trajectory, velocity or radius of the jet. Equations (8.29), (8.32) and (8.34) can be solved computationally using a Runge-Kutta scheme in MATLAB subject to the initial conditions $X_s = 1, X = Z = Z_s = 0, u_0 = R_0 = 1$ at $s = 0$. The leading order apparent viscosity η_0, which describes the rheology of a given non-Newtonian fluid, is computed using the expression $\eta_0 = (1-\xi)[1 + (\sqrt{3}\tilde{h}u_{0s})^2]^{\frac{f-1}{2}} + \xi$, by substituting the value for u_{0s} computed numerically from (8.33).

8.3.2 Linear Stability Analysis

This section examines the linear stability of disturbances about our steady state solution from the above section. Again, we use a multiple scales approach by introducing $\bar{s}$ and $\bar{t}$

and perturb the steady state solution by adding small disturbances

$$u = u_0 + \delta\hat{u}\exp(ik\bar{s} + \omega\bar{t}) + c.c., \tag{8.35}$$

$$R = R_0 + \delta\hat{R}\exp(ik\bar{s} + \omega\bar{t}) + c.c., \tag{8.36}$$

$$p = p_0 + \delta\hat{p}\exp(ik\bar{s} + \omega\bar{t}) + c.c., \tag{8.37}$$

$$X = u_0 + \delta\epsilon\hat{X}\exp(ik\bar{s} + \omega\bar{t}) + c.c., \tag{8.38}$$

$$Z = Z_0 + \delta\epsilon\hat{Z}\exp(ik\bar{s} + \omega\bar{t}) + c.c., \tag{8.39}$$

$$\eta = \eta_0 + \delta\epsilon\hat{\eta}\exp(ik\bar{s} + \omega\bar{t}) + c.c., \tag{8.40}$$

where $k(s)$ is the wavenumber, $\omega(s)$ the frequency, δ is a small dimensionless constant and c.c. denotes complex conjugate. These expansions are substituted into the steady non-Newtonian equations and linearised by taking terms of $O(\delta)$. Examining normal modes, we obtain the following eigenvalue relationship

$$\begin{gathered}
-2ik^5\eta_0 We I_1(\tilde{k}R_0)R_0^2u_0 + k^5 I_1(kR_0)ReI_1(\tilde{k}R_0)R_0^2 \\
+k^4 I_0(kR_0)WeRe{R_0}^2 I_1(\tilde{k}R_0)u_0^2 - 2ik^4\eta_0 We I_1(\tilde{k}R_0)I_1(kR_0)R_0u_0 \\
-2k^4\eta_0 We I_1(\tilde{k}R_0)I_0(kR_0)R_0^2\omega + 4ik^4\eta_0 We I_1(kR_0)I_0(\tilde{k}R_0)\tilde{k}R_0^2u_0 \\
+4k^3\eta_0 We I_1(kR_0)I_0(\tilde{k}R_0)\tilde{k}R_0^2\omega - 2ik^3\eta_0 We I_1(\tilde{k}R_0)I_0(kR_0)R_0^2\tilde{k}^2u_0 \\
-I_1(kR_0)k^3 ReI_1(\tilde{k}R_0) - 2ik^3 I_0(kR_0)WeReR_0^2 I_1(\tilde{k}R_0)\omega \\
-2k^3\eta_0 We I_1(\tilde{k}R_0)I_1(kR_0)R_0\omega - k^3\tilde{k}^2 I_1(kR_0)ReI_1(\tilde{k}R_0)R_0^2 \\
-2k^2\eta_0 We I_1(\tilde{k}R_0)I_0(kR_0)R_0^2\tilde{k}^2\omega + k^2 I_0(kR_0)WeReR_0^2 I_1(\tilde{k}R_0)u_0^2\tilde{k}^2 \\
-k^2 I_0(kR_0)WeReR_0^2 I_1(\tilde{k}R_0)\omega^2 + 2ik^2\tilde{k}^2\eta_0 We I_1(\tilde{k}R_0)I_1(kR_0)R_0u_0 \\
-2ikI_0(kR_0)WeReR_0^2 I_1(\tilde{k}R_0)u_0\tilde{k}^2\omega + I_1(kR_0)kReI_1(\tilde{k}R_0)\tilde{k}^2 \\
+2k\tilde{k}^2\eta_0 We I_1(\tilde{k}R_0)I_1(kR_0)R_0\omega - I_0(kR_0)WeReR_0^2 I_1(\tilde{k}R_0)\omega^2\tilde{k}^2 = 0
\end{gathered} \tag{8.41}$$

where

$$\tilde{k} = \sqrt{k^2 + \frac{Re(\omega + iku_0)}{\eta_0}}, \tag{8.42}$$

and I_n is the modified Bessel function of order n. This gives the dispersion relation for a non-Newtonian jet incorporating the apparent viscosity η_0 which is calculated by solving the steady state equations (8.29)-(8.34) and describes how the steady state affects it. Note that for a straight non-Newtonian liquid jet, $u_{0s} = 0$ since $u_0 = 1$. Therefore, if $\eta_0 = 1$, the non-Newtonian dispersion relation (8.41) becomes equivalent to the Newtonian dispersion relation for a straight jet.

8.4 Absolute Instability in Non-Newtonian Liquid Jets

We now proceed to examine absolute instability in curved non-Newtonian liquid jets. The critical curve calculated in Chapter 2 can not be applied in this case as the dispersion relation now depends on the apparent viscosity and we are required to take into account the rheology of the non-Newtonian liquid. Therefore, we cannot use the concept of calculating the Re_{local}-We_{local} trajectory. Thus we are required to adopt a rather lengthy methodology involving the computation of u_0, R_0 and η_0 by solving equations (8.29)-(8.34) numerically. These values are substituted into the eigenvalue relation (8.41) along with parameters We, Rb and Re. We then solve the dispersion relation by using the same approach that is exercised in Section 2.2 to compute the critical curve. If we denote the dispersion relation (8.41) by

$$F(\omega(k), k) = 0, \tag{8.43}$$

then differentiating it with respect to k gives

$$G\left(\frac{\partial \omega}{\partial k}, \omega, k\right) = \frac{\partial}{\partial k} F(\omega(k), k). \tag{8.44}$$

We know that at the onset of absolute instability, we have zero group velocity of the disturbances ($\frac{\partial \omega}{\partial k} = 0$). Substituting this in (8.44) we get

$$G\left(\frac{\partial \omega}{\partial k} = 0, \omega(k), k\right) = 0. \tag{8.45}$$

We can then solve equations (8.43) and (8.45) simultaneously for ω and k, by substituting numerical solutions for u_0, R_0 and η_0 obtained from equations (8.29)-(8.34) for a given s and choosing We, Rb and Re. To solve these equations computationally, we apply a two-dimensional Newton-Raphson method, starting with an initial guess for k and ω. Depending on the sign of $Re(\omega)$, we are able to ascertain the type of instability the jet is undergoing for that particular value of s. If the solution has $Re(\omega) < 0$, then the jet is convectively unstable and for $Re(\omega) > 0$ the jet is considered to be absolutely unstable. Based on this concept, we have established three different kinds of solutions:

- Convective: When the dispersion relation produces a solution having $Re(\omega) < 0$ for all s.
- Mode 4: When solutions to the dispersion relation result $Re(\omega) < 0$ for $s = 0, ..., m$ and for $s > m$ the solution to the dispersion relation results in $Re(\omega) > 0$. The s value at which $Re(\omega)$ changes sign from negative to positive, marks the onset of absolute instability and indicates a transition from convective to absolute instability (similar to Mode 4 type behaviour in the Newtonian case).
- No Jet: When the solution to the dispersion relation computes $Re(\omega) > 0$ for $s = 0$, implying that the jet is absolutely unstable to start with.

Tables 8.1-8.6 show the results obtained by solving the dispersion relation for various values of s and identifying the nature of the instability. Equations (8.29)-(8.34) are solved to obtain numerical solutions for u_0, R_0 and η_0 as s increases. These are then substituted into the dispersion relation along with chosen parameter values for $Re, We, Rb, F, \xi, \tilde{h}$ and f and the dispersion relation is then solved for k and ω. In the Newton-Raphson method, we try initial conditions for k and ω originating from all possible combinations of quadrants.

Tables 8.1, 8.2, 8.3 and 8.6 having $F = 20, Re = 10, Rb = 2, \xi = 0.5, \tilde{h} = 1$ and $f = 0.7$ with $We = 1.1, 1.2, 1.3$ and 1.8, respectively, show a No Jet type solution where the dispersion relation returns a solution with $Re(\omega) > 0$ for $s = 0$, implying that the

s	R_0	u_0	η_0	Nature of instability
0	1.000	1.000	0.9937	Absolute

Table 8.1: Table showing the u_0, R_0 and η_0 values for a given s for $F = 20, Re = 10, Rb = 2, We = 1.1, \xi = 0.5, \tilde{h} = 1$ and $f = 0.7$. Since the dispersion relation produces a solution which is absolutely unstable to start with at $s = 0$, this case is categorised as the No Jet solution.

s	R_0	u_0	η_0	Nature of instability
0	1.000	1.000	0.9933	Absolute

Table 8.2: Table showing the u_0, R_0 and η_0 values for a given s for $F = 20, Re = 10, Rb = 2, We = 1.2, \xi = 0.5, \tilde{h} = 1$ and $f = 0.7$. Since the dispersion relation produces a solution which is absolutely unstable to start with at $s = 0$, this case is categorised as the No Jet solution.

s	R_0	u_0	η_0	Nature of instability
0	1.000	1.000	0.9930	Absolute

Table 8.3: Table showing the u_0, R_0 and η_0 values for a given s for $F = 20, Re = 10, Rb = 2, We = 1.3, \xi = 0.5, \tilde{h} = 1$ and $f = 0.7$. Since the dispersion relation produces a solution which is absolutely unstable to start with at $s = 0$, this case is categorised as the No Jet solution.

s	R_0	u_0	η_0	Nature of instability
0	1.0000	1.0000	0.9928	Convective
10	0.9545	1.0976	0.9975	Convective
20	0.9946	1.0110	0.9925	Convective
49.9	0.9582	1.0891	0.9944	Convective

Table 8.4: Table showing the u_0, R_0 and η_0 values for a given s for $F = 20, Re = 10, Rb = 2, We = 1.4, \xi = 0.5, \tilde{h} = 1$ and $f = 0.7$. Since the dispersion relation produces a solution which is convectively unstable up to $s = 50$ (which is sufficiently large), this case corresponds to a convective solution and the jet being convectively unstable through out.

s	R_0	u_0	η_0	Nature of instability
0	1.0000	1.0000	0.9925	Convective
0.01	0.9991	1.0019	0.9924	Convective
0.1	0.9905	1.0193	0.9919	Absolute
0.2	0.9811	1.0389	0.9920	Absolute

Table 8.5: Table showing the u_0, R_0 and η_0 values for a given s for $F = 20, Re = 10, Rb = 2, We = 1.5, \xi = 0.5, \tilde{h} = 1$ and $f = 0.7$. Since the dispersion relation produces a solutions which are convectively unstable up to $s = 0.1$ and absolutely unstable after that, this case corresponds to the Mode 4 type solution.

s	R_0	u_0	η_0	Nature of instability
0	1.000	1.000	0.9919	Absolute

Table 8.6: Table showing the u_0, R_0 and η_0 values for a given s for $F = 20, Re = 10, Rb = 2, We = 1.8, \xi = 0.5, \tilde{h} = 1$ and $f = 0.7$. Since the dispersion relation produces a solution which is absolutely unstable to start with at $s = 0$, this case is categorised as the No Jet solution.

jet is absolutely unstable right at the start (as in the No Jet scenario in the Newtonian case). Table 8.4 lists the results (computed for $F = 20, Re = 10, Rb = 2, \xi = 0.5, \tilde{h} = 1, f = 0.7$ and $We = 1.4$) obtained by solving the dispersion relation as s increases. For this particular set of parameters, we find that the dispersion relation always produces a solution for ω which has $Re(\omega) < 0$. This corresponds to the convective instability type solution, where $Re(\omega)$ continues to remain negative for various values of s. Table 8.5 shows results calculated for $F = 20, Re = 10, Rb = 2, \xi = 0.5, \tilde{h} = 1, f = 0.7$ and $We = 1.8$. In this case, the dispersion relation produces solutions having $Re(\omega) < 0$ up to $s = 0.1$ and $Re(\omega) > 0$ after that point, indicating a transition from convective to absolute instability, like in Mode 4 type break-up in the Newtonian case. This is a Mode 4 type solution.

8.5 Conclusion

In this chapter, we have introduced a non-Newtonian model for curved liquid jets incorporating the Carreau rheology. We have presented the curved jet equations which calculate the trajectory of the centreline of the jet. A linear stability analysis on the steady state was carried out and a linear dispersion relation which takes into account the apparent viscosity function η_0 is shown.

Using this dispersion relation, we have studied absolute instability in curved non-Newtonian jets and found preliminary results corroborating our methodology. We have found solutions of each type described in Section 8.4; convective, Mode 4 and No Jet type solutions. A more detailed parameter search needs to be carried out. The technique applied here is very time consuming and, therefore, in order to carry out further computations and conduct a full parameter search, the process needs to be automated.

Chapter 9

Microjets

Microjets and nanojets (jets having radius of the order of micrometers and nanometers, respectively) have found important applications in the fields of biotechnology, drug manufacture, ink-jet printing, fibre spinning, electrospraying and many more. The dynamics of fluids at a microscopic scale is found to be significantly different from what is observed at a macroscopic scale. At small scales the surface area to volume ratio becomes large and consequently increases the effect of surface and interfacial properties. Incorporating these effects into the Navier-Stokes equations at small scales becomes difficult. Even though the classical continuum model is excellent for modelling jets on a macroscopic scale and gives good predications for the breakup lengths and droplet sizes, it violates the continuum hypothesis at very small scales, where the jet is made up of only a small number of molecules and becomes invalid at a microscopic level. With the increasing popularity of nanotechnology in various scientific and industrial processes, it becomes essential to understand the dynamics of fluids at very small scales.

Molecular forces play a major role as the thread breaks up to form droplets. At this point the fluid can not be treated as a continuum and the continuum mechanics model becomes invalid here. At very small scales a molecular dynamics approach, which examines the interaction between a few particles of a fluid via a computer model is used. Therefore, molecular dynamics simulations allow a better understanding of the system at a nano scale where the molecular forces become more dominant and therefore provide

more accurate results. Koplik & Banavar [33] describe the use of molecular dynamics simulations to study the rupture process at very small time and length scales in different flow situations. They found their results to agree with the Navier-Stokes equations up to length and time scales as small as 10nm and 10^{-10}s respectively.

Moseler & Landman [45] also used the molecular dynamics approach to study the formation and stability of nanojets. They derived a stochastic lubrication equation which includes the effects of thermal fluctuations as they influence the jet dynamics of small scales. They found that noise affects the dynamics of jet breakup. Eggers [20] studied the breakup of nanojets using Moseler & Landman's [45] stochastic equation and found that at small scales, thermal fluctuations become more dominant than surface tension and lead to breakup.

Furlani [24] developed a linear theory and performed a parametric study of instability and pinch-off of a viscous microjet subject to a spatially varying surface tension. They extended their theory by accommodating the effects of a Marangoni flow induced by thermal modulation of surface tension which initiates jet instability in ink-jet printing.

In this chapter we study the instability of microjets using the interface formation model which is based on dynamic surface tension. The theory of interface formation was first developed by Shikhmurzaev [58] to study the problem of moving contact lines. As the rate at which free-surface is created tends to infinity as rupture occurs, a singularity arises as the jet approaches pinch-off. This results in a deviation of surface tension from its equilibrium value which causes a surface tension gradient (Shikhmurzaev [59]). The thread is then pulled apart by this surface tension gradient leading to a mass transfer between the bulk fluid and its interface which results in a flow-induced Marangoni effect. This difference in surface tension along the jet which produces a flow-induced Marangoni effect along with capillary pressure causes the thread to break-up. The interface formation model allows for a flow-induced Marangoni effect and re-evaluates the free-surface boundary conditions incorporating the surface tension gradient. The variation between classical theory and the theory of interface formation is found to be greatest at microscopic scales

and therefore we use the interface formation model to study microjets. We compare the results obtained from the interface formation model and the classical model to molecular dynamics simulations in Section 9.2 to test their accuracy.

9.1 The Problem

The break-up of a liquid jet using the interface formation model was examined in Shikhmurzaev [59] considering the moment of rupture. We review the problem studied in Decent [13] where an axi-symmetric viscous liquid jet emerging from an orifice of radius a with exit speed U is considered. The stability of a microjet before it breaks up into droplets is studied using the interface formation model. The results for the most unstable travelling wave mode propagating down the jet are then compared with those produced by the standard classical model. We first describe the interface formation model.

9.1.1 Interface Formation Model

We examine an axi-symmetric viscous jet surrounded by a gas or vacuum having radius of the order of micrometers or nanometers. The usual conservation of mass and momentum equations are applied in the bulk fluid

$$\nabla\cdot\mathbf{u} = 0, \tag{9.1}$$

$$\frac{\partial\mathbf{u}}{\partial t} + (\mathbf{u}\cdot\nabla)\mathbf{u} = -\frac{1}{\rho}\nabla p + \nu\nabla^2\mathbf{u} \tag{9.2}$$

where $\mathbf{u}$ is the velocity of the liquid, t is time, p the pressure, ρ the density and ν the kinematic viscosity of the liquid.

The interface formation model incorporates dynamic surface tension, which causes a flow induced Maragoni effect, into the conventional boundary conditions of the classical model. The kinematic condition for a liquid-gas interface is given by

$$\frac{\partial G}{\partial t} + \mathbf{w}\cdot\nabla G = 0 \tag{9.3}$$

where $G(\mathbf{r}, t) = 0$ is the free-surface, $\mathbf{r}$ the free-surface position vector and $\mathbf{w}$ the velocity of the free-surface. The tangential stress boundary condition on the free-surface is given by

$$(\mathbf{I} - \mathbf{nn}) \cdot \mathbf{P} \cdot \mathbf{n} + \nabla\sigma = \mathbf{0} \tag{9.4}$$

where $\mathbf{I}$ is the identity tensor, $\mathbf{n}$ the unit normal to the interface pointing into the liquid, $\mathbf{P} = -p\mathbf{I} + \mu[\nabla\mathbf{u} + (\nabla\mathbf{u})^T]$ is the stress tensor, σ the variable surface tension, μ the liquid viscosity and the superscript "T" denotes transpose. The final boundary condition is the normal stress condition

$$p_0 + \mathbf{n} \cdot \mathbf{P} \cdot \mathbf{n} = \sigma\nabla \cdot \mathbf{n} \tag{9.5}$$

where p_0 is the external gas pressure.

The interface formation model employs the idea of "surface phase" which is used to describe the thin layer at the free-surface. The classical model ignores this layer. The theory of interface formation incorporates this interface layer by taking into account the surface density ϱ which is the density of the surface phase of the fluid at the free-surface to construct the surface equations. The equation of state is given by

$$\sigma = \frac{\sigma_e \varrho(\varrho_0 - \varrho)}{\varrho_e(\varrho_0 - \varrho_e)} \tag{9.6}$$

where ϱ_0 is a constant which corresponds to the value of surface density that gives zero surface tension, σ_e is the equilibrium surface tension of the free-surface and ϱ_e is the equilibrium surface density with $\varrho_0 > \varrho_e$. So when $\sigma = 0$, $\varrho = \varrho_0$ and when $\sigma = \sigma_e$, $\varrho = \varrho_e$. Also, note that in equation (9.6) $\sigma = 0$ when $\varrho = 0$. The surface continuity equation is given by

$$\frac{\partial\varrho}{\partial t} + \nabla \cdot (\varrho\mathbf{w}) = -\left(\frac{\varrho - \varrho_e}{\tau}\right) \tag{9.7}$$

where τ is known as the relaxation time and gives a characteristic timescale over which the surface tension relaxes to its equilibrium value. Blake *et al.* ([5], [6]) carried out experiments and found that the surface relaxation time depends on the viscosity of the

fluid. For liquids with low viscosity the surface relaxation time was estimated to lie between 10^{-9} to 10^{-7}s and can go up to 10^{-3}s for high viscosity fluids. It is thought that τ is proportional to μ (Blake *et al.* ([5], [6])). The next equation relates the surface tension gradient with the velocity gradient

$$(1 + 4\alpha\beta)\nabla\sigma = 4\beta(\mathbf{I} - \mathbf{nn}) \cdot (\mathbf{w} - \mathbf{u}) \tag{9.8}$$

where α and β are constants which correspond to the properties of the fluid. The following equation represents the mass transfer between the bulk fluid and the liquid-gas interface

$$\rho(\mathbf{u} - \mathbf{w})\cdot\mathbf{n} = \frac{\varrho - \varrho_e}{\tau}. \tag{9.9}$$

9.1.2 Instability of Microjets

To study the stability of a microjet prior to breakup, we consider an axisymmetric viscous liquid jet emerging from an orifice of radius a with exit speed U. An axisymmetric cylindrical polar coordinate system is used to describe the jet where the central axis of the system coincides with the centreline of the jet. The equations of the interface formation model introduced in the previous section are non-dimensionalised. Velocities are non-dimensionalised with respect to U, radial lengths with respect to the radius of the orifice a and axial lengths with respect to the (unknown) length of the jet s. The scales used for time, pressure, surface tension and surface density are $s/U, \rho U^2, \sigma_e$ and ϱ_e, respectively.

The origin of the axisymmetric cylindrical polar coordinate system coincides with the centre of the orifice and, after non-dimensionalisation, the coordinate system is given by (r, z), where r is the radial coordinate and z the axial coordinate with z-axis pointing upstream. The velocity of the liquid is $\mathbf{u} = u\mathbf{e_z} + v\mathbf{e_r}$, where $\mathbf{e_z}$ and $\mathbf{e_r}$ are unit vectors in the z and r directions, respectively. The free-surface is given by $r = R(z, t)$ and surface velocity by $\mathbf{w} = u^s\mathbf{e_z} + v^s\mathbf{e_r}$, where t is the non-dimensional time. We consider only

non-dimensional quantities from here on.

We use the slender jet expansions introduced by Eggers & Dupont [21]

$$u = u_1(z,t) + \epsilon^2 u_2(r,z,t) + O(\epsilon^4), \tag{9.10}$$

$$v = \epsilon v_1(r,z,t) + \epsilon^3 v_2(r,z,t) + O(\epsilon^5), \tag{9.11}$$

$$u^s = u_1^s(z,t) + \epsilon^2 u_2^s(z,t) + O(\epsilon^4), \tag{9.12}$$

$$v^s = \epsilon v_1^s(z,t) + \epsilon^3 v_2^s(z,t) + O(\epsilon^5), \tag{9.13}$$

$$p = p_1(z,t) + \epsilon^2 p_2(r,z,t) + O(\epsilon^4), \tag{9.14}$$

$$R = R_1(z,t) + \epsilon R_2(z,t) + O(\epsilon^2), \tag{9.15}$$

$$\sigma = \sigma_1(z,t) + \epsilon\sigma_2(z,t) + O(\epsilon^2) \tag{9.16}$$

$$\text{and} \quad \varrho = \varrho_1(z,t) + \epsilon\varrho_2(z,t) + O(\epsilon^2), \tag{9.17}$$

where $\epsilon = a/s$. Here ϵ is taken to be small so that the jet is slender. These expansions are then substituted into the interface formation model (9.1)-(9.9) and the limit $\epsilon \to 0$ is taken to give the following set of equations

$$u_{1t} + u_1 u_{1z} = \frac{\sigma_{1z}}{We}\left(\frac{2}{R_1} - \kappa\right) - \frac{\sigma_1 \kappa_z}{We} + \frac{3u_{1zz}}{\hat{Re}} + \frac{6R_{1z}u_{1z}}{R_1 \hat{Re}}, \tag{9.18}$$

$$\kappa = \frac{1}{R_1}\left(1 + \epsilon^2 R_{1z}^2\right)^{-1/2} - \epsilon^2 R_{1zz}\left(1 + \epsilon^2 R_{1z}^2\right)^{-3/2}, \tag{9.19}$$

$$R_{1t} + u_1 R_{1z} + \frac{1}{2}R_1 u_{1z} = \hat{L}\left(\varrho_1 - 1\right), \tag{9.20}$$

$$\varrho_{1t} + \varrho_{1z}u_1^s + \varrho_1 u_{1z}^s + \frac{\varrho_1 v_1^s}{R_1} = \frac{1}{\hat{Y}}\left(1 - \varrho_1\right), \tag{9.21}$$

$$\sigma_1 = \varrho_1\left(1 + \lambda - \lambda\varrho_1\right), \tag{9.22}$$

$$v_1 = -\frac{r}{2}u_{1z}, \tag{9.23}$$

$$v_1^s = R_{1t} + u_1^s R_{1z}, \tag{9.24}$$

$$u_1^s = u_1 + \hat{A}\sigma_{1z} \tag{9.25}$$

$$\text{and} \quad p_1 = \frac{\sigma_1 \kappa}{We} - \frac{u_{1z}}{\hat{Re}}, \tag{9.26}$$

where subscripts denote differentiation with respect to the subscript. Here $\hat{Re}$, We, $\hat{Y}$, λ, $\hat{A}$ and $\hat{L}$ are non-dimensional parameters defined as

$$\hat{Re} = \frac{sU}{\nu}, We = \frac{\rho U^2 a}{\sigma_e}, \hat{Y} = \frac{\tau U}{s}, \lambda = \frac{\varrho_e}{\varrho_0 - \varrho_e}, \hat{A} = \frac{(1+4\alpha\beta)\,\sigma_e}{4\beta s U}, \hat{L} = \frac{\varrho_e s}{\tau U \rho a} \tag{9.27}$$

where $\hat{Re}$ is Reynolds number, We is the Weber number, $\hat{Y}$ relates lengths s and τU, λ relates the equilibrium surface density ϱ_e to the surface density that gives zero surface tension ϱ_0, $\hat{A}$ relates constants in (9.8) and $\hat{L}$ relates constants in (9.9).

As in the standard procedure for studying stability in liquid jets using the classical model, the higher order terms have been retained in the equation for curvature (9.19) in order to prevent instability subject to waves with zero wavelength (see Middleman [44]). When $\hat{Y} = 0$ in the equations above, we find that they correspond to the classical model for a slender viscous jet.

Two different scalings for s were considered in Decent [13]. The first case assumes that $a/(\tau U) = O(1)$ since, if $a/(\tau U) = O(1)$ then $\hat{Y} = O(\epsilon)$. Here s is taken to be the unknown breakup length. In the second case it was assumed that $a << \tau U$ and the axial lengthscale was taken to be $s = \tau U$, since we have $\hat{Y} = 1$ if $s = \tau U$. The jet is considered to be slender with a small aspect ratio $\epsilon = a/s << 1$ in both cases. We will only consider the first of these cases which is thought to be physically more realistic: see Decent [13].

The first case the steady state of equations (9.1)-(9.9) (and also (9.18)-(9.26)) is found to be $u = R = u^s = \sigma = \varrho = 1, p = 1/We$ and $v = v^s = 0$ which corresponds to a uniform straight jet. These are perturbed by using the unsteady expansions

$$u_1 = 1 + \delta\hat{u}(z,t)\exp(ik\bar{z} + \omega\bar{t}) + c.c. + O(\delta^2), \tag{9.28}$$

$$R_1 = 1 + \delta\hat{R}(z,t)\exp(ik\bar{z} + \omega\bar{t}) + c.c. + O(\delta^2), \tag{9.29}$$

$$\sigma_1 = 1 + \delta\hat{\sigma}(z,t)\exp(ik\bar{z} + \omega\bar{t}) + c.c. + O(\delta^2), \tag{9.30}$$

$$\text{and} \quad \varrho_1 = 1 + \delta\hat{\varrho}(z,t)\exp(ik\bar{z} + \omega\bar{t}) + c.c. + O(\delta^2) \tag{9.31}$$

where δ is the scale for the non-dimensional amplitude of the small linear unstable travelling wave such that $0 < \delta \ll \epsilon \ll 1$, k is the wave number of the travelling wave, ω is the temporal growth rate and frequency, $\bar{z} = z/\epsilon$ is a short lengthscale, $\bar{t} = t/\epsilon$ is a short timescale and *c.c.* denotes complex conjugate. These multiple scales reflect that the waves which cause break-up are short compared to the length of the jet. The above expansions (9.28)-(9.31) are substituted in the slender jet equations (9.18)-(9.26) and linearised in δ. Then by taking $\epsilon \to 0$ it is found that the relationship between ω and k is given by setting the determinant of the following matrix equal to zero. This matrix is

$$\begin{pmatrix} \omega + ik + 3k^2/Re & ik\,(k^2-1)/We & -ik/We \\ ik/2 & \omega + ik & L/(\lambda - 1) \\ ik\,(1-\lambda)/2 & 0 & \omega + ik + Ak^2\,(\lambda - 1) + L + 1/Y \end{pmatrix} \tag{9.32}$$

where

$$Re = \frac{aU}{\nu},\ \ Y = \frac{\tau U}{a},\ \ A = \frac{(1 + 4\alpha\beta)\,\sigma_e}{4\beta a U},\ \ L = \frac{\varrho_e}{\tau U \rho}. \tag{9.33}$$

Here Re is Reynolds number, Y gives the relationship between a and τU, A relates constants α and β and L relates ϱ_e and ρ. Note that the unknown breakup length s has dropped out of the formulation, as required.

We briefly mention the classical results before examining the results of the interface formation model as we will compare the results obtained from the two models in the next section. Rayleigh [55] and Weber [69] carried out an instability analysis of the steady state in the classical model (given by $u = R = 1$ and $v = 0$). Chapter 1 gives a brief review of their work. The eigenvalue relation using the slender jet approximation is given by

$$\omega = -ik + k\left(\frac{-6Ohk + 2\sqrt{9Oh^2k^2 - 2k^2 + 2}}{4\sqrt{We}}\right) \tag{9.34}$$

where $Oh = \mu/\sqrt{\sigma_e a \rho} = \sqrt{We}/Re$ is the Ohnesorge number. The wave mode where $Re(\omega)$ is a global maximum corresponds to the most unstable mode. From the expression

above, the wavenumber of the most unstable wave mode is given by

$$k = k^* = \frac{1}{\sqrt{2 + 3\sqrt{2}Oh}} \tag{9.35}$$

It is found that this mode is always unstable as the $Re(\omega)$ value obtained by substituting this k^* value into (9.34) gives $Re(\omega) > 0$ at $k = k^*$.

We now compute the most unstable wave mode using (9.32) and compare it to (9.34) and (9.35) for small Y. (Remember, $Y = 0$ turns the interface formation model into the classical model.) Setting the determinant of (9.32) to zero gives a relation between ω and k. Therefore, we have an equation for ω in terms of k. We go through each solution of ω to find the value of k for which $Re(\omega)$ is a maximum. For the inviscid limit, i.e. $Y \to 0$, $Re \to \infty$ and $Oh \to 0$, we have the following asymptotic result for the wavenumber of the most unstable mode from (9.32)

$$k^* = \frac{1}{\sqrt{2}} + Y\left(\frac{1-\lambda}{8\sqrt{We}}\right) \tag{9.36}$$

$$+Y^2\frac{\sqrt{2}(1-\lambda)}{128We}\left(8\sqrt{2We}A(1-\lambda) - 12\sqrt{2We}L + 8WeAL - 3\lambda - 1\right) + O(Y^3).$$

For $Y = 0$ and $Oh = 0$, the above result is equivalent to (9.35), as should be expected. For $Y \to 0$ and $We \to 0$, with $Y/\sqrt{We} \to 0$, we have

$$k^* = \frac{1}{\sqrt{2}} + Y\left(\frac{1-\lambda}{8\sqrt{We}}\right) + Y^2\frac{\sqrt{2}(3\lambda+1)(\lambda-1)}{128We} + O\left(\frac{Y^3}{We^{3/2}}\right). \tag{9.37}$$

This result agrees with (9.35) for $We \to 0$. Therefore, for $Y = 0$ in (9.36) and (9.37), we obtain the same results as those produced by the classical continuum model.

9.2 Comparison of Results

We now compare the results of the interface formation model to molecular dynamic simulations carried out by Kawano [30] to study the rupture of a nanojet of argon (without an orifice) into tiny droplets using the Lennard-Jones 12-6 potential. Even though this is a slightly different problem from a jet emerging from an orfice, it produces the same results for the most unstable travelling wave mode for temporal instability ([44]). Here we use more realistic parameters than those used in [13] to compare the most unstable wavenumbers predicted by the theory of interface formation and the classical model to molecular dynamics simulations.

In Kawano [30], five simulations were carried out for different values of a, the initial undisturbed radius of the jet. We carry out our computations using parameters which correspond to microjets having a very small initial radius and use estimates of parameters A and L from Blake *et al.* ([5], [6]) given by

$$A \approx \frac{5\sigma_e \delta l}{4\mu a U}, L \approx \frac{\lambda \delta l}{\tau U\left(\lambda+1\right)}. \tag{9.38}$$

These estimates hold since $\varrho_0 \approx \rho\delta l, \beta \approx \mu/\delta l$ and $\alpha \approx 1/\beta$, where δl is the thickness of the interface (about 10^{-9} metres for most liquids).

The liquid density in Kawano [30] is taken to be $\rho = 1223\text{kgm}^{-3}$ which we take as our bulk density. The undisturbed jet speed is taken as $U = 10\text{ms}^{-1}$. We take $\sigma_e = 5.04199\times10^{-3}\text{Nm}^{-1}$ (Upstill & Evans [66]) and $\mu = 1.34762\times10^{-4}\text{kgm}^{-1}s^{-1}$ (Haynes [27]) which are the surface tension and viscosity of argon, respectively, corresponding to the density $\rho = 1223\text{kgm}^{-3}$. The surface relaxation time is taken to be $\tau = 10^{-9}$s (estimated by Davis & Rideal [12] for water (no experiments are available for τ for argon)) and the thickness of the interface for most liquids is taken to be $\delta l = 10^{-9}$m. The value of λ is taken to be the experimental value measured by Blake *et al.* [6]. Since no information regarding these parameters is given in Kawano [30], these estimates for the parameters seem plausible. Decent [13] showed that the values of k^* are found to be independent of

the value of U and U scales out e.g. see equation (9.35). Other values of U were tried and the results in Tables 9.1 and 9.2 for the values of k^* in each case were found to be unaffected. The value of U quoted is indicative of typical velocities, but unimportant to the evaluation of k^*.

The results of the most unstable wavenumber predicted by the interface formation model (9.32), the classical continuum model (9.35) and molecular dynamics simulations (presented in Kawano [30]) are shown in Table 9.1. The table shows the the results of the most unstable wavenumber found by molecular dynamics simulations k^*_{MD} (from [30]), the most unstable wavenumber found by the interface formation model k^*_{IF} (using (9.32)) and the most unstable wavenumber found by the classical viscous theory k^*_{cv} (using (9.35)) along with the corresponding values of We, Re, Y and A. Table 9.2 shows the results of the corresponding dimensional wavelengths l_{MD}, l_{IF} and l_{cv} of the most unstable wave found by molecular dynamics simulations k^*_{MD} (from [30]), the interface formation model k^*_{IF} (using 9.32) and the classical viscous theory k^*_{cv} (using 9.35), respectively. From Tables 9.1 and 9.2 it can be seen that the classical results are in fairly good agreement with molecular dynamics simulations. However, we observe that better agreement is found between the results obtained from the interface formation model and molecular dynamics simulations.

To better understand and test the validity of the interface formation model, more elaborate experiments on the micron scale need to be conducted to compare drop-sizes and breakup length of viscous liquid jets. This is a suggestion for future work.

9.3 Conclusion

In this chapter, we have studied the linear instability of viscous liquid jets at micron and nano scales using the interface formation model. A comparison has been made between the most unstable wavenumber produced by the theory of interface formation (which uses the concept of surface phase and dynamic surface tension) and the standard classical continuum results to molecular dynamics simulations at nano scales. Encouraging agreement

Simulation	k^*_{MD}	k^*_{IF}	k^*_{cv}	We	Re	Y	A
1.	0.433	0.342	0.252	0.0067663	0.0253156	35.8485	16.765444
2.	0.500	0.354	0.268	0.0091019	0.0340540	26.6496	12.463368
3.	0.418	0.349	0.261	0.0080629	0.0301667	30.0837	14.069404
4.	0.386	0.370	0.319	0.0209979	0.0785619	11.5518	5.4024885
5.	0.400	0.369	0.348	0.0328013	0.1227009	7.39492	3.4584215

Table 9.1: Table showing the comparison between the results of the most unstable wavenumber found by molecular dynamics simulations k^*_{MD} (from [30]), the most unstable wavenumber found by the interface formation model k^*_{IF} (using (9.32)) and the most unstable wavenumber found by the classical viscous theory k^*_{cv} (using (9.35)). The table also shows the corresponding values of We, Re, Y and A.

Simulation	l_{MD} (m)	l_{IF} (m)	l_{cv} (m)
1.	4.047822×10^{-9}	5.124874×10^{-9}	6.955186×10^{-9}
2.	4.715404×10^{-9}	6.660176×10^{-9}	8.797397×10^{-9}
3.	4.996485×10^{-9}	5.984328×10^{-9}	8.002033×10^{-9}
4.	14.09105×10^{-9}	14.70039×10^{-9}	17.05061×10^{-9}
5.	21.24156×10^{-9}	23.02608×10^{-9}	24.41559×10^{-9}
Average	9.818465×10^{-9}	11.09917×10^{-9}	13.04416×10^{-9}

Table 9.2: Table showing the comparison between the results of the corresponding dimensional wavelength l_{MD} of the most unstable wavenumber found by molecular dynamics simulations k^*_{MD} (from [30]), the corresponding dimensional wavelength l_{IF} of the most unstable wavenumber found by the interface formation model k^*_{IF} (using (9.32)) and the corresponding dimensional wavelength l_{cv} of the most unstable wavenumber found by the classical viscous theory k^*_{cv} (using (9.35)).

between the results obtained from the interface formation model and molecular dynamics simulations has been found. To test the theory further, a comparison with experiments is required in order to compare drop-sizes and break-up length of microjets. We will collaborate with Jeremy Marston at King Abdullah University of Science and Technology (Saudi Arabia), who has been conducting experiments on microjets. A comparison can then be made between experiments and theory.

The results that we have obtained in this chapter have concentrated on convective instability of microjets. The study of absolute instability of microjets is a suggestion for future work as the small Weber numbers indicate that absolute instabilities may be important.

Chapter 10

Conclusions and Future Work

In this thesis we have looked at absolute instability in liquid jets. Absolute instability in straight jets has been studied by various authors ([36], [37], [41]) and hence the main focus of this thesis was absolute instability in curved jets produced in the industrial process of prilling. We have paid especial attention to the Mode 4 type break-up regime observed in experiments in [70] as its unique features lead to the speculation of the existence of absolute instability in this case. We have also studied absolute instability in the thin ligaments that are formed as the jet breaks up, which eventually cause the formation of satellite drops. Our study is also extended by incorporating the non-Newtonian effects into the curved jet model and examining absolute instability. Finally, we have looked at microjets and nanojets (having radius of the order of micrometers and nanometers, respectively) using the interface formation model and compared the results to the classical continuum model and molecular dynamics simulations. In this chapter we give a summary of the main results obtained in this thesis and make suggestions for future work.

10.1 Conclusions

In Chapter 1, we started by providing a literature review of the research carried out on liquid jets and gave a brief outline of the work to be carried out in this thesis. We then moved on to look at absolute instability in straight liquid jets in Chapter 2 and described the method used in Lin & Lian [41] of finding the critical Weber number which indicates

a transition from convective to absolute instability. We determined the critical boundary in the *Re*-We plane for small and large Reynolds numbers. The jet is absolutely unstable below the curve and convectively unstable above it. This curve was new for small Reynolds numbers.

In Chapter 3, we presented the Newtonian curved jet model introduced in Wallwork [68] and briefly explained the derivation of the equations which can be solved computationally to determine the trajectory of the centreline of the jet along with its radius and velocity. Also, the linear stability analysis was described and the results of the dispersion relation for curved liquid jets were detailed. This dispersion relation has previously only been used to study convective instability. Experimental work carried out by Wong *et al.* [70] on curved liquid jets was also described. Four different break-up regimes were identified in [70]. Of particular interest is the Mode 4 break-up regime (where disturbances are observed to travel in both the upstream and downstream directions) and the No Jet situation (where no coherent jet is formed as the liquid leaves the orifice) which have features hinting the existence of absolute instability.

In Chapter 4, we begin our study of absolute instability in curved liquid jets making use of the critical curve obtained in Chapter 2. We define the local Reynolds $Re_{local}(s)$ and Weber $We_{local}(s)$ numbers which are computed for every s produced in the Runge-Kutta method (used to numerically solve the curved jet model). Solving the model (neglecting gravity) for a given We, Re and Rb with $Re_{local}(0) = Re$ and $We_{local}(0) = We$, we determine the Re_{local}-We_{local} trajectory. This trajectory is found to oscillate in the *Re*-We space. Using this concept we determine a region above the critical curve in the convective instability region, which we call the Mode 4 region. Re_{local}-We_{local} trajectories starting in this region (i.e. having $Re_{local}(0)$ and $We_{local}(0)$ lying in this region) always cross the critical curve for some value of s (i.e. make a switch over from convective to absolute instability). Mode 4 regions were calculated for different Rossby numbers. The size of the Mode 4 region was found to increase as Rb decreased, in agreement with experimental observations. A singularity is observed at $We = 1$ where we fail to compute the correct

We^* value (where (Re, We^*) is the smallest We for a particular Re at which the Re_{local}-We_{local} trajectory starting at this point does not cross the critical curve). In order to study the singularity region, an asymptotic analysis for $We \to 1$ was carried out. The asymptotics revealed that the Mode 4 region shrinks and the length scale of the calculation tends to zero as $We \to 1$. By incorporating the asymptotic predictions, the complete Mode 4 regions were determined within the gap close to $We = 1$ by reducing the step-size in the Runge-Kutta method. We also solved the asymptotic equations numerically and used the results produced to compute the Re_{local}-We_{local} trajectory in the singularity region as $We \to 1$ to find the Mode 4 curves. These Mode 4 curves agree exactly with those found by reducing the step-size of the computation.

The study of absolute instability was extended in Chapter 5 by incorporating the density ratio of the surrounding gas to liquid and the effect of gravity on the Mode 4 curves by considering the full three-dimensional jet equations. The critical curve marking the boundary between convective and absolute instability in the Re-We space was determined for $Q \neq 0$ (where Q is the density ratio) using the method described in Chapter 2. At small Reynolds numbers, density ratio has almost no affect on absolute instability. The critical curves obtained for different values of Q nearly overlapped. The area under the critical curves calculated at large Reynolds numbers for different Q values was found to increase, but not very much. Therefore, it seems sensible not to pursue this line of research, since it has little effect. To include gravity into the model, the full three-dimensional equations in the xyz plane were solved numerically to calculate the Re_{local}-We_{local} trajectory. Mode 4 regions were obtained for different values of Rossby and Froude numbers. When $F = \infty$, the three-dimensional jet equations become equivalent to the two-dimensional jet model in the xz plane. Therefore, the Mode 4 regions determined at a constant Rb with $F = \infty$ were the same as those obtained by using the two-dimensional model in Chapter 4. For small Rossby and Froude numbers, the upper boundary of the Mode 4 region for $Re < 5$ was found to be constant at $We^* = 1.01$, whereas for $Re > 5$ the Mode 4 boundary coincides with the critical curve, implying no Mode 4 type break-up for $Re > 5$. At

small Rb and F as we compute the Re_{local}-We_{local} trajectory, our slender jet assumption becomes invalid and our model breaks down (as $u_0 \to 0, R_0 \to \infty$). At this point the Matlab program which solves the steady state jet equations for X, Y, Z, u_0 and R_0 produces incorrect results by returning complex values. Therefore, to validate the accuracy of our numerics we used a variable step-size method which automatically changes the step-size at each step to meet the error conditions. Using this program we find that the model breaks down only after the Re_{local}-We_{local} trajectory has crossed the critical curve and a transition from convective to absolute instability has occurred.

In Chapter 6 we compared our theoretical predications to the experimental results of Wong *et al.* [70]. More detailed experiments focussing on the Mode 4 and No Jet parameter regimes were carried out as a part of this thesis by the author. To test our theory with the experimental results of Wong *et al.* [70], the curved jet model was solved and the Re_{local}-We_{local} trajectory was determined using experimental parameters corresponding to the different modes of break-up. For experimental parameters representing Modes 1, 2 and 3, we found that the Re_{local}-We_{local} trajectory starts in the convective instability region and always remains above the critical curve in this case. Therefore, the theory here predicts a convectively unstable jet. However, for trajectories calculated by using experimental parameters corresponding to jets experiencing a Mode 4 type break-up, we find that they start in the convective instability region above the critical curve but cross the critical boundary and enter the absolute instability region at some s (i.e. make a transition from convective to absolute instability); while trajectories calculated by using parameters corresponding to the No Jet situation start below the critical curve in the absolute instability region. These results were complied in a table and good agreement was found between theory and experiments. More lab-scale experiments were carried out due to the lack of experimental data at small Weber numbers (where Mode 4 is observed) in [70]. Along with the standard Mode 4 identified in [70], break-up modes varying slightly from Mode 4 in their physical features were discovered along with some borderline cases which switch from convective to absolute instability. Experimental parameters

corresponding to different break-up modes were plotted in the critical Re-We plane along the Mode 4 curve and their position was examined. Most of Re and We data points for Mode 4 and its variations lie in the M4 region for small F and Rb (which is a straight line at a constant We^*) and those corresponding to the convective modes (Modes 1, 2 and 3) lie in the convective instability region above the critical boundary and the M4 region. Very good agreement between experiments and theory was found confirming our hypothesis formulated in Chapter 3. The hypothesis states that jets undergoing Mode 4 type break-up have Re and We lying in the Mode 4 region above the critical boundary in the convective instability region implying that the jet is convectively unstable to start with but becomes absolutely unstable as it grows; while jets that are convectively unstable (Modes 1, 2 and 3) have their experimental Re and We values lying above the critical and Mode 4 curves in the convective instability region. Finally, the No Jet case corresponds to Re and We values lying below the critical curve in the absolute instability region implying that the flow is absolutely unstable at the orifice and hence fails to take the shape of a coherent jet.

In Chapter 7 we use the nonlinear model derived in Parau *et al.* [52] to study absolute instability in ligaments formed during jet break-up. We make use of the multiple scales approach (introduced in Chapter 4) to calculate the Re_{local} and We_{local} along the ligament for various values of s and t and plot their position in the Re-We space along with the critical curve. Our results indicate that the jet is convectively unstable as it approaches break-up, but at pinch-off it becomes absolutely unstable since the Re_{local} and We_{local} values in this case lie below the critical curve in the absolute instability region. We have presented experimental photographs which provide qualitative agreement with our theoretical results as they depict the break-up of a jet along with the formation of ligaments which then break-up to form satellite drops. However, more experiments need to be carried out in order to perform a detailed quantitative experimental comparison.

Chapter 8 looks at absolute instability in non-Newtonian curved liquid jets by incorporating the apparent viscosity into the Newtonian curved jet model. We have obtained

preliminary results and determined three basic types of solutions - (i) convective: when we obtain solutions to the dispersion relation which return $Re(\omega) < 0 \ \forall s$, (ii) Mode 4: when we obtain solutions which give $Re(\omega) < 0$ up to a certain value of s and $Re(\omega) > 0$ for values of s which are greater than this s at which $Re(\omega)$ switches sign and (iii) No Jet: when the solution to the dispersion relation computes ω with $Re(\omega) > 0$ for $s = 0$. We have obtained some preliminary results which validate our approach, however, a more efficient and less time consuming methodology needs to be employed to carry out a thorough parameter search.

Chapter 9 looked at the instability of jets on very small scales (of the order of micrometers and nanometers) using the interface formation model which uses the concept of dynamic surface tension. The most unstable wavenumber was calculated and compared to the result produced by the classical continuum model. The accuracy of these models was tested by comparing the results produced by the interface formation model and the classical continuum model with molecular dynamics simulations. Good agreement was found between the results of the interface formation model and molecular dynamics simulations.

10.2 Future Work

In this section we list the possible future extensions of this thesis. In Chapter 8, we provided a lengthy approach of studying absolute instability using the non-Newtonian model for curved liquid jets. This method needs to be automated in order to make it more efficient so a more detailed parameter search can be carried out. Also, experiments similar to those conducted in Chapter 6 using non-Newtonian fluids need to be carried out. An experimental search for break-up modes in the non-Newtonian case affected by absolute instability or exhibiting Mode 4 like behaviour will be interesting to examine. Results from these experiments can then be used to compare with our primitive theoretical study of absolute instability in curved non-Newtonian jets presented in Chapter 8.

Our study of absolute instability can be extended to compound jets which consist of

an outer jet of fluid enveloped around an inner immiscible fluid. Compound jets have numerous applications in the pharmaceutical and food industry mainly as a means of encapsulation which requires the inner and outer fluids to breakup simultaneously. Even though the break-up dynamics in this case is a lot more complex, a similar approach (as that used for a single jet) can be used to study absolute instability.

Jeremy Marston, currently a research fellow at the King Abdullah University of Science and Technology (Saudi Arabia), will be carrying out experiments on liquid jets on the micron and nano scales. We will collaborate with him in order to carry out a comparison of the theoretical results obtained in Chapter 9 with experiments to further test the accuracy of the interface formation model. We will also look at absolute instability in microjets. This is likely to be important since the Weber number is small on the micron and nano scales and hence an absolute instability approach in Chapter 9 is likely to be important, extending that work.

Bibliography

[1] M. H. I. Baird and J. F. Davidson. Annular jets-I: Fluid dynamics. *Chem. Eng. Sci*, 17:467–472, 1962.

[2] N. J. Balmforth, R. V. Craster, and C. Toniolo. Interfacial instability in non-newtonian fluid layers. *Phys. Fluids*, 15:3370–3384, 2003.

[3] M. P. Berezin, K Hutter, and L.A. Spodavara. Stability analysis of gravity driven shear flows with free surface for power-law fluids. *Arch. Appl. Math.*, 68:169–178, 1998.

[4] A. Bers. *Handbook of plasma physics*, volume 1. North-Holland, Amsterdam, 1983.

[5] T. D. Blake, M. Bracke, and Y. D. Shikhmurzaev. Experimental evidence of nonlocal hydrodynamic influence on the dynamic contact angle. *Phys. Fluids*, 11:1195–2007, 1999.

[6] T. D. Blake and Y. D. Shikhmurzaev. Dynamic wetting by liquids of different viscosity. *J. Colloid Interface Sci.*, 253:196–202, 2002.

[7] R. J. Briggs. *Electron stream interaction with plasmas*. MIT Press, Cambridge, MA, 1964.

[8] K. C. Chaudhary and T. Maxworthy. The nonlinear capillary instability of a liquid jet. Part 2. Experiments on jet behaviour before droplet formation. *J. Fluid Mech.*, 96:275–286, 1980a.

[9] K. C. Chaudhary and T. Maxworthy. The nonlinear capillary instability of a liquid jet. Part 3. Experiments on satellite drop formation and control. *J. Fluid Mech.*, 96:287–297, 1980b.

[10] N. Chieger and R. D. Reitz. *Recent advances in spray combustion: Spray atomization and drop burning phenomena*, volume I. AIAA, 1996.

[11] C. Clasen, J. Eggers, M. A. Fontelos, J. Li, and G.H. McKinley. The beads-on-string structure of viscoelastic threads. *J. Fluid Mech.*, 556:283–308, 2006.

[12] J. T. Davies and E. K. Rideal. *Interfacial Phenomena*. Academic Press, second edition, 1963.

[13] S. P. Decent. On the instability of microjets. *Continuum Mechanics and Thermodynamics*, 17:525–543, 2006.

[14] S. P. Decent, A. C. King, M. J. H. Simmons, E. I. Părău, I. M. Wallwork, C. J. Gurney, and J. Uddin. The trajectory and stability of a spiralling liquid jet: Viscous theory. *Applied Math. Modelling*, 33:4283–4302, 2009.

[15] R. J. Donnelly and W. Glaberson. Experiments on the capillary instability of a liquid jet. *Proc. R. Soc. Lond.*, A 290:547–556, 1966.

[16] P. Doshi, R. Suryo, O. E. Yildirim, G. H. McKinley, and O. A. Basaran. Scaling in pinch-off of generalised newtonian fluids. *J. Non-Newton. Fluid Mech.*, 113:1–27, 2003.

[17] V. Dravid, C. M. Loke, and P. E. Sojka. Drop formation in non-newtonian jets at low reynolds numbers. *J. Fluid Eng.*, 130:081504, 2008.

[18] J. Eggers. Universal pinching of 3D axisymmetric free-surface flow. *Phys. Rev. Letters*, 71:3458–3460, 1993.

[19] J. Eggers. Nonlinear dynamics and breakup of free-surface flows. *Rev. Mod. Phys.*, 1997.

[20] J. Eggers. Dynamics of liquid nanojets. *Phys. Rev. Lett.*, 89:1165, 2002.

[21] J. Eggers and T. F. Dupont. Drop formation in a one-dimensional approximation of the Navier-Stokes equation. *J. Fluid Mech.*, 262:205–221, 1994.

[22] J. Eggers and E. Villermaux. Physics of liquid jets. *Rep. Prog. Phys.*, 71, 2008.

[23] D.S. Finnicum, S. J. Weinstein, and K. J. Ruschak. The effect of applied pressure on the shape of a two-dimensional liquid curtain falling under the influence of gravity. *J. Fluid Mech.*, 255:647–665, 1993.

[24] E. P. Furlani. Temporal instability of viscous microjets with spatially varying surface tension. *J. Phys. A: Math. Gen.*, 38:263–276, 2005.

[25] E. F. Goedde and M. C. Yuen. Experiments on liquid jet instability. *J. Fluid Mech.*, 40:495–511, 1970.

[26] C. J. Gurney. *The stability and control of curved liquid jet break-up.* PhD thesis, University of Birmingham, 2009.

[27] W. M. Haynes. Viscosity of gaseous and liquid argon. *Physica*, 67:440–470, 1973.

[28] J. H. Hilbing and S. D. Heister. Droplet size control in liquid jet breakup. *Phys. Fluids*, 8:1574–1581, 1996.

[29] C. Hwang, J. Chen, J. Wang, and J. Lin.

[30] S. Kawano. Molecular dynamics of rupture phenomena in a liquid thread. *Phys. Rev. E*, 58:4468–4472, 1998.

[31] J. B. Keller and J. Geer. Flows of thin streams with free boundaries. *J. Fluid Mech.*, 59:417–432, 1973.

[32] J. B. Keller, S. I. Rubinow, and Y. O. Tu. Spatial instability of a jet. *Phys. Fluids*, 16:2052–2055, 1973.

[33] J. Koplik and R. Banavar, J. Molecular dynamics of interface rupture. *Phys. Fluids A*, 5:521–535, 1993.

[34] T. A. Kowalewski. On the separation of droplets from a liquid jet. *Fluid Dynamics Research*, 17:121–145, 1996.

[35] H. C. Lee. Drop formation in a liquid jet. *IBM J. Res. Dev.*, 18:364–369, 1974.

[36] S. J. Leib and M. E. Goldstein. Convective and absolute instability of a viscous liquid jet. *Phys. Fluids*, 29:952–954, 1986.

[37] S. J. Leib and M. E Goldstein. The generation of capillary instabilities on a liquid jet. *J. Fluid Mech.*, 168:479–500, 1986.

[38] J. Li and M. A. Fontelos. Drop dynamics on the beads-on-string structure for viscoelastic jets: A numerical study. *Phys. Fluids*, 15:922–937, 2003.

[39] S. P. Lin. *Breakup of liquid sheets and jets.* Cambridge University Press, 2003.

[40] S. P. Lin and D. J. Kang. Atomization of a liquid jet. *Phys. Fluids*, 30:2000–2006, 1987.

[41] S. P. Lin and Lian Z. W. Absolute instability in straight liquid jets. *Phys. Fluids*, 1:490–493, 1989.

[42] S. P. Lin and Lian Z. W. Absolute and convective instability of a viscous liquid jet surrounded by a viscous gas in a vertical pipe. *Phys. Fluids*, 5:771–773, 1993.

[43] E. Mariotte. *Traité du mouvement des eaux et des autres corps fluides.* E. Michallet, Paris, 1686.

[44] S. Middleman. *Modelling axisymmetric flows: Dynamics of films, jets and drops.* Academic Press, 1995.

[45] M. Moseler and U. Landman. Formation, stability and breakup of nanojets. *Science*, 289:1165, 2000.

[46] B. O'Donnell, J. N. Chen, and S. P. Lin. Transition from convective to absolute instability in a liquid jet. *Phys. Fluids*, 13:2732–2734, 2001.

[47] T. Papageorgiou, D. On the breakup of viscous liquid threads. *Phys. Fluids*, 7:1529, 1995.

[48] L. Partridge, D. C. Y. Wong, M. J. H. Simmons, E. I. Părău, and S. P. Decent. Experimental and theoretical description of the break-up of curved liquid jets in the prilling process. *Chem. Eng. Res. Des.*, 83:1267–1275, 2005.

[49] W. T. Pimbley and H. C. Lee. Satellite droplet formation in a liquid jet. *IBM J. Res. Dev.*, 21:21–30, 1977.

[50] J. Plateau. *Statique Experimentale et Theoretique des Liquides Soumis aux Seules Forces Moleculaires*, volume II. Gauthier Villars, 1873.

[51] E. I. Părău, S. P. Decent, A. C. King, M. J. H. Simmons, and D. C. Y. Wong. Nonlinear travelling waves on a spiralling liquid jet. *Wave Motion*, 43:599–613, 2006.

[52] E. I. Părău, S. P. Decent, M. J. H. Simmons, D. C. Y. Wong, and A. C. King. Nonlinear viscous liquid jets from a rotating orifice. *J. Eng. Math.*, 57:159–179, 2007.

[53] J. I. Ramos. Upward and downward annular liquid jets: Conservation properties, singularities, and numerical errors. *Appl. Math. Modelling*, 20:440–458, 1996.

[54] J. W. S. Rayleigh. On the stability of liquid jets. *Proc. Lond. Math. Soc.*, 10:4–13, 1878.

[55] Lord Rayleigh. On the instability of a cylinder of viscous liquid under capillary force. *Phi. Mag.*, 34:145, 1892.

[56] F. Savart. Memoire sur la constitution des veines liquides lancees par des orifices circulaires en mince paroi. *Annal. Chim.*, 53:337–374, 1833.

[57] R. M. S. M. Schulkes. Dynamics of liquid jets revisited. *J. Fluid Mech.*, 250:635–650, 1993.

[58] Y. D. Shikhmurzaev. The moving contact line on a smooth solid surface. *Int. J. Multi-phase Flow*, 19:589–610, 1993.

[59] Y. D. Shikhmurzaev. Capillary breakup of liquid threads: a singularity-free solution. *IMA J. Appl. Math.*, 70:880–907, 2005.

[60] A. M. Sterling and Sleicher C. A. The instability of capillary jets. *J. Fluid Mech.*, 68:477–495, 1975.

[61] S. Tomotika. On the stability of a cylindrical thread of a viscous liquid surrounded by another viscous fluid. *Proc. R. Soc. Lond.*, A 150:322–337, 1935.

[62] J. Uddin, S. P. Decent, A. C. King, and M. J. H. Simmons. Non-linear waves along rotating non-newtonian liquid jets. *Int. J. Eng. Sci.*, 46:1253–1265, 2008.

[63] J. Uddin, S. P. Decent, and M. J. H. Simmons. The instability of shear thinning and shear thickening spiralling liquid jets: Linear theory. *J. Fluids Eng.*, 128:968–975, 2006.

[64] J. Uddin, S. P. Decent, and M. J. H. Simmons. The effect of surfactants on the instability of a rotating liquid jet. *Fluid Dynamics Research*, 2008. Article in Press.

[65] Jamal Uddin. *An Investigation into Methods to Control Breakup and Droplet Formation in Single and Compund Liquid Jets.* PhD thesis, University of Birmingham, 2007.

[66] C. E. Upstill and R. Evans. The surface tension and density profile of simple liquids. *J. Phys. C: Solid State Phys.*, 10:2791–2799, 1977.

[67] I. Vihinen, A. M. Honohan, and S. P. Lin. Image of absolute instability in a liquid jet. *Phys. Fluids*, 11:3117–3119, 1997.

[68] I. M. Wallwork. *The trajectory and stability of a spiralling liquid jet.* PhD thesis, University of Birmingham, 2002.

[69] C. Weber. Zum zerfall eines flussigkeitsstrahles. *Z. Angew. Math. Mech.*, 11:136–141, 1931.

[70] D. C. Y. Wong, M. J. H. Simmons, S. P. Decent, E. I. Părău, and A. C. King. Break-up dynamics and drop size distributions created from spiralling liquid jets. *Int. J. Multiphase Flow*, 30:499–520, 2004.

[71] A. L. Yarin. *Free liquid jets and films: Hydrodynamics and rheology.* Longman, 1993.

[72] M. C. Yuen. Non-linear capillary instability of a liquid jet. *J. Fluid Mech.*, 33:151–163, 1968.

[73] Z. W. Zhou and S. P. Lin. Absolute and convective instability of a compressible jet. *Phys. Fluids*, 4:277–282, 1992.